Nanotribology of Ionic Liquid-Solvent mixtures

A Thesis Submitted for the degree of

Doctor of Philosophy

Aurora Kismet Guerrini

Worcester College

Physical and Theoretical Chemistry

University of Oxford

March 30, 2023



Abstract

Ionic liquids (ILs) have gained notoriety within the field of liquid matter, specifically as a lubricant. Fascination with ILs as lubricants is due to their physio-chemical stability and strong interactions with solid surfaces, marking an improvement over industrial lubricants. IL lubricants can therefore operate in high-pressure regimes without compromising the integrity of the surfaces.

While studies have demonstrated that pure ILs are excellent lubricants, using large amounts is costly and unfeasible for industry. A route around this problem is to use trace amounts of IL as an additive to make an industrially efficient lubricant.

This thesis explores the interfacial structure and frictional response across a range of IL-solvent mixtures to explore their performance as lubricant additives. Using the surface forces balance (SFB), the structural and frictional forces at the nanoscale can be simultaneously measured while the applied load is controlled. Macroscale friction behaviour is also studied using a ball-on-disc tribometer.

Both nanoscale and macroscale measurements across a range of ILs, mixed with either a polar solvent or a model base oil, showed that friction is influenced by the liquid film structure. Using the SFB, we were able to understand the molecular mechanisms underlying the friction, as we could probe the simultaneous confined structure. Varying the composition of these mixtures revealed that while macroscale performance could be improved with trace additions of ILs, the nanoscale behaviour was not as reliable.

The SFB measurements of oil-soluble ILs showed a lack of layering and ineffective lubrication when compared to the base oil, while the water-soluble IL showed reliable and superlubric performance across both length scales, with the nanoscale studies showing that a switch in the structural forces was reflected in the frictional forces.

These results indicate that while ILs can become lubricant additives, a wide-scale systematic study over multiple length scales and surfaces is required.

Declaration

This thesis is submitted for the degree of Doctor of Philosophy in Physical and Theoretical Chemistry at the University of Oxford. I confirm that the work presented here is my own. Where information has been derived from other sources, I confirm that this has been indicated in the thesis.

The measurements, analyses and interpretations reported in Chapter 6 and Chapter 8, were completed in partnership with Joshua Bowesman-Jones, a Part II student in the academic year 2021/2022.

Acknowledgements

This thesis would not have been possible if it weren't for the contribution and support of many people that I wish to thank.

Firstly, and perhaps most importantly, I would like to thank my supervisor Prof. Susan Perkin for her constant support. I am particularly grateful for her belief in my capabilities to undertake such a challenging task. Her advice, guidance and above all, her curiosity have inspired me and helped to grow and learn whilst undertaking this project.

Praise for past and current members of the group is also necessary. Along with Prof. Perkin, I owe much of my knowledge and development in the use of the Surface Forces Balance to Dr. Carla Perez-Martinez. Her enthusiasm and thorough knowledge was crucial in my early foray into using the Surface Forces Apparatus. Along with this, her patience and willingness to match my piqued interest in the technicalities has contributed greatly to my project. I would also like to thank everyone in the group I had the joy of interacting with and working with on a daily basis for their guidance, discussions and general friendliness: Hannah, Tim, Astrid, Josh, Illaria, Josie, Rachel, Kieran, Luis, James, Catherine, and Weichao. I would also like to acknowledge the tireless and crucial support provided by the mechanical and electrical workshops in the PTCL and members of the building management team (Paul and Martin).

I am wholeheartedly indebted to my parents for their love, support and their nurturing of my boundless curiosity. I am particularly grateful for their belief in me. On my mothers' part, her work-ethic and strive to succeed has greatly inspired me and helped me through any tough times during this project. The calm, serenity and belief in me that my father has shown throughout has been immensely important.

I would like to thank all my friends, specifically KA, JH, HS, KB, CL, TQ, AK, RO for reminding me that sometimes someone can work a bit too hard.

Finally, I would like to thank JSE for giving me the courage to even apply for a Doctorate and NMJS and my cat, Donatella, for supporting me throughout the writing of this thesis.

Funding for this studentship is gratefully received from EPSRC.

Contents

Abstract ii

Delcaration iv

Acknowledgements v

1 Introduction 1
- 1.1 Motivation . . . 1
- 1.2 Ionic Liquids: an Introduction . . . 2
  - 1.2.1 Classes and Structure of ionic liquids . . . 3
  - 1.2.2 Physical properties of ionic liquids . . . 5
- 1.3 The Interfacial Nanostructure of ionic liquids . . . 7
- 1.4 The Interfacial Nanostructure of ionic liquid mixtures . . . 12
- 1.5 Nanotribological properties of ionic liquids . . . 18
- 1.6 Scope of this study . . . 21
  - 1.6.1 Miscibility . . . 22
  - 1.6.2 Performance . . . 23
  - 1.6.3 Performance of Diluted mixtures . . . 23
- 1.7 Aims of this study . . . 25
- 1.8 Project Outline . . . 25

2 Theory 27
- 2.1 Surface Forces . . . 27
  - 2.1.1 DLVO Theory . . . 28
  - 2.1.2 Non-DLVO Structural Forces . . . 29
  - 2.1.3 Underscreening in Concentrated Electrolytes . . . 32
- 2.2 Tribological Theory . . . 33
  - 2.2.1 Contact Mechanics . . . 34
  - 2.2.2 Macroscale Friction . . . 37
  - 2.2.3 Lubricated Sliding . . . 41
  - 2.2.4 Lubrication Regimes . . . 47

3 Experimental Methods 51
- 3.1 Surface Force Balance . . . 51
  - 3.1.1 Surface Preparation . . . 51
  - 3.1.2 Lens Mount . . . 53
  - 3.1.3 Lens Motion . . . 54
  - 3.1.4 Minimising External effects . . . 57
- 3.2 Procedure and Analysis . . . 58
  - 3.2.1 Liquid preparation and Introduction . . . 58
  - 3.2.2 Determination of Surface Separation . . . 59
  - 3.2.3 Determination of Shear Forces . . . 61
  - 3.2.4 Measurement of Normal Forces . . . 62

3.2.5 Measurement of Shear Forces . . . 68
3.2.6 Analysis of Shearing Data . . . 70
3.2.7 Representative Data . . . 73
3.3 Tribometer . . . 74
3.3.1 Apparatus . . . 74
3.3.2 Calibration and Set-up . . . 74
3.3.3 Measuring Friction . . . 76
3.4 Comparison between macroscale (TRB) and nanoscale(SFB) . . . 76
3.5 Materials . . . 77

4 Normal and Lateral Forces of Salt-Dominant $[C_4C_1P_{yrr}][TFSI]$-Propylene Carbonate Mixtures 78
4.1 Introduction . . . 78
4.1.1 Aims of this section . . . 79
4.2 Normal Forces of Salt-Dominant $[C_4C_1P_{yrr}][TFSI]$-PC mixtures . . . 80
4.2.1 Structural Forces . . . 82
4.2.2 Oscillatory Forces . . . 85
4.3 Lateral Forces of Salt-Dominant $[C_4C_1P_{yrr}][TFSI]$-PC Mixtures . . . 93
4.3.1 Quantised Friction across the Salt-dominant films . . . 93
4.4 Summary . . . 107

5 Normal and Lateral Forces of Solvent-Dominant $[C_4C_1P_{yrr}][TFSI]$-Propylene Carbonate Mixtures 110
5.1 Introduction . . . 110
5.2 Normal Forces across Solvent-Dominant $[C_4C_1P_{yrr}][TFSI]$-PC mixtures 110
5.2.1 Structural Forces . . . 111
5.2.2 Oscillatory Forces . . . 113
5.3 Hydrodynamic Forces . . . 116
5.3.1 Fast Velocities . . . 119
5.3.2 Intermediate Velocities . . . 119
5.4 Friction Forces of Solvent-Dominant $[C_4C_1P_{yrr}][TFSI]$-PC mixtures . 123
5.4.1 Breakthrough point . . . 130
5.4.2 Effect of Shearing Velocity . . . 132
5.4.3 Friction Coefficients . . . 133
5.5 Summary . . . 137

6 Normal and Lateral Forces of $[P_{6,6,6,14}][(^iC_8)_2PO_2]$ Dodecane mixtures 139
6.1 Introduction . . . 139
6.2 Normal Forces of $[P_{6,6,6,14}][(^iC_8)_2PO_2]$-Dodecane mixtures . . . 141
6.2.1 Pure $[P_{6,6,6,14}][(^iC_8)_2PO_2]$ . . . 141
6.2.2 50 vol % $[P_{6,6,6,14}][(^iC_8)_2PO_2]$, 50 vol % Dodecane . . . 143
6.2.3 1 vol % $[P_{6,6,6,14}][(^iC_8)_2PO_2]$, 99 vol % dodecane . . . 147
6.2.4 Pure Dodecane . . . 149
6.3 Lateral Forces of $[P_{6,6,6,14}][(^iC_8)_2PO_2]$-Dodecane mixtures . . . 150
6.3.1 Pure $[P_{6,6,6,14}][(^iC_8)_2PO_2]$ . . . 150
6.3.2 50 vol % $[P_{6,6,6,14}][(^iC_8)_2PO_2]$, 50 vol % dodecane . . . 153

6.3.3 1 vol % $[P_{6,6,6,14}][(^iC_8)_2PO_2]$, 99 vol % dodecane 157
6.3.4 Pure Dodecane 159
6.4 Summary 160

7 Normal and Lateral Forces of $[P_{6,6,6,14}][TFSI]$ 163
7.1 Introduction 163
7.2 Normal Forces of pure $[P_{6,6,6,14}][TFSI]$ 164
7.2.1 Hydrodynamic Forces of pure $[P_{6,6,6,14}][TFSI]$ 164
7.2.2 Fast Velocities 165
7.2.3 Intermediate Velocities 165
7.2.4 Slow Velocities 166
7.2.5 Structural Forces of Pure $[P_{6,6,6,14}][TFSI]$ 167
7.3 Lateral Forces of Pure $[P_{6,6,6,14}][TFSI]$ 172
7.3.1 0.3Hz/ 639 nm/s 172
7.3.2 0.5Hz/ 1918 nm/s 174
7.3.3 0.7Hz/ 3197 nm/s 175
7.4 Summary 177

8 Macroscale Tribological studies using a Tribometer 179
8.1 $[C_4C_1P_{yrr}][TFSI]$ 181
8.1.1 Mica-Steel contact 181
8.1.2 Steel-Steel contact 182
8.2 $[P_{6,6,6,14}][(^iC_8)_2PO_2]$ 183
8.2.1 Mica-Steel contact 183
8.2.2 Steel-Steel contact 185
8.3 $[P_{6,6,6,14}][TFSI]$ 187
8.3.1 Mica-Steel contact 187
8.3.2 Steel-Steel contact 188
8.4 $[P_{1,4,4,4}][TFSI]$ 189
8.4.1 Mica-Steel contact 189
8.4.2 Steel-Steel contact 190
8.5 Summary 190

9 Conclusions and Outlook 193
9.0.1 Surface Forces Balance 193
9.0.2 Tribometer 195
9.0.3 Outlook 197

Bibliography 199

10 Appendix 214

1 | Introduction

1.1 | Motivation

The forces that govern the invisible yet tangible interactions at the solid-liquid interface have a unique importance in life.[1] These forces, and our own understanding of how they manifest, affect many significant processes, for example, the capillary action that plays a core role in photosynthesis,[1] the fabrication of novel polymer surfaces for drug delivery,[2] and the industrial processes that underpin how our world works.[1] In industry, the solid-liquid interface is central to the move towards more efficient and more sustainable processes, such as new green batteries,[3,4] and the miniaturisation of processes.[1,4] As our world has an almost universal reliance on machinery,[5,6] it is therefore not only necessary to understand this solid-liquid interface, but to be able to manipulate it and shape it to our needs.

Whilst many theories of the technological evolution of humans are disputed, most within the field of evolutionary anthropology point to two developments as being crucial: fire and the wheel.[6–8] These two elements form the basis of industry and are often at the core of any problems or inefficiencies present.[9] From the initial discovery of the wheel, perhaps the most crucial interface in industry was born, the gear. The gear presents a dichotomy in industry, because its usefulness is also limited by the very essence of its set-up, the interface of two sliding metal surfaces where friction dominates. While friction is a necessary phenomenon behind many processes, such as the characteristic sliding of a snake,[10] but within industry, it is often the limiting factor.[6,7] As a result, there has been a push to try to eliminate or lessen the effect friction has on these interacting surfaces.[6,7]

The key method of reducing friction is one that industry borrowed from the natural world, lubrication.[5,11] By inserting a substance, usually a liquid, the kinetic energy

generated by the motion of those sliding surfaces can be controlled.[5,11] In industry, it is hoped that the lubricant will reduce the friction of those sliding surfaces, with the end-goal to reduce wear and tear to preserve the integrity of those surfaces.[5] Evidence of oil-based lubricants from as early as 1400 BC have been found,[8,12,13] and while the modern-day lubricants are far more effective and advanced than these primitive compounds, they face the same limitations[11,14] These oil-based lubricants are often very sensitive to temperature and pressure, decomposing to exacerbate wear and tear.[7,14] In addition, the push of industry to miniaturise technology down to the nanoscale requires the use of lubricants able to withstand high pressure confinement and to perform well in nano-confinement.[7,14,15] With this in mind, it is clear that an alternative class of lubricants is required.[14,16]

The search for high stability compounds that can act as lubricants down to even nanoscale contacts has yielded a promising solution: ionic liquids.[17–19] This class of compounds have a unique range of chemical and physical properties that distinguish them from commonly-used lubricants.[7,14,15,20] Due to the near-endless number of ionic liquids and properties such as viscosity, electrical conductivity and miscibility[4,19,21,22] with a range of solvents, their use opens up the possibility for the fine-tuning of friction and for a greater understanding of the laws governing lubrication.[17,18]

This Thesis will focus on the interfacial nanostructures of ionic liquids and how their friction depends on this.

1.2 | Ionic Liquids: an Introduction

Ionic liquids(ILs) are a class of compounds that can be formally described as compounds composed entirely of ions with melting points typically below 100 °C (T_m < 100 ° C),[7,14,23] meaning that at room temperature, they are liquids.[24] This definition, while useful, has a general temperature constraint, $T_m < 100$ ° C, that in reality is not necessary to classify a compound as being an IL. It is instead useful

to compare ILs to typical salts, such as sodium chloride, NaCl, which only becomes molten at extremely high temperatures ($T_m < 800$ ° C), and describe them instead as compounds composed solely of anions and cations which have much lower melting points than what is expected and seen in similar purely ionic solutions.[7,14,23]

First observed experimentally by Walden in the 1910s,[24] they have since gone on to become a much studied and intriguing class of compounds,[17,23,24] and are known to thermally stable, highly conductive, and relatively non-toxic.[23] Along with similar compounds such as those used in the manufacture of supercritical fluids,[23] ILs have become one of the most popular of the 'neoteric solvents'[23,24] as their particular chemical and physical properties single them out for use in the ever-increasing push to develop sustainable chemicals.[23]

Their large and often-asymmetrically shaped constituent ions, such as *imidazolium* and *bistriflimide* based groups,[17,23,24] pictured below in Figure 1.1, prevent ILs from crystallising, and mean they remain liquid at room temperature.[23] Aside from the steric contributions, the electrostatics of the IL systems are also impacted by the large and asymmetric ion sizes,[17,23,24] as the large ion size and amphiphilic nature of the ions, where only part of the ion holds charge, greatly reduces the interactions between ions and gives rise to unique non-Debye-Hückel behaviour that has attracted great interest.[25] Furthermore, their unusual electrostatics coupled to certain properties such as high conductivity have provoked interest into their use in electrochemical systems such as supercapacitors.[26,27] However, their unique structure also gives rise to interfacial behaviours that imbue them with the ideal properties for a tribological compound.[15,17,19,21,28,28–30]

1.2.1 | Classes and Structure of ionic liquids

The constituent cations and anions afford the large chemical flexibility that is often associated with ILs.[23] The main types of anions and cations that have received the most attention as potential lubricants are shown below in Figure 1.1.[7] The

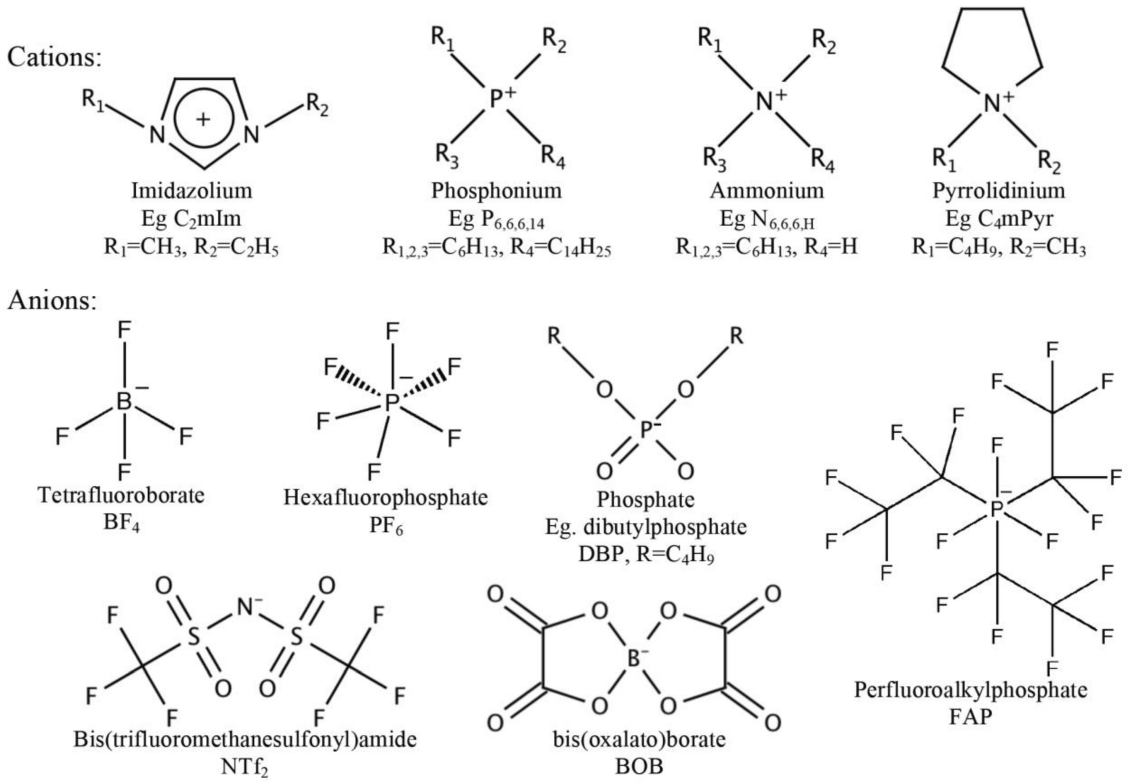


Figure 1.1: Structures of commonly-used cations and anions. Taken from[7]

nature of the bulk of ILs has been investigated using X-ray diffraction.[31–35] There is widespread agreement within the literature that the bulk structures of ILs all show evidence of polar/ non-polar segregation and significant meso-structuring and nano-structuring within the bulk, as pictured in Figure 1.2.[23,31,36–38]

This is analogous to the amphiphilic self-assembly associated with largely amphiphilic systems, with multiple simulation studies indicating slow dynamics and persistent structuring.[33,38,39] However, there is an additional constraint that differentiates ILs from these amphiphilic systems: the volume of the liquid consists only of the constituent ions.[35,37,40] Therefore, the structuring results from a balance between the optimisation of ion correlations, the space-filling requirement,,[33,39–41] and complex interactions.[33,39,41] These interactions can take the form of directional forces such as hydrogen bonding,[33,39,41] and non-directional forces such as van der Waals and electrostatics.[33,39,41]

ILs are often called designer chemicals because of the almost infinite number of

combinations of cations and anions.[15,19,42] Multiple studies, both theoretical and experimental, have found that altering the cation and anion components, both independently and simultaneously, alters the bulk and confined structure.[23,31,36–38] Therefore, careful selection of these components means that ILs are highly tunable.[4] With this in mind, ILs can become the system of choice for a number of applications.[23,42] These 'task-specific' ILs can therefore be designed to accommodate a particular shearing system.[7,23,42] However, before this can be done, a great deal of work is required to investigate their performance so as to find a system that is durable, sustainable, cost-effective, reliable, and if possible, tunable.[43]

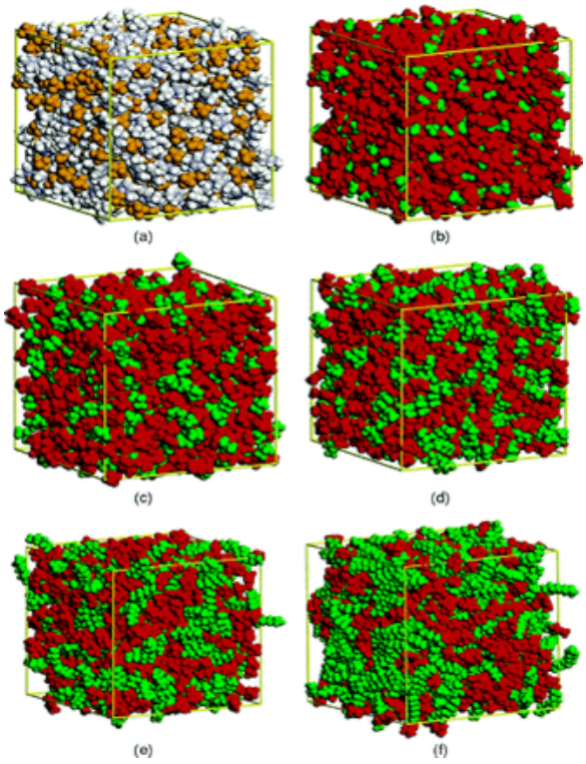


Figure 1.2: Meso-structuring of ILs: Snapshots of simulation boxes of $[C_n mim][PF_6]$ ILs. All boxes aside from (a) use a red/green colour coding where red is used to indicate the charged domains, while green represents the non-polar domains. (a) $[C_2 mim][PF_6]$ represented in CPK colouring; (b) $[C_2 mim][PF_6]$; (c) $[C_4 mim][PF_6]$; (d) $[C_6 mim][PF_6]$; and (e) $[C_8 mim][PF_6]$. Taken from[31]

1.2.2 | Physical properties of ionic liquids

The key physical properties which have singled ILs out as a promising liquid systems for a number of applications such as batteries, lubricant thin films and thermal

storage systems are often determined by the bulk structure.[23,31,42] Such properties are thermal stability, high viscosity and conductivity.[7,19,23,44]

The high thermal stability of ILs is a direct manifestation of the purely ionic composition that characterises ILs.[44–46] The strong electrostatic attractions between constituent anions and cations results in temperatures of vaporisation not seen in liquids of similar melting points.[23,44–47]

Along with thermal stability, high decomposition temperatures of ILs further distinguish them as potential industry-grade lubricants.[21,45,46] For example, two bis(trifluoromethylsulfonyl)imide based ILs: 1-Butyl-3-methylimidazolium bis(trifluoromethyl sulfonyl) imide, [BMIM][TFSI]; and 1-Butyl-1-methylpyrrolidinium bis(trifluoromethyl sulfonyl)imide, [bmpy][TFSI], were reported to have decomposition temperatures of $> 400°C$, with evidence of decomposition first occurring at 250°C.[44] A high decomposition temperature is a property that is severely lacking in current oil-based lubricants, where their decomposition often exacerbates the levels of wear and tear.[19,21,45,46] High decomposition temperatures therefore differentiate ILs from the already used lubricants, and represent a clear improvement.[19,21,45]

Similarly to thermal stability, the high viscosity of ILs is another direct consequence of their unique electrostatics.[22,46] With regards to lubrication, viscosity is perhaps the most important bulk characteristic of an IL.[19,21] This is because viscosity in itself is a measurement of the internal or molecular friction of a liquid and therefore has a bearing on the lubricity of the compound.[19,22,46] In the preparation and selection of lubricant oils, viscosity is often a limiting factor as many of these have low viscosities which are subject to sharp changes with temperature.[7,19,48] Therefore, the ability to couple high thermal stability to high viscosity is another improvement which ILs may offer over conventional lubricants.[45,46,49]

The high viscosity of an IL is thought to stem from the large degree of molecular friction caused by the strong electrostatic attractions between oppositely charged

constituent ions,[21,42] and it is well agreed within the literature that the viscosity of an IL is largely dependent on the ionic makeup.[22] A study concerned with quantifying and qualifying the relationship between structure and viscosity was performed by Kobrak *et al.*[22] Studies such as this enable and give clear credence to the fine-tuning of viscosity.[19] This is important because whilst the high viscosity may be advantageous to use a lubricant, any electrochemical application of ILs would require careful consideration of this as the conductivity may be limited by high viscosity.[22]

1.3 | The Interfacial Nanostructure of ionic liquids

Given the unique physiochemical properties and chemical flexibility of ILs,[37,38,50] it is strange that little interest was given to them for almost 50 years after their initial discovery.[23] It was only in the late 1970s that literature on the topic began to expand with many researchers starting to recognise that the thermal stability, viscosity and large solubility range of these liquids made them ideal solvents for a range of uses.[7,14,19,23,40,42] Whilst this use suited the bulk physiochemical properties of ILs, their classification as 'designer solvents' and an industry-wide push for 'clean', customisable and stable liquids with functionality across multiple length scales, made them the perfect candidate.[7,14,19,23,42]

The recent and quite fervent overwhelming focus in industry towards the fabrication and use of nano-electromechanical systems,[51–53] more sustainable batteries, and, crucially, lubricants, means that in some cases, the practical use of ILs will be at the micro or nanoscale.[49] At these length scale, structural forces will dominate[51–53] and, in this vein, it is necessary to understand the nano- and microscale behaviour of ILs.

The bulk nanostructure of fluids, such as ILs, is a consequence of the several interactions, such electrostatic attractions and repulsion, solvophobic forces, hydrogen-bonding, ligand-pairing, and van der Waals, that can form between the components present in the system.[23,31,42] Furthermore, as previously discussed, it is evident that

significant bulk mesostructure is present.[31,33,39,42,54] However, it is becoming exceedingly clear that the bulk nanostructure and confined nanostructure of a liquid systems are often quite different as they are subject to different interaction forces.[33,39,42] This is because the introduction of a microscopic interface is thought to break the isotropic symmetry of the system, perturbing the interaction forces and accordingly, the structure.[36,42] Furthermore, in most nanotechnological applications for ILs, such as nanotribological film for high pressure systems, ILs will be under fierce geometric confinement.[7,23,40,49]

A liquid is said to be confined when it is bounded by solid walls and whereby a large fraction of the molecules lie in close proximity or in contact with these confining walls.[49,55] Therefore, the bulk isotropic nanostructure becomes increasingly anisotropic in nature as charged and non-charged groups align parallel to the confining surface.[40] Such a geometric constraint often results in the perturbation of the interactions, and resultantly, the structure of the liquid.[56] This change, in turn, may drastically change certain properties of the system, such as viscosity and conductivity.[37,49,57] There have been numerous examples where this has been the case, such as in non-polar liquids, where the properties found in the bulk propagate in the confined structure.[23,42] However, whilst some molecular liquid interfaces, such as OMCTS and related systems,[58] are well understood, the same cannot be said for IL Interfaces. This fundamental lack of insight into this crucial interface prohibits this class of 'designer chemical' from realizing their potential.[23,24]

Investigations into the interfacial structure of ILs started with a paper titled, "Double-Layer and Solvation Forces measured in a Molten Salt and its Mixtures with Water".[59] In using the SFB to study the structural forces present in mixtures of Ethyl Ammonium Nitrate, EAN, and water they found that, at least in the case of the dilute EAN-water systems, the long ranged forces present were consistent with DLVO and Poisson-Boltzmann predictions of a double-layer repulsive force, see Figure 1.3.[23,24,59] However, the study of short ranged forces at various EAN concentra-

tions showed the existence of a pronounced oscillatory force - distance relationship. This oscillatory force was due to the repulsive 'walls' and attractive 'minima' commonly observed in previous SFB studies.[59,60] In this, each layer represents a stable region where squeeze-out cannot occur forming a wall.[40,59,61] At a certain load, the layer is squeezed out and the surfaces jump to a distance that corresponds to the next stable layer, representing a minimum.[42] Although this oscillatory profile had been seen in non-polar and polar liquids, the oscillatory force profile of EAN had spacings that were commensurate with the molecular volume of EAN (≈ 0.53 nm) and was independent of concentration.[59] However, the nature and arrangement of

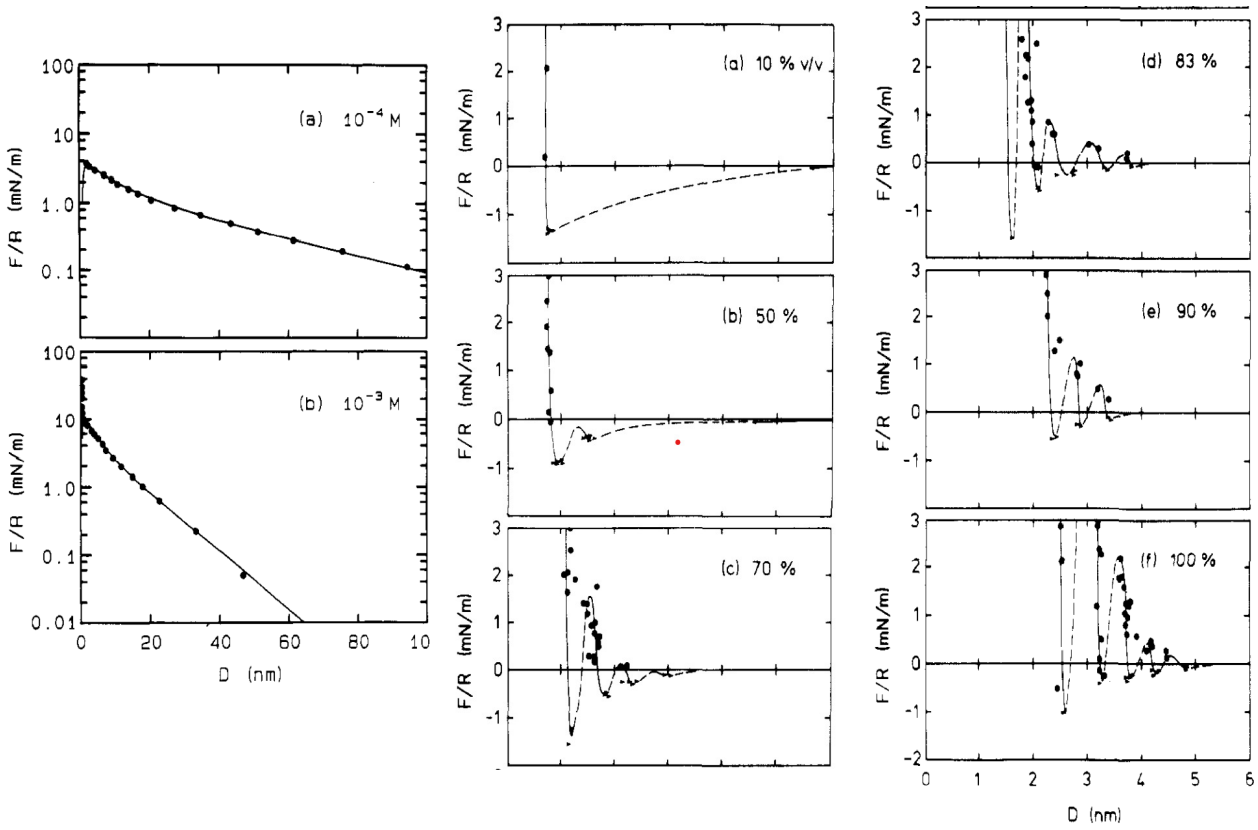


Figure 1.3: Normal Force Profiles for Dilute and Concentrated solutions of EAN: Right: F/R plotted as a function of surface separation, D that show an agreement with Poisson-Boltzmann. Left: F/R plotted as a function of D with increasing volume fractions of (a) 10% (b) 50% (c) 70% (d) 83% (e) 90% and (f) 100%. With increasing volume fraction, and therefore concentration, stable structuring regimes begin to dominate, and an oscillatory function, not predicted by Poisson-Boltzmann theory, dominates. Image taken from[59]

these stable layers could not be confirmed at the time. Consequently, in the mid 2000s, two independent studies, one conducted using AFM,[62] and the other con-

ducted using X-ray reflectivity studies at a charged sapphire surface,[63] confirmed that the oscillatory profile was a result of interfacial layering of cations and anions and is demonstrated in Figure 1.4. Furthermore, the former study had also found evidence that the oscillatory structural force observed changed with both cation and anion structure. Whilst a study using the SFB did once again show clear evidence of cation-anion layering,[62,64] it was disputed whether the charged mica surfaces had induced the layering, rendering it a templating effect and not a property stemming from the IL. In order to answer this, a 2012 study by Zhou[54] utilising both atomistic molecular dynamics simulations and X-ray scattering to study the interfacial layering at a charged surface, mica, and a neutral surface, graphene, showed that there was mixed cation/anion layering adjacent to the graphene.[54] Following on from these initial results, there have since been many reports of oscillatory structural forces of nanoconfined ILs.[40,65–68] In all of these studies, an oscillatory period commensurate with molecular volume and measurements of film thicknesses manifests in the following: an alternating cation-anion layering structure, where at the negatively charged interface (in the case of mica and other commonly used substrates), an initial layer of cations concentrates and 'screens' the surface charge, followed by electroneutral anion-cation layers.[40,49,65,66,69–71] In the case of most ILs, these electroneutral ion layers are odd-numbered, while for ILs with long alkyl chains, electroneutral bilayers aggregates constitute the layers found.[40,65,66,70,71]

This distinct ionic layering has been shown to persist and result in 3-10 distinguishable layers before a bulk-like structure is reported.[40,65,66,70,71] After the initial first layer solely composed of cations adjacent to the charged mica surface, the remaining layers are made up of cation-anion pairs with a decreasing 'purity of structure' away from the charged surface.[40,65,66,70,71] This alternating and eventually diminishing charge density is a manifestation of the overscreening effect expected in dense ionic systems.[26,40,65,66,70,71] The highly charged surface initially overcompensates by drawing too many cations to the surface, which, in-turn, results in a similar, albeit

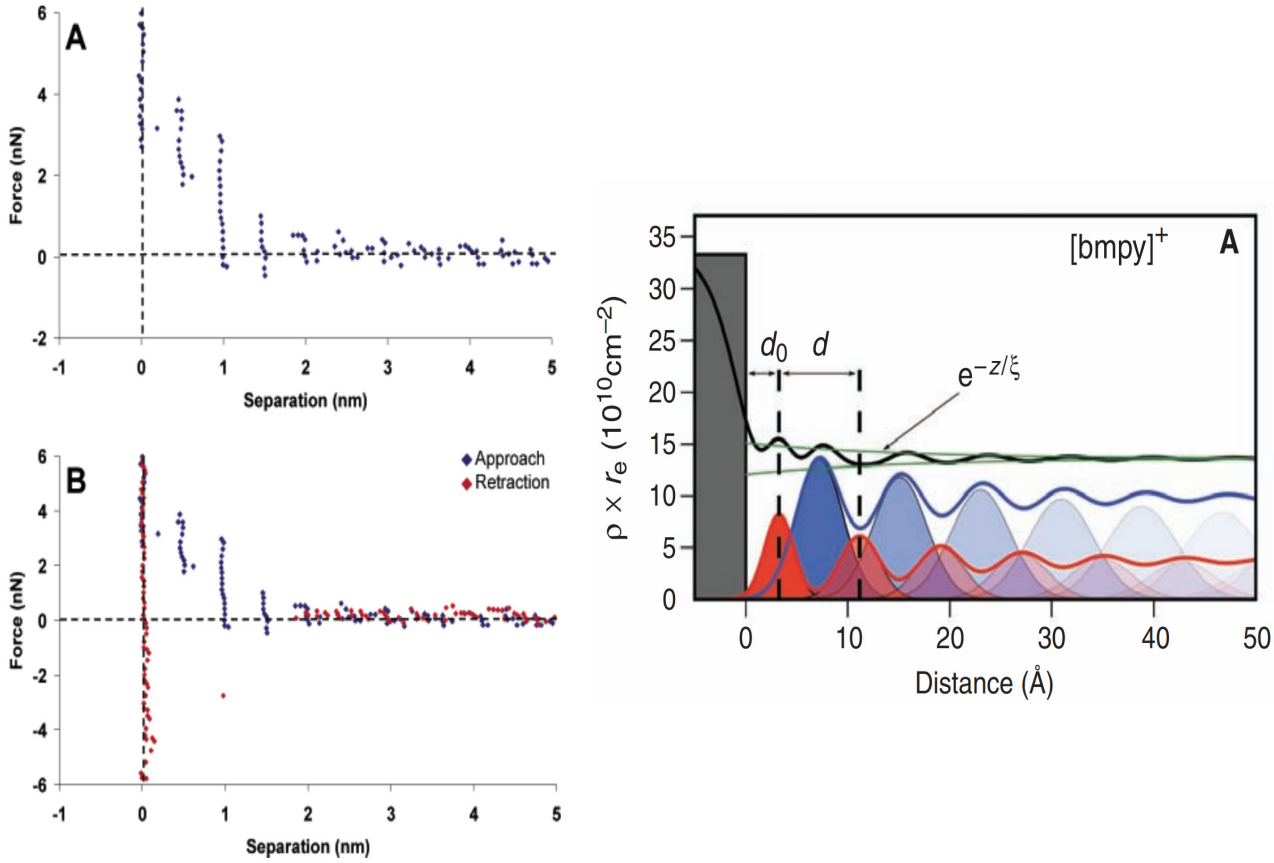


Figure 1.4: Evidence of the Structuring in ILs from an AFM and an X-ray scattering study: Left: (A) Force versus Distance profile for an AFM tip approaching a mica surface in EAN. At least six steps in the force curve can be seen, extending to a separation of 3 nm. Taken from[62] (B) Shows the same approach data along with that recorded as the AFM tip is retracted from the substrate. Right: Cation (red), anion (blue), and total (black) electron densities o. Red and blue lines indicate cation and anion Gaussian distributions contributing to the respective partial electron density profiles; black line, total electron density profile; and grey bar, electron density of the sapphire (001) substrate without roughness. Taken from[63]

depreciating, atonement within the subsequent ionic layers.

However, classical descriptions of dilute electrolytic systems, such as the Debye-Hückel (DH) theory, predict a monotonously and exponentially decaying ion distribution that does not fit the oscillatory decay associated with ILs.[26,65,66] It is thought that this is due to the charge-correlation function that, as described by the Kirkwood line, will change with concentration.[26,72,73]As the concentration increases, there is a cross-over from charge based-monotonic decay to a charge based exponentially damped oscillatory decay at $a/\lambda_D \approx 2$.[26,72,73] Moreover, the DH theory,

however cannot account for the behaviour of electrolyte systems at high concentration, so development of a more complete theory that takes into account factors such as ion-correlation effects, required.[26,72,73]

As previously mentioned, there is strong evidence indicating that the nanometre confinement of liquid films such as OMCTS alters certain physiochemical properties.[74–76] There is, likewise, evidence that this modification of properties is also native to IL systems. Particularly relevant for the development of IL tribofilms, which are films that form at the shearing surfaces and are often key to the real-world reduction of wear and tear and corrosion, is the changeable nature of the viscosity of such films subjected to strict confinement.[22,77–81]

1.4 | The Interfacial Nanostructure of ionic liquid mixtures

The structure of pure ILs adjacent to surfaces has been the subject of intense experimental scrutiny over the years and has become well understood and characterised.[82] However, there is limited knowledge on the interfacial structure where the IL is in near equimolar or intermediate concentration in solvent mixtures.[71,83] This limited understandings of such systems represents a massive obstacle to the development of ionic-liquid based systems.

Consideration of the nature of ILs in a variety of mixtures is important, both for the greater understanding of these systems and because these systems are where ILs will find their greatest practical use.[84,85] This is because the inclusion of a solvent either makes the IL more cost-effective, or modifies physiochemical properties integral to their use.[84–86] Therefore, the inclusion of solvents, and the effect this has on the properties of ILs, can be another route to modulating the properties of these 'designer chemicals'.

Particularly relevant to their use as lubricant films, it has been found that the viscosity of ILs can be changed with addition of solvent.[87,88] As mentioned previously,

the viscosity of a lubricant film is a principal factor in their use. Certain ILs have notably high viscosities[89] that would preclude them from uses as lubricant films, as a thick and highly viscous film would make the shearing process more energy intensive, creating an inefficiency.[19] Therefore, the possibility of retaining the surprising near superlubric behaviour that some IL studies have reported while modifying bothersome physiochemical properties, is an attractive route in the development of lubricant films.[19]

It is well-known that ILs are miscible with in a wide and varied range of solvents.[90,91] Moreover, a number of molecular dynamics and experimental studies have found that phase separation or a changing bulk structure arise in these mixtures.[91] This is because the already complex correlations existing between the constituent ions, which manifests in significant meso- and microstructure, promotes inhomogeneous solvent distribution.[91] An example of this distribution is shown in Figure 1.5, where on increasing concentration of acetonitrile (ACN) the bulk structure of 1-Butyl-3-methylimidazolium hexafluorophosphate ($[C_4C_1im][PF_6]$) changes.[92] Starting from the neat IL (not pictured), a medium composed entirely of ions, initially, the molecular compound will be a diluted solute, interacting with the domains of the IL as described above. As the concentration in the molecular compound increases (moving left to right), it will tend to aggregate on the domain toward which it has a greater affinity.[92] At some point, the presence of ACN disrupted the native IL structuring, and the IL becomes a minority component and the constituent ions will form aggregates. These aggregates (pictured in the bottom right snapshot) are micelles and ion clusters.[92]

There has been recent evidence that indicates that this switch in bulk structuring with changing solvent concentration can be reasoned by considering the changing interfacial structure. To this effect, a study by Perkin *et al.* on the ionic liquid, 1-butyl-1-methylpyrrolidinium bis[(trifluoro-methane)sulfonyl]imide, $[C_4C_1P_{yrr}][TFSI]$ provides sound evidence for this.[90,91] They measured the structural forces of a range of

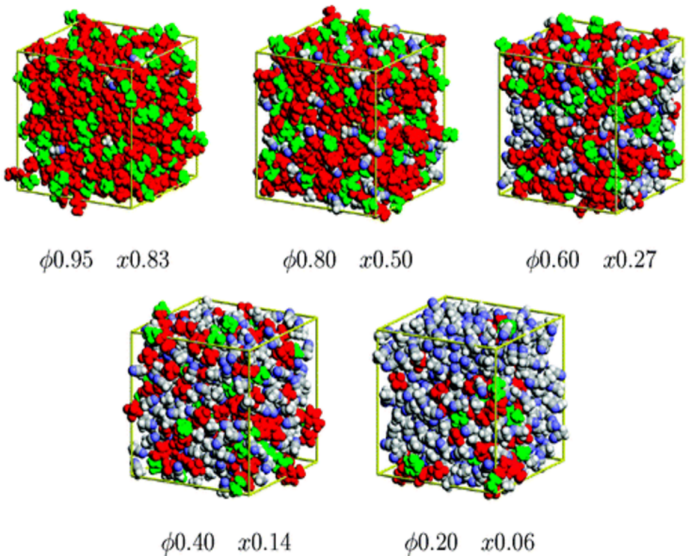


Figure 1.5: Interaction of n-hexane, ACN, and methanol with the non-polar and charged domains of the IL $[C_4C_1im][PF_6]$. The alkane is located in the non-polar domains. ACN, a dipolar molecule, has balanced affinities for both kinds of domain. Methanol establishes strong hydrogen bonds with the anion and weak hydrogen bonds with the hydrogen in C_2 of the imidazolium cation. The IL in the box containing methanol was not colour-coded to highlight the red colour of the oxygen atoms of the alcohol and emphasize the interaction between the hydroxy group and the PF_6. Mixture of $[C_4C_1im][PF_6]$with ACN at different compositions, identified by the volume fraction, ϕ, and the mole fraction, x, of IL. Because the IL and the molecular compound have very different molecular sizes and weights, the volume fraction is for many purposes a convenient quantity to express composition. Taken from[92]

$[C_4C_1P_{yrr}][TFSI]$ mixed with propylene carbonate (PC) using the SFB.[90,91] Due to the solubility of $[C_4C_1P_{yrr}][TFSI]$, they were able to probe the regimes from 0 to 100 % mol wt. The force profiles are shown in Figure 1.6, and the λ_{osc} for the systems are plotted in Figure 1.7. From their results, a clear switch in the oscillatory wavelength, λ_{osc}, in the 2.0-2.5M regime was obvious.[90,91] The change in the oscillatory force-distance profile with increasing $[C_4C_1P_{yrr}][TFSI]$ content is demonstrated in Figure 1.7.

Importantly, the wavelength of the structural force can be determined by measuring the distance between each distinct oscillation[65] and provides a quantitative indication of the structuring. It can therefore be reasoned that the discrete switch in wavelength, seen in Figure 1.7, is a manifestation of a structural change.[90,91]

At low $[C_4C_1P_{yrr}][TFSI]$ concentrations, a solvent-determined wavelength, λ_{osc}, of

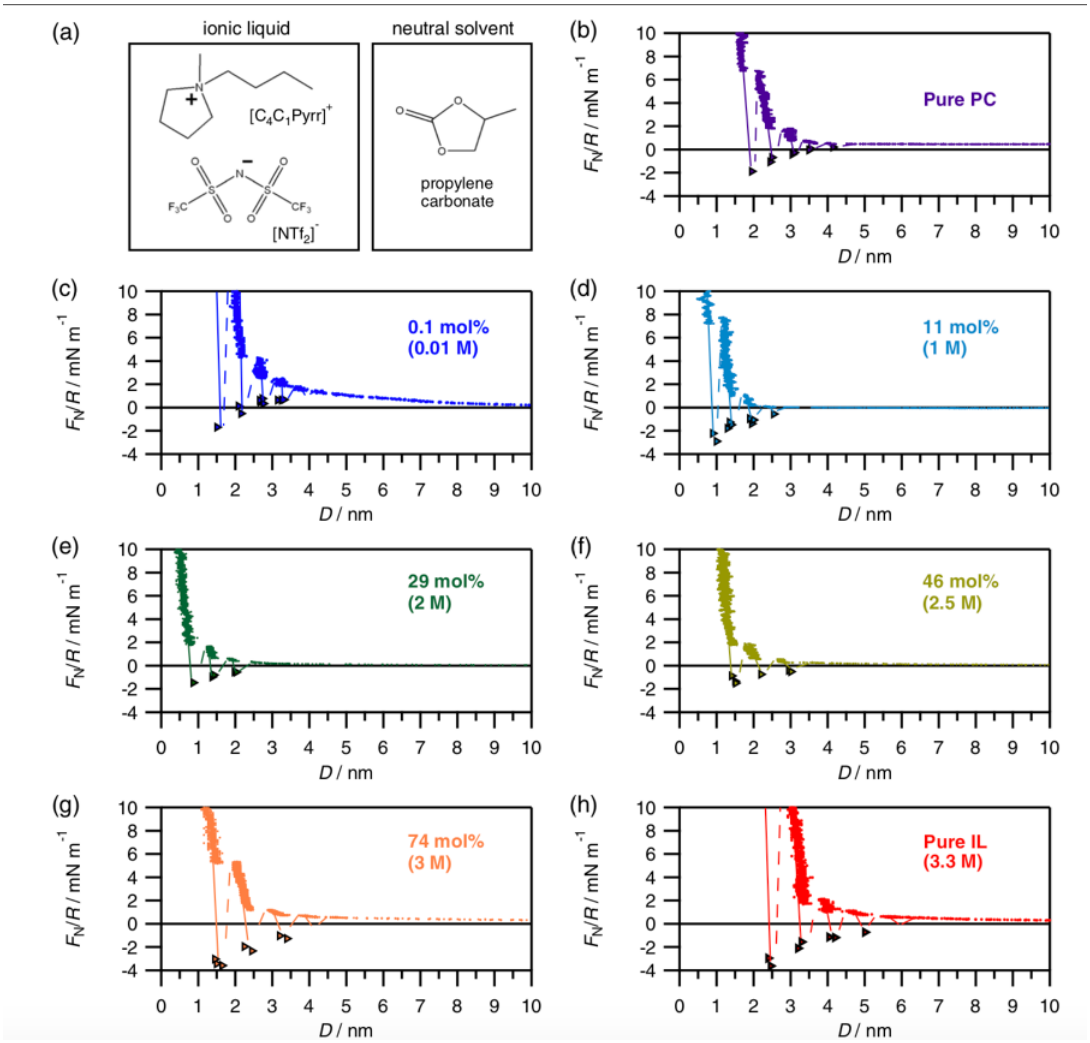


Figure 1.6: $[C_4C_1P_{yrr}][TFSI]$ Layers:Chemical structures and (b)–(h) measured forces FN between two mica surfaces (normalized by radius of curvature R) as a function of surface separation D across liquids with concentrations ranging from pure PC to pure IL. Concentration values correspond to actual concentrations injected into the SFB rather than derived from a fit to data. Coloured data indicate repulsive forces measured on approach of the surfaces, and triangles indicate points measured from the jump apart of the surfaces from adhesive minima. Lines are a guide to the eye to show the oscillatory nature of the forces, with solid lines through the measured regions and dashed lines through regions inaccessible to measurement.Taken from [90]

0.55 nm was observed, whilst at the cross over point, a 0.80 nm wavelength characterised concentrated regimes. This change was coupled to the systematic switch of the decay length of the damped oscillation, ξ, from ξ =0.85 nm in dilute regimes to ξ =1.4 nm in concentrated regimes.[90,91] From these findings, it can be proposed that the IL ions disrupted the solvent structure in dilute regimes and vice-versa in concentrated regimes. The schematic in Figure 1.7 shows the proposed interfacial

structure for these two distinct regimes, showing that the changes in the structural parameters, ξ and λ_{osc}, must be linked to a change in the interfacial structure.[90,91] This changing wavelength can be interpreted as resulting from a structural transi-

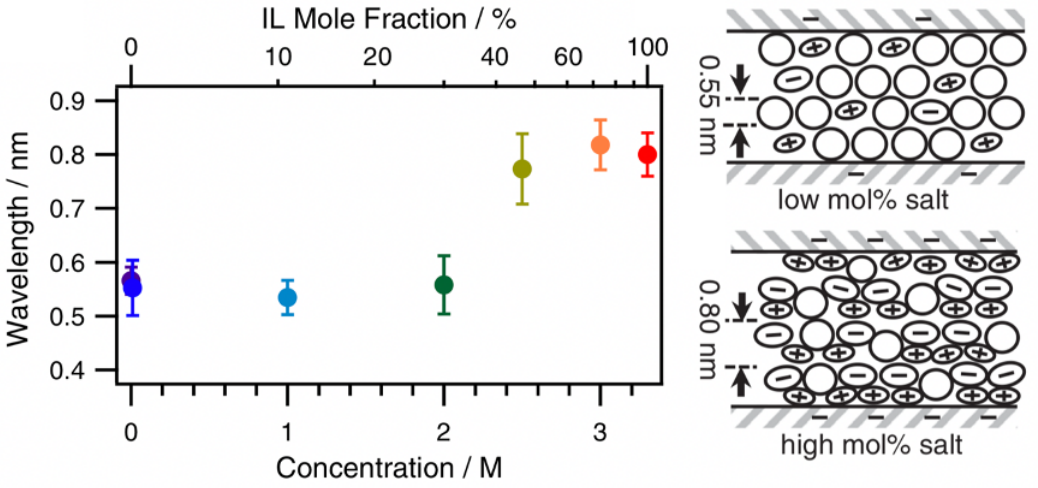


Figure 1.7: $[C_4C_1P_{yrr}][TFSI]$ (a) Wavelength of the measured oscillatory forces, corresponding to each of the concentrations shown in Figs. 1.6(b)–(h). Values were calculated using the measured distances between adjacent minima and between adjacent maxima in the force profiles. The resulting F_N v D profiles reveal the sequential squeeze-out of layers of molecules; cartoons on the right show proffered molecular arrangements at low and at high salt concentration, giving rise to solvation force wavelengths determined by solvent and by ion pairs, respectively. Taken from[90]

tion. At low concentrations, the PC dominates,[60,90,91,93] and the $[C_4C_1P_{yrr}][TFSI]$ packs so as to not disturb the packing. However, eventually the $[C_4C_1P_{yrr}][TFSI]$ assume their preferred alternating ionic layering, and, as seen in X-ray experiments, the PC molecules sit within these layers.[90,91]

Furthermore, a consideration of the following expression, seen in Equation 1.1, which describes the traditional oscillatory force-distance dependence in concentrated systems, can aid in the analysis of the structural forces of these mixed systems.[90,91]

$$\frac{F_N}{R} = Ae^{-\frac{D}{\xi}}\cos(2\pi/\omega D + \phi) + Be^{-D\lambda_S} \tag{1.1}$$

where F_N/R is the force measured in the crossed-cylinder confined geometry, with

Radius of R, at a separation distance of D. These parameters are measured directly in the SFB. The other terms, A, B, ξ, λ_S, $2\pi/\omega$, and ϕ are fitting parameters[90,91] that relate to the structure of the confined film system. A is the amplitude of oscillations, B is the amplitude of the long-ranged monotonic electrostatic force are expected to be surface dependent, ξ is the decay length of the damped oscillation profile, λ_{osc},is the oscillation periodicity or wavelength of the damped decay described by $2\pi/\omega$, ($\lambda_{osc} = 2\pi/\omega$), and ϕ is the phase of the oscillation. λ_{osc}, is thought to be related to the structure of the confined film, effectively quantifying the thickness of the consecutive expulsion layers.[62,90,91]

While the first term of Equation 1.1 represents the short-ranged oscillatory forces, the second term on the right of Equation 1.1 represents the long-ranged monotonic component observed in force measurements across concentrated electrolytes,[90,91] explained in Section 2.1.3. The screening length, λ_S, is distinct from the λ_{osc}, and is believed to be a property of the bulk liquid system while A and B are expected to be surface dependent.[90,91]

The first components in the equation, $2\pi/\omega$ and λ_{osc}, represents the oscillatory force that results from the systematic expulsion of layers when confined between two charged surfaces, is therefore, representative of the molecular-scale structure that manifests in confinement.[90,91] In particular, the wavelength associated with the oscillatory decay, $\frac{2\pi}{\omega}$, is directly linked to the molecular architecture as experiments indicate that the oscillatory period varies with IL structure.[90,91] In fact, it was this parameter that, as established by Perkin *et al.*, undergoes a discrete and discontinuous switch with varying concentrations of an IL-PC mixture.[90]

The decay of the oscillatory force, λ_{osc}, is also believed to scale with concentration.[90,91] Therefore, $\frac{2\pi}{\omega}$ and ξ are determined by the liquid and surface structure, and thus provide an insight into how the presence of solvent alters interfacial nanostructure.[90,91] Therefore, analysis focussed on as to how these parameters change in different IL-solvent mixtures will be central to the work done in this thesis. Simul-

taneous analysis of these parameters and the tribological performance of various IL-solvent lubricant films, will illuminate how interfacial structure at the molecular scale influences how a tribofilm lubricates.

1.5 | Nanotribological properties of ionic liquids

ILs possess many favourable and attractive properties sought-out for durable and effective lubrication systems.[3,7,21,29,51,94]Viscosity, thermal stability, and a wide solubility range offer a unique system, especially when considering the chemical flexibility and thus, tuning capabilities, that can be employed in IL systems.[7,19,21] Studies into discerning the tribological behaviour of ILs, on both the nano and macro-scale, have shown that these liquid films, in some cases, have a friction coefficient, μ, orders of magnitude lower than traditional lubricant systems,[11,14,21,29,55,95,96] see Figure 1.8. Furthermore, these studies have also shown that ILs are capable of resisting squeeze out at extremely high pressures,[19,21] and are superlubric ($\mu < 0.01$).[19,21] In particular, these properties of ILs make them well suited for a boundary lubricant.[14,96] In boundary lubrication, the surfaces are separated by a film of molecular-scale thickness, and are subject to extreme confinement, pressure, and, without proper dissipation, heat.[19,97] The fabrication of traditional boundary lubricants normally employs surfactants mixed in with the lubricant oil to promote high affinity for the surfaces, so as to resist the squeeze out.[7,21,98–100]However, when the system transitions from the classic hydrodynamic regime to the boundary lubrication regime, the lubricating oil is squeezed out leaving the poorly lubricating surfactant, resulting in deleterious wear and tear.[19]

In designing a new durable boundary lubrication system, there are therefore a set of properties or requirements that are of tantamount importance. The most important one is undeniably the ability to resist squeeze-out at extreme pressures.[48] Along with this, the lubricant film must also be robust and be both chemically and physically stable.[48] Finally, there should be an element of control and modification of the

Table 1 Friction coefficients for several frictional pairs lubricated with various lubricants (SRV tester, load 50 N, frequency 25 Hz, amplitude 1 mm)

	Friction coefficient		
Frictional pair (ball/disk)	L106	X-1P	PFPE
Steel/steel	0.065	0.098	0.145
Steel/Al	0.040	0.128	—
Steel/Cu	0.025	0.117	0.145
Steel/SiO_2	0.060	0.110	0.132
Si_3N_4/SiO_2	0.083	0.115	0.132
Steel/Si(100)	0.050	0.102	0.145
Steel/sialon	0.065	0.100	0.120
Si_3N_4/sialon	0.065	0.105	0.130

Table 2 Tribological properties of ionic liquid L206, X-1P and PFPE for steel/steel contact (SRV tester, load 50 N, frequency 25 Hz, amplitude 1 mm, duration 30 min)

	Friction coefficient			Wear volume/$\times 10^{-4}$ mm^3		
Load/N	L206	X-1P	PFPE	L206	X-1P	PFPE
200	0.060	0.070	0.120	0.05	0.07	0.60
300	0.055	0.065	0.110	0.22	2.21	1.90
400	0.050	—	0.105	0.39	—	5.03
500	0.045	—	—	0.45	—	—
600	0.045	—	—	0.53	—	—

'—' lubrication failure.

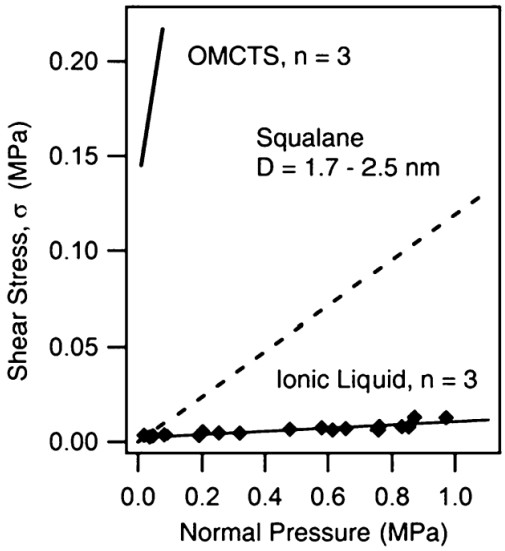


Figure 1.8: Study showing superior performance of ILs when compared to industry-grade lubricant. As shown, the IL 1-methyl-3-methylimidazolium tetrafluoroborate, $[C_1mim][BF_4]$ outperforms PFPE at a 50N, 200N and 300N loads. Taken from.[29] (b) SFB Study showing superior performance of an IL when compared to a model base oil. As shown, the IL $[EMIM][E_tSO_4]$ out performs Squalene and OMCTS. Taken from[55]

friction behaviour, and thus the friction coefficient.[19,21] In considering the properties, chemical flexibility and recorded friction behaviour of ILs, it is clear that they are an attractive boundary lubricant.[19,101]

Two experiments, one of the macroscale[29] and one on the nanoscale,[55] showed that ILs have the potential to outperform commonly used lubricants and model base oils. These results are shown below in Figure 1.8, and the low friction coefficients associated with the IL were attributed to its structuring at the mica surface and the Coulombic interactions that helped maintain the ionic film.[19,55,102,103]

Along with this excellent friction behaviour, there is now overwhelming evidence that

this behaviour is linked to the structuring of the lubricant film with many studies showing that particular cation and anion groups promote superior lubrication.[95,104] This introduces an element of control and manipulation of the friction behaviour that is highly sought after.[105] Further studies, utilising the AFM, SFB and simulations,

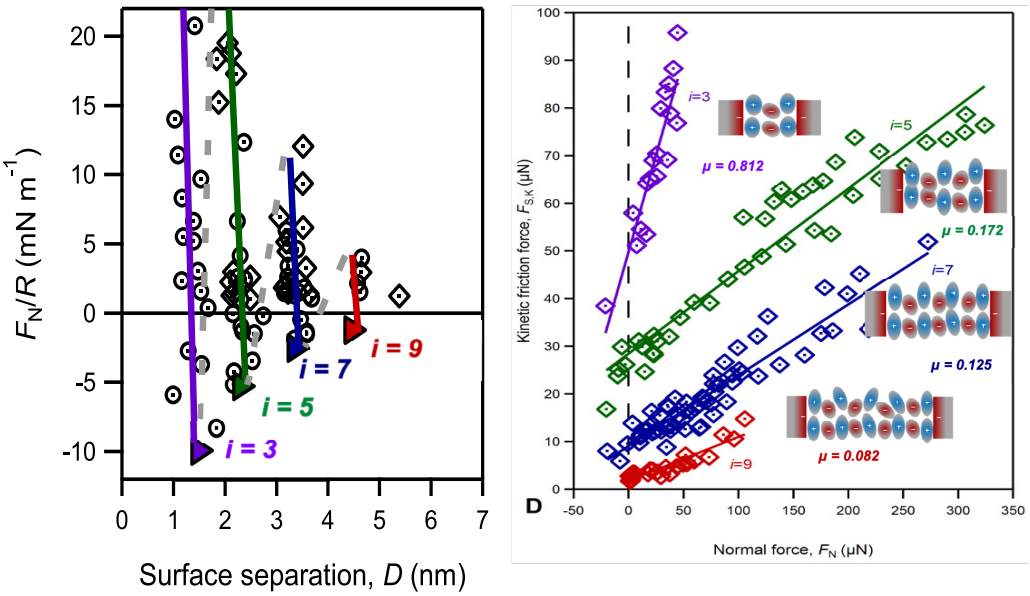


Figure 1.9: SFB study of the normal and frictional forces of a $[C_4C_1P_{yrr}][TFSI]$ IL film. Left: The F_N/R v D profile of pure $[C_4C_1P_{yrr}][TFSI]$ where the layers are indicated. Right: $F_{s,k}$ vs F_N for $[C_4C_1P_{yrr}][TFSI]$ at differing film thicknesses, as identified in the F_N/R v D profile. Each line corresponds to an individual film thickness and the gradient of the lines indicate the friction coefficient. As each different layer gives rise to different μ, the friction is said to be "quantised". Taken from[103]

into other ILs have verified the existence of quantised friction, see Figure 1.9.[11,19,106] This experimental validation also lead to the formulation of an empirical relationship between shear force, F_S, and normal force, F_N in Equation 1.2:

$$F_S^i = \mu^i F_N + \alpha^i \left(\frac{A^i \cdot F_{adh}^i}{\pi D^i R} \right) \tag{1.2}$$

where i is the layer index, μ^i is the load-controlled friction coefficient, α^i is the adhesion-controlled friction coefficient, A is the flat contact area, F_{adh} is the adhesion force between the surfaces, F_S^i is the friction force when $F_N = 0$, and D^i is the distance between shearing liquid layers. In our experiments, we are able to directly measure F_{adh}, F_S^i, the radius of curvature, R, and film thickness, D^i, while we control

F_N.[11,103]

Finally, given the interesting normal, and shear properties of water,[107] it is of no surprise that its exact influence on the structuring, and thus, forces present in IL mixtures has yet to be elucidated. There are a number of studies which do however indicate, that the effect of added water or humidity on the friction forces of an IL are more dependent on the IL itself.[100,108–110] One particular study found that environmental humidity had an antipodal effect on shearing forces when investigating its influence on a monolayer forming IL and on a bilayer forming IL.[106,111] This is another interesting route to tuning friction that would require a comprehensive evaluation of this behaviour. Such an evaluation is necessary when it comes to the manufacture of any lubricant system, as the control of environmental humidity is often not possible.

1.6 | Scope of this study

While ILs may seem like a promising candidate to become the next industry-standard lubricant, there are some fundamental issues.[7,19] As previously described, the manufacture of ILs can be complicated, and requires expensive materials.[7,19,105] This makes ILs a cost-inefffective material to manufacture in bulk.

Furthermore, it has already been stated that their performance as lubricant is sensitive to the presence of moisture.[100,108–110] It is clear that exposure to moisture will change the structure of the layers formed upon confinement, but the magnitude of the response is different for different ILs.[110,112]

Finally, as industry tries to explore 'greener' and more sustainable options, it is important to have in mind that ILs may not be as 'green' as previously described.[7,19,21,49] Fluorine-containing ILs are highly toxic and are to be avoided due to potential degradation effects.[109,113]

Therefore, it is crucial to investigate the influence of small amounts of ILs in tra-

ditional lubricant systems. The surfactant-like structure of ILs suggests their use as oil-additives;[17,114–117] and they would replace additives like zinc dialkyldithiophosphates, ZDDP. This method would reduce the amount of IL required, greatly reducing their cost and negative environmental effects.[17,114–117] It is also hoped that by using minimal amounts of IL, that the mixtures would be less sensitive to moisture. However, there are a very practical considerations to have in mind:[17,116,118]

1. Are ILs and base-oils miscible ?
2. What is the lubrication performance like ?
3. How much of an IL should we add ?

1.6.1 | Miscibility

Unfortunately, most ILs show very poor miscibility in oils, as it involves mixing and charged substance to a non-polar oil.[20] Phosphonium cation-based ILs show the best tribological performance when used as a neat lubricant compared to other cations.[98,119–122] Although, it should be noted that the anion present will change the friction response for the same cation.[123]

Happily, ILs with phosphonium-based cations, pictured in Figure 1.1, also show the best miscibility in various base-oils due to their alkyl chains.[98,116,122,124] The 3D quaternary structure and long alkyl chains dilute the charge on the ion and it is subsequently more miscible in the non-polar base-oil.[122]

In general, the miscibility of the IL will increase with the polarity of the base-oil.[98,116,122,124] The level of association between the ILs and oil and also between cation and anion is important for their miscibility and the formation of a boundary layer.[19] ILs that interact with the base-oil or have a higher degree of ion association will be more miscible but will be less able to form an effective boundary layer. Hence the very thing that makes an oil/IL blend more compatible also reduces its ability to perform as a lubricant.[116]

1.6.2 | Performance

Having identified identified potential candidates that are miscible, it is important to see if these blends perform relative to the neat base-oil and current additives. The best outcome would be to approach the neat IL lubrication performance. Using a ball-on-disc tribometer (TRB) set-up, it is possible to investigate the macroscopic friction and wear for a range of oil/IL blends and surface materials.[98] Predominantly, lubrication performance relative to the neat base-oil is far better: wear and friction are reduced but the most significant reduction is the reduction in wear depth.[116,125] Relative to the ZDDP additive the performance varies with base-oil and IL. Some combinations reduce friction and wear slightly compared to ZDDP whereas some exhibit poorer lubrication performance.[98] Nonetheless, one of the main differences compared to ZDDP is the fact that the IL decomposition is ashless[30]and therefore far greener than the zinc-containing ZDDP decomposition products.[126] The performance of the blends is strongly dependent on the neat base-oil performance; an oil that performs better when neat will also produce better performing blends.[116,125] Surface analysis also confirms the presence of a tribofilm for the oil/IL blends which means that the protective layer is still formed, even when far smaller concentrations of IL are present.[98,116,125] Although, it is possible that the IL reactivity might be inhibited if the normal load is not high enough.[119]

1.6.3 | Performance of Diluted mixtures

Finally, a number of studies have looked at the change in shearing behaviour of model base oils upon addition of incremental amounts of oil-soluble ILs.[118,127,128]

These studies have proved informative, and some are shown in Figure 1.10, and indicate that on addition of a 0.01 % fraction of an IL, the friction coefficient shows a dramatic improvement on that of the pure base oil.[128] Using a sharp-tip AFM, and studying the effect of increasing mol % of $[P_{6,6,6,14}][(^{i}C_8)_2PO_2]$ with octane, that the behaviour of 1 mol % IL is comparable to that of pure IL.[114]

This trend is reproducible on the macroscale as well. A similar study using hexadecane and trihexyltetradecylphosphonium bis(trifluoromethysulfony)imide, $[P_{6,6,6,14}][(^iC_8)_2PO_2]$ similarly showed that lubrication by 0.01 mol % was superior to that of pure hexadecane, seen in Figure 1.10.[114] In the macroscale TRB experiments, the difference in performance between 0.01 mol % and 1.0 mol % was not as apparent as it was in the AFM.[128] Therefore, both nanoscale AFM studies and macroscale TRB stud-

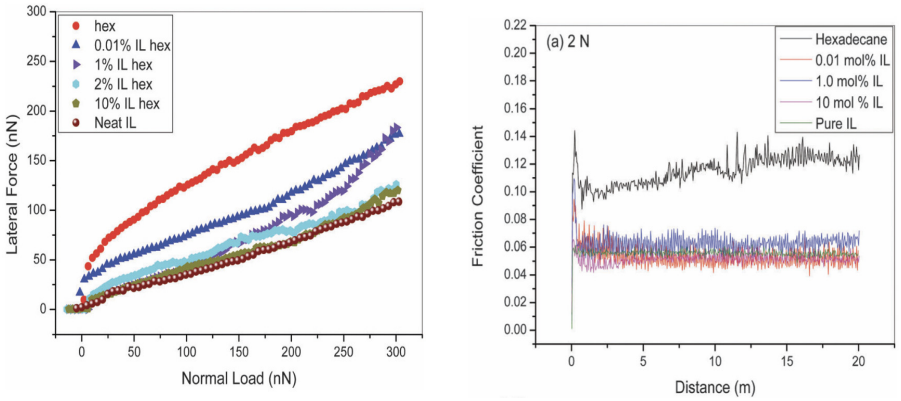


Figure 1.10: AFM and TRB Study of the effect of diluting base poils with $[P_{6,6,6,14}][(^iC_8)_2PO_2]$. Left: AFM study of the effect of hexadecane As shown, the performance of even 0.01mol % IL results in a magnitude order improvement in the friction coefficient. Taken from.[128] Right: Tribometer study of the effect of diluting octane with $[P_{6,6,6,14}][(^iC_8)_2PO_2]$. As shown, the performance of 1 mol % is almost indistinguishable from the pure IL.Taken from[128]

ies have shown that even the smallest amount of IL can dramatically enhance the performance of a lubricant film.[114,128] However, in the nanoscale AFM studies, the performance of the 1 and 0.01 mol % mixtures are quite dramatic. While the 0.01 mol % does significantly reduce the friction compared to that of the base oil, this is still an order of magnitude higher than that seen in the 1 mol % mixture.[114,128]

As previously mentioned, the addition of solvent to an IL has a distinct effect on its confined structure. This structural change eventuates in a pronounced modification of easily measured and extrapolated empirical properties, making the thorough study of the effect of solvent on ILs a realistic objective. Specifically, the discrete and discontinuous change in experimental parameters observed on addition of polar solvents, which culminated in a 'switch' of structuring could be echoed by a similar

switch in the friction behaviour. The work in this thesis is primarily focussed on discerning the behaviour of lubricant thin films composed of ILs and their mixtures with a number of solvents, and whether this represents a route to tuning friction.

1.7 | Aims of this study

The work in this thesis will focus on establishing if IL mixtures can act as effectively as lubricant additives when compared to their neat counterparts. In studying a range of IL-solvent mixtures on both the nano and macroscale, a deeper understanding of the effects of polar solvents and base oils on the structural and frictional forces of ILs will be gained.

1.8 | Project Outline

To answer this question, the following systems will be studied in the SFB:

1. Chapters 4 and 5: 1-butyl-1-methylpyrrolidinium bis[(trifluoro-methane)sulfonyl]imide, $[C_4C_1P_{yrr}][TFSI]$, mixed with the polar solvent, PC, over the entire mol % range.

2. Chapter 6: trihexyltetradecylphosphonium bis(trifluoromethysulfony)imide $[P_{6,6,6,14}][(^iC_8)_2PO_2]$, mixed with the model base oil, dodecane, over the entire mol % range.

3. Chapter 7: Neat trihexyltetradecylphosphonium bis(2,4,4-trimethylpentyl)phosphinate, $[P_{6,6,6,14}][TFSI]$.

To supplement the studies using the SFB, a greater range of systems will be studied on the TRB in Chapter 8:

1. 1-butyl-1-methylpyrrolidinium bis[(trifluoro-methane)sulfonyl]imide, $[C_4C_1P_{yrr}][TFSI]$, mixed with the polar solvent, PC, over the entire mol % range.

2. trihexyltetradecylphosphonium bis(trifluoromethysulfony)imide, $[P_{6,6,6,14}][(^iC_8)_2PO_2]$, mixed with the model base oil, dodecane, over the entire

mol % range.

3. trihexyltetradecylphosphonium bis(2,4,4-trimethylpentyl)phosphinate , $[P_{6,6,6,14}][TFSI]$, mixed with dodecane over the entire mol % range.

4. 1-Butyl-1-methylpyrrolidinium bis(trifluoromethylsulfonyl)imide, $[P_{1,4,4,4}][TFSI]$, mixed with dodecane over the entire mol % range.

2 | Theory

2.1 | Surface Forces

Central to the development and study of ILs as a tribofilm is a grounded understanding of the interactions and forces that govern the behaviour of the IL system. Their unique chemical composition, containing only large, asymmetric ions that promote formation of a liquid phase at ambient temperature, means that ILs are liquid electrolytes.[23,25,72,129] Although theoretical descriptions of liquid electrolyte chemistry have been in development since the early 1900s,[23] it has become increasingly clear that the forces that govern their behaviours exist over multiple length scales, meaning the traditional bulk continuum approaches are insufficient.[1,72,93] In particular, the continuum theories fail when the ion density, or the concentration of the salt-system, is sufficiently concentrated that excluded volume and ion-correlations cause additional driving forces to come into play.[26,73,93] The implications of this are often most evident and important in interfaces.[26,73,93] This is troubling, as all applications of liquid electrolyte systems, whether it be in batteries or in our cellular systems,[23,25] materialise at interfaces. Therefore an understanding of the forces and dynamics that dominate at the solid-liquid electrolyte interface is of utmost importance.

Development of experimental techniques capable of studying interfacial forces has enabled a deeper understanding of liquid systems. Much acknowledgement is owed to Tabor, Winterton and Israelachvili, as the surface forces apparatus, SFA, which is referred to as the SFB in this thesis, has facilitated the study of confined liquid systems.[130,131] From this, crucial insights into the forces dominating in liquid systems have been gained.

2.1.1 | DLVO Theory

The *Derjaguin-Landau-Verwey-Overbeek theory*, commonly called DLVO theory, is a description of the forces that affect colloidal stability.[1,132,133] More pertinently, DLVO theory can be extended to describe the forces acting between two surfaces separated by a liquid medium.[134] Fundamental to this theory is that the forces acting between these surfaces is a combination of short-ranged van der Waals (vdW) attraction and the decidedly more long-ranged repulsive electrostatic (or double layer) forces.[1,60,132,133] This interaction energy can be represented as:

$$DLVO_{interaction} = E_{doublelayer} + E_{vdW} \tag{2.1}$$

Central to this theory is that the van der Waals contribution has an inverse power law-dependency while the electrostatic repulsive force has an exponential distance dependency.[1,93,135] This results in the van der Waals dominating at small separations, giving rise to an adhesive force minima. With increasing separations, repulsive forces prevail, though a shallow attractive minima is present at intermediate separations.[1,60,135] The force profile described by the DLVO theory is shown in Figure 2.1. Figure 2.1 shows an example of how the total interaction energy between two surfaces, W, may vary with surface separation, D, and the corresponding force contributions. As $D \to 0$, the total interaction energy (solid line) must be dominated by the van der Waals attraction (dashed line) due to its inverse power law dependence ($W(D)^{\infty} - 1/D^{n}$) compared with the double-layer repulsion (dotted line) which decays exponentially with D. The van der Waals attraction results in the surfaces coming into adhesive contact.[1] Force measurements techniques, such as the SFB, have validated this expectation.[60,131,135]

The behaviour of such systems at large separations is well described by continuum models such as the Lifshitz theory of attractive van der Waals forces[134,136] and the Poisson-Boltzmann model for double layer repulsions.[137] However, upon near-surface

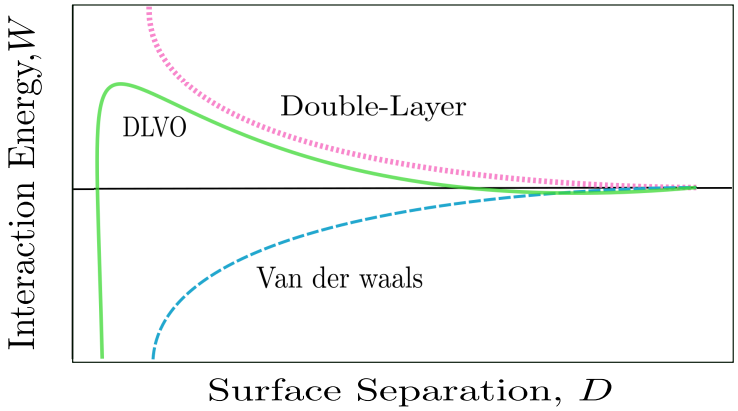


Figure 2.1: The DLVO forces acting between like-charged surfaces. *Left:* Pink: Double-Layer electrostatic repulsion predicted by the Debye-Hückel theory, displaying an exponential decay. Blue: The attractive van der Waals forces acting between the surfaces, with an inverse power law dependence on the system geometry. Green: The resultant DLVO force arising from these forces. A secondary minimum is displayed, and this is commonly known as flocculation in colloidal science.

contact on the order of nm separations, the interfacial behaviour begins to deviate from these 'mean field' models and the observed force law is no longer consistent with theoretical predictions.[59,134]

2.1.2 | Non-DLVO Structural Forces

With the breakdown of continuum descriptions of the confined liquid at nanometre separations, an empirical description must be employed. This new description is one where the liquid medium is considered as a collection of discrete molecules.[134] At these separations, the molecules are ordered due to geometric constraints and additional local effects,and lead to 'structural (or solvation) forces'.[131,138,139] To remain in the gap, the liquid molecules order themselves into layers between the two surfaces, and as the surface separation decreases, this ordering will change, and give rise to the structural force, as shown in Figure 2.2.[107,139,140] The nature of the structural forces depends on the properties of the confining surface and the confined liquid film.[107,139,140] The oscillatory nature is a direct consequence of attractive and repulsive forces that persist in liquid films, giving rise to an oscillatory density distribution function.[138,139,141]

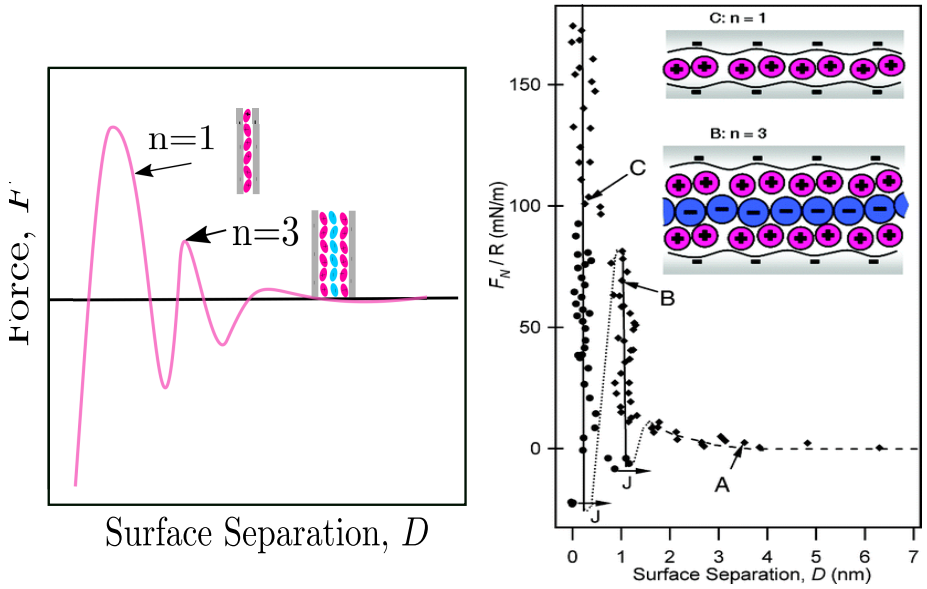


Figure 2.2: The Structural Forces of a confined liquid system. *Left:* A graphical representation of an idealised force profile of an IL showing the alternating cation-anion layering that manifests to preserve electroneutrality of the system. *Right:* An experimentally obtained structural force profile for the IL $[C_4C_1Pyrr][TFSI]$ adapted from Perkin *et al.*

Film thicknesses with energetically favoured molecular layers, give rise to energy minima, and distances which correspond to non-favoured configurations, result in energy maxima.[142] As the periodicity of this function is related to the dimensions of the molecules,[131,138,139] each oscillation therefore corresponds to the 'squeezing out' of molecular layers.[40,65,139]

The oscillation period therefore depends on the confined liquid structure. In a single component molecular fluid, the structural force has an oscillation period corresponding to the molecular diameter of the confined molecules, see Figure 2.3(a).[40,65,139]

However, when an electrolyte is present, the repeat unit must remain charge neutral. Figures 2.3(b) and (c) show two example structures that have been observed previously: a 'checkerboard like' structure and an alternating structure.[40,54,63,71,112,143–145] In the checkerboard structure, the repeat unit contains a single layer of cations, anions, and solvent. The period of oscillation is approximately the molecular diameter of the largest constituent (in Figure 2.3(b), the anion and cation are shown to have similar sizes).[40,63,71,112,143] As the surface charge, σ, increases, it is favourable for the

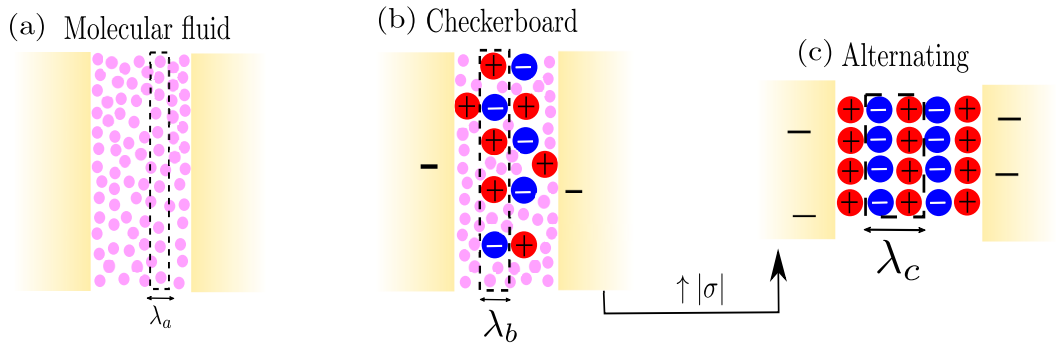


Figure 2.3: Schematics of confined (a) molecular fluid, (b) checkerboard and (c) alternating structures. The charge-neutral repeat units are indicated using dashed black boxes and the oscillation period by λ_{osc}. In (a) the repeat unit contains mostly molecular fluid molecules, and λ_{osc} is approximately the molecular diameter. When ions are present in the confined region e.g. in an electrolyte, the structure can resemble schematics (b) and/or (c). In (b) the checkerboard repeat unit comprises a single layer containing cations (red), anions (blue), and solvent (pink). The period of oscillation λ_b is approximately the molecular diameter of the largest constituent. As the surface charge, σ increases, the interfacial layers are more likely to separate into (c) the alternating structure. In (c) the repeat unit contains a layer of cations and a layer of anions, and λ_c is approximately the ion-pair dimension. The negatively charged surfaces are shown in pink.

interfacial layers to charge-separate into alternating cation and anion layers (Figure 2.3(c)).[40,65,139] In the alternating structure, which has come to be associated with ILs, the oscillation period is approximately the ion-pair dimension.[40,63,71,112,143,144] Countless experiments on a number of confined systems, including ILs, liquid crystals and simple polar liquids, have led to this mathematical description of the decaying oscillatory force, $F_{osc}(D)$, in concentrated electrolytic systems,[71,90] and is analogous to Equation 1.1.

$$F_{osc}(D) = Ae^{-}(\frac{D}{\zeta})cos(\frac{2\pi D}{\lambda_{osc}} + \phi) \tag{2.2}$$

In the simple liquids which formed the basis for this empirical description, λ_{osc} is related to the size of a molecular layer.[129,146] In the case of pure ILs and concentrated electrolytes λ_{osc} is dependent on the constituent ions, and relates to the ion pair diameter.[40,63,71,112,143,144] When such systems are mixed with solvents, the wavelength has been shown to depend on the relative concentrations of the components, reflecting the structuring of the solvent with regards to the ions present.[71,90]

2.1.3 | Underscreening in Concentrated Electrolytes

The Debye-Hückel (DH) theory describes the physics of dilute electrolytic systems.[129,146,147] DH theory states that the electrostatic potential between two charged surfaces immersed in an electrolyte will be screened by the intervening ions, decaying exponentially with distance in a relationship characterised by a decay length, termed the Debye length, λ_D,[129,146,147] given by:

$$\lambda_D = \sqrt{\frac{\epsilon_0 \epsilon_r k_B T}{4\pi e^2 c_{\text{ion}}}} = \frac{1}{\sqrt{4\pi l_B c_{\text{ion}}}} \tag{2.3}$$

for a 1:1 electrolyte, where ϵ_0 is the permittivity of free space, ϵ_r is the dielectric constant of the medium (note this depends on the ion concentration), k_B is the Boltzmann constant, T is the temperature, e is the electronic charge unit, c_{ion} is the volume ion concentration:[146]

$$l_B = \frac{e^2}{\epsilon_0 \epsilon_r k_B T} \tag{2.4}$$

is the *Bjerrum* length the distance between two ions at which their electrostatic interaction energy is equal to the thermal energy unit $k_B T$.[129] These will naturally break down at higher concentrations. As the solvent makes up a smaller fraction of the system it becomes unphysical to treat it as continuous, and ion size and correlation effects will become more significant. There have been attempts to account for this within the theory, such as extending the Debye-Hückel theory to consider additional ion correlation interactions and ion size effects.[148]

In 2013, an experiment showed that electrostatic repulsion between charged surfaces was not being rapidly screened in ILs and instead the screening was of an anomalously long distance, similar to dilute electrolytes.[82]

Since then, in experiments underscreening has been observed in pure ILs, solutions of IL in organic solvents, and in aqueous solutions of sodium chloride, NaCl and lithium chloride, LiCl, and there has been much debate within the literature.[73,82,129,149] It has

been observed to decrease with temperature and to increase with concentration.[146] Theoretically, a simple model study showed ILs exist as free ions in the majority and cannot be considered dilute electrolytes, while attempts have been made to understand underscreening using a lattice model and primitive and semi-primitive models.[129,149] Recently, an empirical law of underscreening was theorised to be:[129]

$$\lambda_s \sim l_B c_{\text{ion}}\, a^3 \tag{2.5}$$

in which l_B is the Bjerrum length, see Equation 1.2, c_{ion} is the volumic ion concentration, and a is the mean ion diameter. This law was then theoretically derived by considering a scaling argument for the system.[146,149]

2.2 | Tribological Theory

Frictional motion, which is the sliding of two surfaces, is prevalent in both the natural and industrial world.[1,6,9,150] A graphical representation is shown in Figure 2.4. The control and, more commonly, the mitigation of friction is central to the function of biological motors, the study of earthquakes, and industry.[5,151] However, friction is both a nuisance and a blessing.[6–9] Friction force, which is the force that resists the relative motion of two sliding objects, is fundamental to locomotion and traction.[1,6–9] However, this same force is detrimental to industry, where it leads to levels of decomposition and wear that renders industrial surfaces no longer usable.[6–9] Therefore, in both nature and industry, the main aim is trying to find the delicate balance between the destructive and beneficial effects of friction.[6–8]

The study of friction forces is termed tribology.[6–9] Specifically, tribology is the study of the adhesion, friction, lubrication and wear of surfaces when coming into relative contact and motion.[6–9] There is evidence that tribological studies have historical precedence as far back as the 15th century when Leonardo da Vinci tried to outline empirical friction laws.[5,150] Since then, there has been a notable effort to better

describe and interpret this pervasive force.[6–8,152]

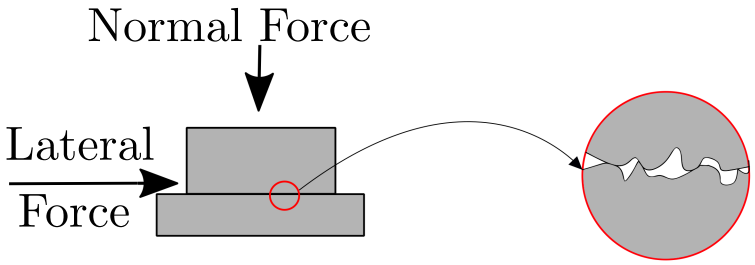


Figure 2.4: Schematic illustrating the basics of friction.

2.2.1 | Contact Mechanics

In order to understand friction, it is first necessary to define the geometry of the frictional interface While there many geometries of sliding surfaces, as this thesis focuses on the frictional forces measured in the SFB, a simplistic model for the Contact Mechanics of SFB will be used.[153–155]

The model system that best mimics the geometry of the SFB is that of a sphere sliding on a flat surface.[1] Furthermore, in the classical SFB set-up, the mica surfaces have strong adhesive forces that persist, even in the presence of a liquid medium,[155] and is importantly a single-asperity system.[152,154]Therefore, the contact mechanics of a sphere adhered to a flat surface will be described.[1,156] A graphical representation of the theoretical contact mechanics model considered and described is given in Figure 2.5. Surfaces are thought to adhere when a force is required to separate them. This adhesion force, F_{adh}, can be related to the work required to separate these adhered surfaces, W_{ad},[154,157] and assuming that the surfaces are completely rigid and incompressible.[1,155,156]

$$F_{adh} = 2\pi(\frac{R_1 R_2}{R1 + R2})W \tag{2.6}$$

where R_1 and R_2 are the radii of the two spheres in contact. This is a direct

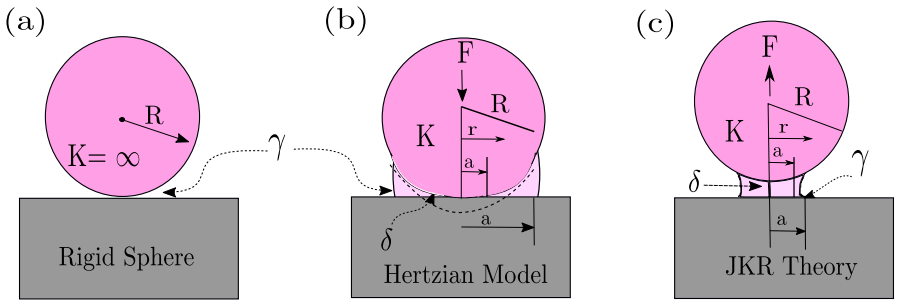


Figure 2.5: Image showing the geometries of Contact Mechanics. (a). Rigid incompressible sphere on a rigid surface (b). Hertzian non-adhesive elastic model where the sphere is treated as deformable and (c). JKR description of a deformable sphere in the presence of adhesive forces where the elastic sphere is about to spontaneously separate from adhesive contact.[134]

consequence of the Derjaguin approximation:[134]

$$F(D) = 2\pi RW(D) \tag{2.7}$$

However, real systems are not incompressible and when surfaces come into contact, they deform elastically under an applied load.[154,158,159]This deformation is often a trade-off between the applied load and the attractive inter-surface forces that promote adhesion.[1,157] The adhesive forces result in a finite contact area even in the absence of an applied load.[154]

The most rigorous theoretical treatment of this system that accounted for the influence of attractive adhesion forces was developed by Johnson, Kendall and Roberts.[134,154,159,160]This treatment is commonly referred to as the 'JKR Theory' and is described in Figure 2.5(c). In JKR theory, under mechanical equilibrium the contact area of the surfaces with radius a is given by:

$$a^3 = \frac{R}{K}[F + 3\pi RW \pm \sqrt{6\pi RWF + (3\pi RW)^2}] = \frac{R}{K}(\sqrt{\frac{3}{2}\pi RW} \pm \sqrt{F + \frac{3}{2}\pi RW}) \tag{2.8}$$

where R_1 and R_2 represent the radii of the spheres, K is the elastic modulus, and W is the surface energy per unit area.

In the case of a sphere on a flat surface:

$$R_2 = \infty \quad \text{and} \quad R = R_1 \quad \text{and} \quad W = 2\gamma_{SV}$$

To give a finite contact radius under no applied load, F=0:

$$a_o = (6\pi R^2 W/K)^{\frac{1}{3}} = (12\pi R^2 \gamma_{sv}/K)^{\frac{1}{3}} \tag{2.9}$$

From this, the dependence of the contact radius on the external applied load is:

$$r = (\frac{R}{K}[L + 6\pi R^2 \gamma_{sv} + \sqrt{12\pi R\gamma_{sv} L + (6\pi R\gamma_{sv}^2}])^{\frac{1}{3}} \tag{2.10}$$

The displacement of the surfaces, δ, is given by:

$$\delta = \frac{a^2}{R}[1 - \frac{2}{3}(\frac{a_o}{a})^{\frac{3}{2}}] \tag{2.11}$$

The relationship between contact area, a, and displacement, δ, with load is shown in Figure 2.6: Crucially, the load-displacement curve in Figure 2.6 is analogous to

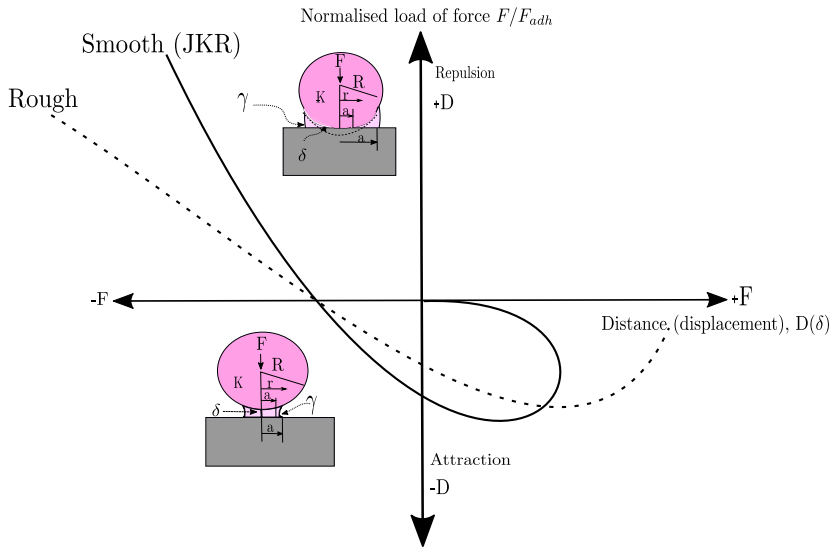


Figure 2.6: JKR Model: Graphical representation of the JKR normal force versus distance curve, $F(D)$, expected for an elastic sphere on approach and separation from a rigid surface.Adapted from[1]

a force-distance profile of the JKR interaction energy.[1] From this, it is clear that if a sphere if pulled by a force, F, it detaches from the surface when F matches the adhesion force of the system, F_{adh}:

$$F_{adh} = -\frac{3}{2}\pi RW = -3\pi R\gamma_{sv} \tag{2.12}$$

Whilst theoretical objections to the JKR theory were made by Derjaguin, Muller and Toporov,[1,161,162] the JKR theory is still widely accepted and used in systems modelling deformation of elastic spheres.

2.2.2 | Macroscale Friction

Friction can be defined formally as the force resisting the movement of surfaces relative to each another.[153] As this resistive force is non-conservative, it gives rise to methods of energy dissipation, or transfer of energy from one body or form to another,[157,159] and it is these energy dissipating forces associated with friction that result in the decomposition, wear and tear that negatively impacts industrial processes.[5,6,154]

In its simplest and most primitive form, friction can be compared to the collision of two hard spheres.[5,6,154] During this collision, the kinetic energy of one sphere is transferred to the other, but since the collision itself is not perfectly elastic, a fraction of the initial kinetic energy is lost or dissipated as heat.[153,154,156]

Coulomb Model

From this very simplistic starting point, consideration of the parameters involved in a real tribological system is then required. The Coulomb description of friction is one that takes into account real tribological parameters:[134,153,154]

i The system consists of many molecules that interact through a potential function

ii The top molecule is subjected to both normal, F_N, and lateral forces, F_L.

This is represented below in Figure 2.7. In this model, for the top molecule to move

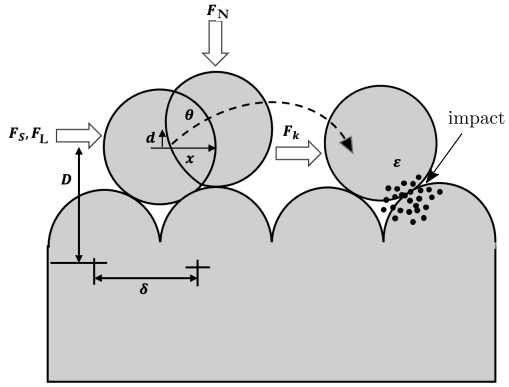


Figure 2.7: Coulomb Model. Schematic of the normal and lateral forces, F_L and F_N, and normal and lateral displacements, d and x, associated with moving one surface relative to other. On impact, a fraction of the kinetic energy, E, is transferred from the top surface to the bottom one. Furthermore, from this schematic it is clear that the surface roughness, on the sub-Angstrom scale, is important in determining the friction force, F_L, but not the normal force, F_L.Adapted from[134]

laterally by a distance x under subject of the lateral force, F_L, it also needs to rise, or dilate, by a distance d.[134] *Dilation* is a phenomenon closely associated with the induction of motion or flow in a system that was initially at rest, and therefore force needs to be applied to the system to overcome opposition to dilation.[156]

First, force is required to initiate the lateral motion, F_L, that will overcome the externally applied normal force, F_N:

$$F_L = F_N tan\theta = \mu F_N \tag{2.13}$$

Secondly, force is required to overcome the intermolecular adhesion forces that hold the two surfaces in contact.[1] Assuming that the number of bonds, and therefore energy, is proportional to the contact surface area, A:

$$F_L = \sigma A \tag{2.14}$$

Combining these two leads to this expression for the lateral force required to achieve

lateral motion:

$$F_L = \mu F_N + \sigma A \tag{2.15}$$

where the first term is the load-controlled contribution, and μ represents the friction coefficient, and the second is the adhesion-controlled contribution, where σ is the shear stress of the system.

Importantly, Equation 2.15 shows the lateral force, F_L required to move the molecule to the next lattice site. At this next lattice site, it has a kinetic energy ε it has acquired from moving from its initial position x to this new position $(x + \delta)$. Notably, motion may or may not continue dependent on what fraction of this kinetic energy is transferred to the bottom molecule.[1] From this, the '*static*' and '*kinetic*' friction coefficient have their origin.[1,156]

Friction Coefficient

When measuring the relationship between load and friction forces in a sphere on a flat surface geometry, such as in the SFB or the traditional ball-on-scale setup, a clear load-friction dependency exists. Comparison of experimental observations of this relationship indicate that this dependency manifests at multiple length scales.[1,153,154]

$$\mu = \frac{Lateral\ Friction\ Force}{Normal\ externally\ applied\ Load} = \frac{F_L}{F_N} \tag{2.16}$$

where the friction coefficient, μ, is independent of the surface area or contact area, A.[1,153,154]

From Equation 2.16, it is clear that the friction coefficient, μ, is an effective measure of the relationship between applied load and friction forces.[134,153,154] Notably, the friction coefficient, μ, is often used as a comparison point between tribological systems.[48] This is attributable to the nature of the friction coefficient. It is an empirical property that materialises from the tribological system.[1] It can encapsulate the surface roughness, adhesion forces, and further intermolecular forces that

characterise the interacting surfaces.[5,48,153] In the case of a lubricated tribological system, the friction coefficient may also reflect the structural forces that dominate when the lubricating film is put under strict confinement.

Stick-Slip Motion

When one surface is moved relative to another, the resulting motion may take up many forms. One of the most common forms of motion encountered with the lateral movement of one surface relative to another is termed stick- slip friction.[163–169] A typical stick-slip friction trace is displayed in Figure 2.8, showing the characteristic 'sawtooth' motion that results when measured friction force, F_L, is plotted versus time in a 'friction trace'. The "saw-tooth" motion indicates that the relative motion of the surfaces is non-uniform, despite the constant velocity applied displacement. The response is composed of repeating cycles of sticking and slipping which arise

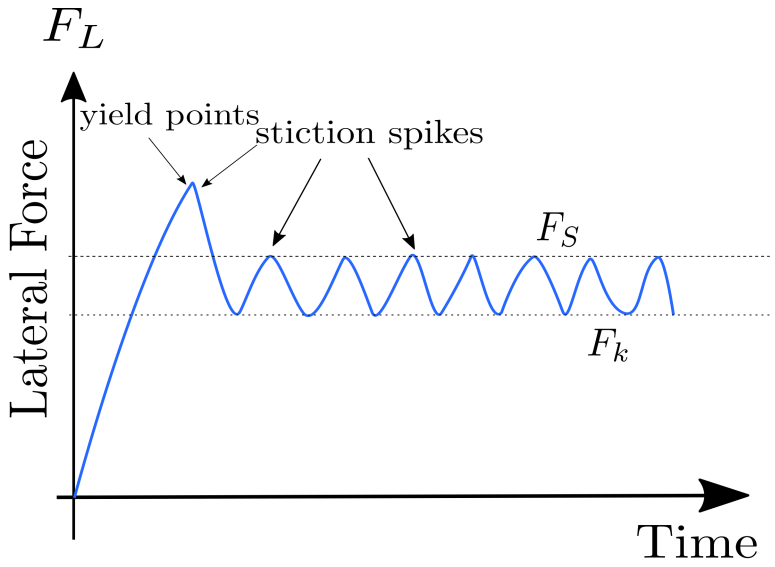


Figure 2.8: Stick- Slip Motion of shearing surfaces: Graphical representation of the typical "saw-tooth" motion characteristic with stick-slip motion which arises from a constant shear-velocity displacement if a contact between two solids. The stiction peaks indicates the yield force; stiction is a portmanteau of static and friction. F_S is static friction, measured at the peak of the trace and F_k is kinetic friction, taken at the trough of the trace. Adapted from[165]

due to the roughness of the surface: the collective motion of the asperities slipping from one to the next.[163–169] During the 'stick phase', the energy is stored in elastic

deformation in the solid as there is no frictional displacement.[165–168,170,171] Once a threshold is reached, the surfaces then 'slip' until they stick at the next asperity. During the slip phase, the stored energy is turned into lattice vibrations which eventually dissipate as heat in the solid material.[164,167,169] The lateral force then varies between F_S and F_k over one cycle.[74,75]

Stick-slip friction is the mechanism from which musical instruments, such as the violin, generate sound.[6,166,169] However, stick-slip friction is the source of great ruin in industry, as this motion often results in decomposition and wear to surfaces.[166,169] One reason for this is 'stiction'[6,48] Stiction arises due to the strong adhesion of surfaces when they are at rest. The intermolecular interactions between surfaces are more significant and thus more work is required to overcome them to initiate motion.[165,167,168,170,171] As a result, a higher yield force is required to initiate sliding compared to the yield force of individual stick-slip cycles, and this produces that spike at the beginning of the friction trace. The energy required to break the adhesion, often causes wear and tear.[6,48,134,166,169]

Smooth Sliding

If the sliding velocity is increased, then the kinetic energy acquired by the top surface exceeds the energy barriers encountered as each contact moves from asperity to asperity and so it slides smoothly at a steady state kinetic friction force.[134,168]

2.2.3 | Lubricated Sliding

Lubricated sliding or friction can be formally defined as the friction forces that arise when two surfaces in relative motion are separated by a liquid or solid film, see Figure 2.9.[30,164,168] If the film has strong enough intermolecular forces, the surfaces are prevented from coming into contact as the film is strong enough to withstand significantly high pressure.[19] Importantly, this film, henceforth termed a lubricant, protects the surfaces from shear-induced damage and reduces the friction forces

present in the system.[17,30,172] A simple mathematical relation for the dependence of

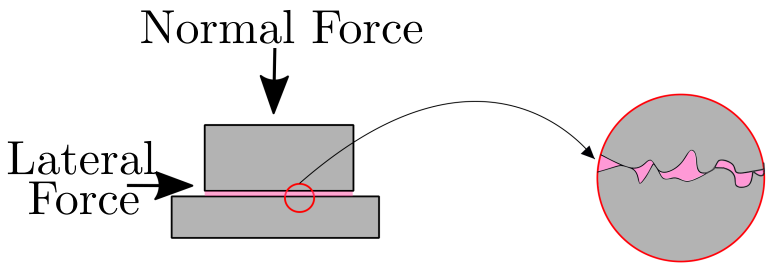


Figure 2.9: Schematic illustrating the use of a lubricant film

friction force, F_L, on the properties of a hydrodynamic lubricant, explored below, is:[134]

$$F_L = \eta A V_L / D \tag{2.17}$$

where η is the viscosity of said lubricant, A is the contact area of the surfaces, D is the separation of the two surfaces, and V_L is the velocity of the lateral motion. From this equation it is clear that the viscosity of a lubricant plays a significant role.[19] Moreover, the introduction of a lubricant film reduces the shear stress, σ, characterising the system.[1]

Despite the great benefits a lubricating substance provides, it is unwise to ignore the changes in the structuring of the lubricant at these high pressured and confined contacts.[19] Within the literature there is much evidence and thus agreement that under such severe conditions, the molecules of a liquid begin to adopt a more ordered, and perhaps a 'solid-like' structure.[168,173]

Experimental results, shown in Figure 2.10, measuring the lateral displacement of mica surfaces separated by an Octamethylcyclotetrasiloxane film (OMCTS) illustrates this confinement-induced ordering quite well.[74–76] Note that the lateral displacement measured was not induced by application of an external lateral motion.

By comparing the oscillatory force profile of OMCTS at changing confinement distances, to the lateral displacement traces, the changing nature of the OMCTS film is clear. At large separations, 116 nm, the resulting shear trace Figure 2.10(a) is

characteristic of a liquid film. At these large separations, random vibrations persist, though damped, up to a separation distance of 6.2 nm, shown in trace (b).[74–76] A drastic change in the lateral displacement, at surface separation of 5.2 nm, is

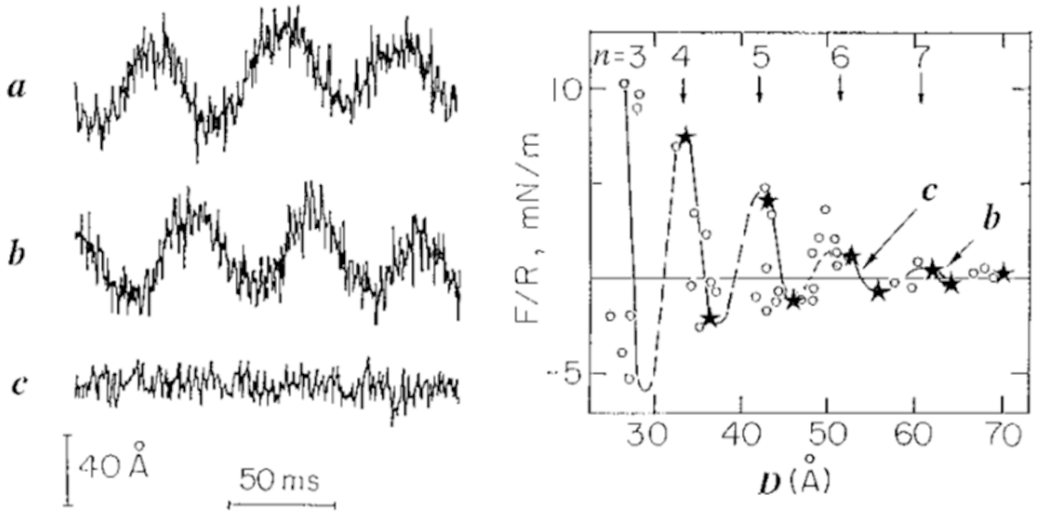


Figure 2.10: Experimental evidence for confinement-induced ordering. *Left:* Direct recordings of the variation in time of the relative lateral displacement of mica surfaces immersed in OMCTS with no applied lateral motion at separations of: trace (a) D=116 nm; trace (b) D=62.2 nm ; trace (C) D=54.2 nm. Traces (b) and (c) correspond to points b and c on the force distance profile for this liquid. *Right:* Oscillatory Force- Distance profile of an OMCTS film immersed between mica surfaces. Points b and c are indicated, and correspond to film thicknesses of 62.2 nm and 54.2 nm, respectively. Taken from[74,75]

recorded in trace (c). At this distance, the random lateral vibrations cease. Therefore, the film is able to resist the random shear behaviour induced by ambient noise, characteristic of a solid film. By comparing this to the *Force* vs *Distance* profile, it is thought that the transition occurring from trace (b) to (c) is coupled to a change in film thickness from seven to six molecular layers.[74,75]

This behaviour can be reasoned by considering Equation 2.18 and comparing it to a simple relationship showing the dependency of film thickness, D, on applied normal load, F_N, see Equation 2.19. Similar behaviour has been observed in a number of experiments on non-polar molecules, ILs and linear alkanes.[19,68,69,103,171,174–180] This, along with molecular dynamics simulations, has provided the crucial evidence that

this experimentally-observed phase transition is solely linked to confinement.

$$F_L = \eta A V_L / D \tag{2.18}$$

$$F_N = 1/D \tag{2.19}$$

Therefore, as the load, F_N, increases, the thickness of the lubricating liquid film, D, decreases. With this, the effective viscosity of the liquid film under confinement, η_{eff},can be orders of magnitude greater than that characterising the bulk.[74,75,170] This is because the molecules of the confined liquid begin to adopt an ordered state and the interacting surfaces, are therefore, said to induce epitaxial ordering.[74,75,170]

This confinement-induced ordering forms the basis for theories of stick-slip friction in a lubricated system.[163,165,170] However, the exact mechanism by which this ordering results in stick-slip motion is still disputed.[153,163,181] A graphical illustration of the two competing theories: interlayer slip, and shear-induced melting, is provided below in Figure 2.11. Crucially, in both theories, the 'stick' of the sliding motion is said to result from adoption of an ordered structure, called static loading.[1,163,165,182] The mechanisms diverge in their accounting for the effect of applied shear stress on the liquid structure. In the interlayer slip mechanism, applied shear stress to this now ordered film, is thought to result in dilation and formation of a slip boundary between molecules, leading to a 'slip'.[1,163,165,182] Contrastingly, the 'slip' in the shear-induced melting mechanism is a result of melting of the liquid film back to its more liquid-like disordered state.[1,163,165,182] In both mechanisms, the stick-slip motion is believed to persist only if re-ordering of the film occurs.[1,163,165,182]

However, there are some cases where the liquid film does not undergo confinement-induced ordering, and thus displays smooth motion which is preferable for tribological applications:

i. If the interacting surfaces and the liquid film are incommensurate, then the

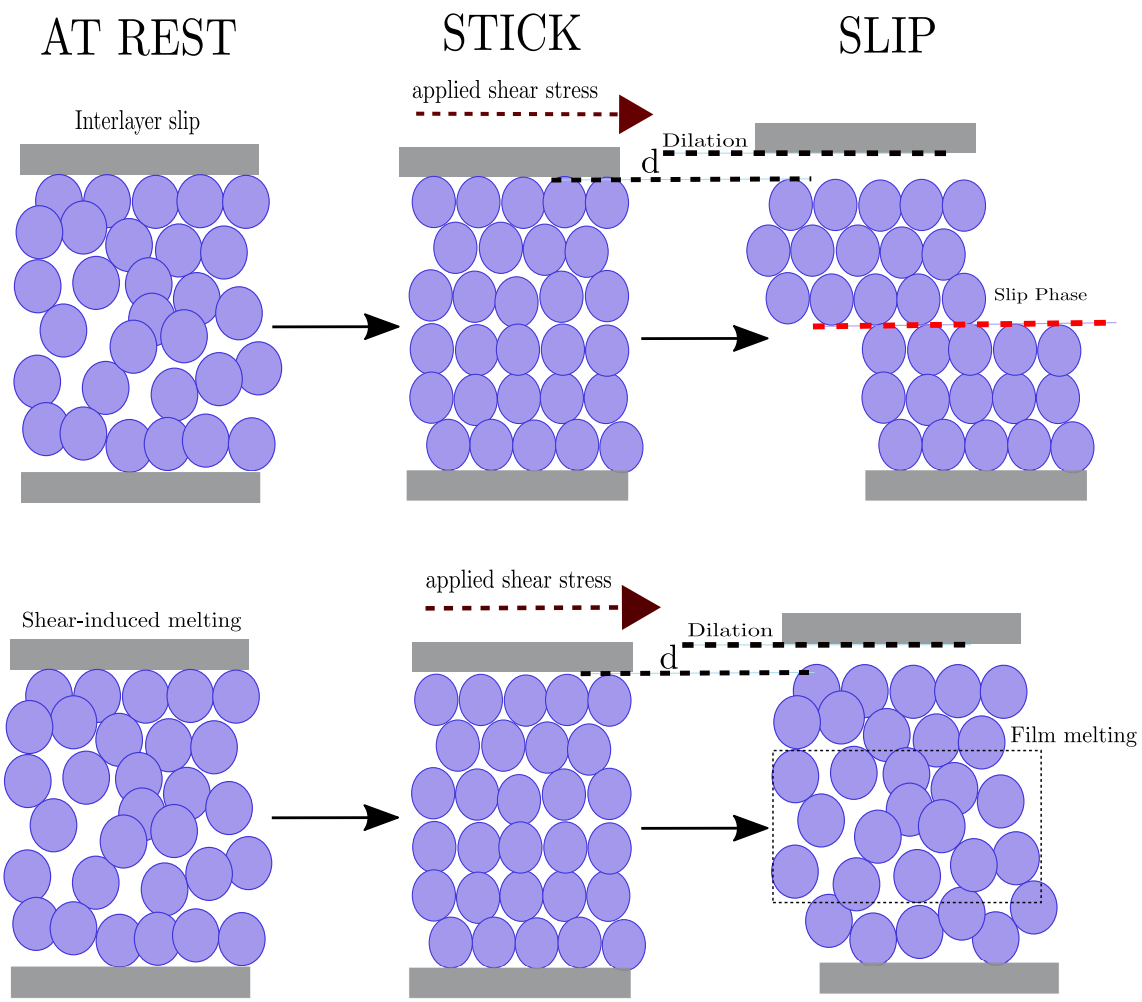


Figure 2.11: Graphical Illustration of the structural mechanisms associated with stick-slip frictional motion. (a) Sample of the traditional stick-Slip motion observed experimentally when two surfaces come into shearing contact, measured using a piezoelectric tube (PZT). (b) Schematic of the structural mechanisms associated with stick-slip friction, with the two main theoretical mechanisms: inter-layer slip, and shear-induced melting, illustrated.Image adapted from [1,165]

epitaxial ordering promoted by the solid surfaces, may not occur.[178]

ii. The liquid film itself may be too disordered to adopt the ordered configuration promoted by confinement. Such is the case for many common lubricant films, such as polymer melts and highly-branched hydrocarbons.[183,184]

iii. The surface may be of sufficient roughness or dynamic lability, such as is the case for surfactant coated walls, that the confined liquid cannot order.

The study of the nature of confined films and how this affects the shearing behaviour

is therefore an idea suited for further study. Importantly, the nanoscale contacts provided by the SFB, provides a well-defined and controlled system to study this relationship in.[74,75] The ability to control film thickness down to the nanometre scale, and the high-resolution measurements of both normal and lateral force, enables a detailed understanding of the frictional behaviour of confined liquid films.[19] Consequently, the work in this thesis will focus on investigating the shear behaviour of liquid films confined down to nanoscale contact in the SFB and to the macroscale in a tribometer.

What makes a suitable lubricant

While the basic principle of lubrication is very rudimentary, in practice it is difficult to achieve. The ideal lubricant should be able to reduce the coefficient of friction by providing alternative and lower energy barriers for shear motion, and reduce surface wear.[19]

Criteria

i. The coefficient of friction should be controlled so that reproducible motion is possible.

ii. The lubricant must be able to sustain a relevant normal load without being squeezed out as this prevents the two surfaces from coming into direct contact which would cause significant damage and wear to the surfaces.

iii. Despite maintaining a normal load, it must remain fluid or maintain other dissipation modes

iv. The lubricant must be minimally dependent on changes in the environment and be able to perform in a similar manner regardless of temperature or pressure.

Industrial Lubricants In industry, these factors are difficult to achieve. Liquids are normally 'squeezed out' under pressure.[6,7,14,126]

There are two different categories of conventional lubricants in use today: synthetic and natural. Perfluoropolyethers (PFPE's), shown in Figure 2.12, are synthetic, high-end lubricants used in particularly hostile and challenging environments as they have a high thermal and chemical stability.[14,185] Despite this, at high pressures, they

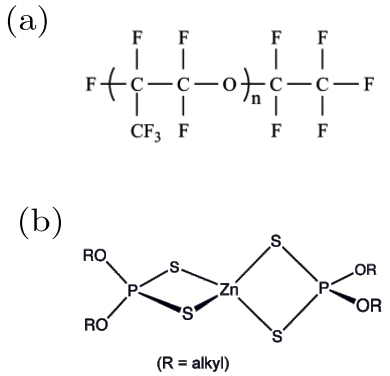


Figure 2.12: Common types of lubricants: PFPEs and ZDDP. Images taken from[14,185]

decompose and wear and this causes damage. Engine oils and similar lubricants use mineral oils and are classed as 'natural'.[185] Lubricant additives are also common, such as zinc dialkyldithiophosphate (ZDDP), shown in Figure 2.12(b), which is commonly used in hydraulic and motor oils with the aims of improving lubrication performance. however, its decomposition products have environmentally damaging effects.[14,98,185–187]

2.2.4 | Lubrication Regimes

As previously mentioned, the mechanism of lubrication depends highly on the conditions and the lubricant. As a result, there are three main regimes of lubrication observed: the hydrodynamic regime, the boundary regime, and the mixed lubrication regime.[14,128]

Hydrodynamic Regime

The hydrodynamic regime is characterised by a thick film of lubricant between the surfaces, greater than 10 molecular diameters and often up to micrometric thickness.[14,19,128] This prevents the surfaces from coming into contact and is depicted in

Figure 2.13.

This regime can only really occur at low normal loads, high viscosity, and high shear velocity.[14,19,128] As the surfaces are not in contact, the lateral friction forces are dictated by the viscosity of the lubricant:[19]

$$F_L = \frac{Av\eta}{D} \tag{2.20}$$

where A is the area of the surfaces, v is relative shearing velocity, D is surface separation and η is viscosity.[134,175] In this regime, friction coefficients are generally the lowest. Elastohydrodynamic lubrication is a subset of hydrodynamic lubrication and is where there is significant elastic deformation of the two surfaces in contact which modifies the shape, thickness, and viscosity of the lubricant film.[14,188]

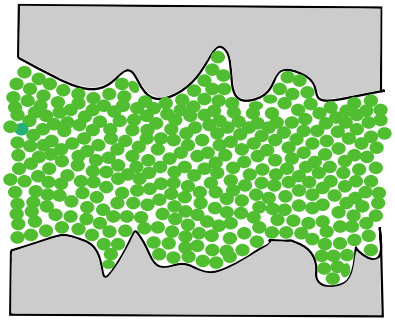


Figure 2.13: Hydrodynamic Lubrication A simplified graphic of hydrodynamic lubrication conditions. The surfaces are not in contact due to the thick film and the normal load is supported by the film of lubricant. Shearing the film will result in Couette flow conditions[134]

Boundary Regime

The second main type of lubrication is the boundary lubrication regime. This is where the two surfaces are separated by a lubricant film of a few molecules in thickness on a single asperity.[97,101,169,189] This film arises from a boundary layer of molecules that are adsorbed to the surfaces, see Figure 2.14. Friction is at its highest as the surfaces are in near contact and normal loads are high.[97,101,169,189]

Experimentally, the friction response follows Equation 1.2, although modelling the

actual friction tends to be challenging.[97] The film is not just a two-dimensional slice as depicted in Figure 2.14: it spreads laterally to far larger dimensions. A good boundary lubricant will reduce both the attractive forces that contribute to friction and reduce adhesion or reduce the dependence on the normal load as in this regime surface and molecular interactions dominate.[97] As would be expected, both

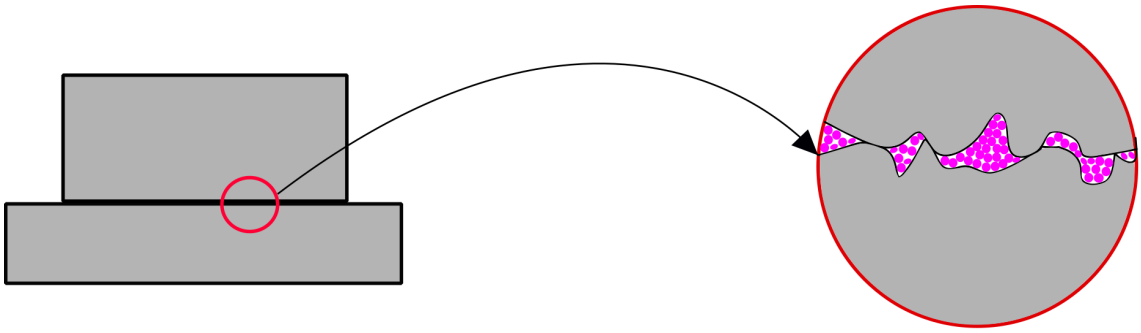


Figure 2.14: Boundary Lubrication A simplified graphic of boundary lubrication conditions. Whilst in some places the film is thicker, some of the asperities are separated by a film that is 'one' lubricant molecule thick, which forms the boundary. The zoomed in image highlights what can be resolved by a Surface Force Balance: a single point of contact separated by a layer of molecules.

stick-slip friction and smooth sliding may occur in the boundary lubrication regime, dependent on the conditions to which the system is subjected.[97,101,169,189] stick-slip friction may even occur on a single contact point, such as in SFB experiments.[103] This is due to the thin film solidifying under confinement and hence a shear response that is typical of a solid; the film sustains a finite stress before sliding occurs.[134,178] Accordingly, the elastic energy stored in the film must be dissipated during the slip and upon the instant of the stick, at which point the residual momentum of the top surface is lost. During the slip, energy is dissipated by viscous heating of the film.[1,75] At the point the surfaces abruptly stick together, the transfer of momentum causes "ringing" oscillations due to the excitation of vibrations in the system seen in Figure 2.8. These vibrations decay as their energy is dissipated as heat.[166]

The Stribeck Curve

The friction behaviour of the boundary and hydrodynamic regimes are related by a Stribeck curve as shown in Figure 2.15.[1,170,190] On a Stribeck curve, the μ of the

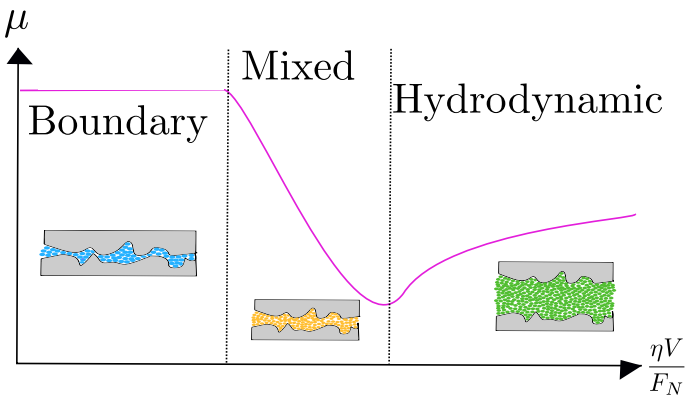


Figure 2.15: A model Stribeck curve for μ against the *Hersey* number $= \frac{\eta V}{F_N}$. Where η is the lubricant viscosity, V is the shearing velocity, and F_N is the normal load. Friction is non-linear and the three lubrication regimes are visible. Adapted from [134,190]

film is related to the *Hersey number*. The Hersey number, H, is described below as:

$$H = \frac{\eta V}{F_N} \tag{2.21}$$

where η is the viscosity of the lubricant film. This illustrates shows that the friction coefficient of lubricated contacts can be related to the normal load, shearing velocity, and viscosity of the lubricant.[134] The progression of the friction coefficient with these three variables enables the identification of three lubrication regimes: boundary, mixed and hydrodynamic, as seen Figure 2.15. Mixed lubrication involves elements of both the boundary hydrodynamic regimes and thus viscosity and ability to form a boundary layer are both intrinsic to a lubricant's performance.[1,170,190,191]

3 | Experimental Methods

The work in this thesis is primarily concerned with the measurement of normal and shear forces using a *Surface Force Balance*, SFB. The SFB was first developed by Tabor *et al.* in order to measure long-ranged Van der Waals forces between surfaces in air.[130] Further development by Israelachvili *et al.* successfully adapted the SFB in order to measure the forces between thin liquid films.[131,192] Subsequently, the SFB has now been used to measure both normal and shear forces across a range of confined systems including liquid crystals,[193] water-in salt electrolytes,[149] deep-eutectic solvents[194] and liquid polymers.[195] This chapter will describe the main experimental details and set-up of the SFB that permits the study of both normal and shear forces.

3.1 | Surface Force Balance

The SFB is a high resolution force measurement technique that accommodates the study of confined systems.[192] As displayed in Figure 3.1, the SFB's operating principle relies on a pair of surfaces separated by a confined liquid film whereby the surface separation is controlled.[75,192,196] The surfaces may be brought into contact using either an electric motor or a sectored piezoelectric tube.[192] Crucially, the separation of the surfaces, equivalent to the liquid film thickness, can be determined down to the nanometer precision using multiple-beam interferometry, MBI.[197,198] In this thesis, the particular SFB set-up proposed by Klein and Kumacheva is employed.[196]

3.1.1 | Surface Preparation

The core of the SFB is a pair of surfaces between which a liquid is confined. The most commonly used material for the surface is Muscovite mica.[93,107,195,199,200] Whilst other materials have been used, mica is the preferred material because it is trans-

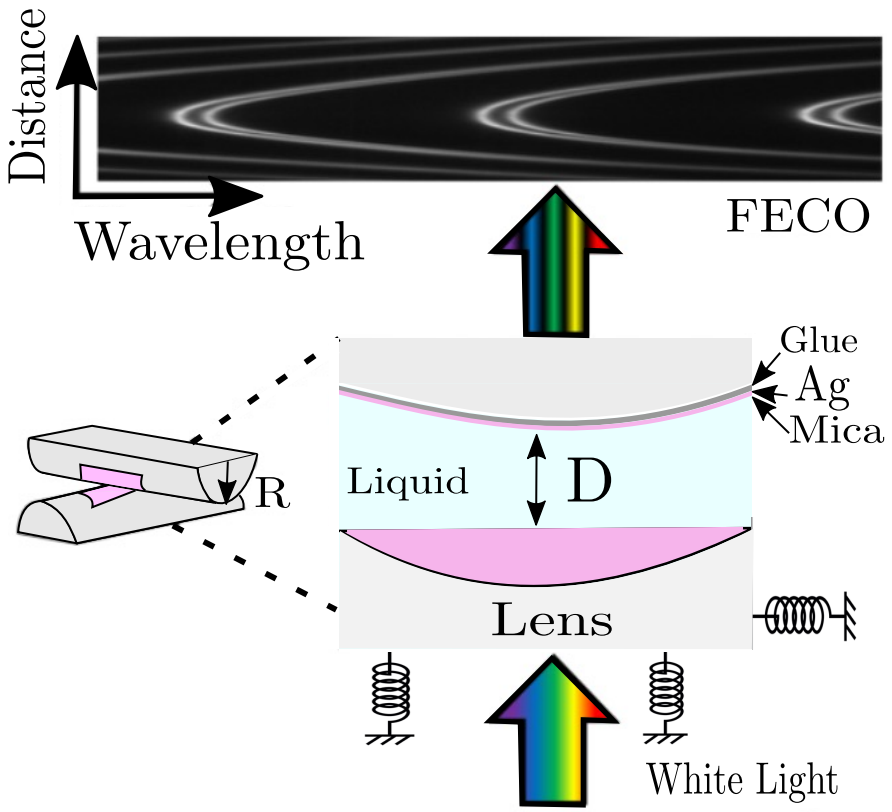


Figure 3.1: Schematic of the SFB experiment that allows for the measurement of the normal, F_N, and shear forces F_S, acting between two surfaces separated by a liquid medium. Adapted from[194]

parent, inert and can be cleaved to produce large (several cm^2) atomically smooth sheets (RMS $<$ 0.1nm) down to one micrometer (μm) in thickness.[93,107,195,199,201]

Thin, single-faceted mica pieces are cleaved, see Figure 3.2(a), then cut with an electrically heated platinum wire to produce cut mica pieces. Although the use of the platinum wire may release platinum nanoparticles, and thus introduce contaminants, characterisation by AFM showed that their abundance can be reduced with the use of thin platinum.[201] Once cut, the mica pieces are transferred and adhere to a large freshly cleaved mica base sheet.[201] Each base sheet therefore holds multiple pieces of mica that are of suitable size for an experiment. The whole base sheet is then placed in an evaporator under vacuum (10^{-6} mbar) while silver is evaporated onto the surface at a rate of 0.1 $nms^{-}1$ to deposit a smooth silver surface of 50 nm thickness, shown in Figure 3.2(b). The now silvered base sheet is then stored under

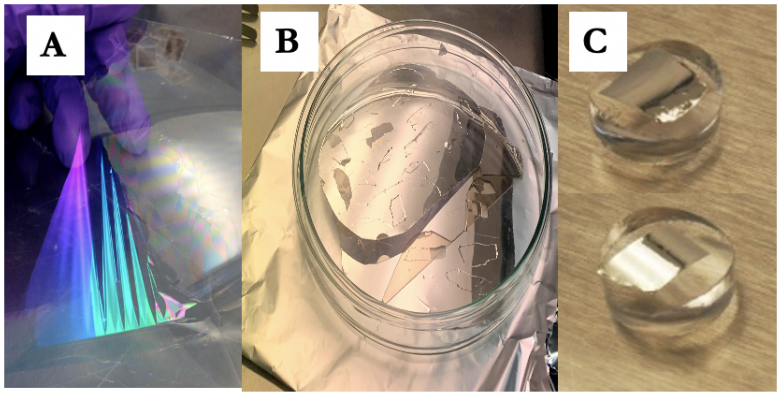


Figure 3.2: (a) Muscovite mica cleaved to thin sheets which are atomically smooth and free of steps over a large area. (b) Mica pieces adhered to a large mica sheet that had a thin layer of silver (50 nm) evaporated onto it to produce a highly reflective surface. (c) Back-silvered mica pieces glued to cylindrical lenses.

vacuum in a desiccator to prevent contamination and oxidation of the surface.

The atomically smooth silvered mica pieces are peeled off the base sheet with tweezers and glued to a cylindrical lens silver mirror- side down in the configuration displayed in Figure 3.2(c). Importantly, the glue used must be insoluble in the studied liquid . To ensure that the mica has the same thickness on each lens, both lenses are prepared using a single piece of silvered-mica that is divided with a scalpel. The glue used in the set of experiments was either EPON 1004 (Shell chemicals) or D-glucose (Sigma Aldrich). The EPON 1004 glue was used in experiments where the ionic liquid concentration was high (> 1.5M). While D-glucose was used in experiments where the ionic liquid concentration was low (< 1.5M). This is because EPON 1004 easily decomposes and deforms in solutions of significant propylene carbonate composition.[90]

3.1.2 | Lens Mount

Lenses are mounted in the crossed-cylinder configuration that results in a macroscopic contact at a single position, often called a spot, demonstrated in Figure 3.3.[1] The crossed-cylinder geometry is beneficial because it is theoretically well-defined and thus permits comparison between experiments and calculations. The radius

of the cylinder at the spot will vary between spots and experiments depending on glue and mica thickness, glass lens radius, and glue homogeneity. It is therefore necessary to normalize or scale the absolute force measurements by the geometry of the experiment. This scaling is convenient and applicable to the *Derjaguin approximation*, which relates the force, F, between curved bodies separated by a distance, D, to the interaction energies between equivalent parallel surfaces, W, at the same separation.[131,134] The Derjaguin Approximation therefore gives a direct link between the measured forces and the energy profile of the confined system. The *Derjaguin Approximation* is:

$$F_{cylinders}(D) = 2\pi R_{eff} W_{flat}(D) \tag{3.1}$$

where R_{eff} is the effective radius, and is thus the scaling parameter necessary for comparison. In the perpendicular crossed cylinder geometry used in the SFB, the effective radius becomes:

$$R_{eff} = (R_1 R_2)^{1/2}$$

The Derjaguin approximation is experimentally valid once the separation between the surfaces, D, is much smaller than the radius of curvature, R.[134]

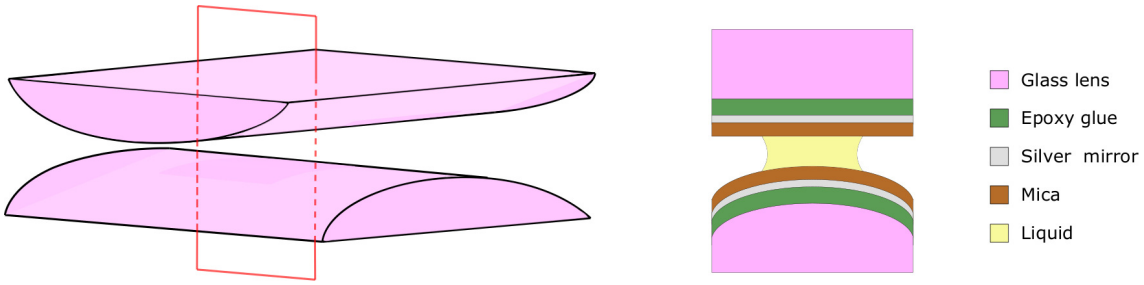


Figure 3.3: The crossed cylinder geometry of the lenses, showing the radii of curvature, R, of each lens and the cross section of their layered structure within the SFB. Note this is not to scale as in the typical experiment mica ≈ 2 μm thick and Au ≈ 50 nm.

3.1.3 | Lens Motion

The lenses are positioned vertically in the crossed-perpendicular cylinder configuration. Their mounts and position within the SFB chamber are presented in Figure

3.4 and are described below: The upper or top lens is mounted in the removable

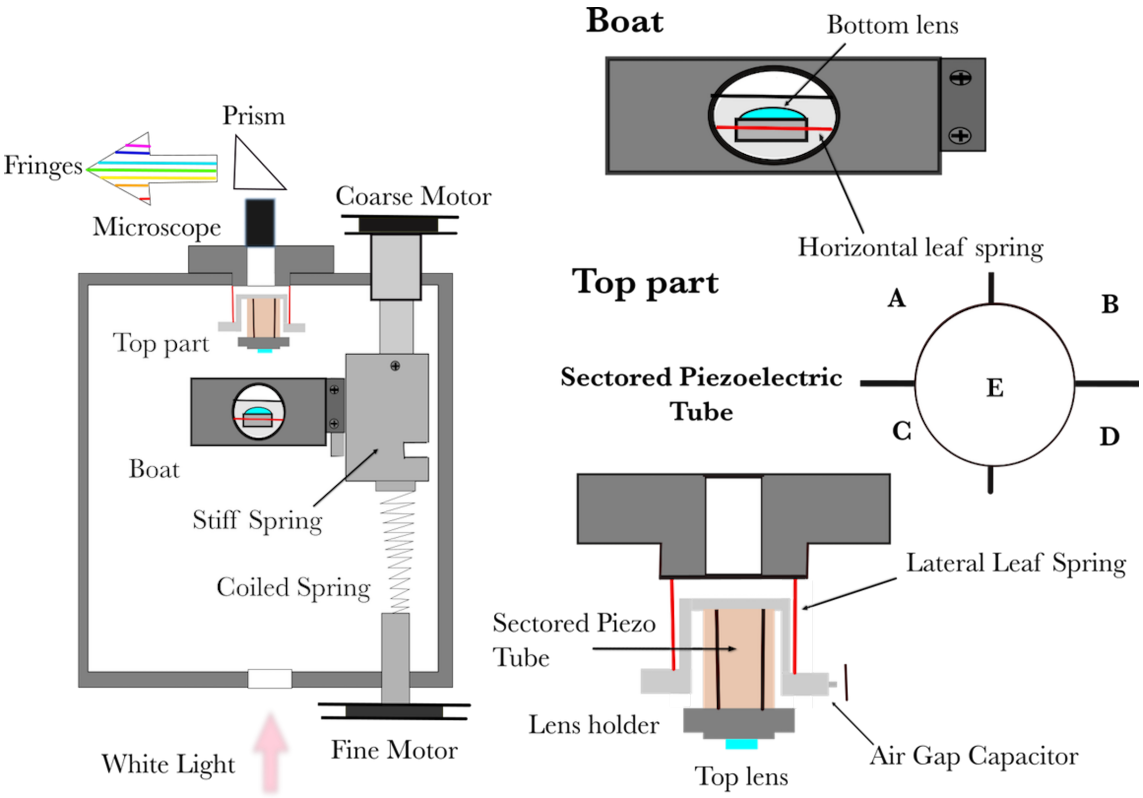


Figure 3.4: The interior and removable parts of the SFB chamber, with lenses shown in blue and springs shown in red. *Left:* A cross section of the SFB chamber showing optical path and motor-differential spring mechanism. Fringes are focused onto a spectrometer grating by a microscope and prism. *Right:* The boat and lower lens set up. The lens sits in a mount supported by horizontal leaf springs. Below this, the top part part and sectored piezoelectrictube (PZT) is shown. The upper lens holder screws into the piezo tube. When motion between the lenses is restricted and lateral motion is forced by the piezo, deflection of the vertical leaf spring is recorded using the air gap capacitor. Diagram adapted from[74]

'top part' of the SFB. The top part contains the sectored piezoelectric tube, PZT, and the vertical leaf springs that are used for measurements of lateral motion. The lower or bottom lens is mounted in the removable stainless steel 'SFB Boat'. It is suspended above the boat by horizontal leaf springs. Vertical motion between the lenses is controlled by the following methods:

COARSE MOTOR: The SFB Boat is mounted by a dovetail slide to a stiff spring that is connected to a step motor. This is known as the *coarse motor* as this motor supports adjustments to lens separation with a μm precision over a cm

range. This motor is susceptible to internal vibrations and is thus poorly controlled and imprecise. Therefore, the coarse motor is primarily used to approach the lenses prior to an experiment and is disabled during experiments.

FINE MOTOR: There is a second step motor, termed the *fine motor*, that while being identical to the coarse motor, is separated from the SFB boat by both coiled and stiff springs to create a differential spring mechanism. The stiff spring has a much greater spring constant than the coiled spring, resulting in a gearing mechanism that provides nm precision as well as damping of motor vibrations and thus far smoother motion when compared to the coarse motor. Furthermore, whole the stepping of the fine motor is similar to that of the coarse motor, the springs "gears" it down to nm/s. The fine motor therefore allows for adjustments in lens separation within the μm range, and with a precision of around 1 nm, it is used to control distance within experiments.

PIEZOELECTRIC TUBE: Finally, precise vertical motion may also be achieved using a sectored piezoelectric tube, PZT, that is mounted within the top part of the SFB. The sectors of the piezo tube are shown in Figure 3.4. The motion achieved through the use of the piezoelectric tube is significantly smoother than that of the fine motor. Application of an equal voltage to sectors ABCD whilst applying the opposite voltage to sector E results in controlled axial extension and retraction of the piezo tube over a range of around 500 nm and with precision of < 0.1 nm. The piezoelectric tube can also be used to apply lateral motion to the top lens in order to measure shear forces. The motion of the piezoelectric tube is monitored with a capacitance probe and a flag, both located in the top part of the SFB.

Lateral motion of one lens with respect to the other is achieved through the use of the piezoelectric tube:

LATERAL MOTION OF THE PIEZOELECTRIC TUBE: Given the sectored architecture of the piezo tube PZT, lateral motion is possible upon application of equal and opposite voltages to opposing sectors, such as B and D. This leads to a contraction in one whilst an expansion in the other that results in an arc-like motion that alters the surface separation, D. Any change in D is likely to alter the load or normal forces present, thus changing the shear force, $F_L(D)$ In order to correct for this, a certain proportion of this voltage is applied to sector E, which provides for purely vertical movement. Overall, this correction ensures that surface separation changes by no more than 1 nm with the full range of lateral motion (around 1000 nm). As the piezoelectric tube permits both lateral and vertical movement and there can be independent control of the sectors, it is possible to apply both vertical and shear motion in order to simultaneously monitor the normal and shear forces of a confined liquid.

In this thesis, normal force profiles are constructed using data obtained during both fine motor and piezo vertical motion while the piezo's lateral motion is used to obtain shear force profiles.

3.1.4 | Minimising External effects

Mica is a high-energy surface that readily adsorbs any particulate contaminant as well as water and organic residues.[201] The presence of any contaminant on or near the contact spot can alter the measurements. In order to prevent contamination, the following steps and procedures are followed:

- In order to minimise particulate contamination, all surface preparation takes place in a laminar flow hood, LFH, and the mica surfaces are exposed to air for as little time as possible.
- All glassware is sonicated in solvents (Ethanol, Toluene then Chloroform) before being rinsed in ultrapure water (Millicule, 18.2MΩcm and <2 ppb TOC) and then left for several hours in the strongly oxidising Piranha Solution (3

parts concentrated Sulphuric Acid to 1 part Hydrogen Peroxide) in order to eliminate organic residues. It is rinsed in ultrapure water before being stored in ethanol before use.

- All stainless steel tools and parts of the SFB that can be washed (such as the SFB boat) are also sonicated in solvents (Ethanol, Toluene then Chloroform) and rinsed in ultrapure water before being washed in concentrated Nitric Acid solution (2 parts water to 1 part Nitric Acid). They are then rinsed in ultrapure water before being stored in ethanol.

- In addition to surface preparation, all work concerned with the set-up of the SFB is performed in an LFH.

The SFB Chamber is constructed from thick, chemically inert stainless steel. One side of it, called the door, can be removed to provide access to the chamber for experimental set-up and is bolted during experiments. This ensures that contaminants are prevented from entering the system once the experiment is in progress. The chamber is mounted on an adjustable tripodal base that is levelled before each experiment. As surface separation is extremely sensitive to any external vibration, the SFB rests on an active vibration isolation table and is enclosed in a polystyrene box to dampen any air vibrations. As variations in temperature cause thermal drift, in order to eliminate or lessen this experimental error, the entire experiment takes place within a temperature controlled environment.

3.2 | Procedure and Analysis

3.2.1 | Liquid preparation and Introduction

Dry solvents were either used from freshly opened bottles (Sigma-Aldrich, anhydrous 99%) or filtered after being stored over molecular sieves for several days. The Molecular Sieves (Sigma Aldrich 0.3mm) were pre-dried at 250 ° C for 24 hours immediately before use. This reliably affords dry solvents with extremely low residual

moisture (50 ppm).

Ionic Liquids used in the work described here were purchased from Iolitec (99% purity). As all the ionic liquids have negligible vapour pressure, they can be dried *in vacuo* to eliminate water. However, the injection process is likely to introduce a small amount of water resulting in an estimated water content below 200 ppm.

The liquid or mixture of interest is injected once all the calibration measurements are performed in air. It is injected between the surfaces with a clean syringe where it forms a capillary bridge between the lenses.

3.2.2 | Determination of Surface Separation

The distance between the mounted surfaces is measured with MBI. The optical set-up that accommodates this form of measurement is described below:

White light from an arc lamp enters the SFB chamber through a window in the base and passes through the two lenses, as seen in Figure 3.4. The thin highly reflective silver layer serves as an optical interferometer, and thus the classical SFB set-up can be defined as a three-layer interferometer, see Figure 3.5. Multiple reflections between the silver mirror results in emerging light that leaves the chamber through a window in the top part. The light is then focussed, through the use of a microscope and a glass prism, into the slit of a grating spectrometer. The light passing through the MBI cavity takes the form of a series of fringes known as *Fringes of Equal Chromatic Order*, (FECO).[113,192,198,202] FECO are parabolic in shape due to the crossed-cylinder geometry of the system. The typical parabolic shape of the FECO obtained from experiments is shown in Figure 3.6. Tolansky described a formal mathematical treatment of the FECO which was later adapted for use in the SFB by Israelachvili.[113,192,198,202] The treatment is simply described below:

Given the crossed-cylinder geometry of the system, the following equation can be



Figure 3.5: A simplified graphical version of the typical symmetrical 3-layer interferometer used in the SFB. The two mica sheets are known to be the same thickness, T_{mica}, as they are taken from the same piece of cleaved mica. They are separated by a film of thickness D, which is monitored throughout the experiment. The refractive indices of the mica and the medium are given by μ_{mica} and μ_{medium} respectively.[192]

applied

$$tan(\kappa\mu_{medium}D) = \frac{2\bar{\mu}sin\theta}{(1+\bar{\mu}^2)cos\theta + (\bar{\mu}^2 - 1)} \tag{3.2}$$

where κ is the wavenumber of light, $\kappa = 2\ \pi\ /\ \lambda$p, and

$$\bar{\mu} = \frac{\mu_{mica}}{\mu_{medium}} \quad \text{and} \quad p = \frac{\lambda_{p-1}}{\lambda_{p-1} - \lambda_p} \quad \text{and} \quad \theta = \frac{p\pi(\lambda_p - \lambda_{p,D=0})}{\lambda_p}$$

with μ_i being the refractive index of component i.[134] A fringe of order p, termed the *p-fringe*, is followed throughout the experiment. Firstly, a calibration in air is performed by bringing the surfaces into contact. In order to avoid damaging the lenses, the approach is performed using the fine motor and the piezoelectric tube. Contact is reached at a sudden "jump in" once vdWs attractions overcome spring elasticity. In contact, flattening of the fringes is commonly observed as it corresponds to the flattening resulting from adhesion between the mica surfaces. Calibration in air is performed in order to determine the wavelength of the p-fringe, $\lambda_{p,D=0}$. This can be inferred by comparison to the known wavelengths of Mercury light. Comparison of the air contact wavelength, $\lambda_{p,D=0}$, to the wavelengths of the p-fringe during the experiment, λ_p, enables high resolution distance determination.[134]

Once injection of the liquid has occurred, it is necessary to do a slow and careful approach in order to find liquid contact. Once liquid contact is reached, it is necessary

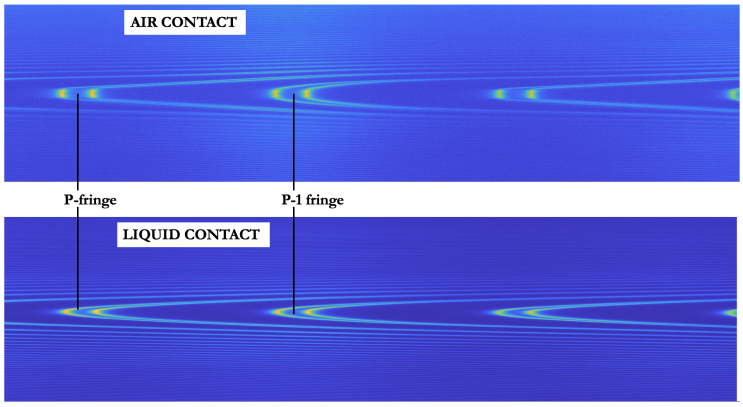


Figure 3.6: An example of the FECO observed and recorded in this work. These are the calibration images used to determine the mica thickness, μ_{Mica}, and the Radius of curvature of the contact position in liquid, R_{liquid},. Their parabolic shapes are a consequence of the crossed-cylinder geometry of the system. In dry contact, flattening of the fringes is observed due to adhesive forces between the mica surfaces. The flattening of fringes is not as pronounced in liquid contact due to the adhesive forces are lessened. In dry contact, the difference in the order of the fringe type (either the p or p_1) is quite obvious and easily determined from the curvature/ flattening of the fringes. Those with negative curvature are termed odd and the p-fringe is chosen to an one of odd order as this is independent of the refractive index of the liquid medium.

to take a further calibration image. This is required to determine the local radius of the interacting surfaces, R, as this is crucial for the normalisation of normal force profiles.

This set-up permits measurements of surface separation with nanometer (nm) precision and errors in our absolute Distance values of $\approx$ 0.03 nm to 0.08 nm.[203] The accuracy of this technique is around 1 nm with any uncertainties arising due to changes in mica compression or in the optical path.[203] Therefore, the use of MBI enables an extremely precise knowledge of relative distances, with uncertainties associated in determining the absolute distance.

3.2.3 | Determination of Shear Forces

As shown in the inset of Figure 3.4, a capacitance probe measures the capacitance of the air gap between it and the flag.[74,75] The voltage is linearly proportional to the gap, L, between the two. The shear force, F_S , is measured with a sensitivity of

10^{-3} mN and is given by:

$$F_S = k_s \left(L - L_0\right) \tag{3.3}$$

where L_0 is the equilibrium position of the flag and k_S is the shear spring constant. To determine the absolute distance of the PZT shearing and the shear velocity it is necessary to calculate the ratio between the applied voltage and the PZT displacement. At rigid coupling of the lenses, the maximum PZT displacement, ΔX, will cause maximum deflection of the springs L_{max}:

$$\Delta x = L_{\max} - L_0 \tag{3.4}$$

3.2.4 | Measurement of Normal Forces

In a normal force experiment, there needs to be simultaneous measurement of surface separation, D, and the normal forces acting on the system, F_N, see Figure 3.7. As

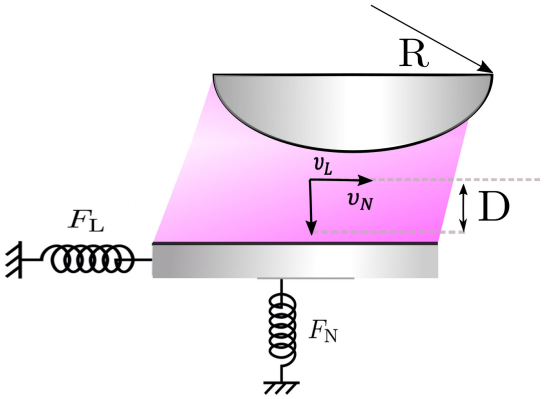


Figure 3.7: Schematic of the SFB experiment to measure the normal and shear force interactions between two mica surfaces separated by a liquid film. The top surface is moved at a normal, v_N, and lateral velocity v_L . The bottom lens is mounted on springs to detect the deflections caused by the normal force, F_N, and lateral force, F_L. The distance, D, and radius of curvature, R, are measured using MBI. Adapted from[11]

the method by which surface separation is monitored was described in Section 3.2.2, the procedure to measure normal force is described below:

In a typical normal force profile, measurement begins with the lenses at large sep-

arations (1μm) where there is no force acting between the surfaces. As the lenses appproach one another at constant velocity, v_s, from a surface separation, D_0 (at time, $t = 0$ s) the surface separation changed by $\Delta x = vt$ during approach time, t. The imposed motion is linear and given by

$$D = D_0 - \Delta x = D_0 - vt \tag{3.5}$$

This baseline is shown in Figure 3.8. Any interactions that occur between the surfaces will result in spring deflection, $\delta(t)$, that can be determined by measuring the difference between the observed $D(t)$ profile and the expected baseline (subtract the red plot from the black plot in Figure 3.8).

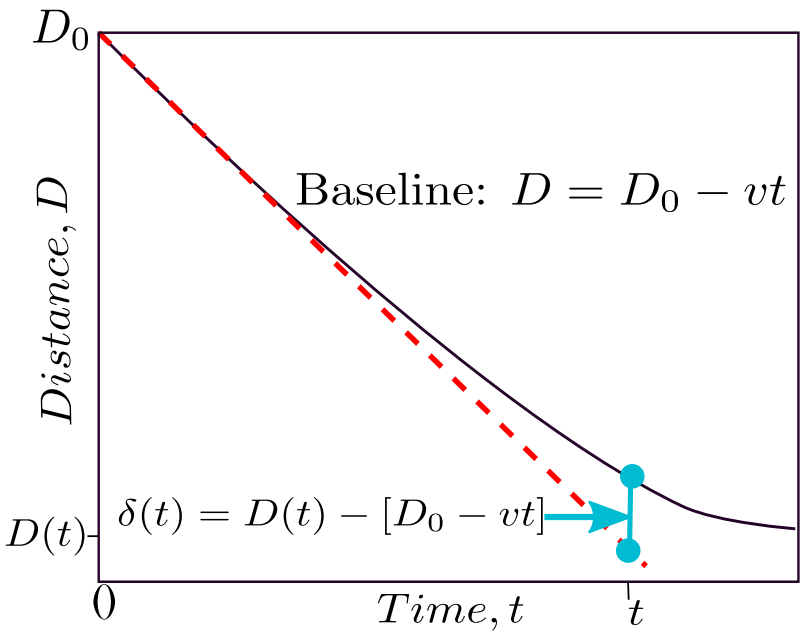


Figure 3.8: Distance, D, versus time, t, schematic. The black line shows the experimental $D(t)$ profile. When the lenses approach one another, the imposed motion is described by a linear baseline: $D = D_0 - vt$, that depends on the starting distance, D_0, approach velocity, v, and time. This baseline is shown in red. The deflection, $\delta(t)$, in blue is given by the difference between $D(t)$ and the linear baseline: δ(t)= $D(t)$ - $[D_0 - vt]$.

$$\delta(t) = D(t) - [D_0 - vt] \tag{3.6}$$

The normal surface force, F_N is then given by,

$$F_N(t) = k_N\delta(t) = k_N[D(t) - D_0 + vt] \tag{3.7}$$

where k_N is the spring constant of our normal springs, and in our experiments this is between k_N = 300- 350 μN

An experimental surface separation versus time profile is shown in Figure 3.9(a), for an ionic liquid. The linear approach is fitted when D > 40 nm (in red). Below

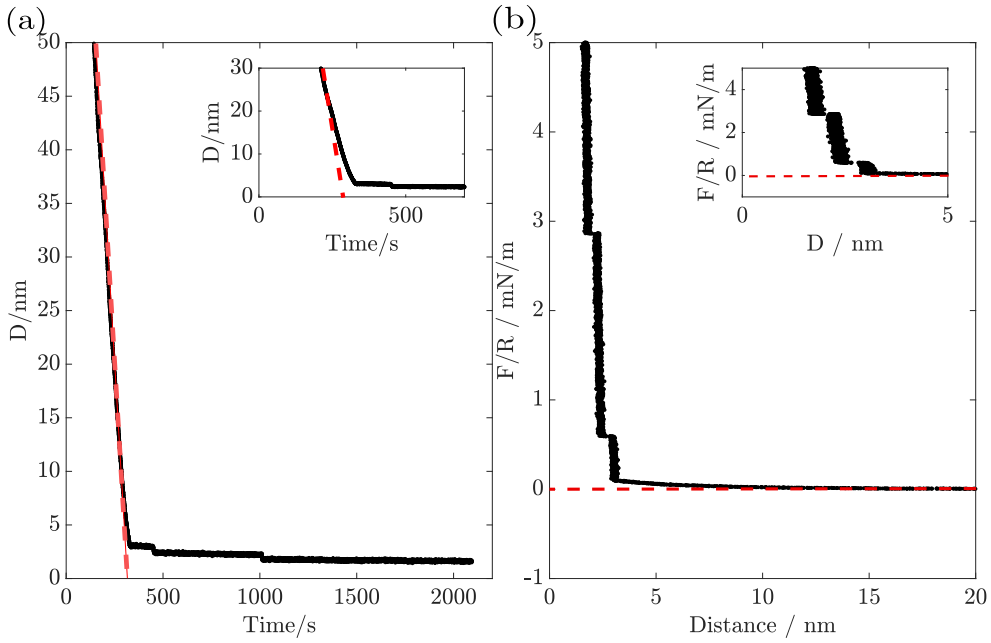


Figure 3.9: Exemplar (a) distance-time and (b) force-distance profiles for an ionic liquid. (a) Surface separation, D, versus time plot in black. When D> 40 nm the surface separation can be fitted linearly with time (red dashed line). A series of steps are observed when D< < 10 nm, shown in the inset. The difference between the black and red plots in (a) gives the deflection needed to calculate the force, F_N. This is normalised by the radius of curvature of the lenses, R, and plotted as a function of D as in (b). The red dashed line in (b) shows the linear fit from (a) corresponds to F_N = 0 mN. The forces at D< < 10 nm are shown in the inset

approximately 20 nm, $D(t)$ deviates from the linear baseline indicating the presence of surface interactions. The normal force is then determined and plotted against surface separation yielding the normal force-surface separation profile in Figure 3.9(b).

If an oscillatory structural force is present, the force-distance profile will exhibit a

series of repulsive steps during the approach, as in the inset in Figure 3.9(b). These steps occur because the normal springs introduce a mechanical instability into the system. A schematic force-distance profile is shown in Figure 3.10 to highlight this instability. As the surfaces approach one another (blue curve), the interaction (normal) force will be balanced by the restoring force of the spring so long as $\partial F_{\mathrm{N}}(D)/\partial D \geq k_{\mathrm{N}}$.

If $\partial F_{\mathrm{N}}(D)/\partial D \geq k_{\mathrm{N}}$ (black dashed regions) the region is unstable and no forces can be measured, resulting in a 'jump in' to a more stable region at smaller D. On retracting the surfaces (in green), the surfaces will remain in the nearest adhesive minimum before 'jumping out' to large separations where $F_N/R = 0$. By approaching and retracting from different surface separations, different adhesive minima can be explored and the corresponding pull-off force can be obtained. Using the SFB, normal forces can be measured with a resolution of 10^{-7} N.

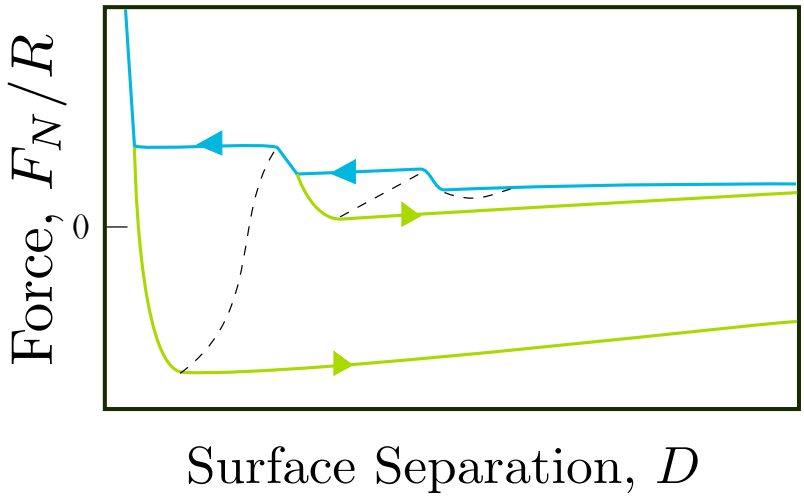


Figure 3.10: Schematic force-distance profile showing the Euler spring instability. On the approach (blue curve), the surfaces 'jump in' when they reach an unstable region (black dashed lines), at the point where $\partial F_{\mathrm{N}}(D)/\partial D \geq k_{\mathrm{N}}$. These jump-in points are shown by the blue left-facing arrowheads. When the surfaces are separated (green curve) they will remain in the nearest adhesive minimum before 'jumping out' to large separations (green right-facing arrowheads). Only one adhesive minimum can be measured during a retraction, so a series of approaches and retractions are required to explore all adhesive minima.

Screening Lengths

Normal force profiles can be plotted on a natural logarithmic-linear scale to most clearly observe the exponential decay of force with surface separation, λ_{exp} as per Figure 3.11. Typically, in force profiles of ILs, a long- range appears in the 6 – 35 nm region and steps are observed in the 2 – 6 nm range. To extract the screening lengths, while we plot the entire profile on a log-linear scale, we focus on the behaviour in the 6- 35 nm region, see Figure 3.11.

If the forces decay linearly in this region when plotted on a log-linear scale of $logF/R$ v D (i.e exponentially on a linear-linear scale), we can obtain a decay length, λ_{exp}, from the inverse of the absolute gradient of the linear region (i.e where we see no step-like profile and the overall shape can be plotted on a straight line), and this value for λ_{exp} can be compared to the expected DH decay length, λ_D to see if our IL systems exhibit underscreening as described in Section 2.1.3. Importantly, the

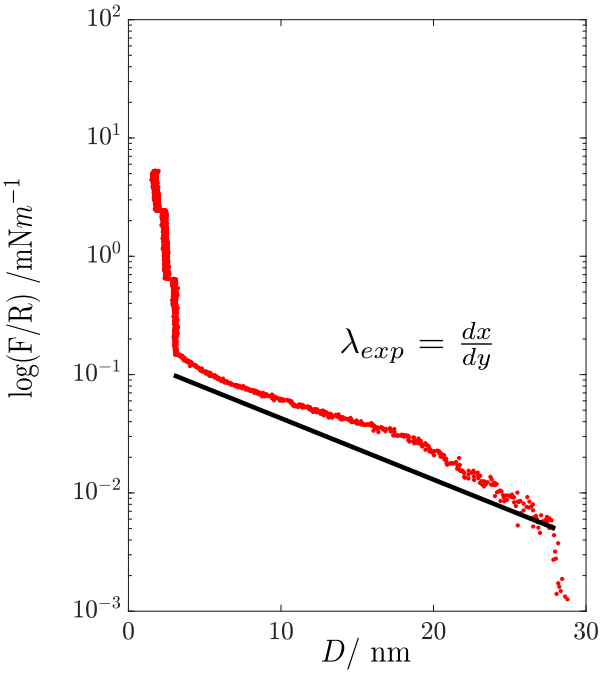


Figure 3.11: Log-linear representation of the normal force, F_N, normalised by the radius of curvature, R, as a function of surface separation, D, profile across 2.7M $[C_4C_1P_{yrr}][TFSI]$-PC. The solid black line indicates the gradient of the long-range exponential decay where the experimental decay length, $\lambda_{exp}= |dx/dy|$.

decay lengths should not be influenced by the fitted approach baseline. To discount

this, the approach baselines are fitted manually using the distance-time plot, and by looking at where the motor approach is most linear. This means that for each different force profile, a unique fit is done to account for the specific conditions. This is called the fixed baseline approach, and is done for every force profile that we measure.

If we are unable to fit the behaviour on the log-linear scale, such as where there is a pronounced curvature or two linear regions, then we do not present experimental decay lengths.

Hydrodynamic Forces

The influence of hydrodynamic (or viscous) forces on the total measured force profiles will be discussed throughout this work, namely in Chapters 5 and 8. Chapter 5 will discuss the work by Lhermerout and Perkin[78] in detail, however it is important to introduce briefly the concept of comparison factors.

Three velocity regimes were studied in the work of Lhermerout and Perkin:[78]

- High - hydrodynamic forces dominate,
- Intermediate - combination of hydrodynamic and electrostatic forces,
- Low - electrostatic forces dominate.

These regimes can be compared with other systems. By using the velocity, v, radius of curvature (R = 0.885 cm), and viscosity (η = 37 mPa s at 25 oC) values from Lhermerout and Perkin,[78] a regime comparison factor, C_{reg}, can be calculated that is proportional to the hydrodynamic force, F_{hydro},

$$C_{\mathrm{reg}} = \eta v R^2 \propto F_{hydro} \tag{3.8}$$

Using the values in Table 3.1, a velocity for each regime can be estimated for any

Table 3.1: Comparison factors for high, low and intermediate velocity regimes for 1-ethyl-3-methylimidazolium bis[(trifluoromethane)sulfonyl]imide ($[C_2C_1im][TFSI]$ ($\rho = 37$ mPa s at 2 5°C) and $R = 0.885$ cm

Regime	**Velocity/ nm** s^{-1}	C_{reg} **x** 10^6 **/Pa** m^2
High	95	275
Intermediate	1.1	3.27
Low	0.24	0.696

system,

$$v = \frac{C_{\text{reg}}}{\eta R^2} \tag{3.9}$$

so long as the viscosity and radius of curvature are known.

3.2.5 | Measurement of Shear Forces

In a shear experiment, in addition to the measurement of distance, D, and normal forces, F_N, two additional outputs are recorded. These are the voltage applied to the piezoelectric tube in order to achieve lateral motion is recorded and the resulting shear forces, F_S of the system, see Figure 3.12. The method by which the shear forces of the system is recorded is detailed below: The lateral motion, x_o, of one lens with respect to the other is achieved through the use of the sectored piezoelectric tube. Any shear forces acting between the lenses is transmitted to the vertical leaf springs, S_1, with a known spring constant, K_S, which is connected to the top lens by a stainless steel mount (BO) This is monitored with extreme precision through an air-gap capacitor system . This system consists of a capacitance probe,CP,that is separated from, with a small gap G, a polished flag,F, that is mechanically coupled to the top lens. Any change in the position of this flag results in a change of the capacitance of G and thus changes in the lateral movement of the top lens with respect to the bottom lens. The aspects of the top part associated with measurement of shear forces are demonstrated in Figure 3.12.[11]

There are two methods by which the shear response of the liquid film can be monitored, but for both of these the range of lateral motion is ≈ 400 nm/s.

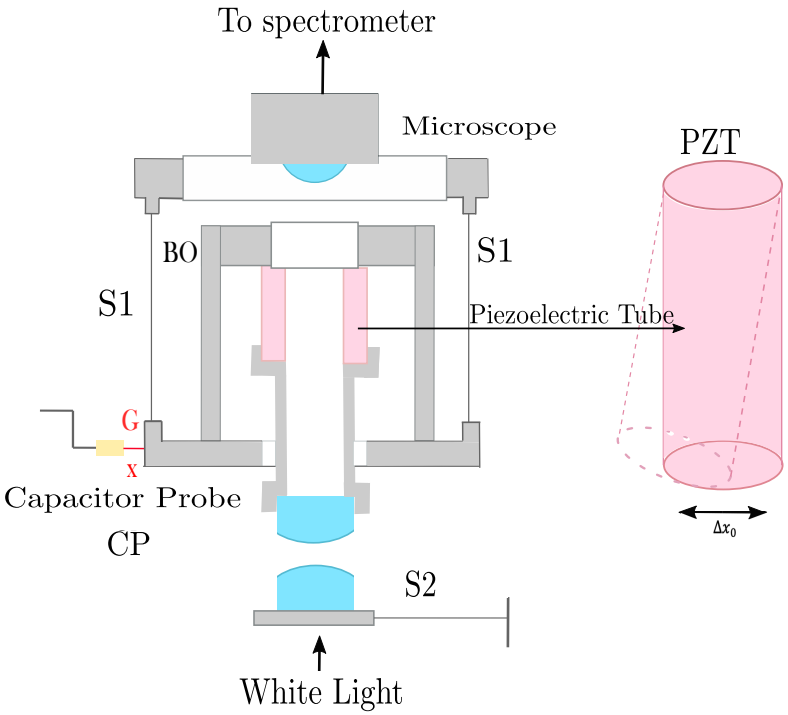


Figure 3.12: Diagram depicting the top part of the SFB, including the piezoelectric tube, probe and springs. The top lens is mounted onto the piezoelectric tube (PZT), which is mounted in a stainless steel boat (BO) connected to two leaf springs (S_1); the unit as a whole is referred to as the 'top part'. When potential is applied to the PZT, the tube bends laterally, shearing the top lens back and forth relative to the bottom lens. This lateral motion causes the S1 springs to bend, which in turn changes the distance G between the capacitor probe (CP) and the BO unit. The change in capacitance is recorded and allows for the monitoring of lateral forces. Normal forces are measured by the horizontal leaf springs (S_2) onto which the bottom lens is mounted. The distance between the lenses is monitored through the FECO resulting from the interference of the light passing through the mirrored lenses, which are captured by the spectrometer. Diagram adapted from Klein *et al.* 1998[74]

Motor Force Profile with Shearing: In this method, the measurement and control of normal and shear motions is carried out alternately. Therefore, the surfaces are approached/retracted to a distance under a set load, and then shearing motion is applied. Approach or retraction of the surfaces is performed using the fine motor and as stated previously, measurement begins with the lenses at large separations to truly gauge the effects structural forces at close separations have on the system. Vertical motion is achieved through discrete stepping of the fine motor. As the fine motor will induce significant mechanical vibrations capable of altering the measured capacitance response, the fine motor is disabled when measurement

of shearing force is performed. Lateral motion of the top surface with respect to the other is achieved through the Piezoelectric tube as described above.

Piezo Force Profile with Shearing: This method, developed by Perkin *et al.*,[11] permits the simultaneous measurement and control of normal and shear motions, allowing for a more detailed and comprehensive determination of friction-load relationships of the liquid medium. The sectored piezoelectric tube is used to apply the simultaneous vertical and lateral motion. Controlled and continuous vertical motion within the range of 500 nm is achieved through the application of a voltage to sectors ABCD, and the opposite voltage to sector E. Lateral motion is accomplished through the application of equal, yet opposite voltages to opposing sectors of the piezo, typically sectors B and D, see Figure 3.4 and Figure 3.12. As stated previously, this results in arc-like motion where vertical contraction or extension is possible, requiring a correction supplied by sector E. Importantly, the shearing rate, v_L, must be much greater than the vertical motion rate, v_N, (typically $v_N \approx 1$ nm/s $< v_L \approx 100$ nm/s) so that the distance and the load can be considered constant within one shearing period.[11]

3.2.6 | Analysis of Shearing Data

When the PZT is used to give the simultaneous normal and lateral motion, we measure the voltage of two PZT sectors (usually B and D), as well as the change in our capacitance. A number of steps are required to get from this raw capacitance signal, V_{sig}, to our final friction force, F_S.[11]

The first step is to remove our normal motion from the voltage signal. This is needed to deconvolute the raw PZT voltage, as it provides both the normal and lateral motion. In Figure 3.13(a) below, the raw voltage,V, is plotted with time, t, for sectors B (normal motion) and D(convoluted) of the PZT. By removing V_B from V_D, the normal motion is removed and we are left with only our applied shearing voltage, see Figure 3.13(b). In our experiments, we apply a regular triangle wave

at a set amplitude of 50V and we change the frequency of this wave, which in turn alters our total lateral velocity, v_l.

We now turn to correcting for the out of contact coupling. When the lenses are out of contact, the applied triangle motion will influence V_{sig}. Figure 3.13 shows this contribution, and it is a triangle-like shape due to our applied triangle wave.

The shearing motion is started before the normal motion is started, allowing us to measure the out of contact system. We can fit this imposed triangle motion, and remove this 'out of contact' signal from our in-contact measurements. Doing this produces a corrected signal, V_{corr} that is thought to be representative of our confined film system, see Figure 3.13(d). Once we have obtained our corrected signal, V_{corr}, we must then shift and centre it around 0. The shifted signal is equal to

$$V_{shift} = V_{corr} - \frac{y2 - y1}{2} - y1 \tag{3.10}$$

Therefore, we shift and centre V_{corr} around 0 V using peak ($y1$), and troughs ($y2$) of our voltage signal, shown in Figure 3.13(e) to yield our shifted signal, V_{shift}. Once we have obtained V_{shift}, we then convert our voltage signal into Newtons. This is done by multiplying V_{shift} by the force constant of our shear spring. K_{shear}, and the conversion factor, $CONV$ of our capacitance amplifier, K_{cap}, to give F_L as a function of time, t and is shown in Figure 3.13(f).

$$F_L = V_{shift} * k_{shear} * CONV \tag{3.11}$$

Once we have obtained our lateral force, F_L, we can obtain our kinetic friction, or more simply, shear force, F_S. This leaves us with shear force values, F_S with an error between 2 μN to 0.5 μN, with higher propagated errors incurred as the measured lateral and shear forces approach the resolution of our system (0.5 μN).

With each peak or plateau identified in the data, F_S is taken as the absolute value

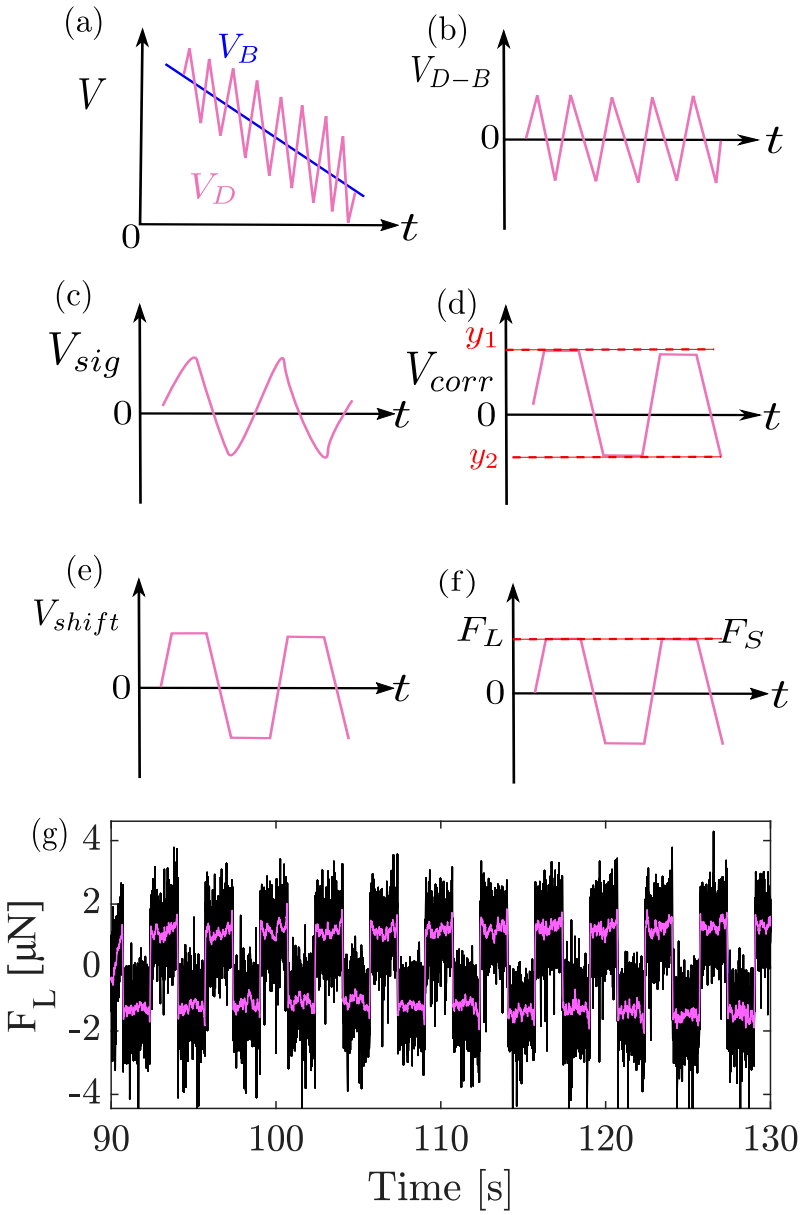


Figure 3.13: (a)-(e) Steps in determining the lateral force-time profile in (f). Voltage-time plots for (a) sectors D (V_D) and B (V_B) of the PZT, (b) applied shearing voltage (V_{D-B}) by removing B from D, (c) raw capacitance signal (V_{sig}), (d) corrected signal (V_{corr}), and (e) shifted signal (V_{shift}) and its calculation. The calculation for determining the lateral force,F_L, from V_{shift}, the spring constant, K_{shear}, and the capacitance amplifier conversion factor, K_{cap}, is given in (f) alongside the resulting lateral force-time profile. The shear force, F_S, is given by the maxima in F_L.(g) The SGOLAYFILT data is shown in pink over our raw lateral force F_L.

of each peak and thus we obtain F_S against time, see Figure 3.13(f). As F_N with time is known, we can produce F_S against F_N from which values for the friction coefficient, μ, can be reached. However,it should be noted that small changes in composition, mica alignment, temperature and contact geometry can influence the

calculated friction coefficients by up to a factor of 2.

While not necessary, to show the general shape of our F_L v t traces we apply an *SGOLAYFILT* smoothing function to our obtained F_L values, seen in Figure 3.13(g).

The Savitzky-Golay filter fits successive sub-sets made up of adjacent data sets. These data points are fitted with a polynomial using the method of linear least squares. As our friction data points are all equally spaced in time, an analytical solution of the least square method can be found, and this is the convolution coefficient.

The Matlab SGOLAYFILT takes the form:

$$y = sgolayfilt(x, order, framelen) \tag{3.12}$$

and this applies a Savitzky-Golay impulse response smoothing filter of the polynomial order *order* and frame length *framelen* on a data set x. In our code, the SGOLAYFILT takes the form:

$$Smooth_{F_L} = sgolayfilt(F_L. * CONV * k_{shear}) \tag{3.13}$$

where the frame length is our spring constant, k_{shear}, and the order is our lateral force, F_L.

Notably, while we apply the SGOLAYFILT to present smoothed lateral forces, $Smooth_{F_L}$, this data is not used to find F_S, and we instead use or corrected F_L.

3.2.7 | Representative Data

As a note, in this thesis, individual force profiles may be presented as 'representative' force profiles for the particular IL-mixture system. These 'representative' force profiles are ones which agree with multiple force profiles taken in one experiment, and with those taken on different experimental days. Typically, a system (a particular

IL-solvent mixture) is studied in at least three different surface force experiments, on different days, with each experiment itself having ≈ 15-25 individual runs at different approach speeds or with the application of shearing motion.

3.3 | Tribometer

The tribometer (TRB) is used widely in industry for measuring friction at the macroscale. In this project, an Anton-Paar TRB^3 is used, and is illustrated in Figure 3.14. This is used in conjunction with the SFB to provide a holistic view of the frictional behaviour of the ionic liquid/ oil blends being studied.

3.3.1 | Apparatus

At its heart, the TRB is a ball-on-disc configuration which allows for the study of an exhaustive range of materials and lubricants to be explored. The rest of the apparatus consists of an elastic-metal polymer arm that holds a rod in place. This rod contains a 6 mm stainless steel ball at its end. Deadweights may be placed upon the top of the arm, as seen in Figure 3.14. These deadweights apply a constant normal load. The substrate is then mounted inside a rotating cup which is spun by a motor whilst in contact with the 6 mm ball. Similar to the frictional set-up for the SFB, two capacitance probes at the base of the arms measure the deflection of the metal arm. This deflection is directly correlated to the frictional forces present at the ball-substrate interface. The voltage of the capacitance probes are converted into a lateral force and subsequently a coefficient of friction.

3.3.2 | Calibration and Set-up

The elastic metal arm is calibrated by hanging a 5 N mass over a pulley and this is repeated weekly. Before the measurement, the arm must also be balanced on the pivot by the positioning of the counterweights to eliminate their effects on the applied normal force.

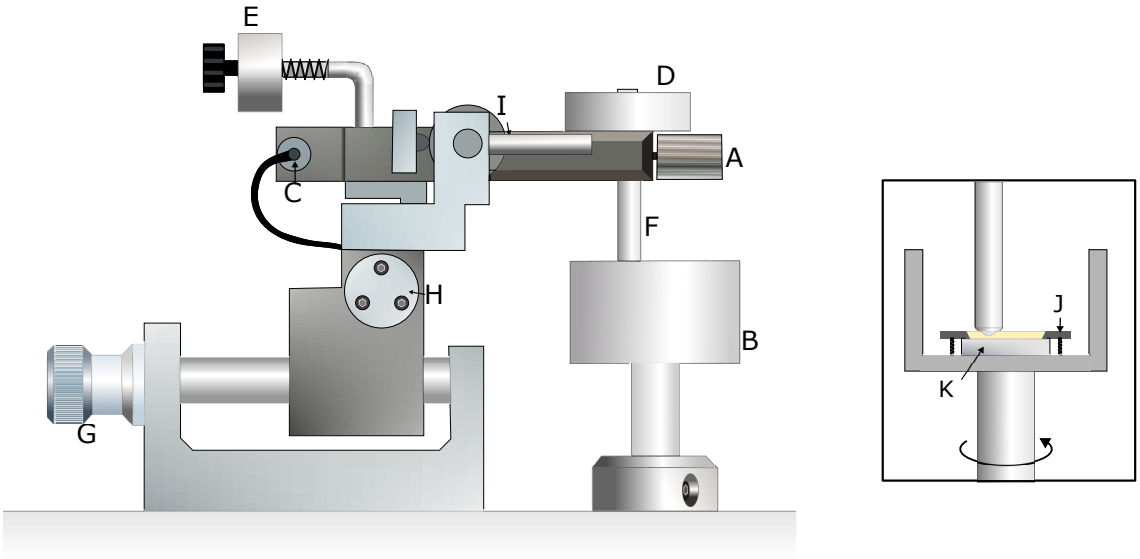


Figure 3.14: TA side on of the TRB apparatus is shown with a cross-section of the liquid cup inset. A. Elastic metal arm, B. liquid cup, C. capacitance probe, D. deadweight, E. counterweight to balance the arm, F. rod holding a 6 mm stainless-steel ball, G. radius of rotation barrel-adjuster, H. arm pivot, I. arm height-adjustment lever, J. substrate clamp, K. solid substrate.

A stainless steel puck is clamped at the bottom of the liquid cup, shown by Figure 3.14. The depth of the liquid cup prevents lubricant from being sprayed over the machine whilst spinning. The motor speeds used in this project were 0.129 ms^{-1} and 0.05 ms^{-1}.

Two types of contact were investigated in this project: steel-steel and mica-steel. In the set-up is for a mica-steel contact, then a thick sheet of mica is glued onto the metal puck prior to being clamped down. The desired deadweight is then placed on top of the metal to provide the normal applied load.

Dilutions of the chosen ionic liquid and chosen solvent are then made up by weighing. For the high viscosity ionic liquids, these mixtures are made up by weighing out the ionic liquid, as the high viscosities prevent an accurate measurement of volume. The solvent is then added, and the mixture is sonicated to ensure complete mixing. Before the mixture is applied on the puck by a volumetric pipette, the mica is cleaved to expose a fresh surface that promotes adhesion of the mixture to the surface. After sonicating, the mixture is applied to the mica surface with a volumetric pipette.

3.3.3 | Measuring Friction

The two contacts are brought together by lowering the arm and the motor is started. The radius traced by the pin is known, and thus the distance travelled is known. In this study,each run was set to 100 m, but two different speeds were used. The high speed of 200 rpm was used with a radius of 6.2 mm, the speed of rotational shearing was 0.129 ms^{-1}. When the lower speed of 60 rpm was used with a radius of 6.2 mm, the speed of rotational shearing was 0.05 ms^{-1}. Higher speeds can be used, but these are more appropriate for dry conditions.

The capacitance probe provides a live trace of the friction coefficient on the TRB's software. Following the completion of each run, the data can then be exported.

Four ionic liquid's were investigated: 1-butyl-1-methylpyrrolidinium bis[(trifluoromethane)sulfonyl]imide ($[C_4C_1P_{yrr}][TFSI]$);trihexyltetradecylphosphonium bis(2,4,4-trimethylpentyl)phosphinate ($[P_{6,6,6,14}][TFSI]$); 1-Butyl-1-methylpyrrolidinium bis(trifluoromethylsulfonyl)imide ($[P_{1,4,4,4}][TFSI]$); and trihexyltetradecylphosphonium bis(trifluoromethysulfony)imide ($[P_{6,6,6,14}][(^iC_8)_2PO_2]$).

$[C_4C_1P_{yrr}][TFSI]$ was mixed with PC, while $[P_{6,6,6,14}][TFSI]$; $[P_{1,4,4,4}][TFSI]$; and $[P_{6,6,6,14}][(^iC_8)_2PO_2]$ were mixed with dodecane. All four systems were studied in a mica-steel and a steel-steel contact. This was done to provide a link to the mica-mica used in the SFB, but to also investigate the industrial relevance of these ionic liquids. Finally, these four ionic liquids were chosen to provide a direct comparison of changing the anion and the cation on the macroscale lubrication.

3.4 | Comparison between macroscale (TRB) and nanoscale(SFB)

Given one of the goals of this project is to illuminate any correspondence between nanoscale friction and friction at the macroscale, it is pertinent to draw a comparison between the two methods of measurement described.

Firstly, the SFB spot resolves an area of tens of nanometres squared on a single

asperity,[152,154,162] whereas the TRB uses a 6 mm diameter ball resulting in a far larger contact area over multiple asperities. The nature of the contact is also different. To mimic the SFB mica-mica contact is far harder to implement on the TRB which is why only one surface is mica thus direct comparison is more challenging.[154,162]However, investigations into mica-steel and steel-steel still allow similarities in trends to be observed. The normal load and shear forces that occur in the TRB are three orders of magnitude greater than seen in the SFB.[128] This results in wear of the surface, something not ever encountered in an SFB experiment.

There are further differences in the way normal force is applied by the instrument. Using the TRB, a static load is applied for one measurement and variation of load must be done over multiple measurements, wherease the SFB grants the ability to continuously increase or decrease normal load and therefore reveal surface forces. The measurement of shear forces by the SFB has substantially higher resolution: data points are collected at 1000 Hz compared to only 50 Hz whilst using the TRB. This elucidates a microfilm's frictional behaviour at the nanoscale

3.5 | Materials

Ruby muscovite mica is supplied by SJ Trading Inc. 1-butyl-1-methylpyrrolidinium bis[(trifluoro-methane)sulfonyl]imide, ($[C_4C_1P_{yrr}][TFSI]$),trihexyltetradecylphosphonium bis(2,4,4-trimethylpentyl)phosphinate($[P_{6,6,6,14}][TFSI]$),trihexyltetradecylphosphonium bis(trifluoromethysulfony)imide ($[P_{6,6,6,14}][(^iC_8)_2PO_2]$), and 1-Butyl-1-methylpyrrolidinium bis(trifluoromethylsulfonyl)imide ($[P_{1,4,4,4}][TFSI]$) are supplied by Iolitec and both dodecane and PC are supplied by Sigma Aldrich. The EPON 1004 glue is from Shell Chemicals and the D-glucose glue is from Sigma Aldrich.

4 | Normal and Lateral Forces of Salt-Dominant $[C_4C_1P_{yrr}][TFSI]$-Propylene Carbonate Mixtures

4.1 | Introduction

$[C_4C_1P_{yrr}][TFSI]$, pictured in Figure 4.1, is an aprotic ionic liquid that is widely studied and has characteristics that make it widely applicable.[71,90] Aside from being well-studied, and therefore a good 'control' system, $[C_4C_1P_{yrr}][TFSI]$ is also readily available and inexpensive when compared to other ionic liquids.

In previous experiments using the SFB and AFM, $[C_4C_1P_{yrr}][TFSI]$ was shown to exhibit an oscillatory force profile, where the wavelength of oscillation, λ_{osc} is consistent with a single cation-anion layer, at λ_{osc}= 0.75 nm.[91] The frictional response of $[C_4C_1P_{yrr}][TFSI]$ has also been studied with an AFM and an SFB.[41,103] These reports found friction coefficients between μ= 0.0002 to 0.0800, and "quantised friction" has been reported.[103] Therefore, $[C_4C_1P_{yrr}][TFSI]$ was found to be superlubric and able to resist squeeze out, making this system an ideal lubricant.[103]

However, the use of neat $[C_4C_1P_{yrr}][TFSI]$ as a lubricant is easily discounted.[19] It has a high production cost compared to industrial lubricants, is known to be sensitive to moisture, and due to its polar aprotic structure, is not widely miscible with oils.[19] However, while studies of $[C_4C_1P_{yrr}][TFSI]$ diluted in oil may not possible, there are already interesting results showing that mixtures with the polar solvent, propylene carbonate (PC), show an interesting "switch" in their structural forces.[90,91] It is therefore useful to study the structural and frictional properties of $[C_4C_1P_{yrr}][TFSI]$ when mixed with PC, at different mol %[90] to investigate how this ionic liquid may

act as "additive" at various dilutions, and if the changing structural forces also leads to a change in the frictional forces.

4.1.1 | Aims of this section

In this chapter, we investigate the structural and frictional properties of $[C_4C_1P_{yrr}]$[TFSI] mixed over the full mol % range in PC solvent under confinement. The ionic liquid used, $[C_4C_1P_{yrr}]$[TFSI], was purchased from Iolitec at 99 % purity (molar mass M= 422.41 $gmol^{-1}$, density ρ = 1.405 gmL^{-1}, refractive index n = 1.422 and dynamic viscosity η = 74 mPa s at 25° C).[11] Its chemical structure and sizes are indicated in Figure 4.1. This liquid is hygroscopic,[109,204] and so measurements of the confined

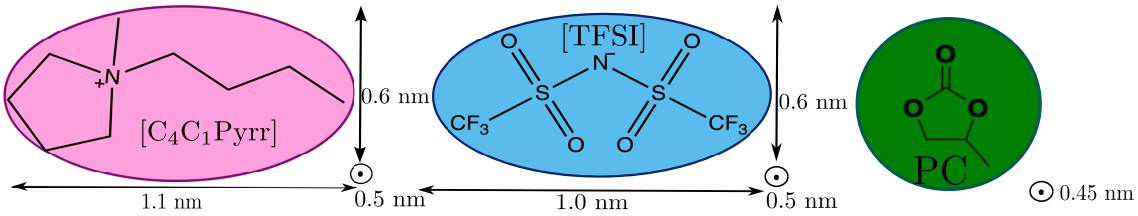


Figure 4.1: Chemical structure and sizes of $[C_4C_1P_{yrr}]$[TFSI], shown as pink and blue circles and PC, shown as a green circle. Ion sizes are estimated from geometry, bond lengths and covalent radii, associated with the most stable configuration found by energy minimization (Chem3D 16.0, PerkinElmer Informatics).[11]Structures were drawn in Chemdraw.

'dry' and 'ambient' films are studied to also investigate the influence of water. Dry conditions are achieved by drying the liquid in a Schlenk line at 60 ° C and 5 x 10^{-3} mbar for 10 hours and by inserting in in the chamber just after, which contains P_2O_5 as the desiccant. This is known to produce water content typically < 100 ppm.

Wet conditions are achieved by letting the ionic liquid equilibrate with particle free air of ambient humidity during several days before the experiment and inserting it in the chamber, which contains no desiccant and is filled with ambient air. In this case, the water content corresponds to the thermodynamic equilibrium of the ionic liquid with ambient humidity. We are able to accurately determine the water content of our system using a Coulombic Karl Fischer titration set-up in the lab. The water content of our "ambient" systems were between 180 -200 ppm.

While the measurements were conducted over the full mol % range of [$C_4C_1P_{yrr}$][TFSI] mixed with PC, it is useful to characterise two different systems: the salt-dominant, and the solvent dominant.

In a previous study, it was found that when characterising the structural forces of [$C_4C_1P_{yrr}$][TFSI]-PC mixtures, at 32 mol % (or 2.0M), the liquid system undergoes a 'switch' from a solvent dominated wavelength, λ_{osc}= 0.55 nm, to a salt dominated wavelength, λ_{osc}= 0.80 nm.[71,90] In line with that, we present the findings of 'salt dominant' and 'solvent dominant' system:

- The 'salt dominant' systems are those systems where the mol % of the ionic liquid, [$C_4C_1P_{yrr}$][TFSI], is > 32 %.
- The 'solvent dominant' systems are those where the mol % of the ionic liquid, [$C_4C_1P_{yrr}$[TFSI], is < 32 %.

Table 4.1 below summarises the different mixtures studied in both Chapter 4 and 5.

Table 4.1: Summary of the [$C_4C_1P_{yrr}$][TFSI]-PC mixtures studied in Chapters 4 and 5.

vol % IL	mol % IL	Concentration	IL vol, μl	PC vol, μl	Dominant species
100	100	3.3M	100	0	Salt
53	80	2.7M	80	20	Salt
65	34	2.15M	65	35	Salt
44	21	1.4M	80	100	Solvent
16	6	0.5M	18	100	Solvent
0	0	0M	0	100	Solvent

4.2 | Normal Forces of Salt-Dominant [$C_4C_1P_{yrr}$][TFSI]-PC mixtures

Before presenting our results obtained from using the SFB to study the forces of nanoconfined liquids, it is useful to explain what information can be obtained from our results. In this chapter, the force profiles presented are all taken from approach profiles, i.e., when the surfaces are moved closer together, and points taken from retractions (when the surfaces are moved apart), are presented as single points de-

noted by triangles. Figure 4.2 shows an example approach profile obtained using an SFB on a 2.15M (or 34 mol %) mixture of [$C_4C_1P_{yrr}$][TFSI] in PC. The approach

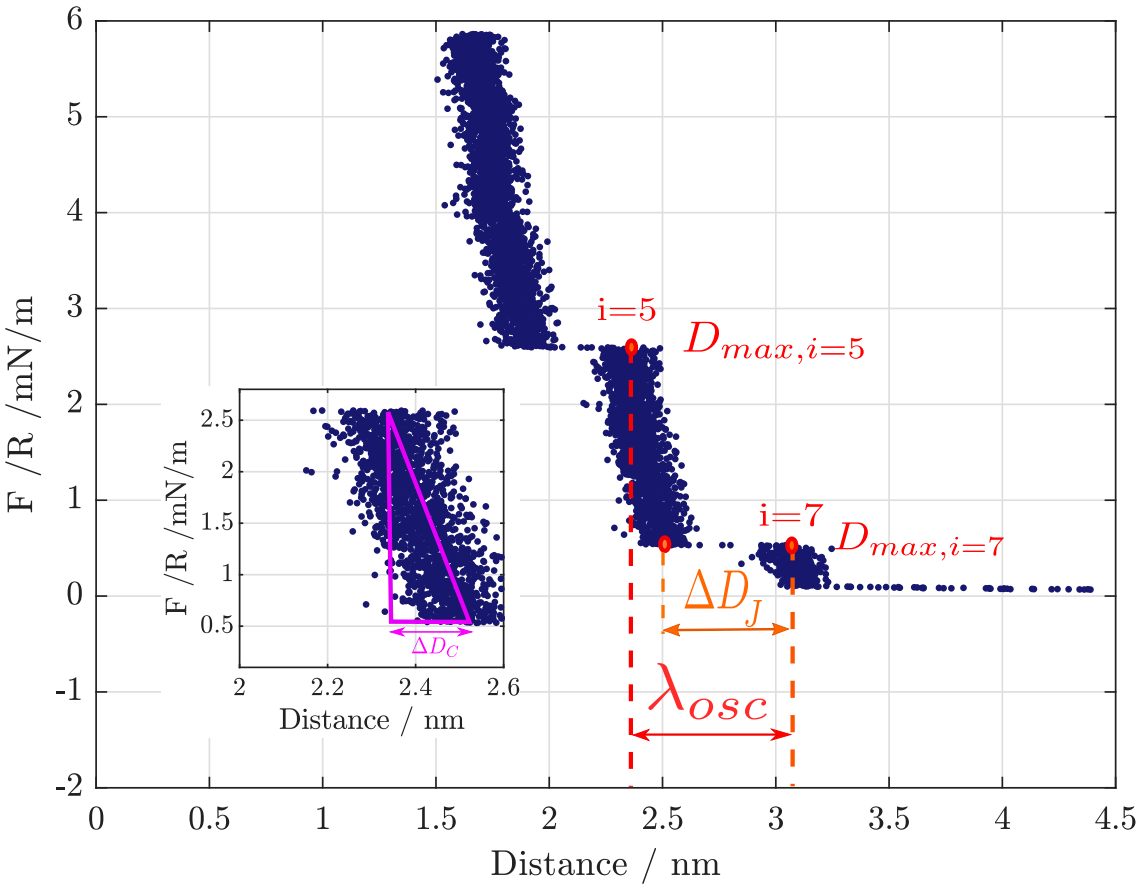


Figure 4.2: Representative normal force, F_N, normalised by the radius of curvature, R, as a function of surface separation, D, profile in 2.15M [$C_4C_1P_{yrr}$][TFSI]. The data is annotated to show the jump-in separation, ΔD_J, layer compression, ΔD_C, and wavelength of oscillation, λ_{osc}, where λ_{osc}= ΔD_J + ΔD_C.

profile shown in Figure 4.2 is step-like and is characteristic of an ionic liquid approach profile.[65,66,68,70,71,102]The step-like structure is understood to arise from the sequential squeeze out of molecular layers that form when these liquids are confined on the nanoscale.,[65,66,68,70,71,102] and was explained in Section 2.1.2.

Importantly, the mica-glue-mica-glue surface used for SFB experiments, is known to be compressible under the large applied normal loads, and this is reflected in the compressibility of the layers shown in Figure 4.2. In this particular experiment, the mica used was 6 μM thick, and this contributes to a compression of $\approx$ 0.15 nm. Table 4.2 below summarises the observations.

Table 4.2: Compressions and jump distances observed in the normal force profile. Compressions are calculated as shown in the inset in Figure 4.2 , while jumps are calculated as $D_{max,i}$ - $D_{max,i-1}$, as shown in Figure 4.2.

Layer Index i	D_{max} nm	**Compression in Layer** nm	**Jump Distance** nm
5	2.25	0.17	-
7	2.96	0.11	0.67

4.2.1 | Structural Forces

3.3 M [$C_4C_1P_{yrr}$][TFSI]-PC

Normal forces profiles for 100 mol %/100 vol %/3.3M, [$C_4C_1P_{yrr}$][TFSI] in dry and ambient conditions are shown in Figure 4.3(a) and (b), respectively. In both the dry and ambient profiles, the short- and long-range forces appear overall similar. As discussed further in Chapter 5, viscous forces can influence the observed structural forces,[78,81,89] but in the case of a relatively low viscosity ionic liquid such as [$C_4C_1P_{yrr}$][TFSI] (η = 0.74 mPa s) this influence is minimal, and the approach velocities used ($\approx$ 0.5 nm/s) are slow enough to discount any hydrodynamic effects. In both the dry and ambient 3.3M [$C_4C_1P_{yrr}$][TFSI] film, an oscillatory force is observed below 10 nm. In Figure 4.3 (a) and (b), there is a series of repulsive hard walls followed by "jump-in" points to smaller surface separations, and as explained above and in Chapter 2, these 'structural forces' are indicative of an ordered liquid structure which forms due to the geometric and electrostatic constraints.[61]

In Figure 4.3, the points obtained from retracting the surfaces are shown as triangles. Retractions of the surfaces from any point on the approach profile leads to a jump-out of the surfaces from the nearest adhesive minimum (marked as filled triangles in Figure 4.3).[90] These outward jumps are observed when using spring deflection to measure attractive forces: on retracting the surfaces ar a particular stable film thickness D_i, the spring extends until the attractive force balances the elastic restoring force.[90] Once the gradient of the attractive force exceeds the spring constant, K_N, the surfaces jump to large separations. This jump multiplied by K_N

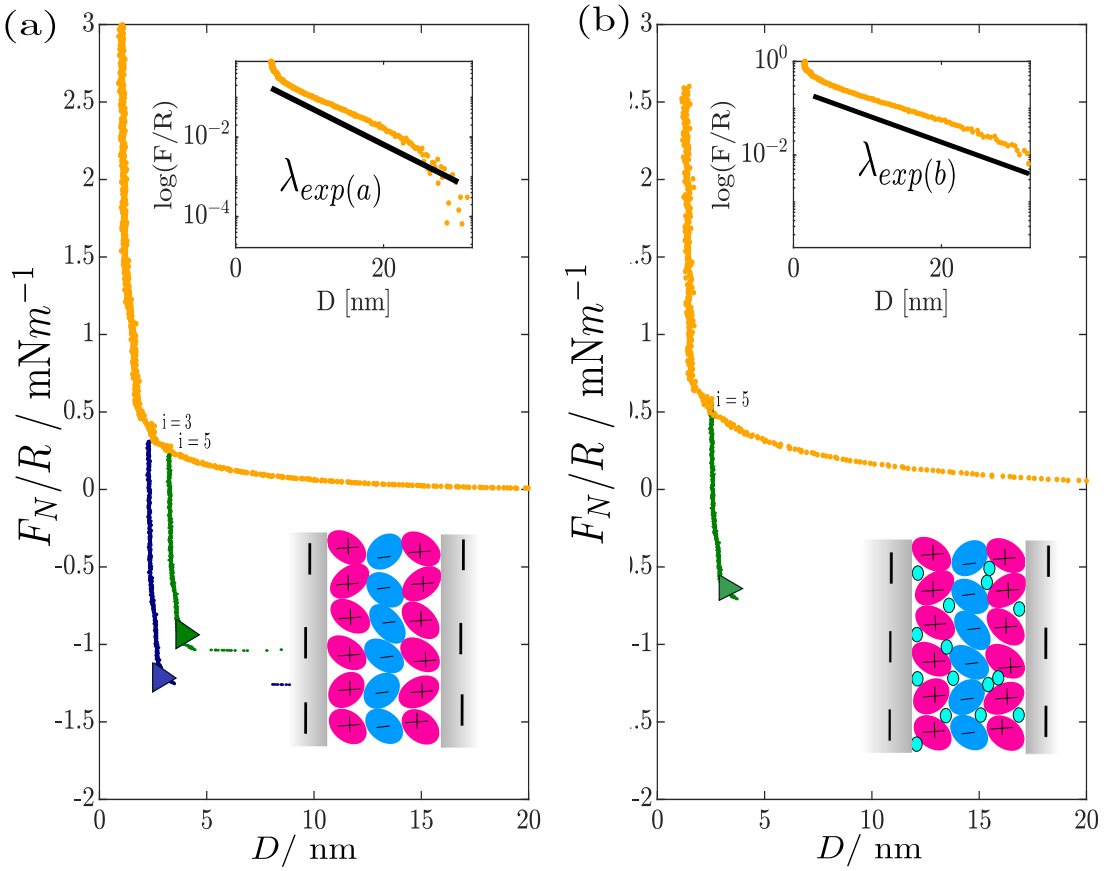


Figure 4.3: Representative normal force, F_N, normalised by the radius of curvature, R, as a function of surface separation, D, measured in nm, profiles in (a) dry and (b) ambient 3.3M [$C_4C_1P_{yrr}$][TFSI]. The profile on approach is shown in orange. The corresponding minimum adhesive force and jump out position obtained from retraction profiles for each layer are indicated by triangular points and force profiles in blue and green. The insets shows a log-linear representation of the normal force on approach for the dry and ambient systems, where the solid black line indicates the gradient of the long-range exponential decay ($\lambda_{exp,(a)} = 5.33 \pm 0.3$ nm and $\lambda_{exp,(b)} = 8.33 \pm 0.3$ nm). The inset cartoons display an interpretation of the layering for the innermost recorded repulsive wall at D= 1.58 nm. This is an interpretation of our oscillatory force where there are force walls which correspond to energy minima where stable films are formed. The stable films contain an odd number of ion layers, alternating between cation and anion-rich layers with cations at each of the negatively charged surfaces. These simplified cartoons do not show how the excess of anions and cations decreases away from the surfaces.

yields the force of adhesion at the minimum.Thus the positions of the repulsive walls in the oscillatory force profile, and the location of the energy minima, can be used to determine the layering structure of the confined film.[71,90]

The separation between the hard walls, ΔD in the dry [$C_4C_1P_{yrr}$][TFSI], is $\Delta D =$

0.70 ± 0.03 nm , and this is thought to correspond to the dimension of the cation-anion pair of [$C_4C_1P_{yrr}$][TFSI], in-line with previous literature measurements.[71,90] The thickness of the layers, $i = 3$ at $D_3 = 1.58 \pm 0.04$ nm and $i = 5$ at D_5 =2.28 ± 0.03 nm is consistent with an alternating and electroneutral cation-anion-cation layering regime, whereby the cations lie next to the negatively charged mica surface, and have been reported in SFB, AFM, and simulation studies.[41,63,109] This is illustrated in Figure 4.3 inset and in Figure 4.4.

The alternating cation-anion-cation layering structure proposed in this thesis is based on the following electrostatic and geometric arguments:[61]

1. In order to preserve electroneutrality of the confined ionic liquid, each maximum in the force law must represent squeeze-out of an equal number of cations and anions.

2. The difference in separation between the repulsive walls is close to the thickness of an ion pair, or a cation layer adjacent to an anion layer, with the cation hydrocarbon tails in the plane of the surfaces.

In the ambient 3.3M sample, the $i = 5$ layer is also present, but the magnitude of F_N/R at the jump-in points for the ambient [$C_4C_1P_{yrr}$][TFSI] are slightly reduced, and the film thicknesses are dilated by ≈ 0.20 nm. As [$C_4C_1P_{yrr}$][TFSI] is hygroscopic,[86] we can attribute this reduction to absorbed water disrupting and weakening the layered structure when compared to the dry [$C_4C_1P_{yrr}$][TFSI], meaning that the film is not packed as tightly, as the water 'screens' the interactions between the charged components.[102]

2.7 M [$C_4C_1P_{yrr}$][TFSI]-PC

Normal force profiles for 53 mol %/ 80 vol %/ 2.7M [$C_4C_1P_{yrr}$][TFSI]-PC, are shown in Figure 4.5. Once more, below 10 nm an oscillatory force is observed, and 2 different layers are discernable, with the $i = 5$ layer at 2.18 ± 0.02 nm and $i = 7$ at

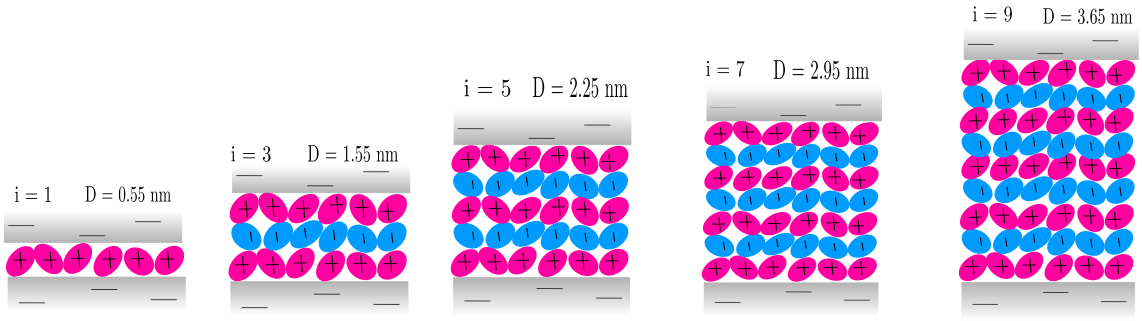


Figure 4.4: Cartoons showing the proposed structuring present in salt-dominant and pure Ionic liquid films of [$C_4C_1P_{yrr}$][TFSI] when confined between negatively charged mica surfaces. In this image,the cation is represented by pink circles, and the anion represented by blue circles.

2.81 ± 0.02 nm. In the ambient system, only the $i = 5$ is observable, at D= 2.15 nm. The separation between the repulsive hard walls is again ΔD= 0.70 ± 0.2 nm, in line with previous literature measurements,[71,90] and there is a slight reduction in the magnitude of F_N/R at these distances for the ambient system.[111,204,205] Measuring the retraction, we are able to identify two points of adhesive minima at D=1.47 ± 0.02 nm and D= 2.20 nm ± 0.02 nm.

2.15 M [$C_4C_1P_{yrr}$][TFSI]-PC

Normal force profiles for 34 mol % /65 vol %/2.15M, [$C_4C_1P_{yrr}$][TFSI], are shown in Figure 4.6, and are qualitatively similar to those obtained for the 2.7 and 3.3 M system. The separation between the hard walls are slightly reduced from the 3.3M and 2.7M to ΔD = 0.65 nm ± 0.05. In the ambient system, under a large applied load of 20 mN, the inner-most layer of $i = 1$ at D =0.60 ± 0.05 nm is accessed. This consists of a single layer of cations, and is illustrated in the inset of Figure 4.6(b) and in Figure 4.4.

4.2.2 | Oscillatory Forces

On retracting the surfaces the adhesive minimum for the corresponding layer can be explored for the three salt-dominant systems, and these can assist in defining the oscillatory forces.[78]

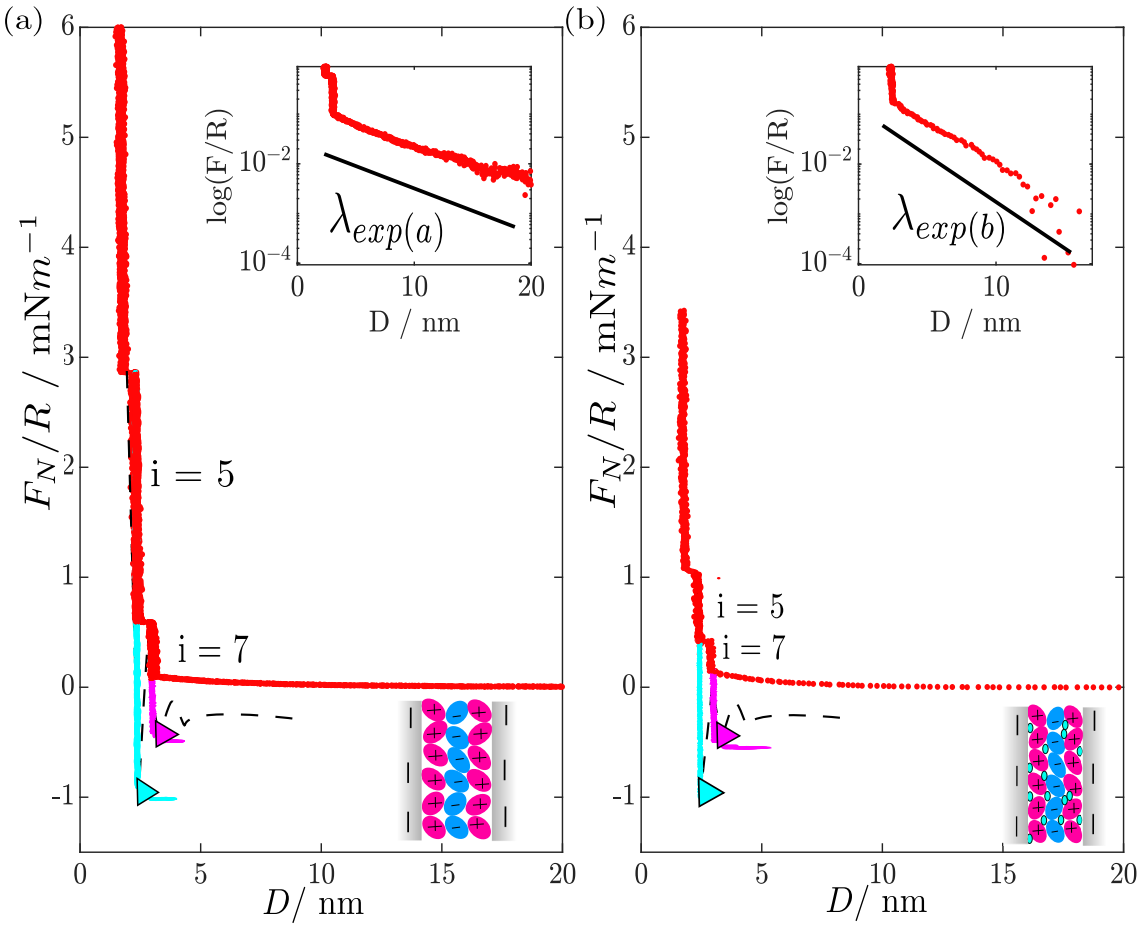


Figure 4.5: Representative normal force, F_N, normalised by the radius of curvature, R,as a function of surface separation, D, measured in nm, profiles in (a) dry and (b) ambient 2.7M [$C_4C_1P_{yrr}$][TFSI]. The profile on approach is shown in red. The corresponding minimum adhesive force and jump out position for each layer are indicated by triangular points and were obtained by performing retractions shown in blue and pink. The oscillatory force (black dashed line) is fitted using the procedure outlined in Section 4.2.2 The insets show a log-linear representation of the normal force on approach for the dry and ambient system. The solid black line indicates the gradient of the long-range exponential decay where $\lambda_{exp,(a)} = 5.51 \pm 0.3$ nm and $\lambda_{exp,(b)} = 6.87 \pm 0.3$ nm.

For each layer, the value of surface separation, D_{min}, and absolute force, $|F_{min}/R|$, at the jump out point can be extracted.[78] These quantities can be used to fit Equation 2.2.

The fitting process is shown in Figure 4.7 for 2.7M [$C_4C_1P_{yrr}$][TFSI], the results of which are quantitatively similar for the 3.3M and 2.15M [$C_4C_1P_{yrr}$][TFSI]. In Figure 4.7(b), D_{min} is plotted as a function of the layer index, i, where the innermost surface layer is denoted $i = 1$ and successively further out layers are denoted $i = 3, 5, ..., n$,

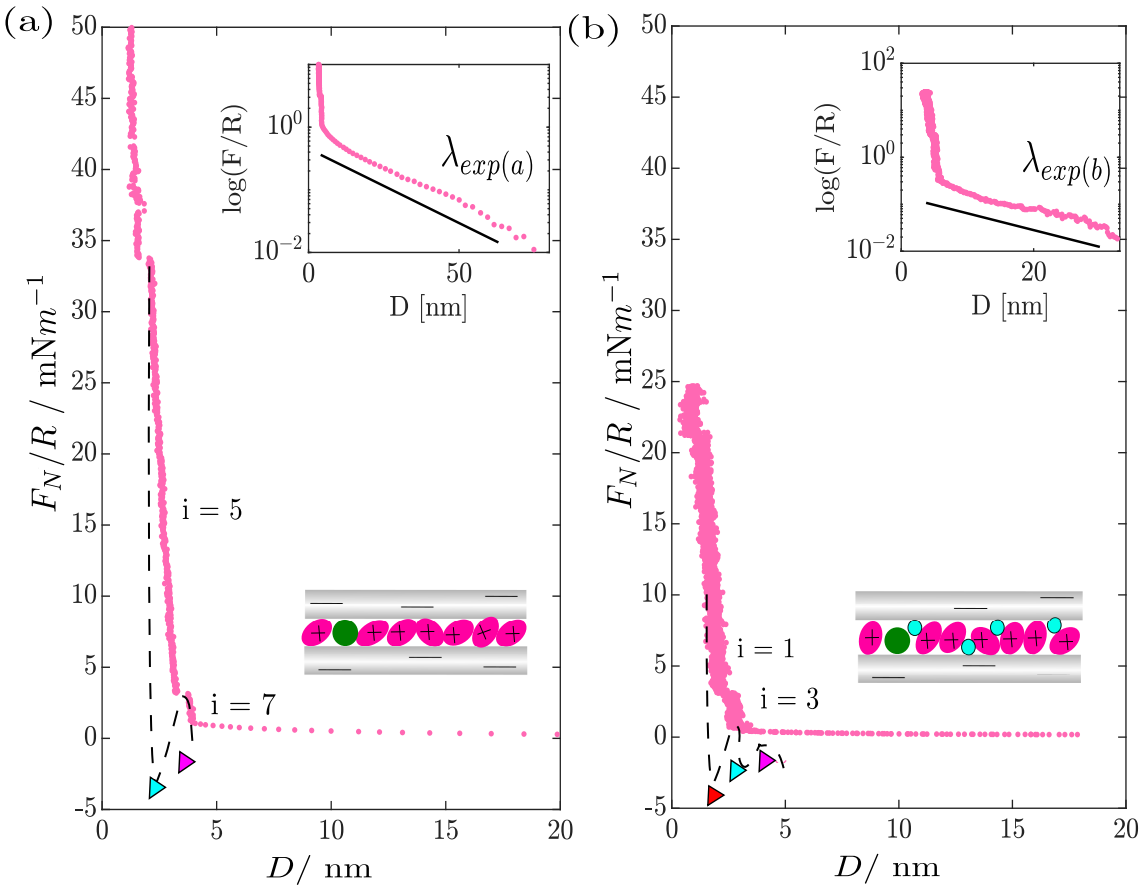


Figure 4.6: Representative normal force, F_N, normalised by the radius of curvature, R, as a function of surface separation, D, measured in nm, profiles in (a) dry and (b) ambient 2.15M [$C_4C_1P_{yrr}$][TFSI]. The profile on approach is shown in pink. The corresponding minimum adhesive force and jump out position for each layer are indicated by triangular points and were obtained by performing retractions from each discrete layer. The insets shows the respective log-linear representation of the normal forces obtained from approach in the dry and ambient system.The solid black line indicates the gradient of the long-range exponential decay where $\lambda_{exp,(a)} = 13.81 \pm 0.5$ nm and $\lambda_{exp,(b)} = 11.98 \pm 0.5$ nm.

This linear fit is done via this relation:[78]

$$D_i^{min} = D_o^{min} + i\lambda^{min} \tag{4.1}$$

Where the slope of λ^{min}= 0.7141 $\pm$ 0.2 nm represents the mean layer thickness, and the intersect, D_o^{min} corresponds to the position of the extrapolated layer $i = 0$. Importantly, the slope, λ^{min} corresponds to the λ_{osc}, and therefore the periodicity of our oscillatory force is 0.71 $\pm$ 0.32 nm, which has previously been interpreted to represent the thickness of the liquid film expelled with increasing confinement.[61,65]

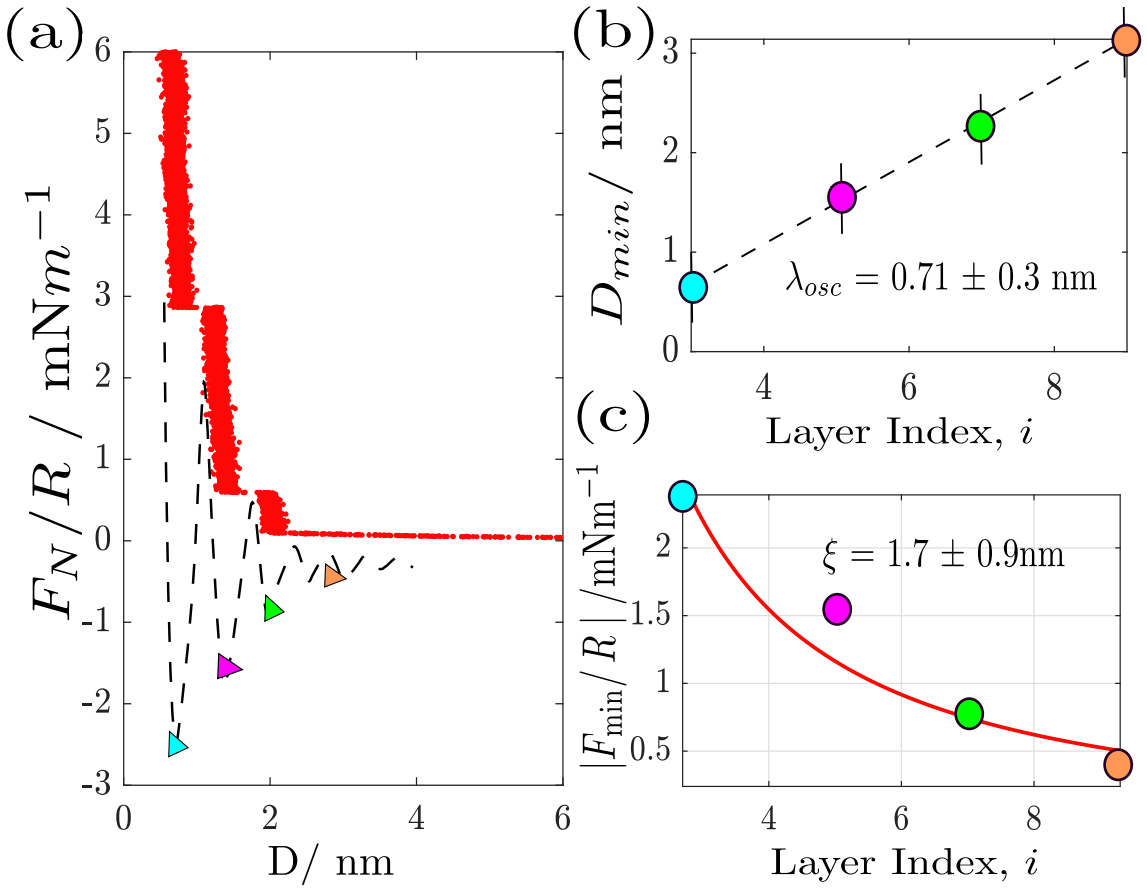


Figure 4.7: (a) Representative normal force, F_N, normalised by the radius of curvature, R, as a function of surface separation D, profile in 2.7M [$C_4C_1P_{yrr}$][TFSI]-PC (red). Adhesive minima for the four layers observed by performing retractions are indicated by the triangular points. The oscillatory force (black dashed line) is fitted using Equation 2.2 and the parameters calculated in (b) and (c). The gradient of the surface separation at the jump out point, D_{min}, as a function of the layer index, i, in (b) Equation 4.1 yields the oscillation periodicity, $\lambda_{osc} = 0.71 \pm 0.32$ nm. The power law the absolute force at the jump out point, $|F_{min}/R|$, as a function of the layer index, i in (c) yields the exponential decay length of the damped oscillation, $\xi = 1.7 \pm 0.9$ nm, see Equation 4.2.The inset of (a) shows the molecular arrangement implied by these results, specifically the squeeze out value of $\Delta D = 0.75$ nm

In molecular liquids, the correlations observed at the nanoscale are equivalent to the bulk correlations.[37,63] We therefore expect λ_{osc} to be similar to the bulk density-density correlations observed in scattering experiments.[66]

Our value for the mean layer thickness, 0.71 nm is smaller than the mean ion pair diameter (given by $(\frac{M}{\rho N A})$, with M being the molar mass of the ionic liquid, ρ its bulk density and N_A the Avogadro's number.) Our value obtained under confinement may indicate a denser packing of ions than in the bulk, and was reported in 2020.[11]

However, these values for λ_{osc} still differ from those reported in measurements on the same ionic liquid using an SFB and an AFM, where both reported a λ_{osc} of 0.80 nm.[41,90] A possible explanation for this difference may be the measurement methodology, as the force profiles from the previous SFB study were obtained with much slower approach and retraction velocities, and the AFM study had a radius of curvature that was magnitudes smaller than those in our experiments ($R = 0.02$).[41]

This measured value of λ_{osc} is useful to identify the composition of the confined layers. As the period is similar to the mean ion pair diameter, it is believed that one squeeze-out event corresponds to the squeeze-out of an electroneutral 'slab' of one cation layer and one anion layer.[40] Indeed, our value of λ_{osc} =0.71 nm is close to our measured separation between hard walls, which ranged from $\Delta D = 0.65$ nm to 0.70 nm across all measurements of confined Salt-Dominant systems.

It is notable to mention that the same fitting procedure was performed for the 3.3M and the 2.15M system. In the 3.3M system, the linear fit of D_{min} with layer index i yielded a λ^{min}= 0.73 ± 0.3 nm, while in the 2.15M system, the obtained slope was slightly reduced to λ^{min}= 0.68 ± 0.2 nm. This reduction in λ_{osc} may be interpreted as a manifestation of the changing structure of the confined films as PC begins to dominate the structure.[90]

The 2.15M system actually contains an approximate 34 mol % of [$C_4C_1P_{yrr}$][TFSI], meaning that PC becomes the dominant species in terms of molar ratio, but it has not yet come to dominate the structure in a way that would alter the structural forces.[90,91]

For each layer, i, we measure the absolute force at the jump-out point, or adhesive force, $|F_{min}/R|$ as a function of the layer index, i. This is an exponential fit, and yields ξ from Equation 2.2 as 1.74 ± 1 nm, and is shown in Figure 4.7(c). However, and to confirm this, ξ can also be obtained by fitting the variation of $|F_{min}/R|$ with

i in a log-linear relation:

$$F_i^{min} = F_o^{min} e(-i\frac{\lambda_{min}}{\xi_{min}}) \tag{4.2}$$

where i is the layer index.

We obtain ξ= 1.74 ± 1 nm from the gradient of the log-linear representation of $|F_{min}/R|$ as a function of D_{min} as the slope gives access to the ratio $\frac{\lambda^{max}}{\xi^{max}}$ = 1.74 nm. This is the period of the oscillation of the decay length and our obtained value corroborates with previous reports.[129]

ξ provides information regarding the decay of the liquid structure with surface separation, with a length on the order of molecular dimensions.[71] The error in ξ ($\approx$ 1 nm) means that we cannot quantitatively conclude the range over which the structure persists. Nonetheless, an exponentially decaying behaviour is observed, that, in combination with the oscillatory density correlations, is akin to the radial distribution function observed in studies of this specific ionic liquid.[91] The resulting damped oscillatory force is shown by the black dashed line in Figure 4.7(a).

The results for the λ_{osc} and ξ can be interpreted as the PC molecules sitting within the [$C_4C_1P_{yrr}$][TFSI]layers at 2.7M and 2.15M, as had been predicted by simulations[37] and observed in previous studies.[90]

Long-Range Forces

Figure 4.8 show representative force profiles for the salt-dominant [$C_4C_1P_{yrr}$][TFSI]-PC systems. In each force profile, a long-range decaying tail appears in the 8 – 30 nm region and steps are observed in the 1 – 6 nm range. As already stated, this value, λ_S is found in the second part of the Equation 1.1 that describes the forces across confined ionic liquid systems. The force profile is plotted on a log-linear scale to show how the long-range normal force decays exponentially with surface separation according to F_N/R where the linear fit of that decay, λ_{exp}, is the experimentally observed decay length.[26] The measured screening lengths range between 5 nm and

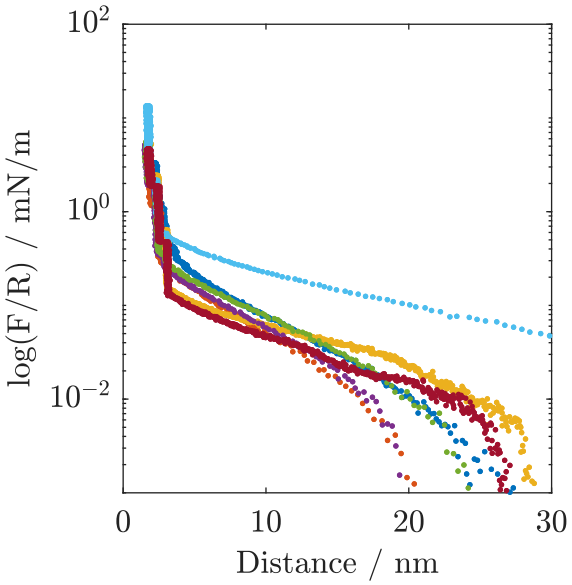


Figure 4.8: Force profiles for the dry salt-dominant [$C_4C_1P_{yrr}$][TFSI]-PC systems plotted on a log-linear scale. The exponentially decaying long-range tail in the 8 – 20 nm range is interpreted as the electrostatic screening length, which is anomalously long. The steps in the 2 – 6 nm range indicate structured molecular layering.This image shows ≈ 9 force profiles.

13 nm, which is a scatter that falls within expected error considering the changing mica thicknesses and contact spot radii, and are also consistent with previous reported experimental screening lengths.[26,91,146] These experimental screening lengths are anomalously long and are greater than what would be predicted by a simple Debye-Hückel application, $\lambda_S \approx 0.01$ nm[26,91,146] This experimental observation of these anomalously long screening lengths λ_S, has been termed *underscreening*.[129] Underscreening manifests in force profiles as a long-range decay length extending several nm from the point of closest approach.[129]

Overall, the structural forces for the 3.3M, 2.7M and 2.15M systems are in-line with previous measurements.[146] Notably, at these concentrations, the wavelength of the oscillatory force varies between 0.68 to 0.75 nm. Due to the margins of error inherent in the particularities of the SFB, such as mica thickness and optics, these wavelengths are internally consistent. Moreover, in these three systems the influence of moisture is consistent with the water making layers more easily compressible.[111]

Role of Absorbed Water

Figure 4.9 shows the influence of ambient humidity on the structural forces present in the 3.3M, the 2.7M, and the 2.15M system. In all three systems, the presence of ambient humidity slightly reduces the normal load required to access the layers. In other systems previously studied the increase in water content lead to dramatic

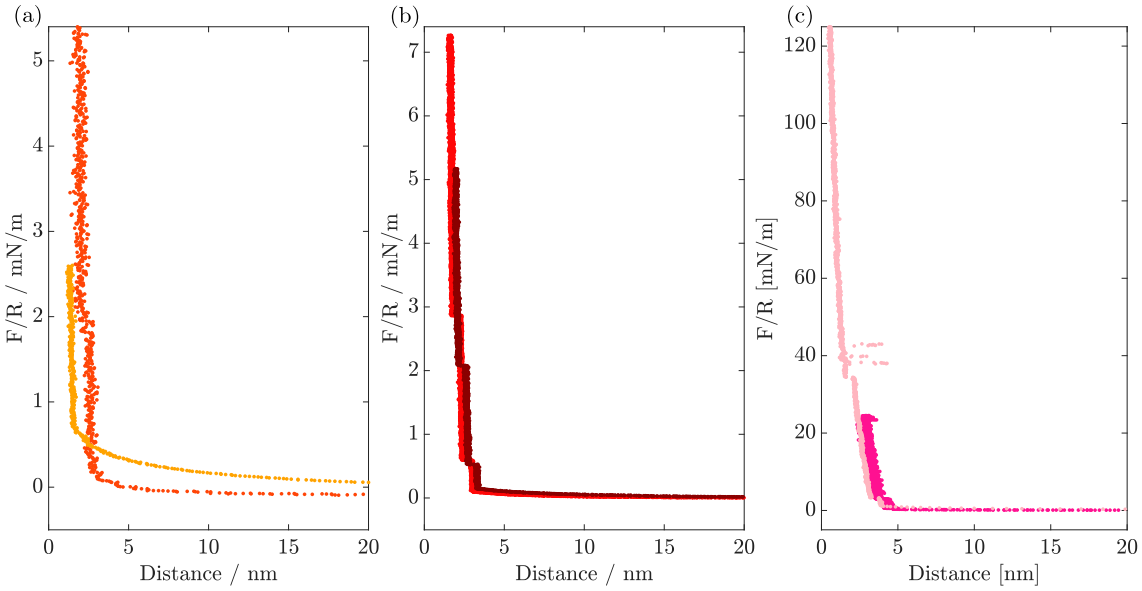


Figure 4.9: Representative normal force, F_N, normalised by the radius of curvature, R, as a function of surface separation, D, measured in nm, profiles in (a) dry and ambient 3.3M [$C_4C_1P_{yrr}$][TFSI] (b) dry and ambient 2.7M [$C_4C_1P_{yrr}$][TFSI]-PC mixture, and (c) dry and ambient 2.15M [$C_4C_1P_{yrr}$][TFSI]-PC mixture. The darker colours in each of these indicate the approach profile obtained from the ambient system.

results.[68,102,112,206] While in our case, we do not precisely know the water content of either our dry or ambient sample, the presence of water within the mono-layer structure causes a small but clearly measurable dilation of the mono-layers.[68,111]

Figure 4.9 shows the film thickness of the accessible layers increases in the ambient sample. Take for example, in the 2.15M, where the film dilates from 2.27 nm for $i = 5$ in the dry system to 2.61 nm in the ambient system for the same layer index, $i = 5$. In the ambient 2.7M film, the difference between repulsive hard walls, ΔD is 0.65 $\pm$ 0.08 nm, which is slightly reduced from the average ΔD of 0.70 $\pm$ 0.04 nm in the dry system.

The hydration of the ionic liquid thus causes a dilation of ≈ 0.4 to 0.5 nm due to the presence of water in the mid-plane ion region, and this is a result previously seen in a bilayer forming analogue of [$C_4C_1P_{yrr}$][TFSI], [$C_10C_1P_{yrr}$][TFSI].[72]

4.3 | Lateral Forces of Salt-Dominant [$C_4C_1P_{yrr}$][TFSI]-PC Mixtures

We now study dry and ambient salt-dominant mixtures of the [$C_4C_1P_{yrr}$][TFSI] and PC under confinement when a shearing motion is applied across the films.

4.3.1 | Quantised Friction across the Salt-dominant films

3.3M [$C_4C_1P_{yrr}$][TFSI]

The frictional response of dry 3.3M [$C_4C_1P_{yrr}$][TFSI] is shown in Figure 4.10. The

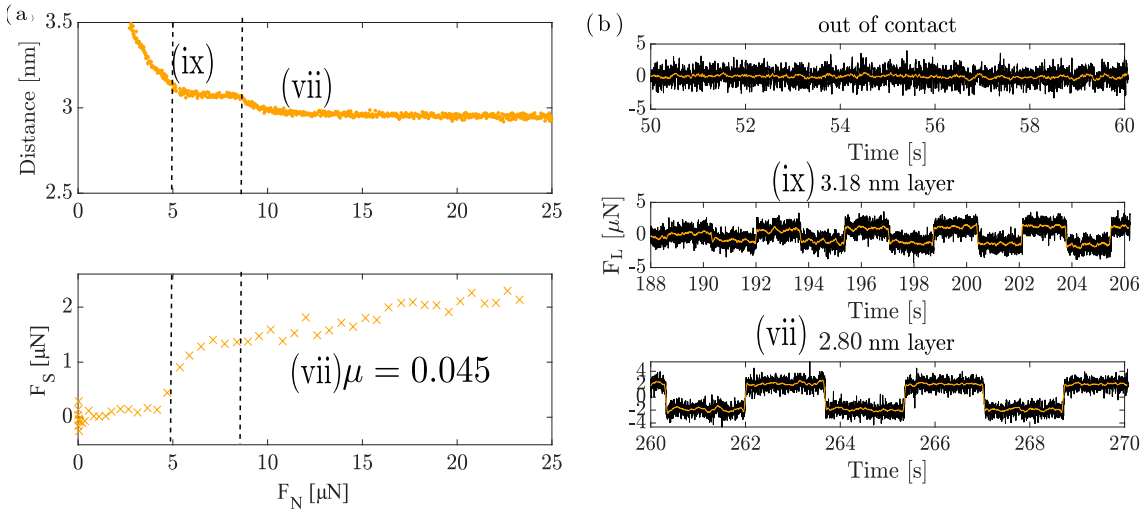


Figure 4.10: Representative (a) shear force, F_S, as a function of the normal force, F_N, across 3.3M [$C_4C_1P_{yrr}$][TFSI]. (b) Lateral friction signals, F_L, as a function of time, with and without a smoothing filter in orange and black, respectively. Two friction regimes are observed in (a) and are indicated by (ix) and (vii). The corresponding lateral friction signals are indicated with the same labels in (b). (a) F_S with increasing F_N is shown in orange. No friction coefficient is resolvable for layer (ix). The friction coefficient of layer (vii) is $\mu = 0.0045$.

surface separation and shear force as a function of the normal force are shown in the top and bottom plots of Figure 4.10(a), respectively. At large separations where the surfaces are not in contact, there is background noise. As the separation decreases,

molecular layers and discrete steps in the F_S-F_N profile are observed. These discontinues arise from the discontinuities in the surface separation as a function of normal force (as per Section 4.1).[11,19] In the outermost layer, (ix), the shear force is still quite small ($F_S \approx 1\ \mu N$), but we are unable to extract a friction coefficient due to the lack of data points. The near-negligible lateral forces are highlighted in Figure 4.10(b) where the lateral force, F_L, is plotted as a function of time, yielding a figure that indicates smooth sliding, where a slight yield point, $F_{S,y}$. can be observed. This small yield point is followed by a F_L profile that does not vary periodically between a minimum and maximum, as would be the case in stick-slip sliding.

As further molecular layers are squeezed out [(ix) to (vii)], we observe a simultaneous increase in the amplitude of the F_L-time oscillations, and in F_S. The discrete increase in F_S yields steps in the $F_S - F_N$ profile in Figure 4.10(a). F_S was previously defined in Equation 1.2 and contained a constant A that represents the flat contact area.

However, we are not able to directly measure A, but we can instead determine A using the JKR equation after an in-situ calibration of the elastic modulus of our lens-glue-mica system.[74,75]

From JKR theory,

$$A = \pi a^2 \tag{4.3}$$

where a is;

$$a = \frac{R}{K}\left[F_N + 2F_p + 2\sqrt{\left(F_N F_p + F_p^2\right)}\right]. \tag{4.4}$$

In this equation, F_N is our normal applied load, while F_p is the adhesive pull off force required to separate the two mica surfaces, R is $(R_1R_2)/(R_1R_2)$ is our contact radius and K is quoted as $1 \pm 0.3\text{x}10^{\ 9}$ Nm $^{-2}$.[75]

In this system R_1 was 0.92 cm and R_2 was 0.98 cm, making $R = 0.48$ cm, and we get a real contact radius of A= 17.42 μm^2.

Thus the discontinuities in $F_S - F_N$ arise from the discontinuities in $D - F_N$, that

are attributed to a different number of molecular layers in the confined film. As the number of molecular layers varies, the contribution from the adhesive force between the surfaces changes. This observation of discrete $F_S - F_N$ regimes, corresponding to a different number of molecular layers in the confined film with a given friction coefficient, has been called "quantised friction".[11,103]

By measuring the surface separation and shear forces concurrently, any changes in the observed frictional response can be directly attributed to the change in film thickness, and relatedly, what we believe the structure of the confined film to be based on the geometric and electrostatic constraints already mentioned in section 4.2.1.

Each of the quantised friction regimes seen here, and in other confined films studied in this thesis, follow a linear relationship between F_S and F_N. This allows for the corresponding friction coefficient for that film thickness to be measured. There is a non-zero $F_{S,k}$ measured at zero values of F_N. This friction at zero applied load is due to the contribution from the adhesion force, F_{adh}, between the surfaces, which will change for each layer.

As shown in Figure 4.10(a), no friction coefficient can be extracted for layer (ix) due to the curvature of the F_S v F_N relationship. This may be a consequence of our data analysis, as we automatically 'pick' peaks to plot for our F_S from our raw F_L trace. However, we are able to obtain a friction coefficient for layer (vii) a shallower gradient is observed corresponding to $\mu = 0.0045$. Therefore, the 3.88 nm layer is said to be superlubric ($\mu < 0.01$).[194]

2.7M [$C_4C_1P_{yrr}$][TFSI]**-PC**

The lateral forces for the 2.7M system are shown in Figure 4.11. From Figure 4.11(a) and (b),at large separations, there is a negligible shear force. As the separation decreases (red curves), molecular layers and discrete steps in the $F_S - F_N$ profile are observed. In the outermost layer, (v), the shear force is still negligible ($F_S \approx$

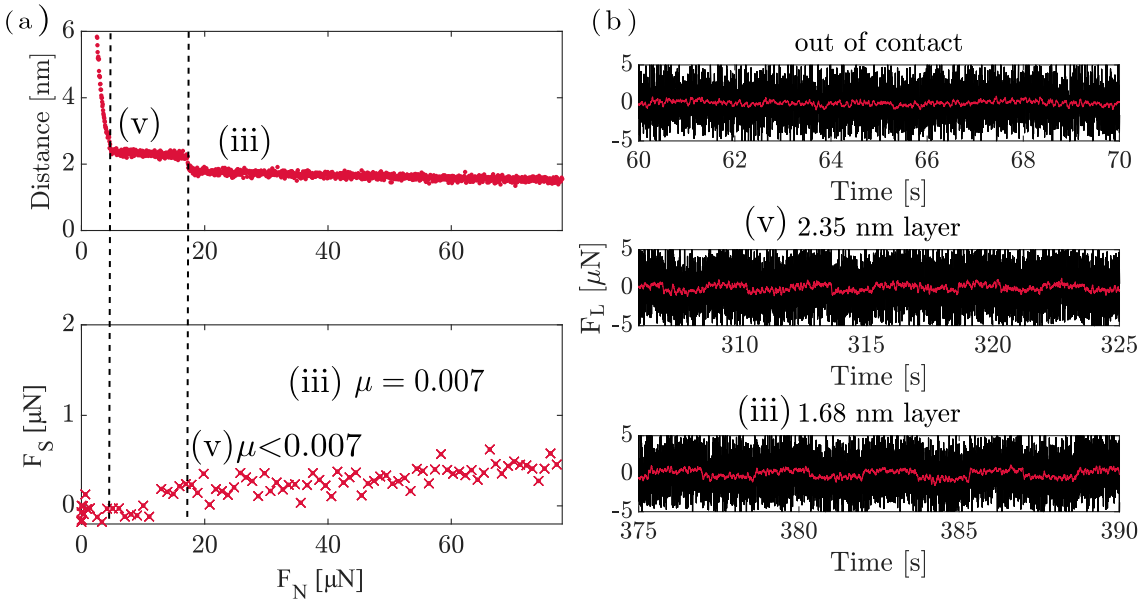


Figure 4.11: Representative (a) shear force, F_S, as a function of the normal force, F_N, across 2.7M [$C_4C_1P_{yrr}$][TFSI].(b) Lateral friction signals, F_L, as a function of time, with and without a smoothing filter in red and black, respectively. Two friction regimes are observed in (a) and are indicated by (v) and (iii). The corresponding lateral friction signals are indicated with the same labels in (b). (a) F_S with increasing F_N is shown in red. No friction coefficient for layer (v) is resolvable, but is expected to be < 0.007. The friction coefficient of layer (iii) is $\mu = 0.007$.

0 μN), and the friction coefficient is believed to be < 0.007. This is highlighted in Figure 4.11(b) where the lateral force, F_L, is plotted as a function of time, yielding a featureless noise-like signal. Overall, as further molecular layers are squeezed out [(v) to (iii)], we observe a simultaneous increase in the amplitude of the F_L-time oscillations, and in F_S. The signal (Figure 4.11(b)) in the outermost observed layer (v) is indicative of a more solid-like confined film, where we observe an initial elastic regime up to a yield point followed by a sharp transition to the plastic regime.[68]

When the surfaces are brought close together, the random vibrations persist down to D =2.35 nm, this corresponds to point (v) on the distance v F_N plot and is thought to be indicative of $i = 5$ molecular layers of [$C_4C_1P_{yrr}$][TFSI]-PC. Upon further compression to $D = 1.68$ nm, corresponding to $i = 3$ and point (iii) on the graph, the vibrations cease. The change in confinement from a far-out distance to molecular distances has rendered the film solid enough to resist the random lateral motion induced by the external shearing motor.[75,76,157,173] As the top mica surface

is moved laterally at a uniform velocity, first in one direction and then in the other, the shear force is transmitted to the lower surface by the confined 2.7M film.

When the surfaces are moved together to $D = 1.68$ nm, which corresponds to $i = 3$, the response is now characteristic of a solid confined between two surfaces: an initial elastic regime, as the shear stress rises to a yield point , $F_{S,y}$ and then a plastic but chaotic deformation of the 2.7M in the gap.[75]

The stick slip observed here is of the chaotic variety, and does not mimic the typical period stick slip profile, which sees a yield point at $F_{S,y}$ followed by a series of discrete stiction peaks where the force, F_L varies between a minimum of $F_{S,k}$ at the stick point and a maximum of $F_{S,st}$ at the slip point, as shown in Figure 2.8 and explain in Section 2.2.2(Stick Slip Friction).

Typically, the $F_{S,y}$ is more than $F_{S,st}$, but in this profile, see Figure 4.12(b), the $F_{S,st}$ does not stay constant and often times is greater than the $F_{S,y}$. However, the lubrication is still being transmitted via stick slip as the gradients of F_L with time are constant. Chaotic stick slip sliding is often times not valued, and a regime of smooth sliding is preferred.[48,153]

Therefore, it is preferable for the $D = 2.35$ nm layer to be the boundary layer instead of the $D = 1.68$ nm layer, as the friction coefficient is both lower, and the magnitude of the chaotic stick-slip is not as strong. The increase in μ as i decreases is likely due to the greater degree of interlocking of the layers for small i: the layers closer to the mica surfaces are more ordered, and have greater anion/cation excess concentration, and therefore have greater inter-layer attractions for the same value of contact area and a greater activation barrier for "unlocking" the surfaces to allow shear.[76,103,163,194] This overall makes the film more solid-like.

However, see Figure 4.13(a), when a force of 90 μN was applied the surfaces underwent a slight compression of around 0.38 nm that while not being obvious on the D v F_N profile, results in a sharp change in the both the F_L v Time trace and the F_S v

F_N profile. A close-up on the F_L v t profile reveals this drastic shift,Figure 4.12(b)

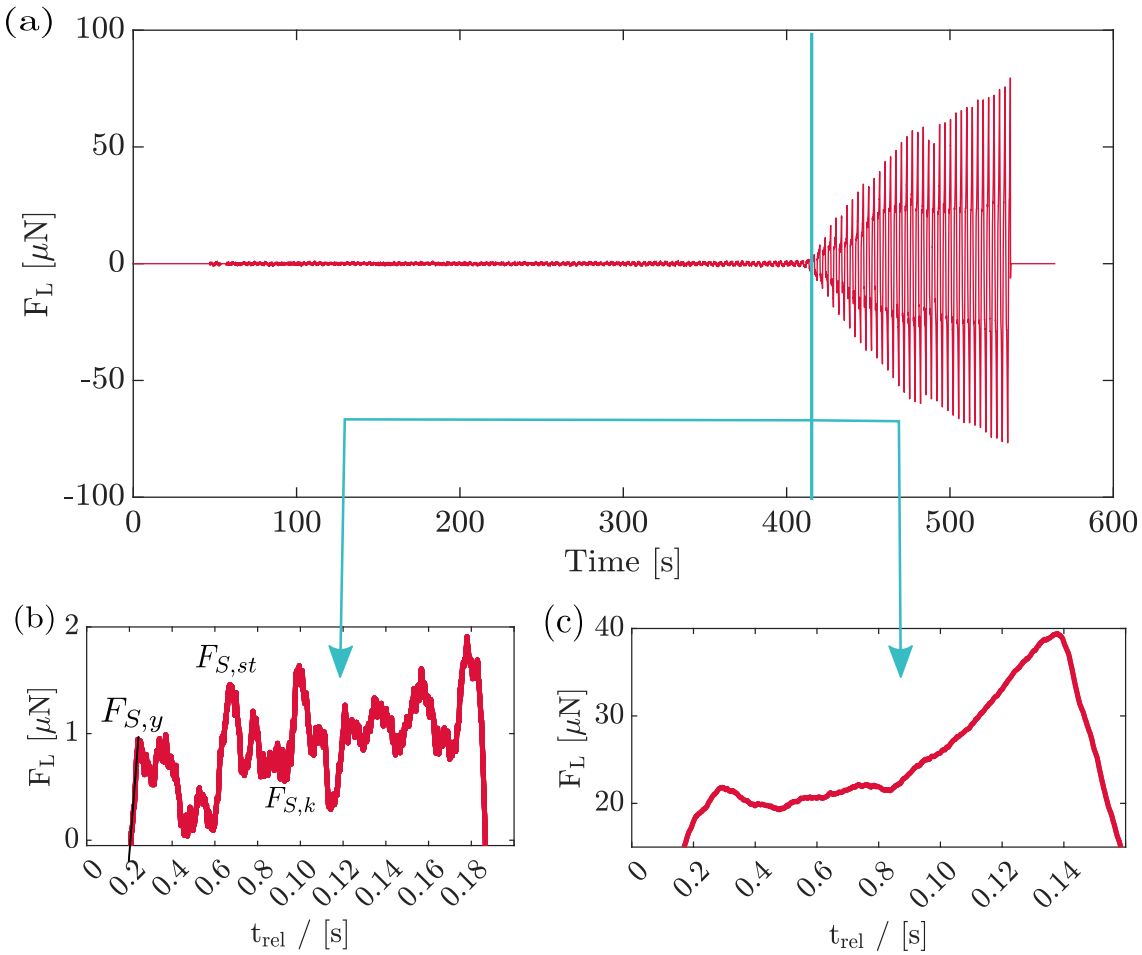


Figure 4.12: (a) Overall temporal evolutions of the lateral force F_L, of the 2.7M film when moving the top surface with the piezoelectric tube at a normal velocity of v_n =0.5nm/s and a lateral velocity of 641 nm/s. At time $t = 0$, approach is started and friction is below the sensitivity limit. The liquid film thickness decreases roughly linearly at large distances, then layer by layer at short distances (D < 5 nm). At t = 300 s, the layer $i = 5$ is reached, friction becomes measurable and increases with load (not visible at this scale but is discernable in Figure 4.11(b). At $t = 350s$ the layer of $i = 3$ is reached, friction magnitude is larger and increases with the load. As we continue applying a simultaneous lateral motion and normal load, at $t = 456$, the film compresses and F_L dramatically increases. (b) F_L v t_{rel} trace for the $i = 3$ 2.17M layer with additional annotations of $F_{S,y}$, $F_{S,st}$ and $F_{S,k}$. (c) F_L v t_{rel} trace for the additional compression layer where the application of a 90 μN load sees the film compress by 0.38 nm.

as the film moves from the chaotic stick slip present, which is more characteristic of a solid-like film, to a profile that is more characteristic of a liquid film. The F_L v t trace is very different from those previously observed. There is a dampened starting spike and during steady sliding the friction forces increased steadily.[207] This is more similar to what would be expected in a very viscous fluid-like system in which the

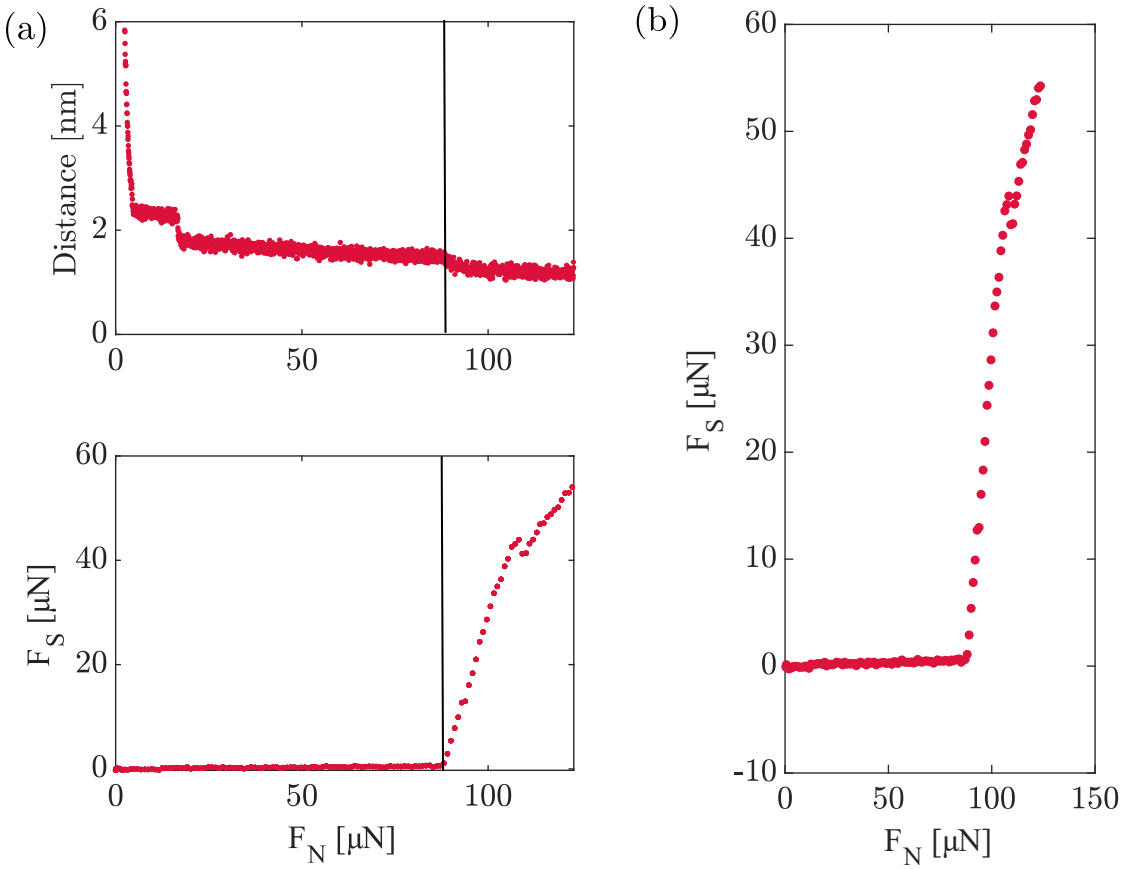


Figure 4.13: Representative (a) D v $F-N$ profile and shear force F_S, as a function of the normal force, F_N, profile of the forces present across 2.7M [$C_4C_1P_{yrr}$][TFSI]. (b) Shear Force F_S as a function of F_N showing the compression after the application of 90 μN of normal force.

system is mainly due to viscous drag. At 456 s, there is a yield point. $F_{S,y}$, followed by a slight levelling off of the force to the kinetic of sliding value, $F_{S,k}$. However, just before the direction of sliding was reversed, a 'stopping spike' was seen. In a paper by Israelachivili, this was reported to be a consequence of the freezing of the liquid films due to the decrease in relative velocity on reversal.[207]

However, upon stopping the lateral motion at around 539 s, the relaxation profile is typical of a liquid-like film. specifically, the lateral force exhibits a relaxation of timescale $\tau = 0.4$ s towards an amplitude $F_L \to \infty$, see Figure 4.14. This slow but clear relaxation indicates a viscous state for this 2.7M system.[11,68,207]

Therefore, the 2.7M system does exhibit behaviour that is qualitatively similar to

that expected for a simple viscous liquid.[11] This is because, for a charge-less Newto-

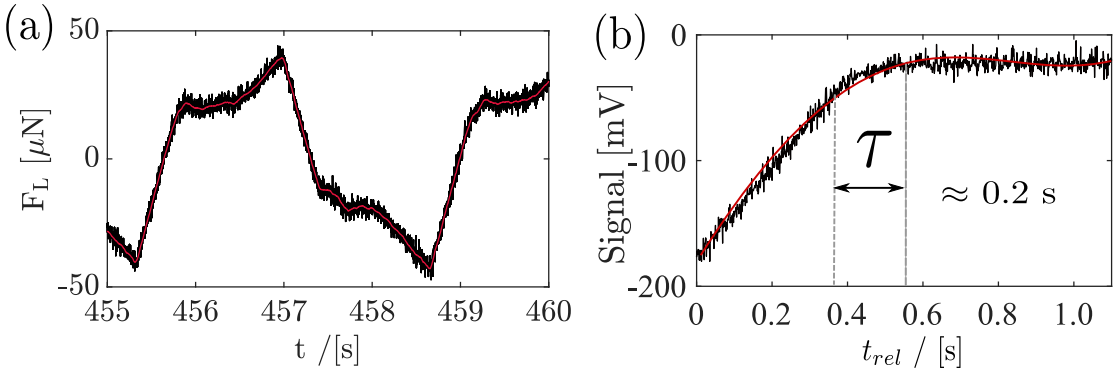


Figure 4.14: (a) Image showing the variation of F_L with time, displaying the more liquid-like shearing regime where there is a sharp 'stopping point' before the direction of lateral motion is reversed, and (b) Image showing viscous-like relaxation 2.7M film when the lateral motion is stopped, $\tau \approx 0.2$ s.

nian liquid, classical hydrodynamics predicts that when a lateral motion is applied at a constant velocity, the lateral force of that system will first exhibit a linear variation of slope k_L x v_l, then an exponential relaxation with a timescale $\frac{A\eta}{k_l D_{liquid}}$ at 10^{-4} s, and then when the direction of the motion is reversed, the lateral force responds in a symmetric manner with respect to the horizontal axis, and will then exhibit an exponential relaxation on timescale τ of 10^{-4}s $\rightarrow \infty$.[11,68]

However, there are two differences between this picture of a charge-less Newtonian liquid and our charged liquid:

1. the forces and timescales involved are more than three orders of magnitude large, and

2. non-zero force is sustained after stopping the motion.

2.15M [$C_4C_1P_{yrr}$][TFSI]-**PC**

The lateral forces observed in the 2.15M are qualitatively different from those observed in the 3.3M and 2.7M systems. As shown in Figure 4.15(a), the friction is once more "quantised" with film thickness,[11,103] and discontinuities in the $F_N - F_S$ profile are linked to changes in the film thicknesses shown on the D v F_N profile.

In the 2.15M system, there are three discrete steps in the D v F_N, moving from out of contact to layer (v) to layer (iii) and this translates to two linear regimes in the F_S v F_N profile. Figure 4.15(b) shows the lateral force as a function of time, t, in

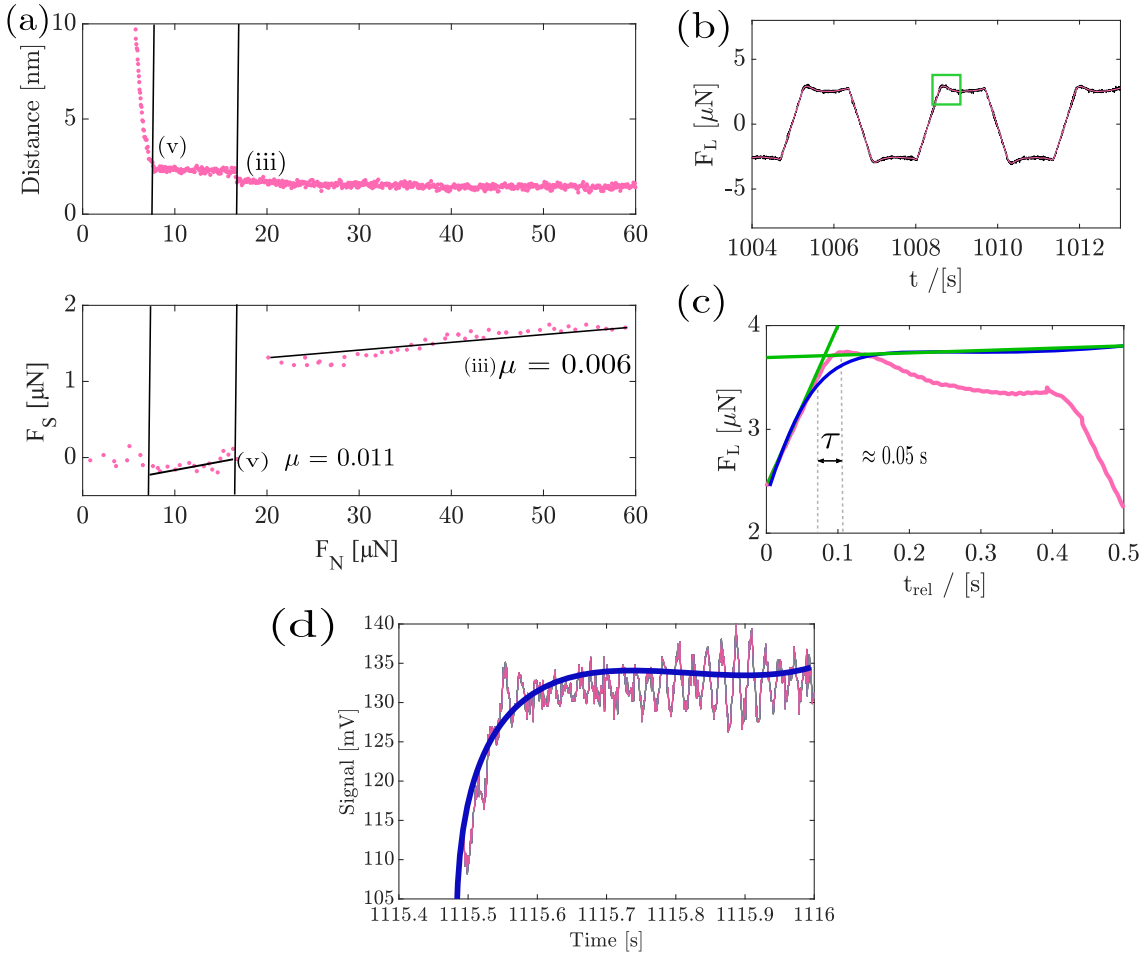


Figure 4.15: Representative (a) surface separation, D, (top plot) and shear force, F_S, (bottom plot) as a function of the normal force, F_N, across 2.15M. Bottom plot: F_S with increasing F_N is shown in pink, The friction coefficients of layer (v) and (iii) $\mu = 0.011$ and μ 0.006, respectively. The vertical dashed lines in (a) highlight the simultaneous discrete steps in surface separation and shear force with normal force. (b) Lateral friction signal, F_L, as a function of time in layer (iii), with and without a smoothing filter in pink and black, respectively. The signal within the green box is shown in (c) highlighting the viscous, liquid-like lateral friction signal that relaxes between the elastic and plastic regimes (pink lines) with time, $\tau \approx 0.05$ s. (d) Image showing the viscous relaxation of the 2.15M film when the lateral motion is stopped.

layer (iii) during two full shearing cycles. A portion of the signal is highlighted by a green square and shown in Figure 4.15(c). Here, the lateral force is plotted as a function of a relative time, t_{rel}, to highlight the timescale of relaxation, τ. When transitioning from the elastic to the plastic regime in the lateral force-time profile, a

distinct curvature is observed (rather than a discontinuity) with a relaxation time, $\tau \approx 0.05$ s.[68,194] This timescale is smaller than what is typically observed across viscous liquid-like films, but the curvature still makes this film more viscous than the 3.3M and 2.7M films. There is therefore a shift in the friction behaviour from the 3.3M and 2.7M, which showed solid-like behaviour upon continued confinement, to behaviour that is liquid-like even at a surface separation of 1.55 nm.

Finally, looking back to Equation 1.2, it is possible to quantify the different contributions to our measured friction force $F_{S,k}$ for the two layers we have identified.[103]

The results of this calculation are shown below in Table 4.3: From these results, the

Table 4.3: Load and adhesion friction coefficients with their propagated errors

System	i	$F_{adh}, \mu N$	$F_S^i, \mu N$	$A_o^i, \mu m^2$	**R, m**	D**, nm**	μ^i	α^i
2.15M	3	28.88	1.281	15.27	0.009	1.61	0.006	0.121
2.15M	5	21.52	0.6617	8.93	0.009	2.32	0.011	0.323

quantised friction seen in the 2.15M films is a direct result of the multiple discrete values of both the load-controlled friction contribution μ, and the adhesion-controlled contribution, α. This is in line with previous observations of discontinuities in the friction across molecular liquids when the number of layers changes.[68,72,102]

Importantly, these results show that in these salt-dominant systems, the friction forces are dependent on the layering, with both the load and adhesion-controlled contributions changing with each layer.

Effect of shearing velocity

In this section we briefly consider the influence of the shearing velocity on the friction force. To investigate this dynamics quantitatively, we have sheared the 2.7M liquid under constant conditions in the normal direction, exploring three decades of lateral velocities, $v_l = 639$ nm/s;$v_l = 1918$ nm/s; and $v_l = 3197$ nm/s, see Figure 4.16.

A solid-like friction behaviour (clear yield point followed by stick-slip friction)[74,75] is obtained for all the friction loops, but with a kinetic friction force that increases

monotonically with the shearing velocity, signalling to us that the film actually behaves like a liquid. At low v_S, shearing of the film then progresses by way of a

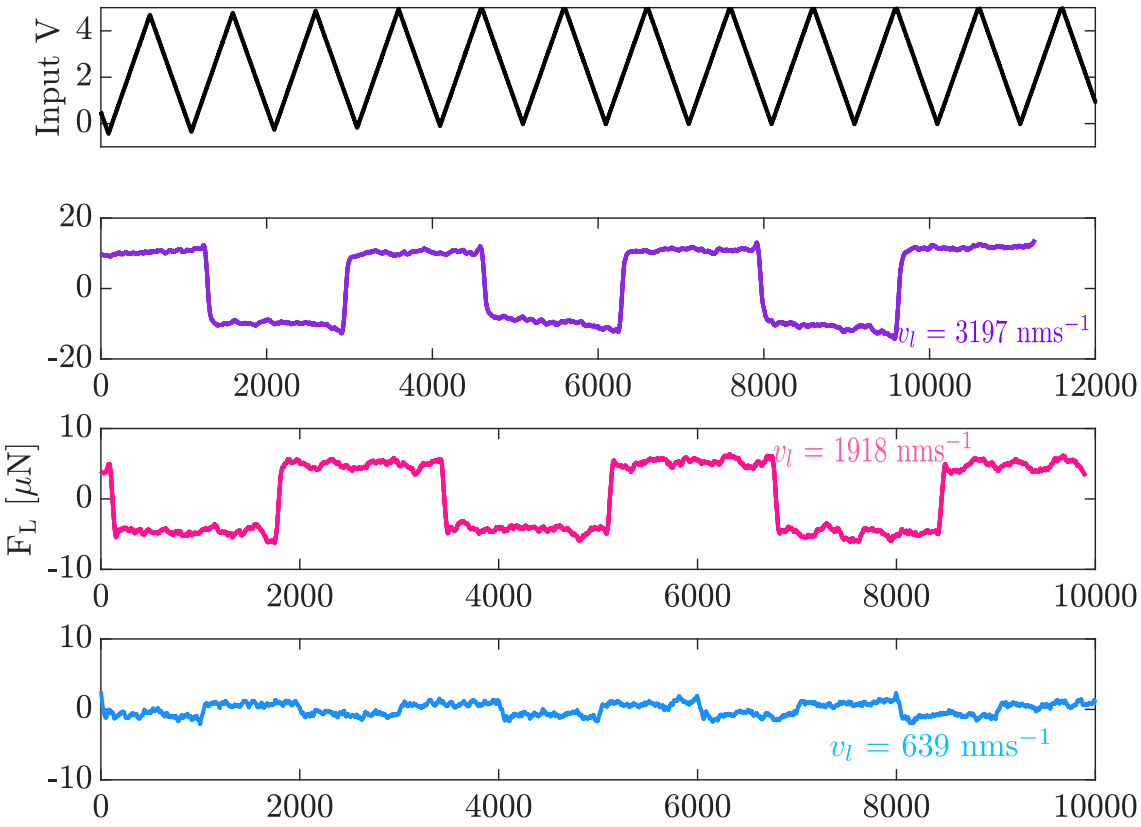


Figure 4.16: Friction cycles, showing F_L at a constant film thickness of $i = 5$, while trying to control F_N. Three decades of velocity are measured, $v_l = 639$ nm/s, 1918 nm/s, and 3197 nm/s.

series of stick–slip cycles characterized by saw-tooth traces, where Figure 4.16(a) resembles that illustrated in Figure 2.8 in Chapter 2)) which have a yield point at the beginning of each cycle. The intermediate velocity retains the more solid-like behaviour seen at $v_l = 639$ nm/s. At higher v_l, the film continues to undergo stick-slip, but the sharp yield point at the beginning is now lost, and instead a 'stopping' peak begins to develop.

Role of Absorbed Water

Figure 4.17 compares the frictional response across dry and ambient 3.3M $[C_4C_1P_{yrr}][TFSI]$. All shear force measurements across both the dry and ambient 3.3M $[C_4C_1P_{yrr}][TFSI]$ were carried out using the piezoelectric tube (PZT) method where both the normal

and lateral motion are imposed by the PZT. The PZT method was also used across

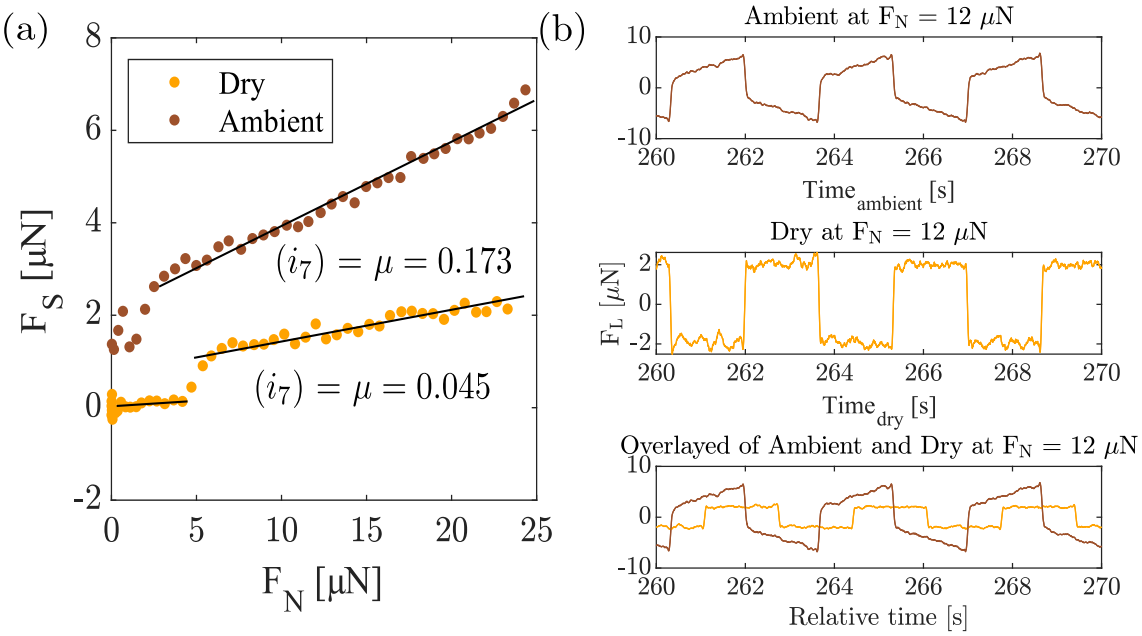


Figure 4.17: (a) Representative shear force, F_S, as a function of the normal force, F_N, across dry (orange) and ambient (brown) 3.3M [$C_4C_1P_{yrr}$][TFSI]. The inset shows F_S over the range F_N = 0 - 25 μN. Under lower loads $\mu = 0.045$ and $\mu = 0.173$ in dry and ambient [$C_4C_1P_{yrr}$][TFSI], respectively. (b) Lateral friction signals, F_L, as a function of time, with and without a smoothing filter in orange and black, respectively.

ambient 3.3M [$C_4C_1P_{yrr}$][TFSI] but this experiment was contaminated. Instead, a second method was used where the normal and lateral motion are applied by the motor and PZT, respectively, allowing access to F_S under higher loads, see Figure 4.17.

In the dry system, as we move closer in with increased F_N, molecular layers are squeezed out and we observe a corresponding increase in the magnitude and gradient of the shear force (indicated by the step in Figure 4.17(a) at $F_N \approx 6.1$ μN), as we move from one confined layering regime ($i = 9$) to another ($i = 7$). This is found at a film thickness of D= 2.50 nm. As we apply a lateral motion, the corresponding friction force, F_S has a linear relationship with the increasing applied normal load, F_N, yielding a friction coefficient of $\mu = 0.045$. Quantised friction is also apparent in ambient 3.3M [$C_4C_1P_{yrr}$][TFSI], but with increased magnitude of the lateral forces and the absence of superlubric friction coefficients at all applied loads. This change

in the friction behaviour can be attributed to water, and can be interpreted as water increasing the adhesive contribution a to the friction forces.[68,72,102,194] Extrapolating the two linear regimes, at zero applied load, F_N=0, the ambient system has a F_S of 2.05 μN, while the dry system gives F_S of 1.11 μN.

As discussed above, absorbed water can influence the equilibrium structure and/or the equilibration dynamics of the film.[72,109] If the in-plane structure is weaker, the activation barrier to sliding reduces, but it is expected that would reduce the magnitude of F_S and therefore the observed friction coefficients. Taking snapshots of the

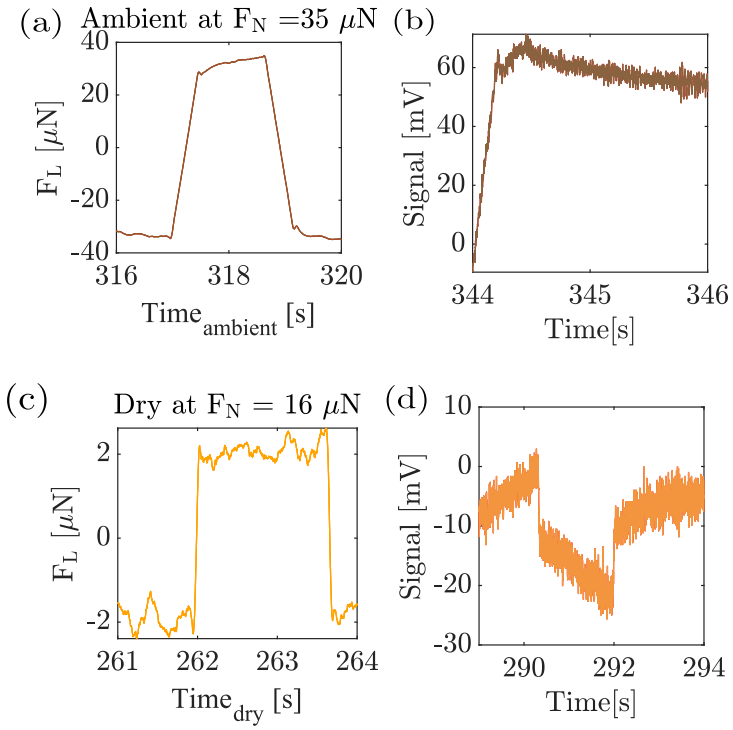


Figure 4.18: (a) Lateral friction signal, F_L, as a function of time in ambient [$C_4C_1P_{yrr}$][TFSI] at an applied load of $F_N = 35\ \mu N$. (b) Trace showing the signal obtained in ambient [$C_4C_1P_{yrr}$][TFSI] when the lateral motion stopped. (c) Lateral friction signal, F_L, as a function of time in dry [$C_4C_1P_{yrr}$][TFSI] at an applied load of $F_N = 26\ \mu N$. (d) Trace showing the signal obtained in dry [$C_4C_1P_{yrr}$][TFSI] when the lateral motion stopped.

friction traces for both the dry and ambient system when the applied normal load is 12 μN reveals that the confined films undergo different shearing mechanisms.[72] The ambient system is more liquid like in its friction trace, shown in Figure 4.18(a), where there is no clear yield point at the beginning of the cycle, but there is instead

a stopping point before the direction of shearing is reversed. As discussed above, this is more indicative of a liquid like film.

However, the dry system is more solid like in its friction trace, which displays a stick-slip profile resembling that seen and discussed in the 2.7M film. This is consistent, as studies by Yoshizawa[170]and Marzal[112]have observed that presence of ambient humidity changes the friction behaviour to being more liquid-like.

However ,this result does not square well with a study by in 2020[11] on the same ionic liquid. In that study, the increased water content made the films more lubricating, and reported superlubric conditions in the humid system. This same paper, however, reported only smooth sliding friction in the dry conditions, while these experiments consistently reveal stick slip friction. Indeed, this difference between the 2020 study[11] and the present observations should not cause concern, and that very study quantitatively showed that opposing effects of ambient humidity were influenced by the contact radius, the mica thickness, and the mica alignment.

These results are more similar to a study in 2014[112] on a different ionic liquid 1-Ethyl-3-methylimidazolium ethyl sulfate, [EMIM][$EtSO_4$]. In this study, the dry film reported a lower frictional force when compared to the ambient system at the same normal applied loads, and this is also the outcome of MD simulations.[109] This result is reproduced in the 3.3M system here, where at 16 μN, the ambient system had lateral forces at 5μN and the dry had 2 μN. At 16 μN, the ambient film thickness is 2.91 nm, which would be an $i = 7$ layer, and is also 2.97 nm in the dry film, again corresponding to a proposed $i = 7$ layer index. At these same applied loads the ambient and the dry show different F_L profiles, and the ambient system has a more fluid like system.

These results contrast to the effect of water on the force profiles of all three concentrations where the inclusion of water reduced the forces required to access the different layers. In that case, it was reasoned that water weakens the structure and

reduces the activation energy barrier to access those layers. However, in the case of the normal forces, the effect of ambient humidity was negligible and reduced forces by at most 1 μN.

Overall, the IL structure under nanoconfinement is affected by the presence of water, and therefore, the intra-layer interactions at the shear plane are modified. Water, as with other contaminant molecules or solutes, can influence the ion-pair coordination, either promoting or hindering the ease with which the ions/ alkyl chains can align parallel to the sliding direction, which in turn also influences interlayer interactions at the shear plane and the speed dependence of friction, as described above.[108] Specifically in our 3.3M film,as there is an increase in friction, bond formation (rather than rupture) is enhanced by water during sliding.[112,208]

4.4 | Summary

In this chapter, the normal and shear forces across dry and ambient $[C_4C_1P_{yrr}][TFSI]$-PC films were studied. The normal force profiles of the 3.3M, 2.7M, and 2.15M were consistent with previous studies, showing structural forces at close confinement, where the jump in points corresponded to the thickness of the film. The short-range oscillatory force was fitted for these systems, and an oscillation period of λ_{osc} of $\approx 0.71 \pm 0.2$ nm was found for all three systems. This value closely mirrored the distance between repulsive hard walls ΔD.

With these measurements in mind, we propose that the salt-dominant $[C_4C_1P_{yrr}][TFSI]$ is arranged in alternating monolayers of anions and cations. This effect is likely to be templated by the negative charge of the mica surface, which induces a monolayer of cations (C)to form in the first layer (which is responsible for the closest repulsive wall observed at 0.3 nm in the 2.15M), followed by a counterion layer of anions, and so on. Each oscillation in the force profile corresponds to squeeze-out of one cation–anion repeat unit, (AC), to preserve electroneutrality of the film, as the obtained oscillatory period of 0.71 nm is consistent with the known ion-pair diameter

of 0.80 nm for [$C_4C_1P_{yrr}$][TFSI].

Overall humidity is found to reduce the resistance of the layers to be squeezed out, but only slightly. The presence of ambient humidity dilates the [$C_4C_1P_{yrr}$][TFSI] films by ≈ 0.4 nm, indicating that water does change the structuring of our confined films. However, more compelling impacts of ambient humidity are found when studying the lateral forces of the confined films. In the case of 3.3M films, the presence of water is followed by an increase in the magnitude of the lateral forces, and a loss of superlubricity. These results therefore indicate that the presence of water influences the ion-pair coordination, and may promote bond formation. In doing so, it increases the energetic barrier to 'unlock' the layers during shearing.[68,112,208]

The frictional response of the dry films also revealed interesting behaviour. By studying the frictional response as a function of load, a linear relationship between these two were found. This linear relationship allows us to calculate values for the load-controlled contribution, μ, and the adhesion-controlled contribution, α.

Quantised friction was also present in all the measured systems, and μ as low as 0.009 were measured in the 2.15M system. The measured μ also differed dramatically from layer to layer, a result that has previously been reported in ionic liquids and deep-eutectic solvents.[194] This behaviour is different from the behaviour of oils, where the μ remains the same with increasing confinement.[74,76,178,209,210] This shows that even with the inclusion of majority volumes of PC, [$C_4C_1P_{yrr}$][TFSI] does not lose its ability to act as a boundary lubricant.

The lateral force traces showed that the confined films underwent a liquid-solid transition under confinement. In these traces, the clear yield points in the stick-slip traces indicate solid-like behaviour of the ionic liquid confined to films of $i < 9$ ion layers. However, while the lateral traces showed solid-like film behaviour, analysis of the influence of shear velocity, and measurements of relaxation times showed that the films displayed a viscous relaxation. It is notable that as the mol % of

PC increases, the lateral force response begins to appear more liquid-like, and the 2.15M film no longer has a yield point. Instead, the film relaxes with a timescale expected for viscous liquids.[74,76,178,209,210]

We can therefore conclude that under confinement, the salt-dominant $[C_4C_1P_{yrr}]$[TFSI]-PC films do show similar structural forces to the pure confined films. When studying the shearing force, we begin to see the influence of PC as the 2.15M film displays different shear forces.

5 | Normal and Lateral Forces of Solvent-Dominant $[C_4C_1P_{yrr}][TFSI]$-Propylene Carbonate Mixtures

5.1 | Introduction

In this chapter, the solvent-dominant mixtures of $[C_4C_1P_{yrr}][TFSI]$-PC are studied. As previously mentioned, studies of dilute IL mixtures are of great importance because this is where IL's will find their greatest practical use. The IL, $[C_4C_1P_{yrr}][TFSI]$, has been found to show superlubric friction behaviour when confined in the SFB,[103] making it stand out as a potential future-lubricant, and the previous chapter showed this behaviour remains even when mixed with minor fractions of PC.

In this chapter, studies of $[C_4C_1P_{yrr}][TFSI]$ mixed with 'larger' amounts of PC, such that the molecular PC is "dominant", to see if the superior IL lubrication continues.

5.2 | Normal Forces across Solvent-Dominant $[C_4C_1P_{yrr}][TFSI]$-PC mixtures

The normal force profiles across dry solvent-dominant $[C_4C_1P_{yrr}][TFSI]$-PC systems are shown in this section. The 1.4M, or 20 mol %, is shown in Figure 5.1(a), the 0.5M, or 6 mol %, is shown in Figure 5.2(a), and the pure PC system is shown in Figure 5.3(a).

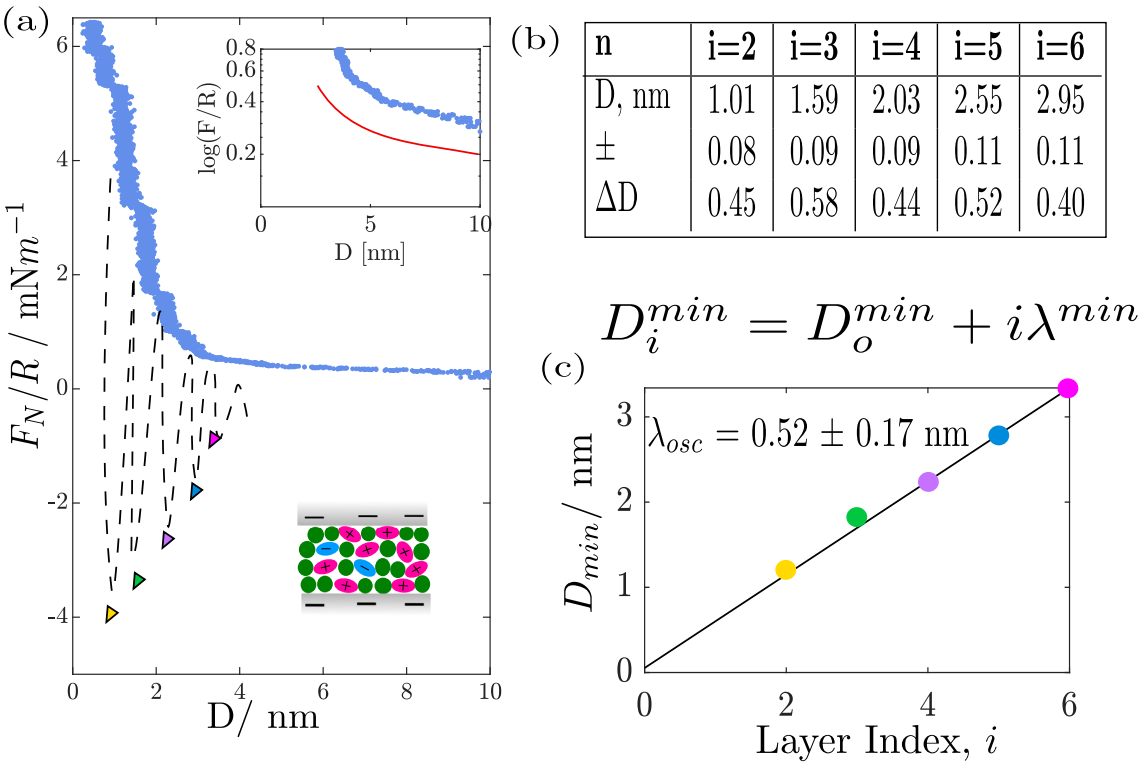
5.2.1 | Structural Forces

1.4M [$C_4C_1P_{yrr}$][TFSI]-PC

We observe an oscillatory force profile for the 1.4M [$C_4C_1P_{yrr}$][TFSI]-PC system, indicative of molecular layering between the surfaces, and in line with previous literature measurements. The separation between the hard walls is uniform with a dimension of ΔD = 0.52 nm ± 0.17 nm, as was previously reported in the same system mixed with PC[90,91] and in a simulation of [$C_4C_1P_{yrr}$][TFSI] with acetonitrile, ACN[83] and is consistent with the size of the PC molecule. This is of course, a stark switch from what was seen in the 'salt-dominant' systems, where the separation was more consistent with the dimensions of a cation-anion pair, at 0.75 nm.[90,91] The inset of Figure 5.1(a) shows the long-range normal force decay. However, this long-range behaviour does not portray the linear shape we would expect for this type of liquid for two reasons. Firstly, the extrapolated decay length, λ_{exp} of 5.1849 nm is anomalously long when compared to previous reported measurements of 0.9 nm,[90,211] and secondly, the shape of this decay on the log-linear scale is not linear over a significant span of data points for the extracted value to be reliable. As shown in Figure 3.11 in Chapter 3, the Decay length is extracted from the linear tail ≈ < 35 nm, and as shown in Figures 5.1(a); 5.2(a); and 5.3(a), when plotted on a log-linear scale, we see a curved profile that consists of statistically significant data points. As explained below in Section 5.3, the solvent-dominant systems studied in this chapter had force profile that were impacted by hydrodynamic forces, and these may have obscured those long-ranged forces that would typically be measurable in these types of systems.

0.5M [$C_4C_1P_{yrr}$][TFSI]-PC

Normal force profiles for 6 % mol, or 0.5M, [$C_4C_1P_{yrr}$][TFSI] in PC, are shown in Figure 5.2(a). An oscillatory force is observed, and 4 different layers are discernable, with $i = 1$ at D=0.58 ± 0.07 nm, $i = 2$ at 1.14 ± 0.07 nm, $i = 3$ at 1.54 ± 0.07 nm,



n	i=2	i=3	i=4	i=5	i=6
D, nm	1.01	1.59	2.03	2.55	2.95
±	0.08	0.09	0.09	0.11	0.11
ΔD	0.45	0.58	0.44	0.52	0.40

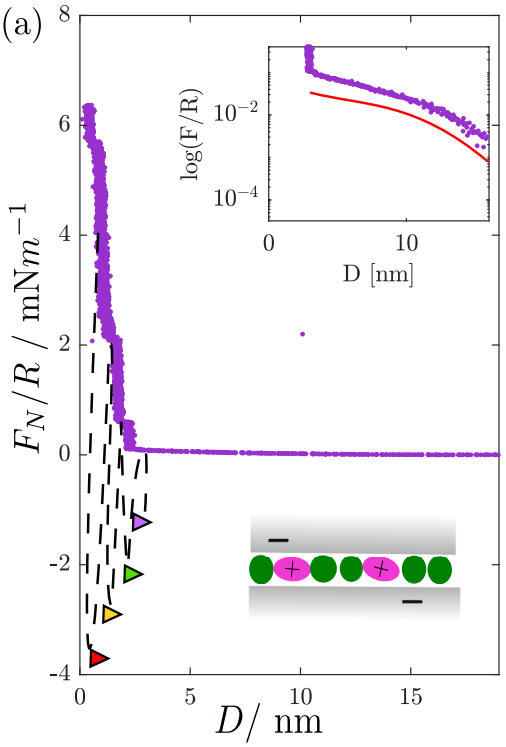
Figure 5.1: Representative normal force, F_N, normalised by the radius of curvature, R, as a function of surface separation, D, measured in nm, profiles in 1.4M [$C_4C_1P_{yrr}$][TFSI]-PC. The corresponding minimum adhesive force and jump out position for each layer are indicated by triangular points in the following order: yellow, green, purple, and pink. The inset shows a log-linear representation of the normal force on approach, where the red line indicates that the force has a viscous element to it, and therefore no value for the long-range exponential decay, λ_{exp} can be obtained. (b) Table showing the layering regimes i identified from this run, which is done by obtaining the film thickness D, nm at the repulsive hard walls. The difference between successive hard walls, ΔD is also shown. The oscillatory force (black dashed line), Equation 1.1, in (a) is fitted using Equation 4.1 and 4.2 and the parameters calculated in Section 5.2.2. (c)The gradient of the surface separation at the jump out point, D_{min}, as a function of the layer index, i, plotted on a linear scale, Equation 4.1 (shown), yields the oscillation periodicity, $\lambda_{osc} = 0.52 \pm 0.17$ nm.

and $i = 4$ at D = 2.05 ± 0.07 nm. The separation between the repulsive hard walls is again ΔD= 0.53 ± 0.17 nm, in line with previous literature measurements.[90,91]

Pure Propylene Carbonate

Normal force profiles for pure PC are shown in Figure 5.3(a). An oscillatory force is observed, and 9 different layers are discernable, with $i = 2$ at D= 1.04 ± 0.06 nm, $i = 3$ at D=1.47 ± 0.05 nm, $i = 4$ at D= 1.95 ± 0.05nm, $i = 5$ at 2.41 ± 0.06 nm,

(a)



(b)

n	i=1	i=2	i=3	i=4
D, nm	0.58	1.14	1.54	2.05
±	0.07	0.07	0.07	0.07
ΔD	-	0.56	0.40	0.51

(c)

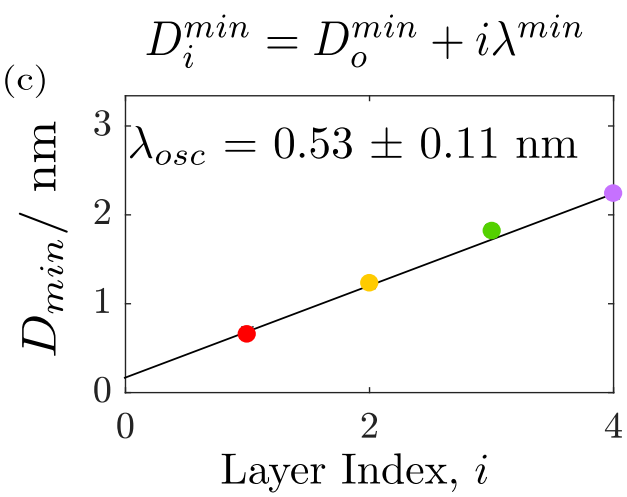
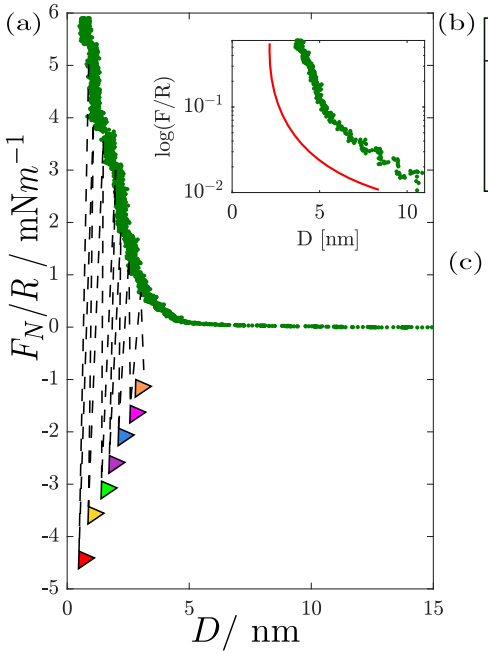


Figure 5.2: Representative normal force, F_N, normalised by the radius of curvature, R, as a function of surface separation, D, measured in nm, profiles in 0.5M [$C_4C_1P_{yrr}$][TFSI]-PC. The corresponding minimum adhesive force and jump out position for each layer are indicated by triangular points in the following order: red, yellow, green, and purple. The inset shows a log-linear representation of the normal force on approach, where the red line indicates that the force has a viscous element to it, and therefore no value for the long-range exponential decay, λ_{exp} can be obtained. (b) Table showing the layering regimes i identified from this run, which is done by obtaining the film thickness D, nm at the repulsive hard walls. The difference between successive hard walls, ΔD is also shown. The oscillatory force (black dashed line), Equation 1.1, in (a) is fitted using Equation 4.1 and 4.1 and the parameters calculated in Section 5.2.2, for example from (c) The gradient of the surface separation at the jump out point, D_{min}, as a function of the layer index, i, plotted on a linear scale, Equation 4.1 (shown), yields the oscillation periodicity, $\lambda_{osc} =$ 0. 53 ± 0.11 nm.

$i =$ at D= 2.86 ± 0.07 mm, $i = 7$ at 3.22 ± 0.1 nm, $i = 8$ at D= 3.63 ± 0.1 nm, and $i = 9$ at D= 4.00 ± 0.1 nm. The separation between the repulsive hard walls is again ΔD= 0.44 ± 0.23 nm, in line with previous literature measurements.[90,91]

5.2.2 | Oscillatory Forces

The fitting procedure outlined in Section 4.2.2 was used to the fit oscillatory forces for the solvent-dominant systems. Firstly, the linear fit using Equation 4.1 was performed and for the 1.4M system the slope of λ^{min} was 0.52 ± 0.17 nm. As



(b)

n	i=2	i=3	i=4	i=5	i=6	i=7	i=8	i=9
D, nm	1.04	1.44	1.95	2.41	2.86	3.22	3.63	4.00
±	0.06	0.05	0.05	0.06	0.07	0.1	0.1	0.1
ΔD	-	0.40	0.51	0.46	0.45	0.36	0.41	0.37

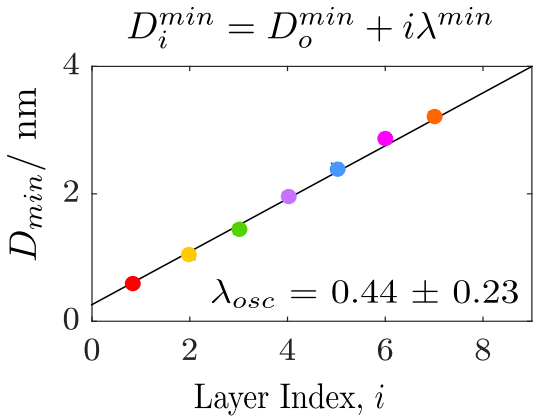


Figure 5.3: Representative normal force, F_N, normalised by the radius of curvature, R, as a function of surface separation, D, measured in nm, profiles in pure PC. The corresponding minimum adhesive force and jump out position for each layer are indicated by triangular points following order: pink, green, cyan, orange, blue-grey. The inset shows a log-linear representation of the normal force on approach, where the red line indicates that the force has a viscous element to it, and therefore no value for the long-range exponential decay, λ_{exp} can be obtained. (b) Table showing the layering regimes i identified from this run, which is done by obtaining the film thickness D, nm at the repulsive hard walls. The difference between successive hard walls, ΔD is also shown. The oscillatory force (black dashed line), Equation 1.1, in (a) is fitted using Equation 4.1 and 4.2 and the parameters calculated in Section 5.2.2. The gradient of the surface separation at the jump out point, D_{min}, as a function of the layer index, i, plotted on a linear scale, Equation 4.1 (shown), yields the oscillation periodicity, $\lambda_{osc} = 0.\ 44 \pm 0.23$ nm.

previously explained, this linear fit corresponds λ_{osc}, and therefore the periodicity of our oscillatory force is 0.52 nm in the 1.4M system. The results for 1.4M, 0.5M and pure PC are shown in Figure 5.4(a).

It was previously observed that the salt-dominant systems had a $\lambda_{osc} \approx 0.70$ nm, and that this value was consistent with both the distance between hard walls, ΔD and the ion-pair diameter.[90,91]

Therefore, this measured value of λ_{osc} is useful to identify the composition of the confined layers and to show that its composition has changed when the salt no longer dominates. As stated above, this result was previously recorded in 2017,[90,91]

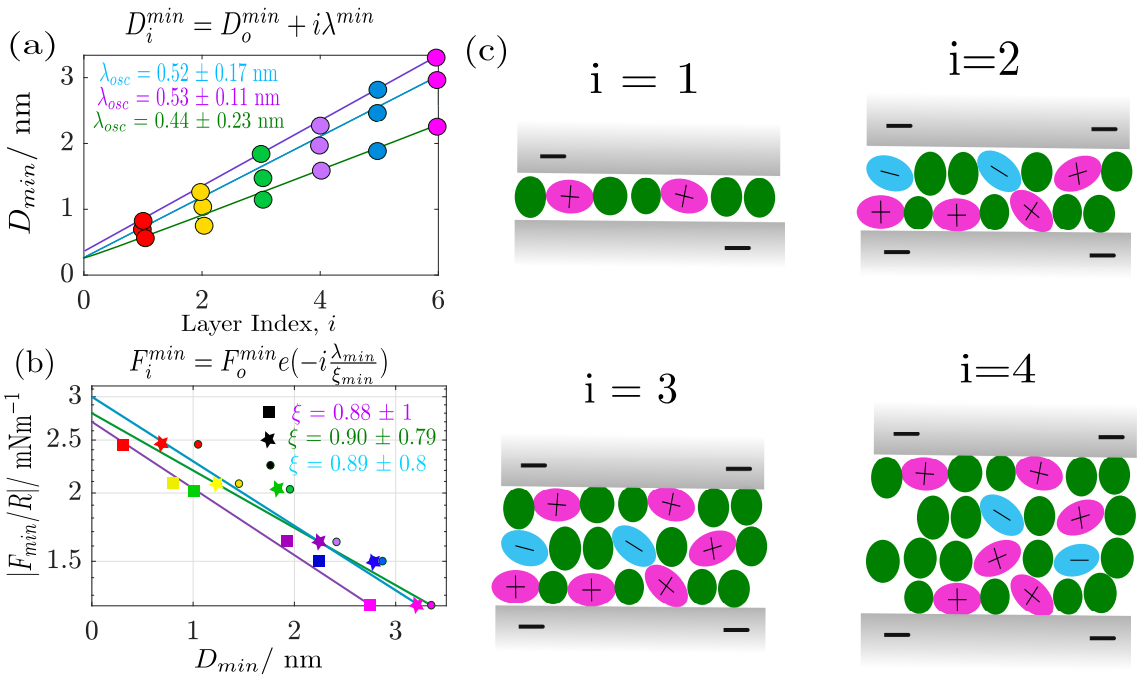


Figure 5.4: The oscillatory forces (black dashed line) seen in Figures 5.1, 5.2, and 5.3 are fitted using Equation 1.1 and the parameters calculated in (a) and (b). In (a) and (b), the data is colour coded as: the blue line corresponds to the data for 1.4M, the purple line corresponds to 0.5M data, and the green line corresponds to the pure PC data. The gradient of the surface separation at the jump out point, D_{min}, as a function of the layer index, i, in (a) yields the oscillation periodicity, λ_{osc}, for the different solvent-dominant systems, using the linear fit of Equation 4.1. The gradient of the absolute force at the jump out point, $|F_{min}/R|$, as a function of the surface separation at the jump out point, D_{min}, on a log-linear plot in (b) yields the exponential decay length of the damped oscillation, ξ. (c) Cartoons illustrating the proposed layering regimes found in the solvent-dominant [C4C1Pyrr][TFSI]-PC films.[91]

and it was reasoned that as the period is similar to the width of PC it is believed that one squeeze-out event corresponds to the squeeze-out of a PC layer. Indeed, our value of λ_{osc} =0.52 nm is close to our measured separation between hard walls, which ranged from ΔD = 0.40 nm to 0.55 nm across all measurements of confined solvent-dominant systems.

It is notable to mention that the same fitting procedure was performed for the 0.5M [C4C1Pyrr][TFSI]-PC and the pure PC system. In the 0.5M system, the linear fit of D_{min} with layer index i yielded a λ^{min}= 0.53 ± 0.11 nm, while in the pure PC system, the obtained slope was slightly reduced to λ^{min}= 0.44 ± 0.23 nm. This reduction in λ_{min} (which is ≈ λ_{osc}) may be interpreted as a manifestation of the changing

structure of the confined films as PC is the only molecular component, and without the influence of the charged IL molecules, can pack more closely.[90,129,204] In this case, as is expected from simple molecular liquids the oscillation period corresponded to the dimension of one molecular layer as this is the "layer" that is squeezed out.[40,61]

Using Equation 4.2, we can obtain the ξ, for our salt-dominant film systems. In the 1.4 system, we can calculate $\xi = 0.88 \pm 1$ nm. This is the period of the oscillation on the decay length, and fits for the three systems are shown in Figure 5.4(a).[37,90,91]

Therefore, an exponentially decaying behaviour is observed, that, in combination with the oscillatory density correlations, is akin to the radial distribution function observed in studies of this and similar ILs.[37,61,91] The resulting damped oscillatory force is shown by the black dashed line in Figures 5.1(a), 5.2(a) and 5.3(a).

5.3 | Hydrodynamic Forces

While PC and [$C_4C_1P_{yrr}$][TFSI] are not expected to be viscous,,[211] and the salt-dominant profiles were not influenced by viscous forces, see Figure 5.6, our measured structural forces, seen in Section 5.2.1, show a viscous influence. Notably, at surface separations exceeding 10nm, we see a non-linear decay, and this indicates that viscous forces are in-fact contributing.[78,89,211,212] With this in mind, it is necessary to investigate and quantify this viscous contribution. To do this, force profiles were measured at different approach velocities. In Chapter 3, comparison factors were introduced allowing us to determine approximate velocities at which viscous forces become dominant. Table 5.1 shows approach velocities for each regime when $R = 0.655$ cm.[78] Viscous forces can be difficult to remove, making accurate interpretation

Table 5.1: Comparison factors for high, low and intermediate velocity regimes for [$C_4C_1P_{yrr}$][TFSI] ($\eta = 74$ mPa s at 25°C) and $R = 0.655$ cm[78]

Regime	**Velocity/ nm** s^{-1}	C_{reg} **x** 10^6 **/mPa** m^2
High	87	275
Intermediate	1.1	3.27
Low	0.22	0.696

of our measured normal force-separation profiles more challenging.[78] As the viscous force is particularly prominent when we are near the surface ($D < 20 - 30$ nm), the behaviour in this region is not well-described by a linear approach baseline, and as a result the features of normal force-separation profiles may be influenced by the viscous forces.

Figure 5.5 highlights the influence of viscous forces on the observed force profiles across 1.4M [$C_4C_1P_{yrr}$][TFSI]-PC nanofilms. At high velocities, we can fit the observed distance-time profile (Figure 5.5(a)) to a purely hydrodynamic force,[78]

$$F_{\text{hydro}} = -\frac{6\pi\eta R^2 v}{D-b} \tag{5.1}$$

As we know the viscosity η, radius of curvature R, and surface separation, we only need to fit the approach velocity, v, and the slip length, b. The fit is shown in orange and $b \approx 7$ nm. In this system, b is a negative slip length, where an immovable layer of molecules within the liquid, of dimension b, sits on the mica surface. This phenomenon is highlighted in Figure 5.5(b). The layer acts to retard the velocity of the neighbouring molecular layers and we subsequently observe a gradient of increasing velocities as we move away from the stopped layer and towards the bulk region.[78,212] Therefore, we are able to alter the equation for our linear motion to correct for any hydrodynamic forces that are present.[78]

$$k\left(D(t) - D_0 + vt\right) = F(t) = -\frac{6\pi\eta R^2 \dot{D}}{D-b} + 2\pi R A e^{-D/\lambda_s}. \tag{5.2}$$

An analytical solution for this exists in the purely viscous case ($A = 0$), therefore the equation of motion is integrated numerically in C++ using our four known parameters: the radius R, the initial measured distances D_0, the spring constant k, and the viscosity taken from the literature η.

The ideal process to take account of the viscous forces is that the four other parameters(A, v, b, and λ_s) are manually tuned to fit the data: first the velocity v

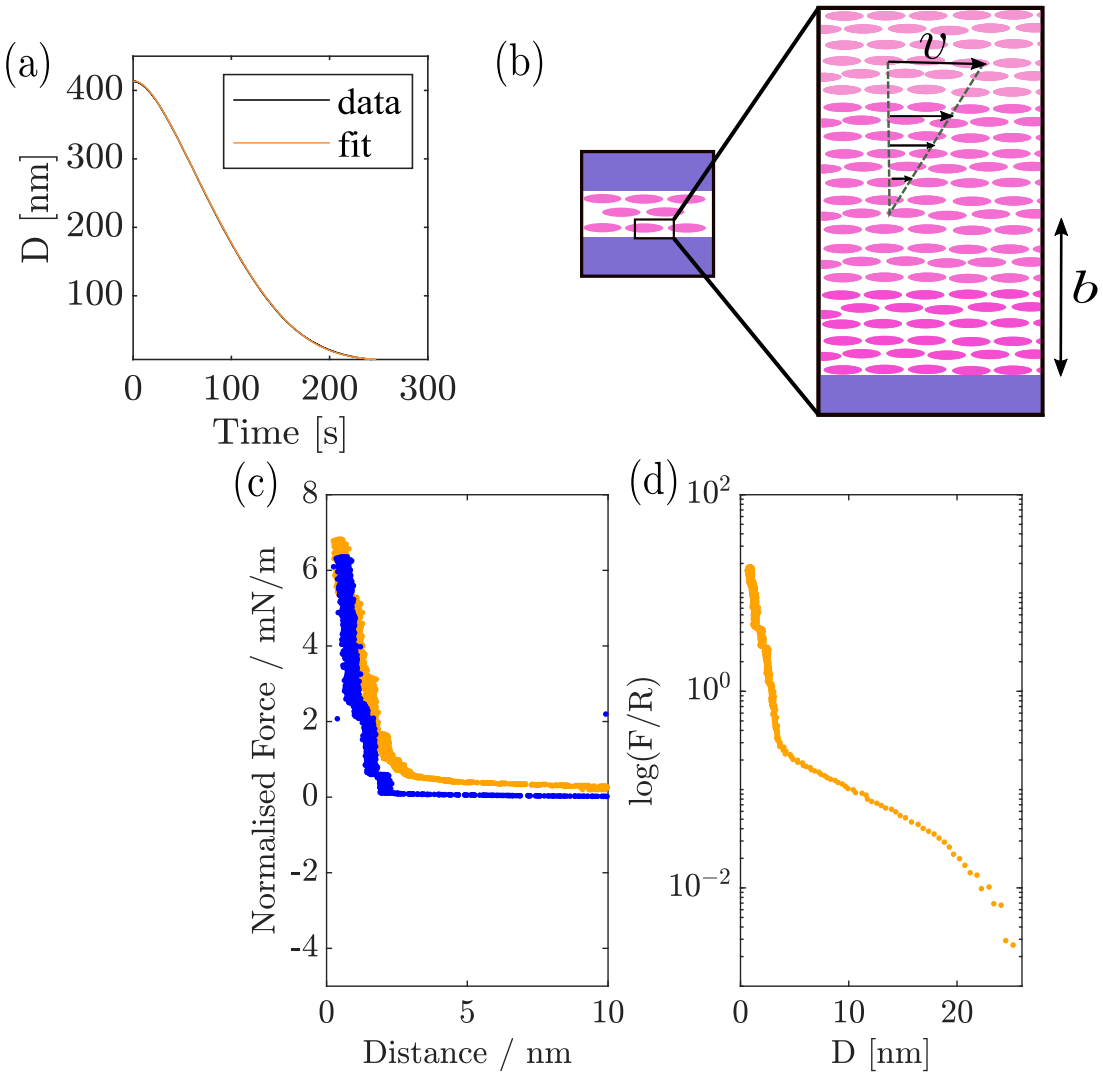


Figure 5.5: The influence of viscous forces across solvent-dominant [$C_4C_1P_{yrr}$][TFSI]-PC nanofilms. (a) Representative surface separation, D, as a function of time at high velocity, v, (black) and the fitted D_{time} profile assuming a purely viscous force (orange) where v_s = 4.2 nm/s and the negative slip, $b \approx$ 7 - 8 nm. (b) Schematic highlighting the stopped layer of molecules corresponding to b (darkest pink) and the velocity gradient away from the stopped layer (lighter pinks = greater v_s). In the case of [$C_4C_1P_{yrr}$][TFSI] in PC, b could correspond to 9-15 molecular layers if they arrange with their long dimension parallel to the surface, or 5-8 molecular layers if perpendicular. The mica surfaces are shown in purple. (c) Velocity of approach has a noticeable influence on the normal force-separation profile. Approach velocities of 11 nm/s and 1.85 nm/s are shown in orange and blue, respectively. (d) Log-linear representation of the orange plot in (c). Even at lower velocities it is difficult to deconvolute any potential long-range electrostatic force from the viscous force.

is fitted at large distances, secondly the hydrodynamic zero b, the screening length λ_s and the amplitude A are fitted at small scales, and finally all the parameters are refined iteratively.[78] For a single trajectory, the parameters b, λ_s and A are interde-

pendent, but by taking measurements at low, intermediate, and fast velocities, the inter relation between these can be explored.

In the current system, 1.4M [$C_4C_1P_{yrr}$][TFSI] in PC, no 'clean' experiment (an experiment where the presence of particles on the mica surfaces distorts the FECO profile and the linearity of our motors) with a low normal velocity ($v_s < 0.22$ nm/s) was obtained, and so at this stage, only measurements with an intermediate and fast velocity will be explored. For the salt-dominant films, the use of a piezo approach without shearing meant force profiles at low velocities ($v_s \leq$ to 0.22 nm/s) were measured, see Figure 5.6. As shown in Figure 5.6, when the data is fitted using the method described above, a slip length, b of 7 nm is measured. This overall indicates that there is a viscous film approximately 7-8 layers thick, and is consistent with previous studies on the pure [$C_4C_1P_{yrr}$][TFSI] film.[78]

5.3.1 | Fast Velocities

Figure 5.7 shows the data obtained when the top lens is moving at a fast velocity. At these fast velocities, the viscous force is expected to dominate and the data is fitted by assuming a purely viscous force, with v_s= 11 nm/s and b= 7.4 $\pm$ 0.3 nm. In this regime, the top lens is moving at v_s= 11.1 nm/s, as illustrated by the dashed-line. When we fit with solely v_s, while this does capture the initial curvature of approach and the area of close confinement (10 nm $< D <$ 20 nm), the no slip boundary is ot appropriate for $D >$ 20 nm, and best fit is obtained with b = 7.3 $\pm$ 0.3 nm, which corresponds to a thick layer of i = 13. The log-linear representation of the orange plot in (a) is shown in Figure 5.7(c). We do not observe a linear decay that would be indicative of a long-range exponentially decaying electrostatic force.

5.3.2 | Intermediate Velocities

Measurements at an intermediate velocity v_s= 1.86 nm/s are shown in Figure 5.8. Similar to the previous profile, fitting with only v_s does not model the data well. The

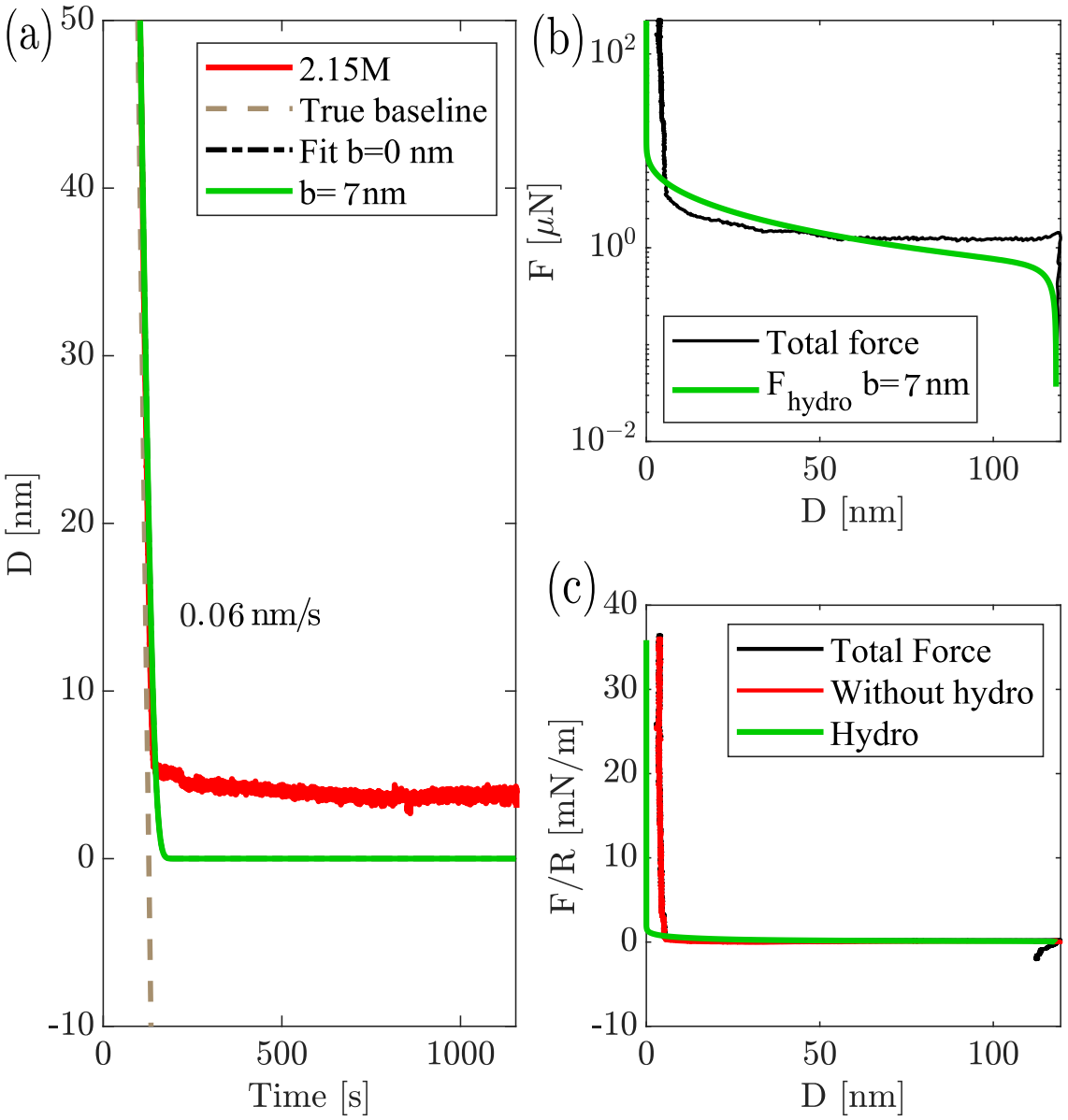


Figure 5.6: (a) Trajectory recorded across a 2.15M [$C_4C_1P_{yrr}$][TFSI]-PC film where the top lens is moving at $v_s = 0.06$ nm/s (Piezo motion indicated by the dashed line in grey). The red curve is the experimental signal: the black-dashed curve is the fit by the model with $b = 0$, the green curve is the fit when b= 0. The black-dashed curve is obscured by the thick experimental data curve. (b) Same measurements, but with data presented in terms of force, in semi-log scales.The black curve is the total force, the green curve is the viscous contribution (when fitting with b= 7 nm (c) F_N/R profile showing the total measured (black), the viscous contribution (green), and the force without the viscous contribution (red).

best fit is obtained with $b = 7.3 \pm 0.3$ nm ($i = 13$). The log-linear representation of the blue plot in (c) is shown in Figure 5.8(d). We do not observe a linear decay that would be indicative of a long-range exponentially decaying electrostatic force.

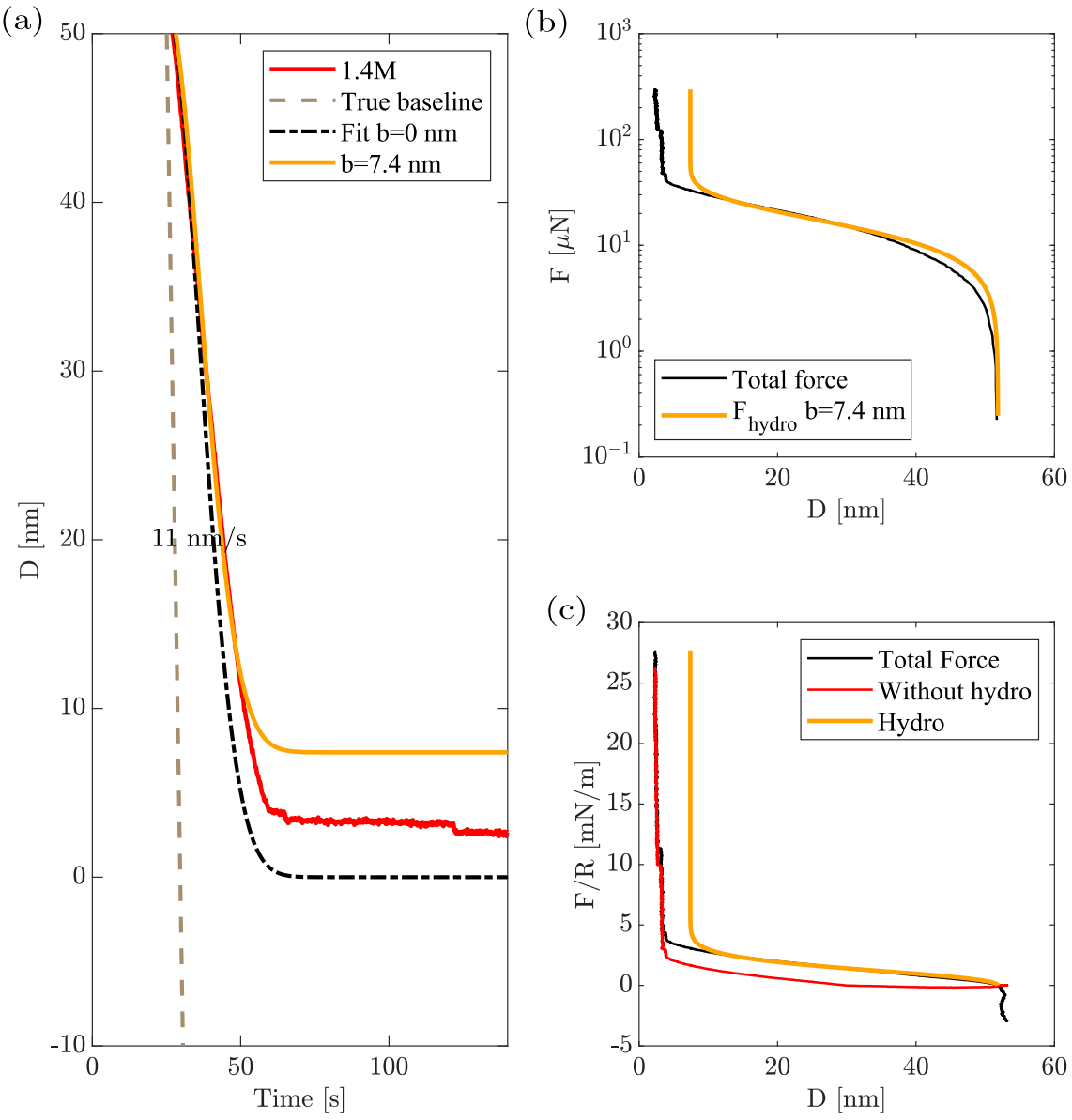


Figure 5.7: (a) Trajectory recorded when the top lens is moving at v_s = 11 .1 nm/s (piezo motion indicated by the dashed line in grey). The red curve is the experimental signal: the black-dashed curve is the fit by the model with b = 0, the orange curve is the fit when b= 7.4 nm. (b) Same measurements, but with data presented in terms of force, in semi-log scales. The black curve is the total force, the orange curve is the viscous contribution (when fitting with b= 7.4 nm (c) F_N/R profile showing the total measured (black), the viscous contribution (orange), and the force without the viscous contribution (red).

It is likely that, even at these intermediate velocities, deconvolution of any potential long-range exponentially decaying electrostatic force from the viscous force would be difficult. We would need to approach at much slower velocities (out of the range of the equipment at v_s = 0.22 nm/s), to successfully reach the low regimes (Table

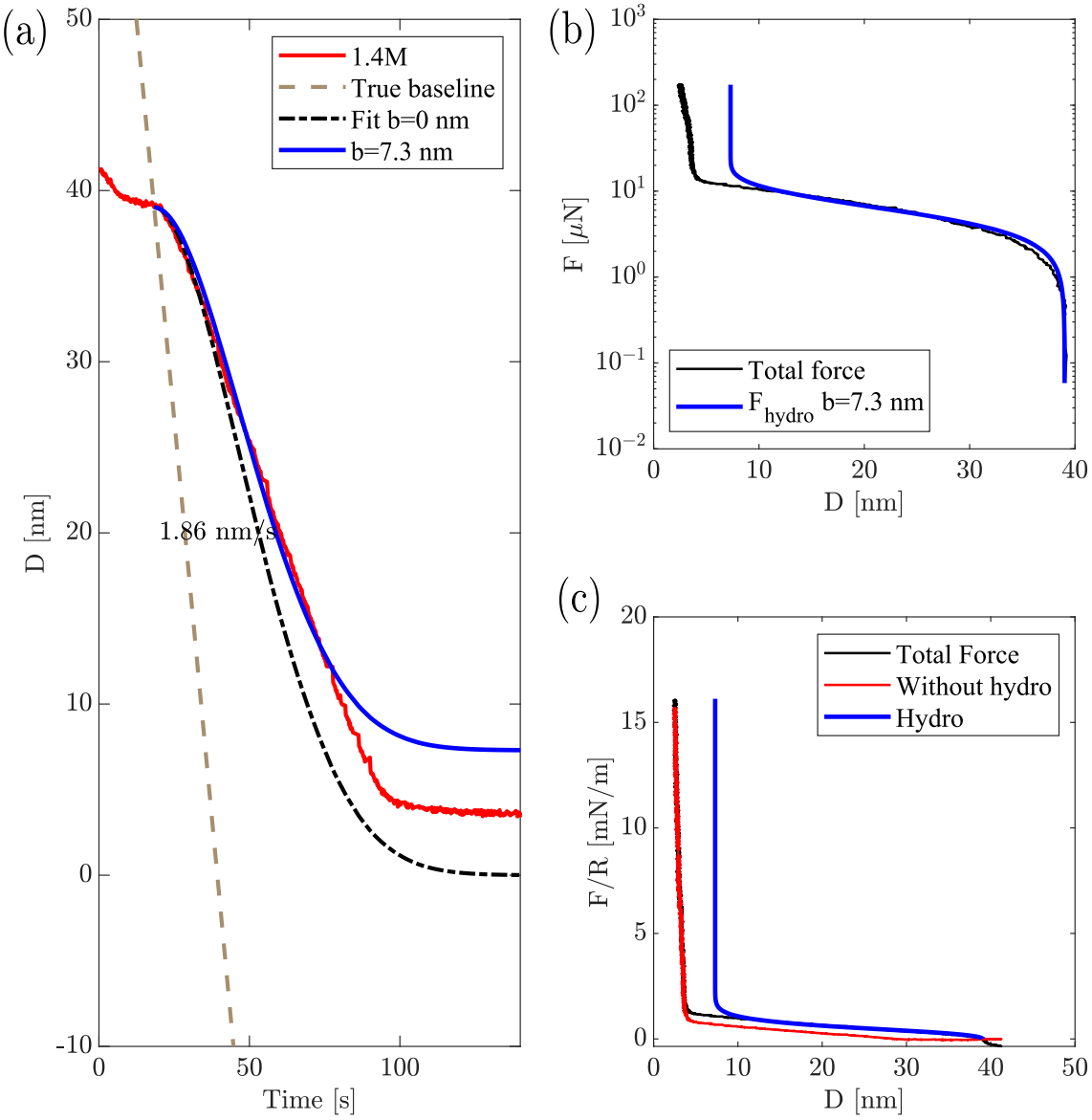


Figure 5.8: (a) Trajectory recorded when the top lens is moving at $v_s = 1.86$ nm/s (Piezo motion indicated by the dashed line in grey). The red curve is the experimental signal: the black-dashed curve is the fit by the model with $b = 0$, the blue curve is the fit when b= 7.4. (b) Same measurements, but with data presented in terms of force, in semi-log scales.The black curve is the total force, the blue curve is the viscous contribution (when fitting with b= 7.3 nm (c) F_N/R profile showing the total measured (black), the viscous contribution (blue), and the force without the viscous contribution (red).

5.1).

As a result of the viscous forces, we may not be able to quantitatively describe all force profile features. However, it will be possible to make observations at small distances, when the change in separation with time is small and so viscous forces becomes negligible.Therefore, for the measurements of the solvent-dominant systems,

it would be misleading to present decay lengths, as none of the approach velocities used were slow enough to allow for a true disentanglement and elimination of the viscous forces.

5.4 | Friction Forces of Solvent-Dominant [$C_4C_1P_{yrr}$][TFSI]-PC mixtures

We now study dry mixtures of confined solvent dominant [$C_4C_1P_{yrr}$][TFSI] and PC under confinement when a shearing motion is applied across the films.

1.4M [$C_4C_1P_{yrr}$][TFSI]-PC

Figure 5.9 shows the lateral force versus time profiles for our 1.4M [$C_4C_1P_{yrr}$][TFSI]-PC mixture various points of surface separation. From Figure 5.9(a) When the surfaces are brought close together, the random vibrations persist down to D=3.58 nm (point (vii) and $i = 7$) see Figure 5.9. Upon further compression to D= 3.17 nm ($i = 6$), the signal adopts a more ordered profile. In the 3.17 nm layer, point (vi) on the D v F_N profile, when starting to apply a constant lateral velocity, $v_l = 639$ nm/s, the lateral force exhibits first a linear variation of slope k_L x v_l, then a relaxation with a typical timescale of $\tau = 0.3$ s, and there is some smooth sliding creep on the order of 0.09 mN. In this layer, stick slip friction is apparent, but there is no yield point that begins the cycle. Instead, the film relaxes exponentially with τ and is then followed by a series of discrete stiction peaks where the force varies between a minimum of $F_{S,k}$ at the stick point a maximum of $F_{S,st}$ at the slip point. Before the direction of shearing is reversed, a stopping point is recorded. Notably, the stopping point is of greater magnitude than the yield point which begins the cycle. At this point, the 1.4M film is more characteristic of a sheared confined liquid.[68,213]

When the surfaces are moved together, to $D = 2.67$ nm ($i = 3$, point (v)), the response remains characteristic of a liquid confined between two surfaces, and stick-slip friction continues as was described for the 3.17 nm layer.

As the film is further compressed, the lateral force traces change and a yield point

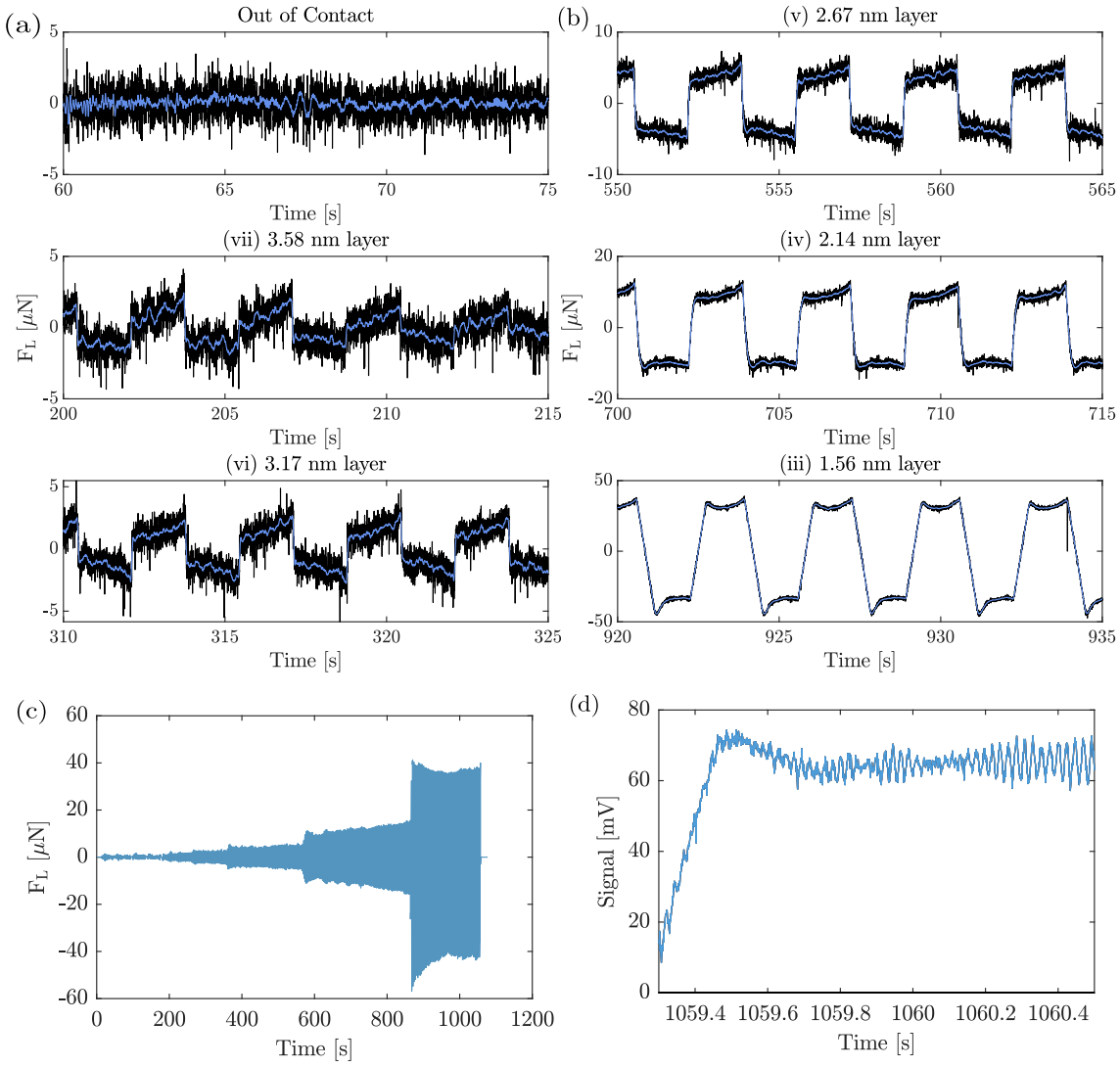


Figure 5.9: Representative lateral force of 1.4M [$C_4C_1P_{yrr}$][TFSI]- PC, as a function of time, with and without a smoothing filter in blue and black, respectively. Six different friction regimes are observed in (a) and (b) and are labelled in Figure 5.10(a). (c) Temporal evolutions of the lateral force F_L, when moving the top surface with the piezoelectric tube at a normal velocity of v_n =0.5 nm/s and v_l of 639 nm/s and (d) response of the film when the lateral motion is stopped.

is now observable. At 2.14 nm, (iv), there is a slight $F_{S,y}$ that is then followed by increasingly rapid levelling off to the kinetic friction force, before a stopping point of greater magnitude than $F_{S,y}$ is seen. At 1.56 nm, the trace has a clearly-defined sea-saw style profile where the yield point and stopping point are of equal magnitude. In between these two points, the steady sliding relaxes from $F_{S,y}$, and the begins to increase towards the stopping point. The friction therefore now begins to mirror that described in 1993,[157] where they labelled the film as being more

solid-like. Therefore, there is a transition from a liquid-like shearing behaviour to a solid-like shearing behaviour with increasing surface confinement. However, once the shearing motion is stopped, the film exhibits a liquid-like relaxation, Figure 5.10(d), indicating that this transition is only temporal. Importantly, as the normal

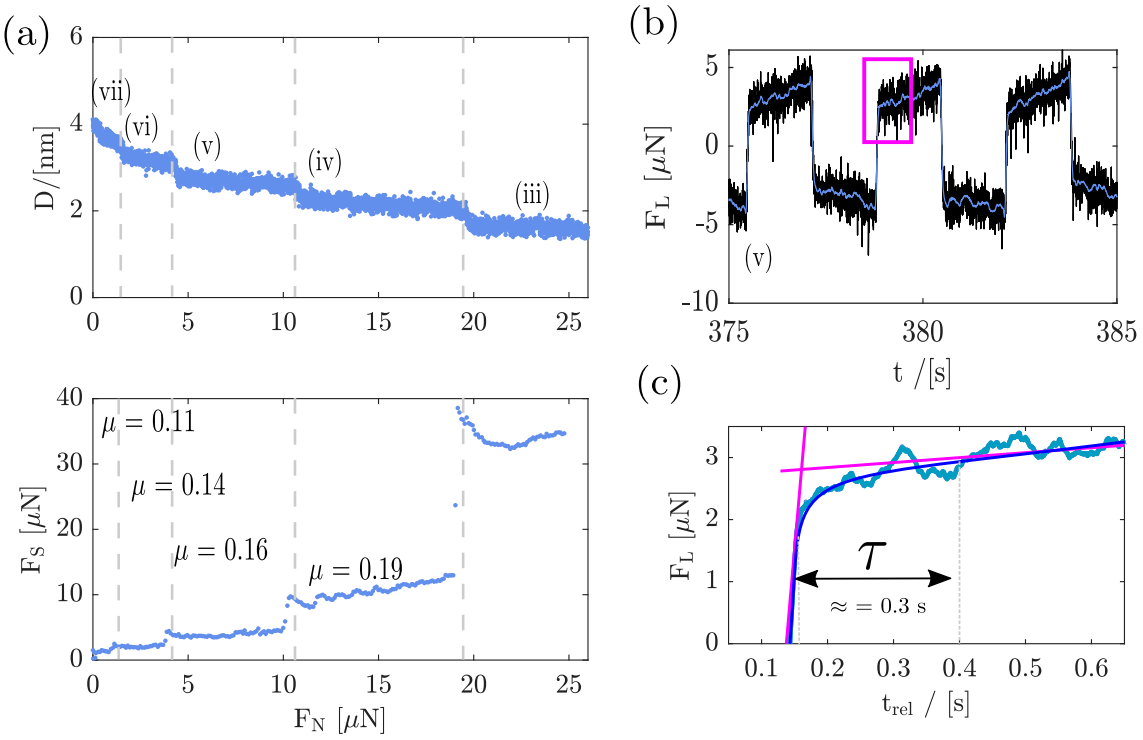


Figure 5.10: Representative (a) surface separation, D, (top plot) and shear force, F_S,(bottom plot) as a function of the normal force, F_N, across a 1.4M [$C_4C_1P_{yrr}$][TFSI]-PC mixture. Bottom plot: F_S with increasing F_N is shown in blue. The obtained μ are shown: μ = 0.019 for layer (iv), μ =0.16 for (v), μ = 0.14 for (vi), and μ - 0.11 for (vii). The vertical dashed lines in (a) highlight the simultaneous discrete steps in surface separation and shear force with normal force. (b) Lateral friction signal, F_L, as a function of time in layer (i), with and without a smoothing filter in blue and black, respectively. The signal within the pink box is shown in (c) highlighting the viscous, liquid-like lateral friction signal that relaxes between the elastic and plastic regimes (pink lines) with time, $\tau \approx 0.3$ s. A dark blue line is plotted on-top to represent ideal Newtonian behaviour.

load is increasing, the magnitude of the friction forces increases with magnitude, see Figure 5.9(c). The average lateral force in the different layering regimes increases from F_L = 1.1 to 2.4 to 7.3 to 12.8 to 40 as the separation decreases from D = 3.58 nm to 3.17 nm to 2.67 nm to 2.14 nm to 1.56 nm. This overall increase in the magnitude with increasing confinement has previously been seen and two causes have been posited. First, it may due to the greater inter- and intra-layer ordering

nearer the mica surface that is believed to increase the activation barrier to sliding across the film, or secondly, there may be change in the active shear plane.

As the friction coefficients in this system remain relatively constant between the different layering regimes, the first reason is more likely. If the relationship between confinement and lateral force magnitude was indeed due to a change in the shear plane, the friction coefficients would differ between the layers. Therefore, the 1.4M does exhibit behaviour that is qualitatively similar to that expected for a simple viscous liquid.[74–76]

0.5M [$C_4C_1P_{yrr}$][TFSI]**-PC**

The lateral forces of the 0.5M [$C_4C_1P_{yrr}$][TFSI]-PC system is shown in Figure 5.11. In the 0.5M system, when the surfaces are brought close together, the random vibrations persist down to D= 3.53 nm, this corresponds to point (vii) ($i = 7$), see Figure 5.11. At this surface separation, the lateral force profile begins to adopt a periodic shearing cycle, see Figure 5.11(a). Upon further compression to D= 3.19 nm($i = 6$), the signal adopts a stick-slip profile, see Figure 5.11(a).

As we compress the film further while applying a shearing motion, stick slip persists, and becomes more clearly defined. However, in both the 3.5 nm and 3.19 nm layer, there is no clear yield point.

At 2.75 nm layer ($i = 5$, (v)), when starting to apply v_l= 639 nm/s, F_L exhibits a linear variation of slope K_s x v_l, then a relaxation of τ= 0.3 s then smooth sliding creep of 0.09 mN, see Figure 5.12(c). While stick slip friction is also present, while we do not see a yield point at $F_{S,y}$, there is a series of discrete stiction peaks where the force varies between a minimum of $F_{S,k}$ at the stick point a maximum of $F_{S,st}$ at the slip point.

However, as we continue to shear at the same surface separation of 2.75 nm the response now becomes increasingly characteristic of a liquid confined between two

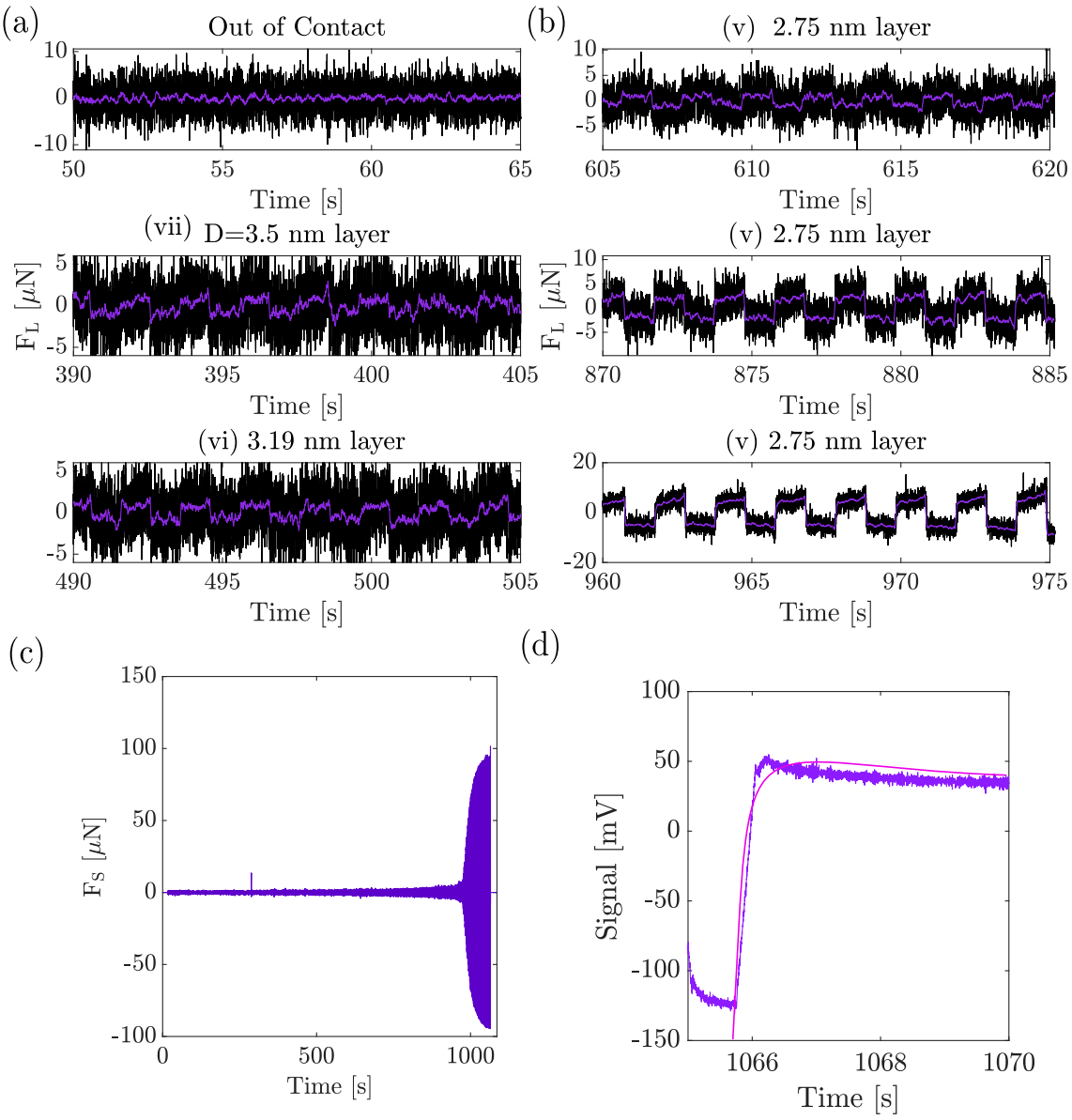


Figure 5.11: Representative Lateral forces, F_L in 0.5M [$C_4C_1P_{yrr}$][TFSI]-PC film, as a function of time, with and without a smoothing filter in purple and black, respectively. Three different friction regimes are observed in (a) and (b) and are labelled in Figure 5.12(a). (c) Temporal evolutions of the lateral force F_L, when moving the top surface with the piezoelectric tube at a normal velocity of $v_n = 0.5$ nm/s and v_l of 641 nm/s and (d) response of the film when the lateral motion is stopped.

surfaces, and instead of stick-slip friction we see smooth sliding, and before the direction of shearing is reversed, a sharp stopping peak is seen.

With a normal applied load of 60 μN, see Figure 5.12(c), the surfaces compress by 0.1 nm and the shearing response drastically changes. The lateral force magnitude rises from $\approx$ 1 μN to $\approx$ 50 μN. The lateral force signal at this distance shows that

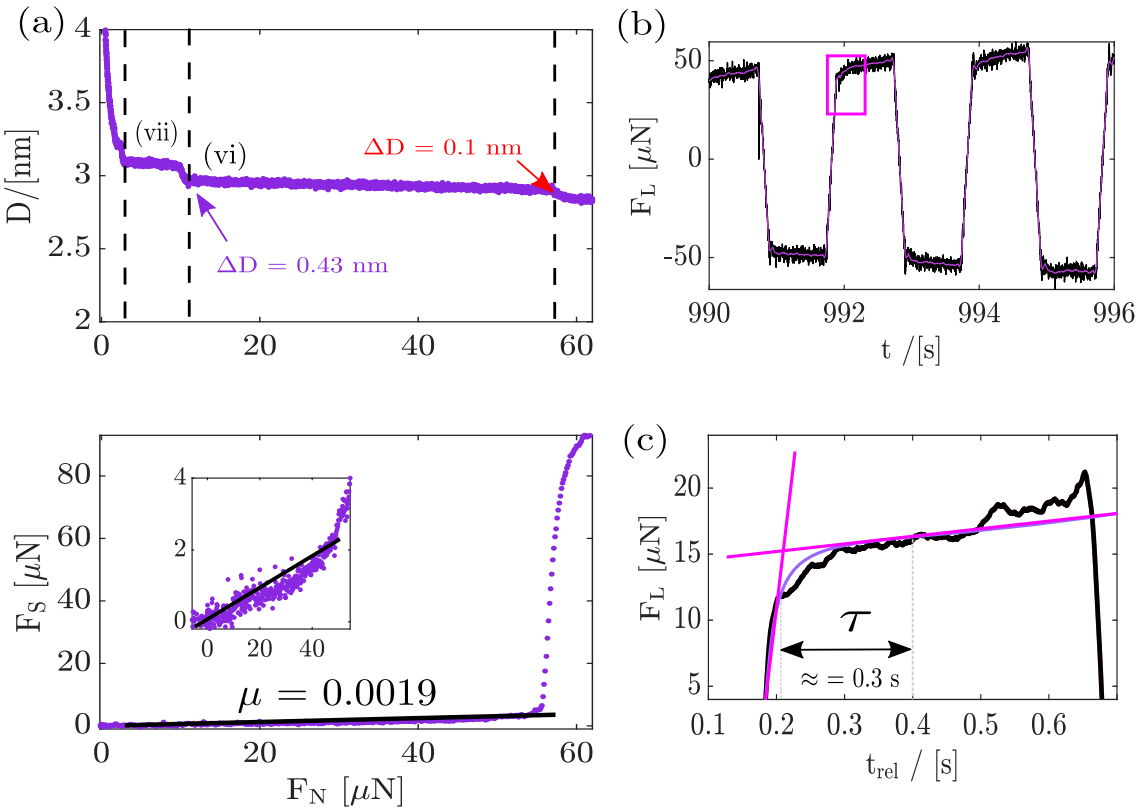


Figure 5.12: Representative (a) surface separation, D, (top plot) and shear force, F_S,(bottom plot) as a function of the normal force, F_N, across a 0.5M [$C_4C_1P_{yrr}$][TFSI]-PC mixture. Bottom plot: F_S with increasing F_N is shown in purple. The obtained μ is shown as μ =0019. The vertical dashed lines in (a) highlight the simultaneous discrete steps in surface separation and shear force with normal force. (b) Lateral friction signal, F_L, as a function of time in layer (i), with and without a smoothing filter in purple and black, respectively. The signal within the pink box is shown in (c) highlighting the viscous, liquid-like lateral friction signal that relaxes between the elastic and plastic regimes (pink lines) with time, $\tau \approx 0.3$ s. A dark blue line is plotted on-top to represent ideal Newtonian behaviour.

liquid-like sliding is present, with the stopping peak seen once more, see Figure 5.12(c). Therefore, like the 1.4M, the 0.5M system does exhibit behaviour that is qualitatively similar to that expected for a simple viscous liquid.

Pure Propylene Carbonate

The lateral forces present in a pure condensed film of PC is shown in Figure 5.13.

As we compress the film further while applying a shearing motion, stick slip persists, and becomes more clearly defined. In the pure PC, when starting to apply a constant $v_l = 639$ nm/s, the lateral force exhibits first a linear variation of slope k_L x v_l, then

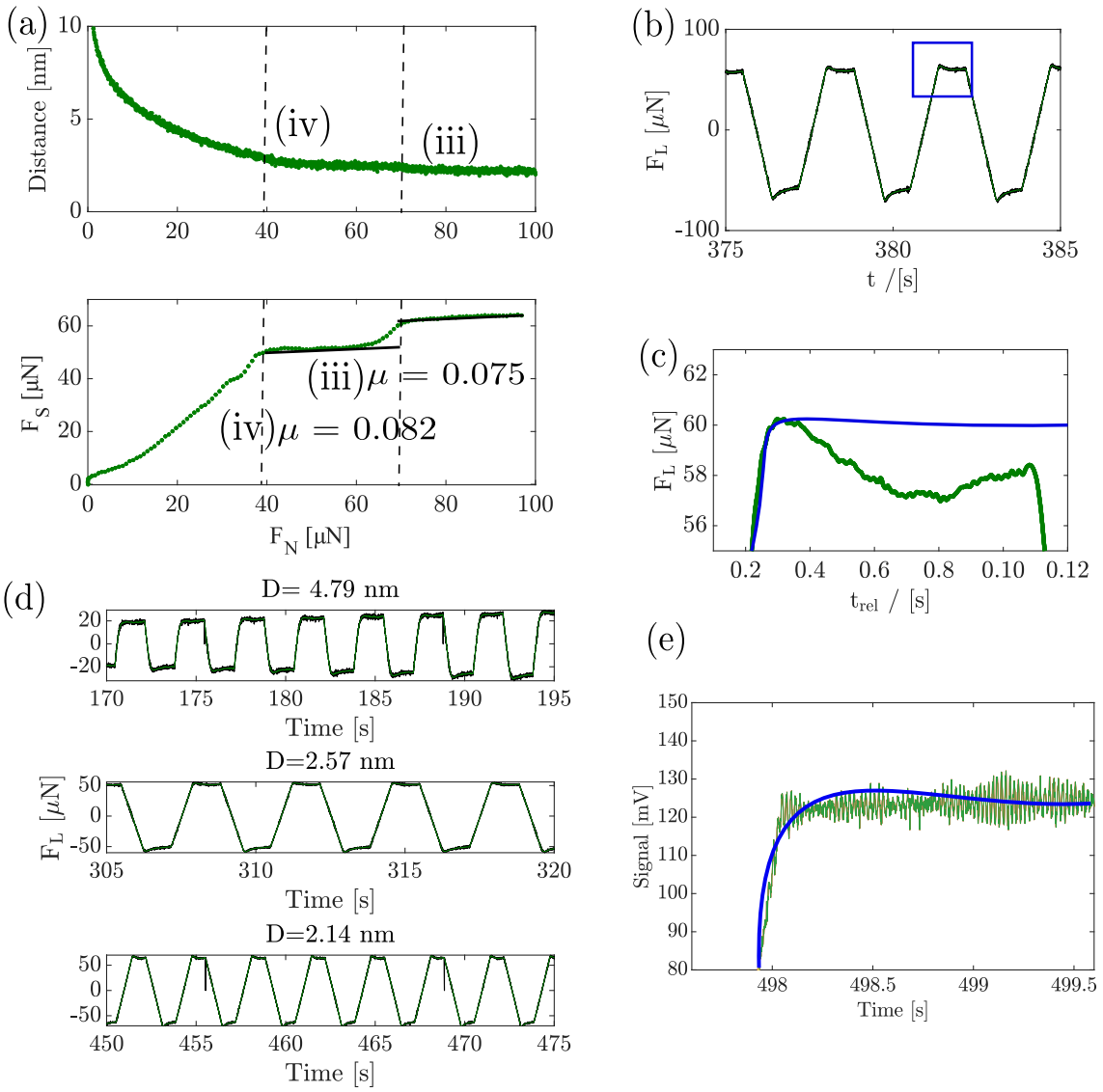


Figure 5.13: Representative (a) surface separation, D, (top plot), and (bottom plot) shear force, F_S as a function of the normal force, $F_N.f_S$ with increasing F_N is shown in green across pure PC. Three friction regimes are observed in (a), and the out of contact, layer (iv) and (iii).The corresponding lateral friction signals are indicated with the same labels in (d),the friction in layer (iv) is $\mu = 0.075$, and in layer (iii) is $\mu = 0.082$. (b) Lateral friction signals, F_L, at 380 s, in layer (iii) as a function of time, with and without a smoothing filter in green and black, respectively. The signal within the blue box is shown in (c) highlighting the sea-saw profile that develops. A dark blue line is plotted on-top to represent ideal Newtonian behaviour. (d) Lateral friction signal, F_L, as a function of time in the film at various confinement lengths, with and without a smoothing filter in green and black, respectively. (e) The response of the film when the lateral motion is stopped.

a yield point $F_{S,y}$ is observed. After the yield point,there is a rapid levelling off of the force to its kinetic value, where smooth sliding is seen. At this point, there is minimal smooth sliding creep, or is at least below the resolution of our experimental

setup.

In Figure 5.13(c), the relationship between lateral force and time, at time 992 s, does exhibit a linear variation of slope k_L v v_l, which relaxes rapidly to a kinetic sliding force, $F_{S,k}$ before once more increasing before the stopping point. When the lateral motion is stopped, Figure 5.13(e), the film shows a slight viscous relaxation.[68]The PC film studied does overall behave like a simple molecular liquid, and our obtained friction coefficients for (iv) and (iii) are quite close.

5.4.1 | Breakthrough point

In the experimental results shown for the 1.4M [$C_4C_1P_{yrr}$][TFSI]-PC film in Figure 5.14, there is a negative linear relationship between F_S and F_N in layer (iii) and overall unstable film behaviour . This is also the case in the friction force profiles obtained from measurements conducted on the 0.5M system. This is an interesting finding as this behaviour would not be suitable for any boundary lubricants.

The profiles shown in Figure 5.14 are representative of those obtained for the 1.4M and the 0.5M system, and are shown in Figure 5.15(a) and (b), respectively. These profiles show that when the surfaces reach their maximum compression for that particular run, and accesses the (iii) layer which is found at $\approx$ 1.50 nm, the magnitude of F_L sharply jumps, before levelling off as shearing motion is continued. This results in a negative linear relationship between F_N and F_S at this layer. In the 1.4M [$C_4C_1P_{yrr}$][TFSI]-PC system, when this point is reached, the F_L rises from $\approx$ 25 μN to 40 μN, see Figure 5.13(a). Figure 5.15(a) shows how this transition happens in real-time during the measurement. As seen in Figure 5.14(a), a sharp stopping point marks the transition from (iv) to (iii), and there is no initial yield point seen in that transition cycle. This single cycle is characteristic of a liquid film compressed between two sliding surfaces, and deviates from the overall trend of this system whereby a liquid to solid confinement was implied by the changing friction traces. However, beyond this point, we can infer that the film once more

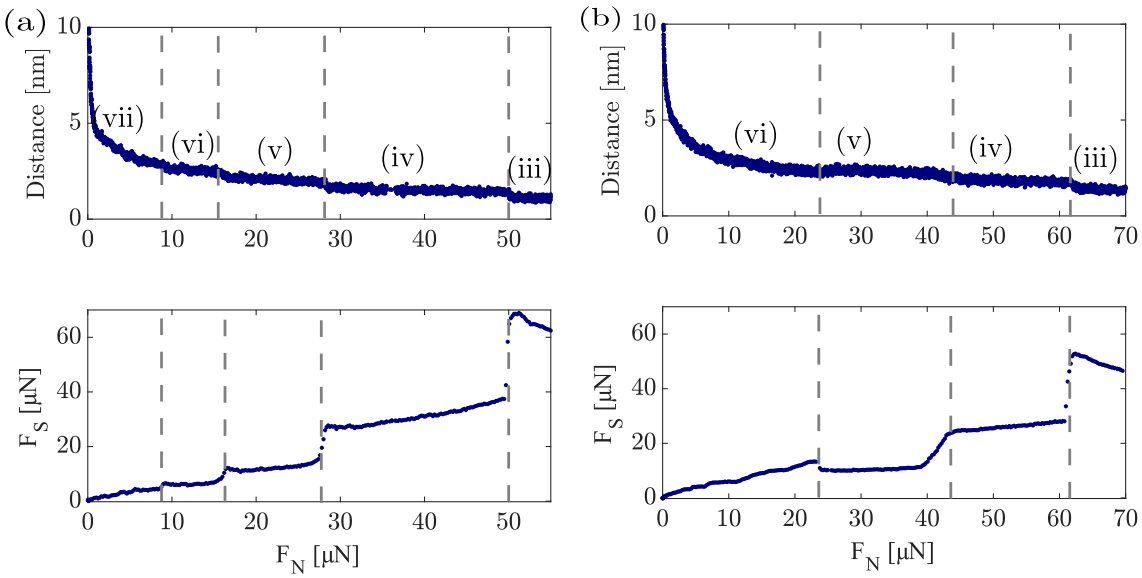


Figure 5.14: Representative (a) surface separation, D, (top plot) and shear force, F_S, (bottom plot) as a function of the normal force, F_N, Bottom plot: F_S with increasing F_N is shown in dark blue, across (a) 1.4M film and (b) 0.5M film

adopts a solid-like structure during this shearing cycle, which is a continuation of the films liquid-like behaviour in (v) and (iv), and we observe the sea-saw profile which has both an initial yield point and a stopping point. Similarly, in 0.5M, when the transition point is reached, the F_L rises from $\approx$ 25 μN to 50 μN, see Figure 5.14(b). Figure 5.15(b) shows that this transition once more has a friction cycle that is more characteristic of a liquid, where there is no yield point but instead a sharp stopping point. Similarly to the 1.4M system, this single cycle departs from the overall trend where the 0.5M film showed a general liquid to solid transition with increasing confinement, which resulted in sea-saw profiles at the $i = 3$ layer, see Figure 5.9(b)

The brief transition takes place at the i= 3 film, where there are three layers of the mixed cation-anion-PC system, leading to a film thickness at $\approx$ 1.50 nm.

This sharp transition that leads to the negative F_S v F_N relationship may be a result of the ongoing transition into a solid-like film. In both Figure 5.15(a) and (b),the transition cycles both show a 'stopping' peak which has been proposed in previous studies to be a result of a freeze-melt transition brought on by the decrease

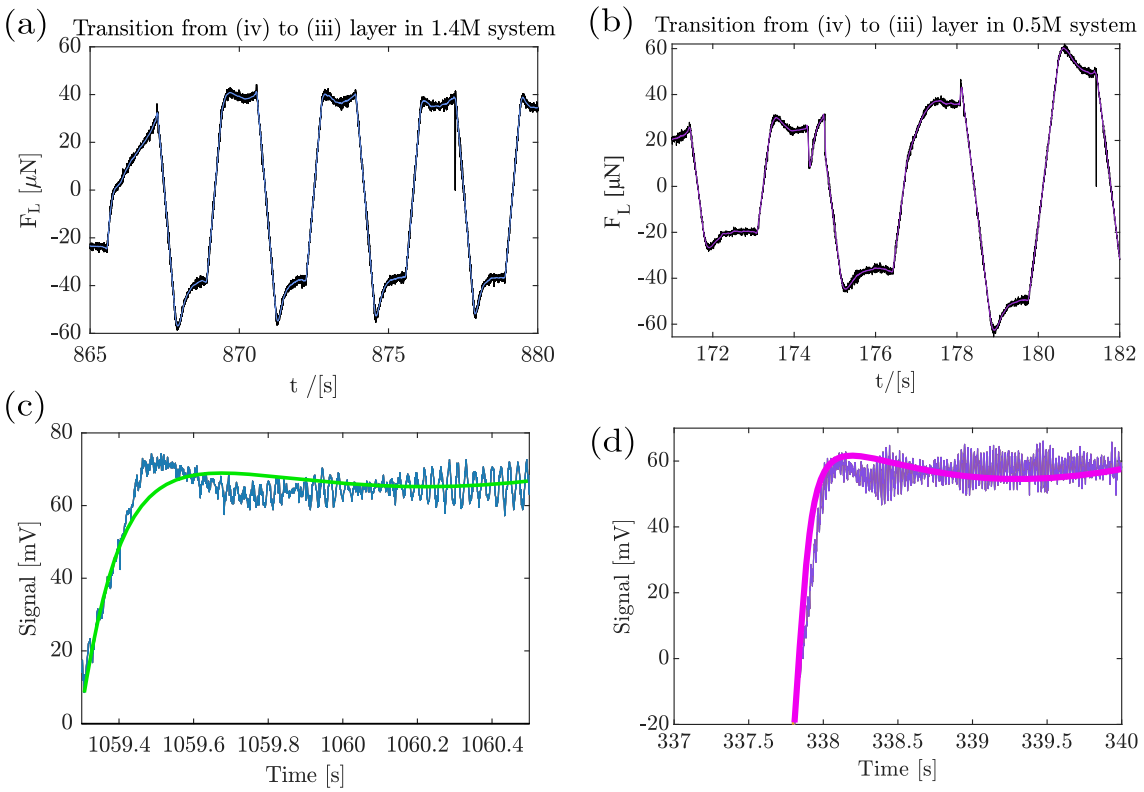


Figure 5.15: (a) and (b) Lateral friction signal, F_L, as a function of time in the 1.4M (blue) and 0.5M film (purple) at the transition point from layer (iv) to (iii), with and without a smoothing filter in black. (c) and (d) The response of the film when the lateral motion is stopped.

in relative velocity.[207,213] As discussed, this system is viscous, with a η of 74 mPa s reported for pure [$C_4C_1P_{yrr}$][TFSI], and it is likely that the effective viscosity, η_{eff} of the confined film is much higher at our nanoscale confinement.

5.4.2 | Effect of Shearing Velocity

In this section we briefly consider the influence of the shearing velocity on the friction force. To investigate this, we have sheared the liquid under constant conditions in the normal direction, exploring three decades of lateral velocities. The liquid was studied at v_l= 639 nm/s, v_l = 1918 nm/s and v_l = 3917 nm/s, and the results shown in Figure 5.16.

A liquid-like friction behaviour is obtained for all the friction loops, with the films showing a relaxation instead of a yield point at the start of a cycle. Furthermore, the

kinetic friction force (the plateau of the shearing cycle) increases monotonically with the shearing velocity, once more showing the viscous behaviour of the film.[103,213] At

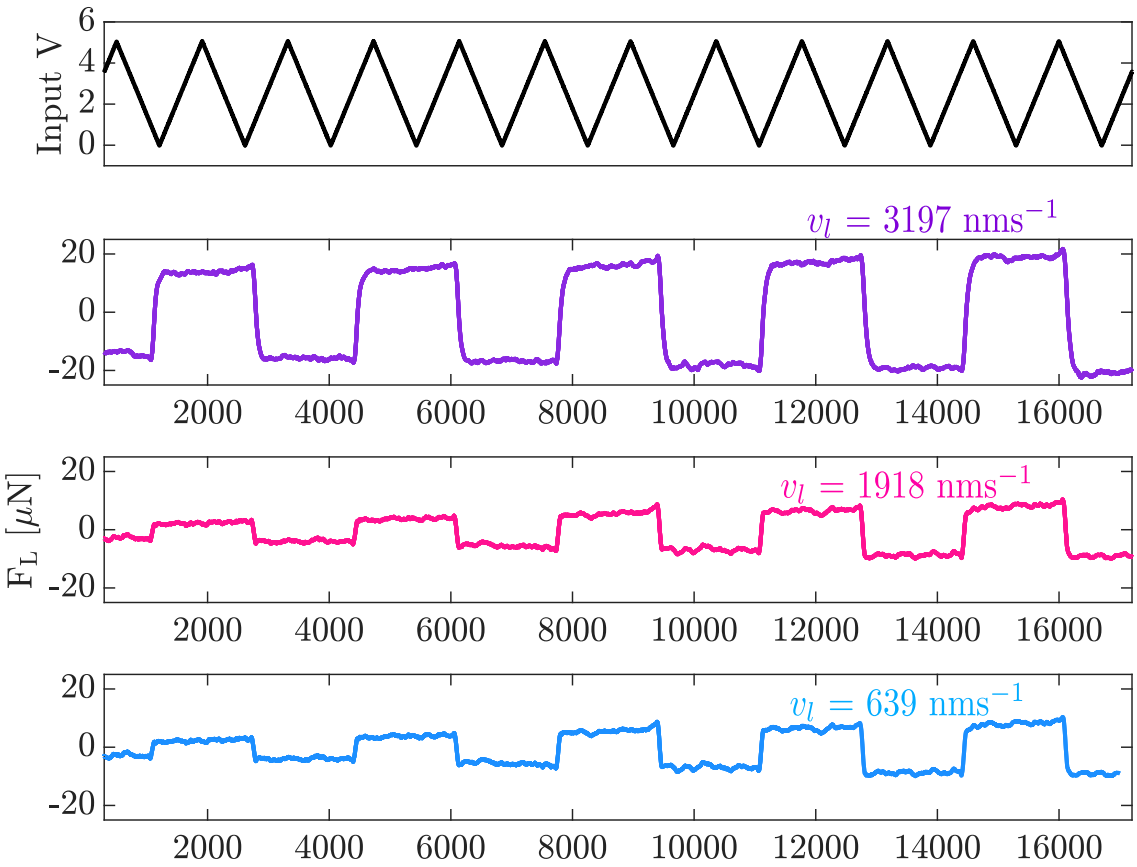


Figure 5.16: Friction cycles, showing F_L at a constant film thickness of $i = 4$, while trying to control F_N. Three decades of velocity are measured, $v_l = 639$ nm/s, 1918 nm/s, and 3197 nm/s.

low v_l, shearing of the film progresses by way of a relaxation of timescale $\tau = 0.3$ s, which is followed by smooth kinetic friction sliding (Fig. 5.16(a) and (b)) which have a yield point at the beginning of each cycle.

At higher v_l, a sharp yield point is now seen at the beginning of the trace and is accompanied by a 'stopping' peak . This is consistent with the overall change seen when the (iii) layer was sheared, and the 'sea-saw' profile is now present.

5.4.3 | Friction Coefficients

As mentioned above, in all of the solvent-dominant [$C_4C_1P_{yrr}$][TFSI]-PC systems, while the friction is found to be "quantised" with the layer thickness and the applied

normal load, and exhibits a linear relationship between F_S and F_N, extracting the gradient of this relationship yields friction coefficients, μ that are overall quite similar for each experimental run.

For example, in Figure 5.8, the friction coefficients obtained for the 1.4M system are all ≈ 0.1. Table 5.2 below shows a sample of the obtained friction coefficients for 1.4M, 0.5M, and pure PC, at a shearing velocity of $v_l = 639$ m/s. From this sample, it is clear that for each experimental run (where the Radius, mica thickness, and other external parameters is assumed to remain constant), the friction coefficients remain relatively constant. The only discernable difference is that with increasing confinement, i.e decreasing distance, the friction coefficients slightly increase layer-to-layer.[68,103,213] This behaviour is very different from what was observed in the

Table 5.2: Measured friction coefficients across the solvent-dominant systems

System	i=3	i=4	i=5	i=6	i=7	i=8
1.4M	-	0.19	0.17	0.14	0.11	0.10
1.4M	-	0.19	0.17	0.11	-	-
1.4M	-	0.24	0.20	0.20	0.19	-
1.4M	-	-	0.08	0.07	-	-
0.5M	-	0.36	0.33	0.30	-	-
0.5M	-	0.002	0.002	-	-	-
0.5M	-	0.003	0.002	0.002	0.002	-
Pure PC	0.077	0.071	-	-	-	-
Pure PC	0.08	0.08	0.08	-	-	-
Pure PC	0.90	0.88	0.87	-	-	-

salt-dominant mixtures, where the obtained friction coefficients varied dramatically from layer-to-layer. Those results are also similar to what has previously been observed in studies of the pure [$C_4C_1P_{yrr}$][TFSI] system.[103]

The behaviour of the solvent-dominant systems when a shearing motion is applied is more reminiscent of the shearing response for simple liquids where the friction coefficient remains relatively constant even as different film thicknesses are sheared.[74–76,170,178,183,214]

As previous explained, relationship between applied normal load F_N and shear force

F_S in a confined nano-metre contact such as the one found in the SFB, can be described by Equation 1.2. Using Equations 1.2, 4.3 and 4.4, we can calculate F_{adh}, μ^i, a^i, and A for the 1.4M film system, and the results are shown below in Table 5.3: As we access different film thicknesses, and therefore different layering regimes, F_{adh},

Table 5.3: Load and adhesion friction coefficients for the 1.4M $[C_4C_1P_{yrr}][TFSI]$-PC film

System	i	$F_{adh}, \mu N$	$F_S^i, \mu N$	$A_o^i, \mu m^2$	**R, m**	**D, nm**	μ^i	α^i
1.4M	4	23.31	7.81	12.89	0.007	2.14	0.19	0.918
1.4M	5	10.44	3.27	10.98	0.007	2.67	0.16	1.017

D and a are expected to change. As we compress different films, the structure of these films change as more or less molecules are confined in this boundary layer, and thus the adhesive force, F_{adh}, required to 'jump out' changes and in turn the adhesive contribution to the friction force α changes.[215] These values are all dependent on the layering.[103]

In addition, the load-controlled friction contribution μ is another parameter that can be affected by the layering, if the applied load has an effect.[103] This is the case in the salt-dominant systems where the load-controlled contribution changes with each changing layer. In the solvent-dominant systems however the load-controlled contribution remains relatively constant with changing film thickness.[74–76,103,170,178,183,215]

It is clear that the inclusion of PC not only influences the structural forces present, but also the frictional forces present. The friction has gone from being dependent on layering to being independent of layering, and therefore more consistent with a simple molecular liquid.[74–76,170,178,183] Therefore, the switch in the oscillatory forces discussed in Section 5.3.2 can be linked to the 'switch' in these frictional forces.

This is an important finding as it shows that when mixed with polar organic molecular solvents, the structural and lateral forces of our confined $[C_4C_1P_{yrr}][TFSI]$ films do change. As these change, the films lose that ability to mitigate friction, and we saw higher friction coefficients across the range of solvent-dominant systems studied. As mentioned above, it is unlikely that the plane of shearing is changing in these

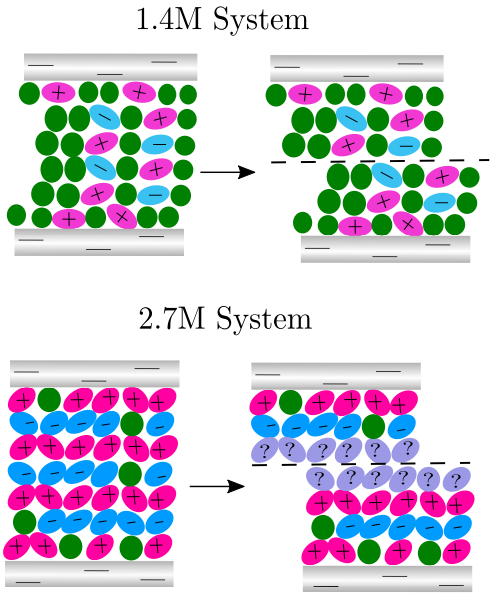


Figure 5.17: Cartoon illustrating the conclusion inferred from the lateral forces of the salt-dominant and solvent-dominant [$C_4C_1P_{yrr}$][TFSI]-PC films.

solvent-dominant films, as this is believed to influence the friction coefficient.[11,68] From these observations, we can infer that in the solvent-dominant films, there is no change to chemistry at the shearing plane. Notably, these results do not imply that the shearing plane itself remains constant, only that the chemistry at the shearing plane remains constant, as illustrated in Figure 5.17. This would imply one of two things:

1. the shearing plane is located in the middle of the film, as this is unlikely to change with increased confinement, or

2. the PC has come to dominate the structure so much that the IL no longer adopts the strict cation-anion layering that has been both reported and observed in this thesis, and instead adopts a less-ordered structure whereby it would not matter where the plane of shearing was located.

This inference is further backed up by the fact that the F_L v t traces of the solvent-dominant systems show behaviour that is overall more liquid like: (i) no clear yield point is discernable in the F_L trace, (ii) dependence on shearing velocity, and (iii) total film relaxation with an exponential timescale of $\tau = 0.3$ s.

5.5 | Summary

In this chapter, the normal and shear forces across solvent-dominant $[C_4C_1P_{yrr}][TFSI]$-PC films were studied. The normal force profiles of the 1.4M, 0.5M, and pure PC were consistent with previous studies, showing structural forces at close confinement, where the jump in points corresponded to the thickness of the film. The short-range oscillatory force was fitted for these systems, and an oscillation period of λ_{osc} of ≈ 0.50 was found for all three systems. This value closely mirrored the distance between repulsive hard walls ΔD.

With these measurements in mind, we propose that the solvent-dominant $[C_4C_1P_{yrr}][TFSI]$ is arranged in a less ordered interfacial structure than the salt-dominant films. Instead of the strict alternating monolayers of anions and cations, the dominance of the PC forces the IL molecules to sit within the PC system.[90,91]

As previously concluded, the confined films adopt even-numbered PC_{cation} PC_{anion} layers.The oscillatory period of 0.50 nm shows this, as 0.50 nm thick electro-neutral slabs are squeezed out with increasing confinement.[90,91] The proposed layering regime is shown in Figure 5.10. The decreasing magnitude of the energy barriers and the small increase in the ΔD values as D increases suggest that the layering structure softens, and becomes more disordered in ion arrangement the further away from the surfaces.

Quantised friction was also present in all the measured systems, and friction coefficients as low as 0.0019 were measured in the 0.5M system. However, the measured μ remained relatively constant from layer to layer, a result that has previously been reported in simple molecular liquids and oils.[74–76,170,178,183] This shows that the inclusion of dominant amounts of polar solvent, makes the $[C_4C_1P_{yrr}][TFSI]$ films less effective as lubricants than their pure or concentrated counterparts.

Looking to the lateral force traces showed that the confined films overall had a more liquid like behaviour than their salt-dominant counterparts. In these traces, the

clear yield points which were seen in the 3.3M and 2.7M, are no longer present, and analysis of the influence of shear velocity, and measurements of relaxation times showed that the films displayed a viscous relaxation.[11,68] These solvent-dominant films therefore continue the trend that started with 2.15M. Specifically, with increasing mol % PC content, the lateral forces begin to resemble those of a simple molecular liquid.[74–76,170,178,183] Moreover, there is evidence that the chemistry of the shearing plane does not change with increasing surface confinement, and that the boundary layers of these solvent-dominant films all show similar low friction, without the same discrete behaviour per layer that was seen in the salt-dominant systems.[55] This is an important finding for those interested in diluting neat ILs with polar solvents, as it shows that this dilution, while being cost-effective, erases the unique friction properties of these films.

We can therefore conclude that under confinement, the solvent-dominant $[C_4C_1P_{yrr}]$[TFSI]-PC films do behave more like a simple molecular liquid.

6 | Normal and Lateral Forces of $[P_{6,6,6,14}][(^{i}C_8)_2PO_2]$ Dodecane mixtures

6.1 | Introduction

While ILs seem to posses favourable characteristics for application as an excellent boundary lubricant, such as resistance to squeeze out, superlubric friction, and durability,[7,122,187,216] there is one major problem, their cost.[187] ILs are expensive to manufacture, making any large-scale industrial use of the neat systems impossible fin most cases.[7,98,99,187] However, as previously mentioned, there is now growing evidence from AFM and marcoscale experiments that minimal amounts of IL can be mixed with base oils to produce excellent lubricant films.[98–100,100,114,117,118,128,217] This route of adding minimal amounts of IL to a base oil would make ILs a suitable additive in lubricant mixtures, as these systems would be both cheap to produce and have the hallmarks of an IL boundary lubricant.[7,116,122]

However, before the use of ILs as lubricant additives can become a realistic choice for industry, three things need to be established:[7,99,122,187]

1. Is the IL miscible with a base oil ?
2. What is the IL's lubrication performance like ?
3. How much of the IL should we add ?

To answer these questions, a nanoscale study of IL-base oil mixtures will be performed, using the SFB with dodecane as the model base oil. This chapter will focus on the SFB studies of trihexyltetradecylphosphonium bis(2,4,4-trimethylpentyl)phosphinate,

$[P_{6,6,6,14}][(^iC_8)_2PO_2]$ with dodecane, while the next chapter, Chapter 7, will focus on trihexyltetradecylphosphonium bis(trifluoromethylphosphonium) $[P_{6,6,6,14}][TFSI]$ with dodecane. The macroscale behaviour of these systems will also be determined, and Chapter 8 will focus at the behaviour of multiple IL-solvent mixtures in a tribometer.

The IL studied in this chapter, $[P_{6,6,6,14}][(^iC_8)_2PO_2]$, is chosen because it has been previously studied in an AFM and TRB with other base oil systems, octane[114,118] and hexadecane,[128,217] and is a readily available and safe liquid that may well be the most appropriate potential IL additive.[100,114,116] Furthermore, when compared to the pyrrolidinium based liquid studied in Chapters 4 and 5, this phosphonium based liquid is less toxic, more thermally stable, readily available in bulk quantities, and is overall less expensive.[118,127] More importantly and more relevant to industrial use, these ILs are also oil miscible,[114,118,218] and are a suitable alternative to commonly used lubricant additives if their tribological behaviour can be determined, and eventually controlled. The structure of $[P_{6,6,6,14}][(^iC_8)_2PO_2]$ is shown below in Figure 6.1. Experiments were performed on three mixtures of $[P_{6,6,6,14}][(^iC_8)_2PO_2]$

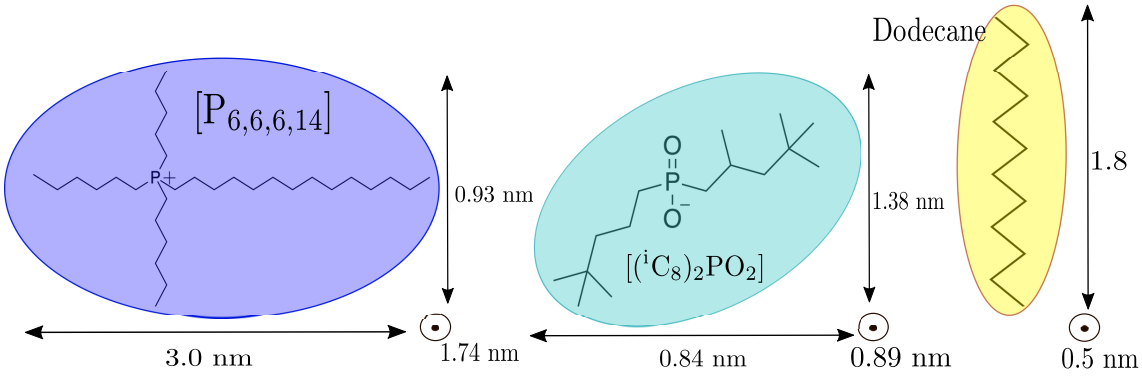


Figure 6.1: Chemical structure and sizes of $[P_{6,6,6,14}][(^iC_8)_2PO_2]$ and Dodecane. $[P_{6,6,6,14}][(^iC_8)_2PO_2]$ ion sizes are estimated from geometry, bond lengths and covalent radii, associated with the most stable configuration found by energy minimization (Molecular weight, M_w,= 805 g/mol, density ρ = 0.89 gmL^{-1}, and ion pair dimension D_m = 1.14 nm).Dodecane:(Molecular weight, M_w,= 170 g/mol, density ρ = 0.74, and molecular dimension = 0.55 nm) $[P_{6,6,6,14}][(^iC_8)_2PO_2]$ values are taken from,[218] while dodecane values are taken from.[178]

in dodecane: 50 vol % (20.7 mol %), 20 vol % (6.4 mol %) and 1 vol% (0.3 mol %).

These mixtures should allow us to see how little IL is necessary to maintain the high lubrication performance seen in the pure or 'neat' systems as moving from the pure system to 1 vol % should give us an idea of how the shear response changes with changing concentration.

In addition, two control systems were also studied: pure dodecane, and pure $[P_{6,6,6,14}][(^iC_8)_2PO_2]$. The pure IL studied in this chapter,$[P_{6,6,6,14}][(^iC_8)_2PO_2]$, is highly viscous (1058 mPa s),[77,128] and so we also investigate the hydrodynamic forces present.

6.2 | Normal Forces of $[P_{6,6,6,14}][(^iC_8)_2PO_2]$-Dodecane mixtures

Overall, the F_N/R profiles for the $[P_{6,6,6,14}][(^iC_8)_2PO_2]$ systems did not show evidence of the IL layering that was present in $[C_4C_1P_{yrr}][TFSI]$.

6.2.1 | Pure $[P_{6,6,6,14}][(^iC_8)_2PO_2]$

The normal forces in pure $[P_{6,6,6,14}][(^iC_8)_2PO_2]$ is shown below in Figure 6.2. From our F/R v D plot, we are unable to resolve the 'steps' that were previously seen in AFM study of this IL.[114,218] That paper reported average step lengths, or ΔD of 1.1 nm, which is much larger than the approximated ion pair dimension,[114,218] see Figure 6.1. However, they reasoned that the steric effects of the branched alkyl chains of phosphonium cation meant that use of a cubic packing approximation would no longer be valid.[114,218]

The lack of a structural profile may be a result of the hydrodynamic forces present in the system, see Figure 6.2(b).[78] As stated previously, $[P_{6,6,6,14}][(^iC_8)_2PO_2]$ has a viscosity of 1058 mPa s.[77,128] From Figure 6.2(b), the hydrodynamic contribution to the confined film in pure $[P_{6,6,6,14}][(^iC_8)_2PO_2]$ is present, and our fast approach velocity of 36.4 nm/s means that viscous forces obscure our profile, see Figure 6.2(d).

Interestingly, when fitting our data with hydrodynamic forces in mind, similar to the process followed in Section 5.3 in Chapter 5, we get a slip length, b, of $\approx$ 21 - 23 nm,

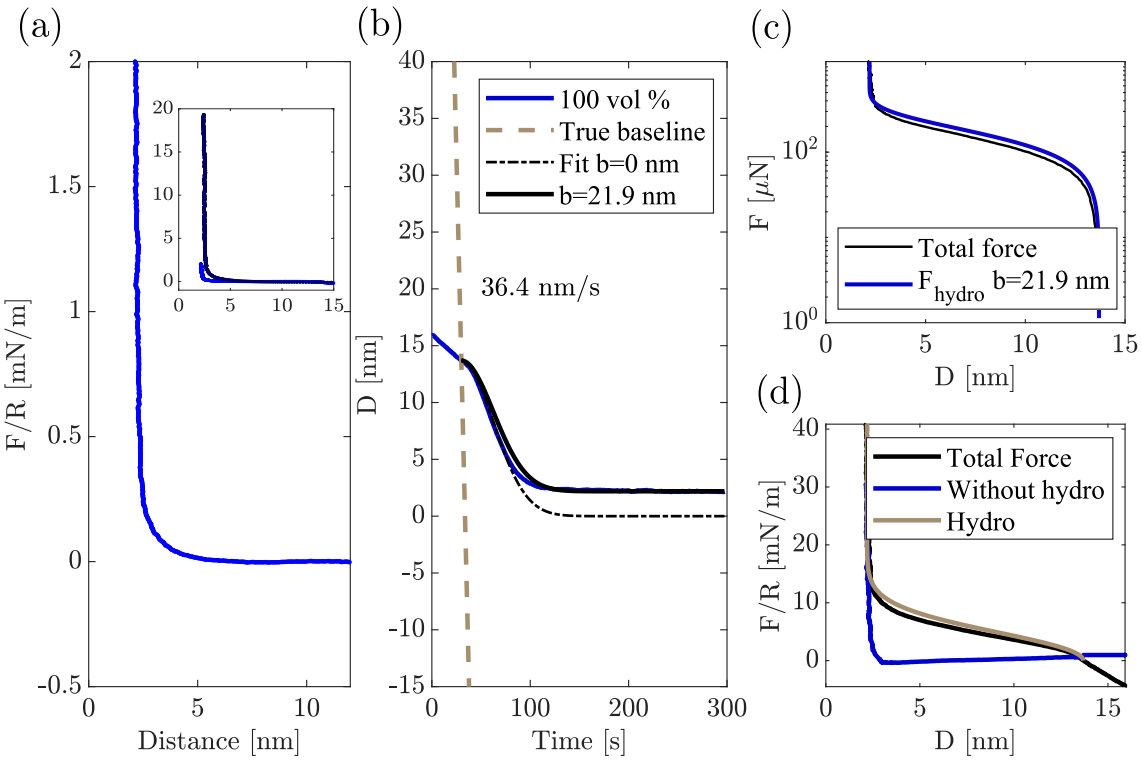


Figure 6.2: (a) Representative normal force, F_N, normalised by the radius of curvature, R, as a function of surface separation, D, measured in nm, across a confined nanofilm of pure $[P_{6,6,6,14}][(^iC_8)_2PO_2]$. Inset shows the approach (blue) and retraction (dark blue) overlayed. (b) Trajectory recorded when the top lens is moving at $v_s = 36.4$ nm/s (Piezo motion indicated by the dashed line in grey). The blue curve is the experimental signal: the black-dashed curve is the fit by the model with $b = 0$, the dark vlue curve is the fit when b= 21.9 nm. (c) Same measurements, but with data presented in terms of force, in semi-log scales.The black curve is the total force, the blue curve is the viscous contribution (when fitting with b= 7.4 nm) (d) F_N/R profile showing the total measured (black), the viscous contribution (grey), and the force without the viscous contribution (blue).

indicating a thick layer of $[P_{6,6,6,14}][(^iC_8)_2PO_2]$ on the surface that further indicates we are dealing with a hydrodynamic lubricant,[1,7] a conclusion that is backed up by the lateral forces seen in Section 6.2.

Looking at the structure of the anions and cations, see Figure 6.1,[116,217,218] however, the lack of clear structuring is not surprising. In the previous papers that used the AFM, the sharp tip meant that they were probing an area much smaller than that in the SFB, and are able to observe local structuring.,[218] whereas in the SFB, the average structure in the z direction is measured over a much larger lateral area. In the SFB, we do not observe any local structure, but we do observe a repulsive force

as we bring our confining surfaces together. In Figure 6.2 (a), this repulsive force is found at 3 nm.

6.2.2 | 50 vol % $[P_{6,6,6,14}][(^iC_8)_2PO_2]$, 50 vol % Dodecane

The normal force profile of the 50 vol % of $[P_{6,6,6,14}][(^iC_8)_2PO_2]$ in dodecane is shown in Figure 6.3, and was obtained by performing two approaches and retractions using the fine motor, without shearing. The second approach and retraction are shown

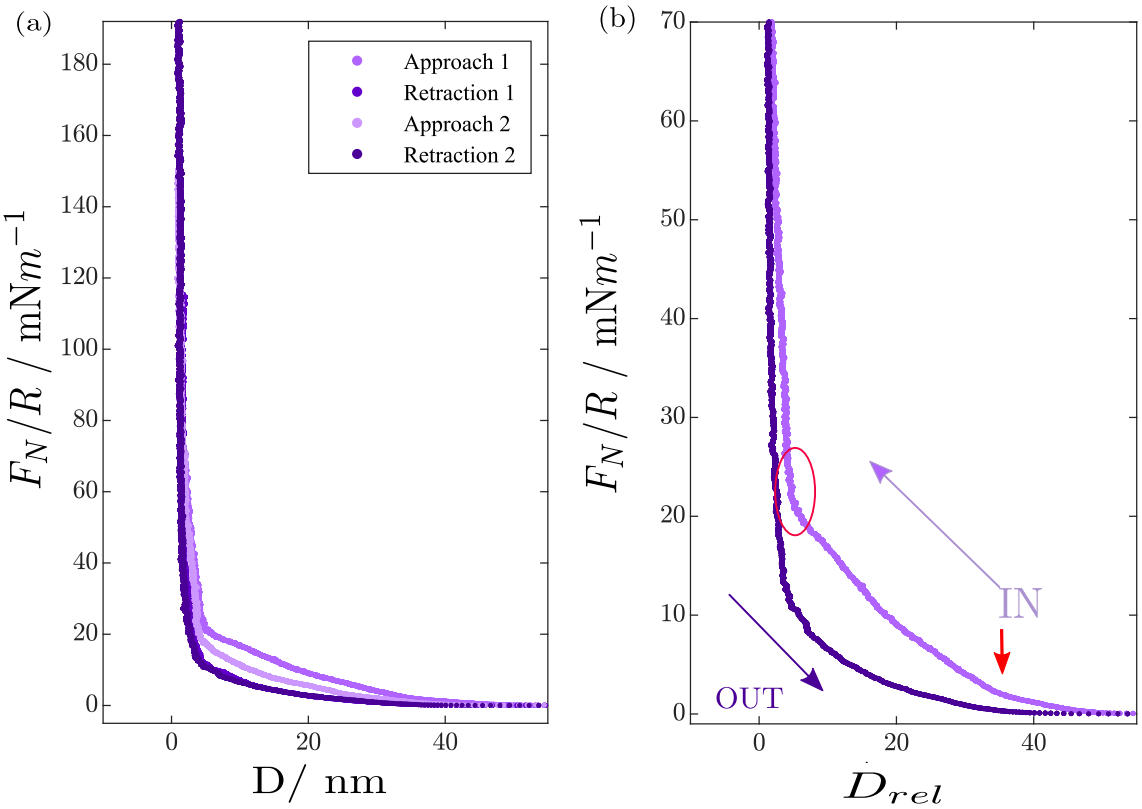


Figure 6.3: Representative F_N/R v D profile obtained from measurements across a 50 vol % of $[P_{6,6,6,14}][(^iC_8)_2PO_2]$ in dodecane.The legend shows indicates the approach and retraction profiles, and arrows indicate the direction of the lenses. (b) The approach and retraction profile with features highlighted.

overlayed at the same distance with the first to make comparison easier, see Figure 6.3(b). However, the 'zero' of distance measured in the second approach was found to be incorrect, potentially due to compression of the glue and/or mica from the first approach, or due to calibration errors. For this reason, the closest approach distance from the first run was taken as a pseudo-calibration for absolute distance

in this measurement, and so the F/R is plotted against D_{rel}.

The profiles for 50 vol % $[P_{6,6,6,14}][(^iC_8)_2PO_2]$ in dodecane show a continuously increasing repulsive force with decreasing film thickness, D. This contrasts with observations in the literature for smaller ILs, pure alkanes, and their respective mixtures.[19,90,178] Although, it is consistent with similar systems of varying concentrations of $[P_{6,6,6,14}][(^iC_8)_2PO_2]$ in octane when probed by AFM.[114,117,218]

The lack of layering observed in the 50 vol % (and the 1 vol %, see below) is likely due to the geometrically irregular long alkyl chains on both the cation and anion, see Figure 6.1. The resulting mixture of the ions' long chains and dodecane produces an amorphous structure, and we expect that instead of the discrete squeeze-out of electroneutral slabs, that continuous squeeze-out dominates. A previous study of 1 vol % $[P_{6,6,6,14}][(^iC_8)_2PO_2]$ in octane reasoned that octane disrupts the interfacial structure.[128,217]

A deflection in the spring, beginning at around 40 nm on the approach, see Figure 6.3(b), where it is circled, implies the existence of a long-range repulsion. This is because there is a favourable interaction between $[P_{6,6,6,14}][(^iC_8)_2PO_2]$ and the surfaces, as a result of the ions' interaction with the mica's negative charge, and this must be overcome to squeeze out the intervening liquid.

However, two distinct gradients can be seen in the form of the approach profile so it is appropriate to suppose two distinct processes are occurring. Firstly, the shallower gradient, from 40 nm to around 6 nm, see Figure 6.3(b), suggests a weaker interaction with the mica and could therefore be due to the squeeze-out of the non-polar dodecane from in-between the ions' alkyl chains.

At ≈ 5 nm, a shoulder followed by a far steeper gradient indicates the switch to the squeeze-out of mainly $[P_{6,6,6,14}][(^iC_8)_2PO_2]$. It interacts with the mica more strongly, despite the alkyl chains reducing the ions' charge density, thus much greater force is required. At the highest applied normal force, around 70 mN/m, it is expected

that the composition of the liquid film is mostly $[P_{6,6,6,14}][(^iC_8)_2PO_2]$. The form of the retractions is far smoother in the 3 - 10 nm range, with less sharp changes of gradient in the profile.

These features can be credited to either a Reynolds lubrication force[1] or a change in mole fraction of $[P_{6,6,6,14}][(^iC_8)_2PO_2]$ relative to the immediately preceding approach. We find that the Reynolds equation is not applicable for this case as the 50 vol % mixture is non-Newtonian: the relation between its shear properties and shear rate is not linear. This will be discussed further in Section 6.3.

Hence, it is plausible that as the lens is being retracted, the higher mole fraction of $[P_{6,6,6,14}][(^iC_8)_2PO_2]$ gives rise to different and slower dynamics on the receding profile whilst the dodecane is sucked back into the gap between the lenses. This gradual drawing of dodecane back in also fits with the lack of a kink in the retraction profile.

One of the significant problems encountered carrying out these measurements was phase separation despite dodecane and $[P_{6,6,6,14}][(^iC_8)_2PO_2]$being completely miscible as known both from our own investigations and the literature.[115,116]

Nevertheless, many experiments were ended by this apparent phase separation where two phases could clearly be seen on the lenses.[115] Consequently, one can only assume that this phenomenon was confinement-induced. This resulted in visible phase separation that had an impact on the optics of the system,see Figure 6.4(c) making measurements at the 80 vol % impossible. Thus, the confinement causes a local change in composition which drives local phase separation, and slow kinetics of equilibration cause the two phases to remain over our experimental timescales. However, using the experiments in 1 vol %, see Figure 6.6, and 50 vol %, see Figure 6.3, we can attempt to rationalise the structure of the film at the closest measured approach of $\approx$ 1.8 nm as follows:

We can use an estimated average ion pair diameter of $\approx$ 1.1 nm/ion pair, estimated

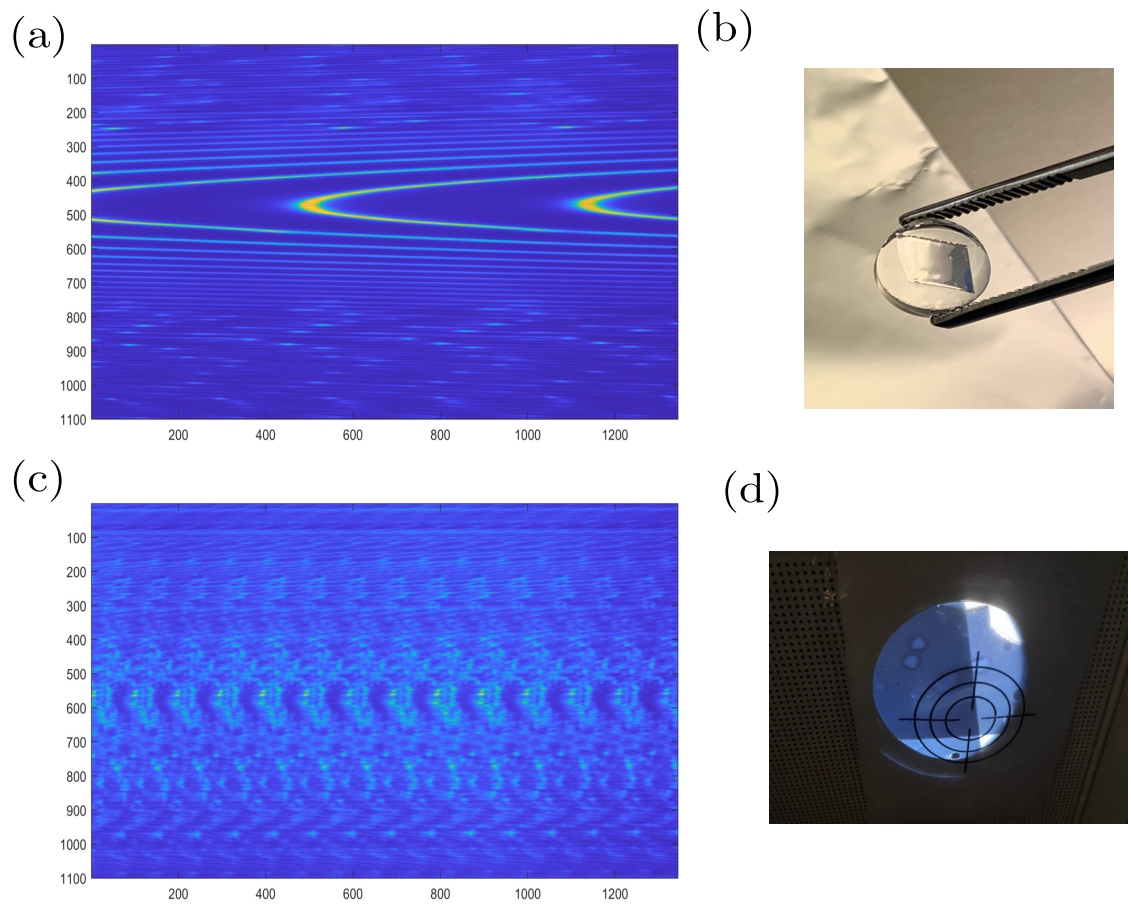


Figure 6.4: (a) Typical FECO seen during an SFB experiment. (b) Picture of lens showing visible phases. (c) The FECO seen when phases begin to form on our lenses. (d) Image of the $[P_{6,6,6,14}][(^iC_8)_2PO_2]$-dodecane phase when surfaces are in contact in the SFB.

using the following:

$$a = (\frac{N_A \rho}{M_R}) \tag{6.1}$$

where a is the mean ion pair diameter,M_r is the formula mass of the IL, N_A is Avogadro's number and ρ is $[P_{6,6,6,14}][(^iC_8)_2PO_2]$'s density. This estimated value is in line with other estimates calculated by the Gardas and Coutinho model.[46]

It has been suggested that the adsorption of an ion pair of $[P_{6,6,6,14}][(^iC_8)_2PO_2]$ is in a 'piggy-back' fashion,[114,218] with just the cation in contact with the surface due to the negative surface charge of mica; this is implied by the small area of adsorption per ion pair.[114]

Therefore, if we do in fact have pure $[P_{6,6,6,14}][(^iC_8)_2PO_2]$ at the closest approach then we can suppose that the structure of the film has a cation-anion-cation-anion-cation layering from one mica surface across to another, see Figure 6.5. This structure would give a single cation thickness of $\approx$ 0.7 nm which is comparable to the phosphonium-phosphonium $g(r)$ of 0.6 - 0.7 nm in a $[P_{6,6,6,14}][Cl]$ system, albeit with a smaller cation.[32] This would seem to reinforce the train of thought of having a

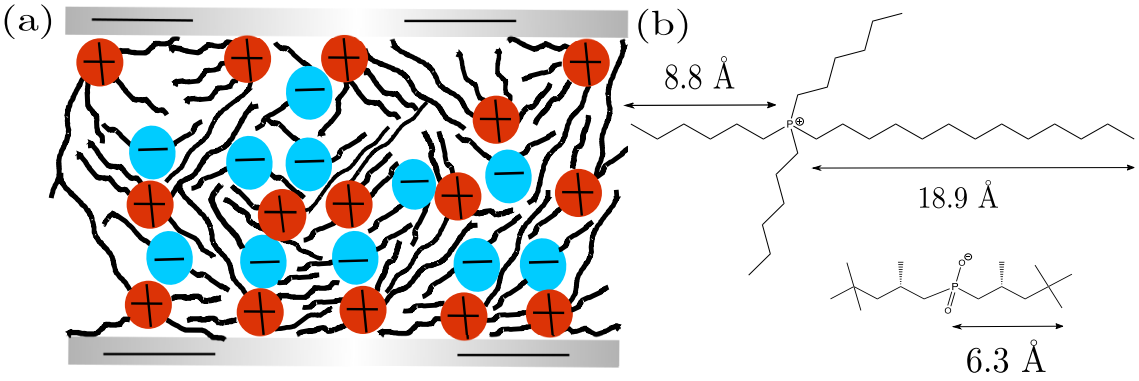


Figure 6.5: (a) Schematic illustrating the proposed nano-structure of the pure $[P_{6,6,6,14}][(^iC_8)_2PO_2]$.(b) Image showing the molecular structure of $[P_{6,6,6,14}][(^iC_8)_2PO_2]$, taken from.[217]

pure IL with a cation-anion-cation alternating structure at closest approach, and gives us some similarity to our previous $[C_4C_1P_{yrr}][TFSI]$ system.

6.2.3 | 1 vol % $[P_{6,6,6,14}][(^iC_8)_2PO_2]$, 99 vol % dodecane

The normal force profile for 1 vol % of $[P_{6,6,6,14}][(^iC_8)_2PO_2]$ in dodecane is shown in Figure 6.6. The form of the force profile of the 1 vol % of $[P_{6,6,6,14}][(^iC_8)_2PO_2]$ shows a very similar form to that of the 50 vol % mixture. The normal force applied before the shoulder in the profile is not as high, potentially as there is less $[P_{6,6,6,14}][(^iC_8)_2PO_2]$ with which the dodecane would have favourable interactions and so is easier to squeeze out. The gradient of the steeper section is very similar to the 50 vol % mixture which again suggests $[P_{6,6,6,14}][(^iC_8)_2PO_2]$ is being pushed against and some squeezed out. However, the closest approach reached is not quite as close as in the previous force profile, and the mica used for this experiment was exceedingly thick (7.74 μm) which leads to higher uncertainty in absolute distances.

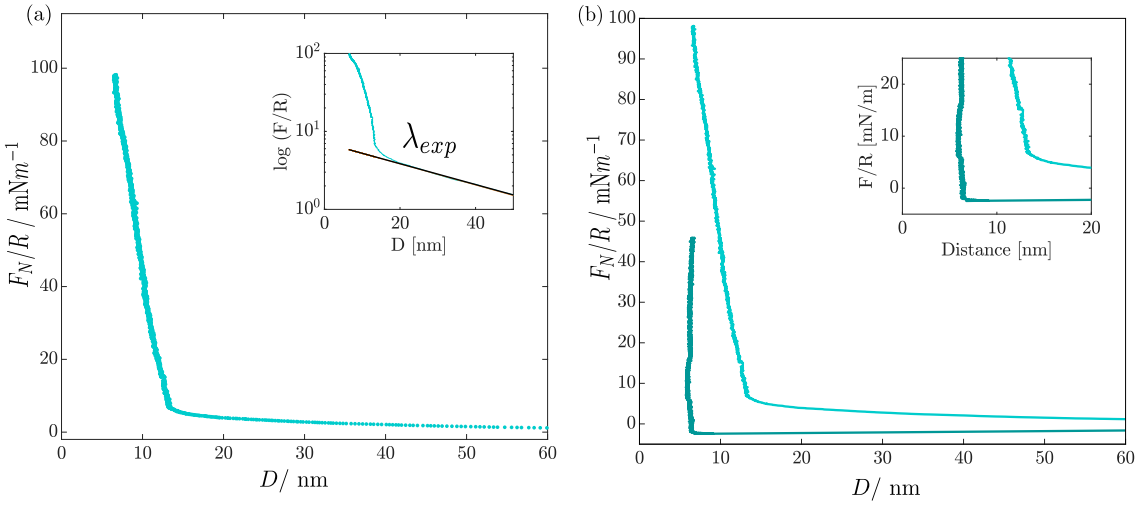


Figure 6.6: (a) Representative F_N/R v D profile across a confined film of a 1 vol % of $[P_{6,6,6,14}][(^iC_8)_2PO_2]$ in Dodecane. The inset shows the normalised force plotted on a log-linear scale against D. (b) Image showing the approach and retraction profiles obtained from the 1 vol % of $[P_{6,6,6,14}][(^iC_8)_2PO_2]$ in Dodecane

Unlike the 50 vol % retraction, the retraction for the 1 vol % shows a negative F/R at 6 nm. It must be noted that this negative force is interpreted as an adhesive force holding the lenses together: the leaf spring is bent upwards as the lenses stick together until suddenly they jump apart.[78] Pure dodecane, see Figure 6.8 and previous studies,[178] exhibits adhesion upon retraction, hence, these adhesive retraction dynamics can be attributed to the significantly higher dodecane content of the mixture.

In a previous specular neutron reflectometry study on 2 mol % $[P_{6,6,6,14}][(^iC_8)_2PO_2]$ in octane at an SiO_2 surface,[217] they investigated the composition of the 8 Å (0.8 nm) boundary layer. After synthesising $[P_{6,6,6,14}][(^iC_8)_2PO_2]$ with deuterated cations, instead of finding a boundary layer composed solely of cations, they instead found a mixed layer system at 60°C and 80 °C.They also did measurements at 25 ° C, but this had high level's of uncertainty, and strangely found a 1:1.4:1.4 ratio for cation: anion: octane.[217] The studies at 60 °C and 80 °C were more reasonable, and found a 2:1:1 ratio of cation:anion:octane in that 0.8 nm boundary layer, which would lead to a boundary layer structure that resembles Figure 6.7.[217] Figure 6.7 is a graphical representation of what this would look like in our 1 vol % $[P_{6,6,6,14}][(^iC_8)_2PO_2]$, 99

vol % dodecane sysem.

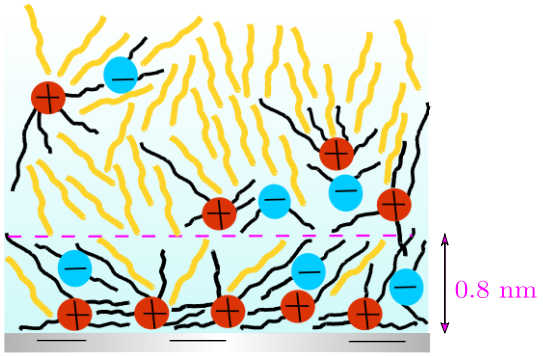


Figure 6.7: Schematic illustrating the proposed structure of the 1 vol % of $[P_{6,6,6,14}][(^iC_8)_2PO_2]$ in Dodecane when confined in a nanoscale contact in the SFB.[217]

6.2.4 | Pure Dodecane

The F/R v D profile of pure dodecane is shown in Figure 6.8. This is a system that

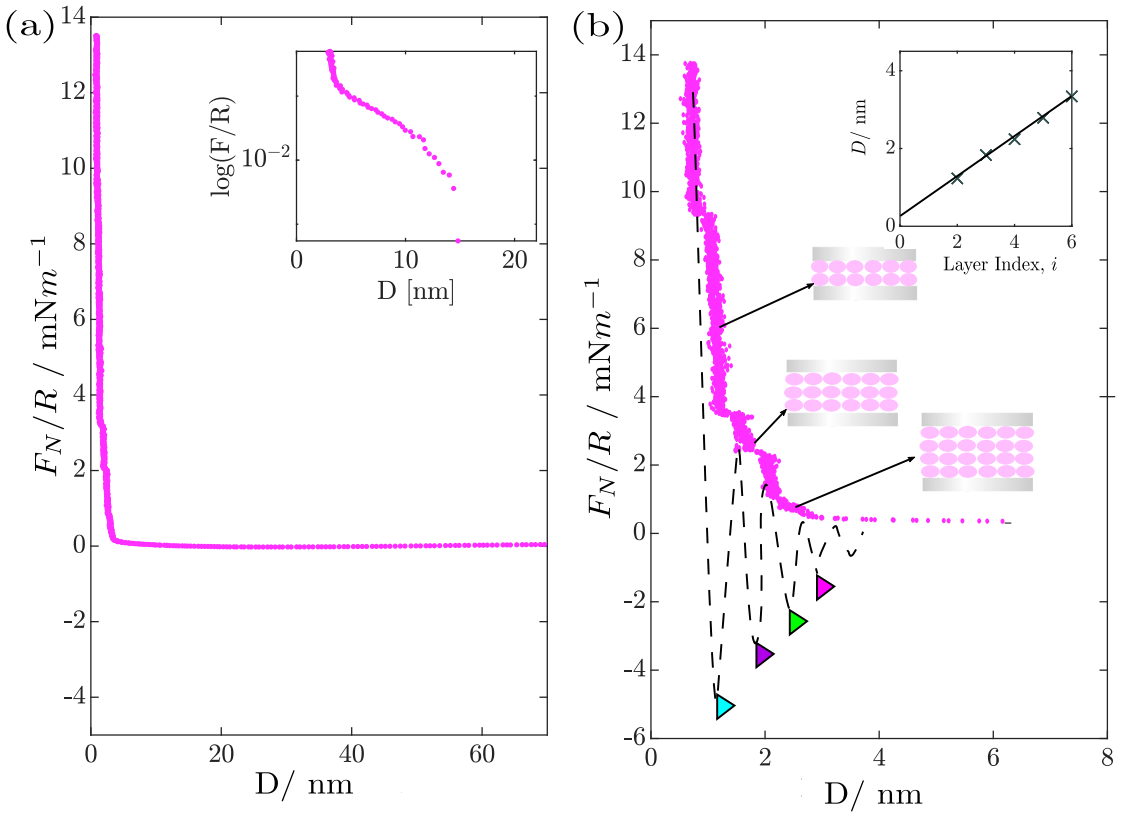


Figure 6.8: (a) Representative F_N/R v D profiles obtained across a pure dodecane film. (b) Close-up of an approach profile with the oscillatory force (black dashed line) plotted which was calculated by obtaining the λ_{osc} (seen in the inset) and the ξ. Cartoons depicting the proposed dodecane layering is shown.

has previously been studied using the SFB,[178] and our results match those previously reported. In pure dodecane, we saw an oscillatory-like relationship between F/R and distance, and we compute the wavelength of the oscillation, λ_{osc}, of 0.50 nm. This is consistent with the width of dodecane, and this indicates that the molecules lie parallel to the mica surface.[178] As we get in to close distances, D < 10 nm, we see repulsive hard walls where stable layering regimes of the pure dodecane are formed. The distance between these successive repulsive walls is $\Delta D = 0.51$ nm across the experiments.

Extracting the oscillatory force law for dodecane leads us to obtain a λ_{osc} of 0.50 nm, indicating that the 'squeeze out' layers are single dodecane-thick films.[178] This result has previously been reported on the SFB,[178] and previous experiments on similar molecular liquids show that these liquids 'layer' in single repeating units, as shown in Figure 6.8(b).

6.3 | Lateral Forces of $[P_{6,6,6,14}][(^iC_8)_2PO_2]$-Dodecane mixtures

We now study dry mixtures of confined $[P_{6,6,6,14}][(^iC_8)_2PO_2]$and Dodecane under confinement when a shearing motion is applied across the films.

6.3.1 | Pure $[P_{6,6,6,14}][(^iC_8)_2PO_2]$

The lateral forces in the 100 vol % $[P_{6,6,6,14}][(^iC_8)_2PO_2]$ is shown below in Figure 6.9(a)-(e). In the pure $[P_{6,6,6,14}][(^iC_8)_2PO_2]$ system, we find that as the surfaces are brought closer together, the random vibrations that persist at far separation distances become damped and we begin to see periodic lateral force cycles, and an overall linear relationship between F_S and F_N begins to develop. This is consistent with a liquid-to-solid film transition, as is apparent in the 'stick slip' cycles that persist.[74,76,171]

When the surfaces are brought close together to a separation distance of 5 nm with normal applied load of 37 μN, we see a 'stick slip' cycle,[165,167,168,170,171] as

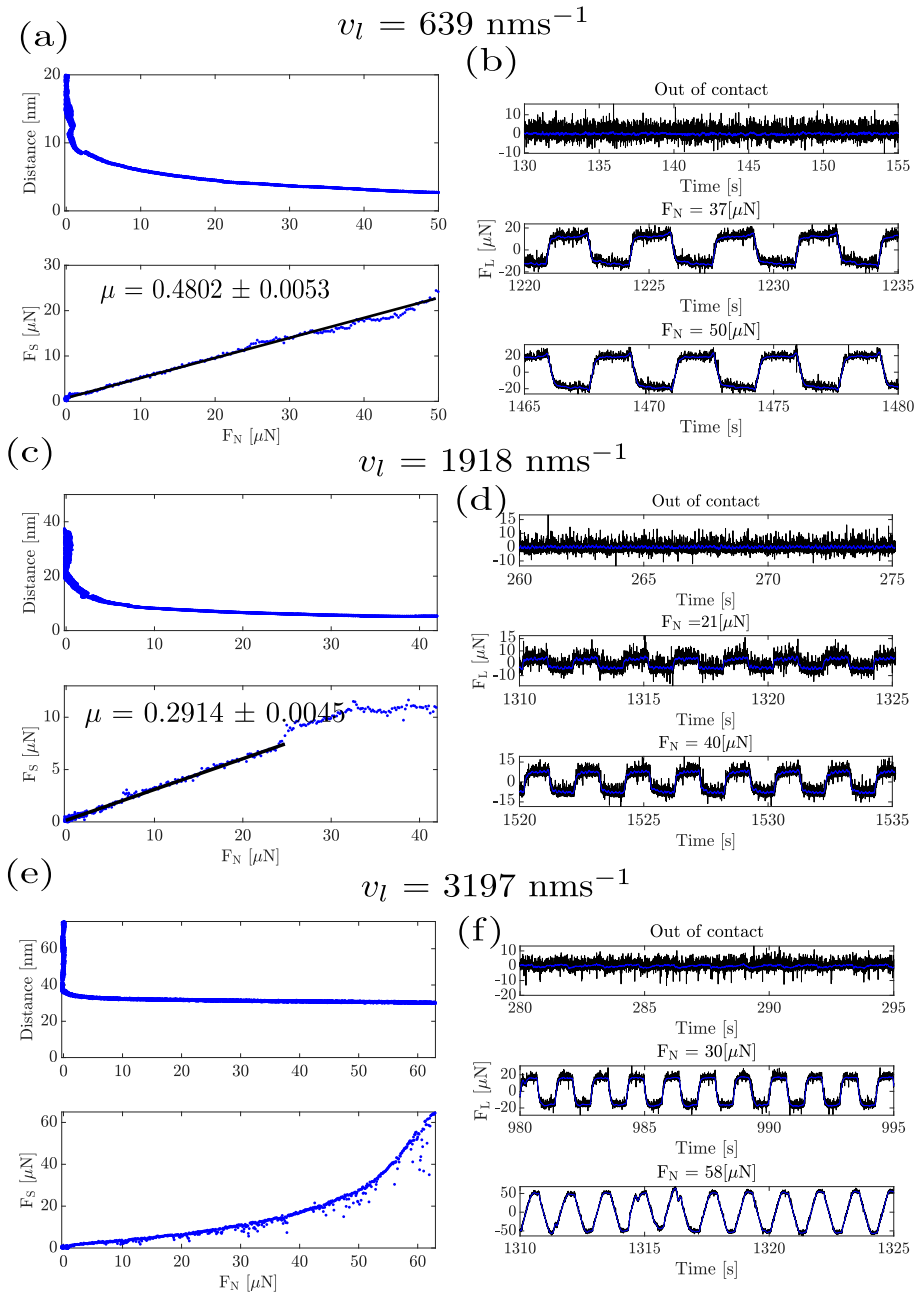


Figure 6.9: (a),(c), and (e) Representative surface separation, D, (top plot) and shear force, F_S,(bottom plot) as a function of the normal force, F_N, across a pure $[P_{6,6,6,14}][(^iC_8)_2PO_2]$ film at a shearing frequency of (a) 0.3Hz, (c) 0.5Hz, and (e) 0.7Hz. Bottom plot: F_S with increasing F_N is shown in red. (b), (d), and (f): Lateral friction signal, F_L, as a function of time with and without a smoothing filter in blue and black, respectively.

demonstrated by the sawtooth motion in Figure 6.9(b). At this distance of 5 nm, and using our understanding of how this $[P_{6,6,6,14}][(^iC_8)_2PO_2]$ may structure, this corresponds to a thick amorphous film, resembling Figure 6.5(a).

Looking now at the lateral force profiles in Figure 6.9, we can determine if the film is behaving more like a liquid or a solid. When starting to apply a constant lateral velocity, v_l = 639 nm/s, the lateral force exhibits first a linear variation of slope k_L x v_l, then a relaxation with a typical timescale of τ = 0.2 s, and there is some smooth sliding creep on the order of 0.09 mN, see Figure 6.10. When the direction is reversed the lateral force responds in a symmetric manner with respect to the horizontal axis. In this layer, stick slip friction is apparent, but there is no yield point that begins the cycle. Instead, the film relaxes exponentially with τ and is then followed by a series of discrete stiction peaks where the force varies between a minimum of $F_{S,k}$ at the stick point a maximum of $F_{S,st}$ at the slip point. Before the direction of shearing is reversed, a stopping point is recorded. Notably, the stopping point is of greater magnitude than the yield point which begins the cycle. Overall, the friction is more characteristic of a liquid.[68]

Importantly, as the normal load is increasing, the magnitude of the friction forces increases with magnitude, see Figure 6.9. However, unlike what was seen in the $[C_4C_1P_{yrr}][TFSI]$, as we do not observe layers in the force profiles, we similarly cannot attribute frictional behaviour to specific layers.

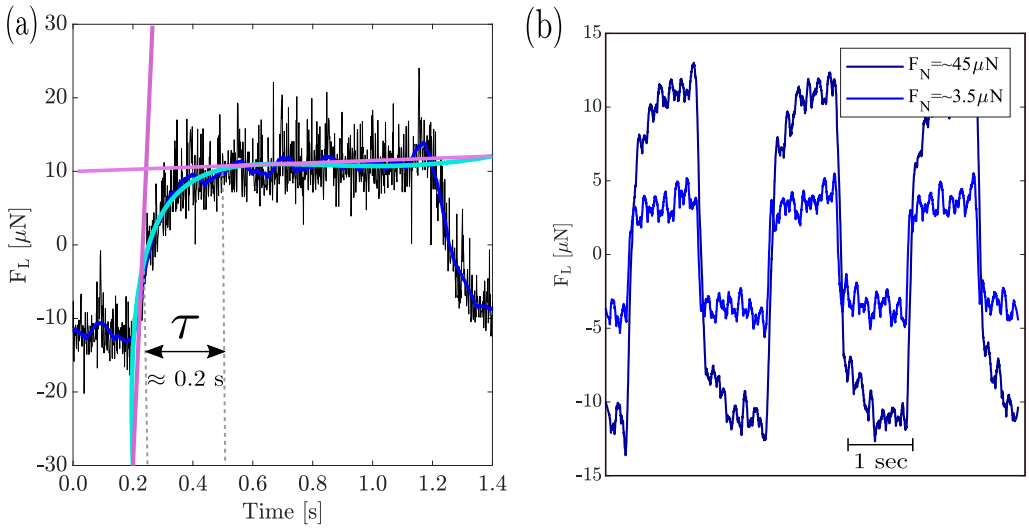


Figure 6.10: (a) Close-up of one friction cycle in pure $[P_{6,6,6,14}][(^iC_8)_2PO_2]$ at 0.7Hz (v_l = 3197 nm/s) with the relaxation profile ($\tau \approx$ 0.2 s) shown (b) Shear response traces corresponding to specified normal loads.

6.3.2 | 50 vol % $[P_{6,6,6,14}][(^iC_8)_2PO_2]$, 50 vol % dodecane

The lateral forces of the 50 vol % system are shown in Figure 6.11, where a plot of D and F_S against F_N is shown alongside the trace of the lateral response, F_L at different normal loads. Similarly to before, the coefficient of friction, μ, is given by the slope of the F_S vs. F_N plot. Initially, from normal loads of 0-7 μN, the relationship between F_S and F_N is not quite linear, resulting in very low friction. For $F_N > 7$ μ N, the relationship becomes linear, where $\mu = 0.646$. This is surprisingly high compared to the values obtained for similar systems ($\mu = 0.3$) and pure dodecane in the literature ($\mu = 0.0005$ to 0.0055).[114,178]

This is possibly due to the fact that the closest approach reached with the PZT is ≈ 4 nm, indicating that we needed much greater applied normal load to reach those inner confined layers. This is a trait that is seen in all the reported friction forces for the systems. This may indicative that we are observing a hydrodynamic friction regime rather than a boundary layer.[117,188] This inference is supported by the fact that $[P_{6,6,6,14}][(^iC_8)_2PO_2]$ is highly viscous, and our long slip lengths of 20-30 nm.[212]

An inspection of Figure 6.11(b),(d), and (f) reveals the characteristic shearing response of the confined film. At both the low and high normal applied loads, when transitioning from the elastic to the plastic regime, where the lenses begin to slide past each other, a distinct curvature is seen, reminiscent of what we would expect for a viscous liquid-like film.[68] This curvature has previously been linked to what is termed Couette Flow,[218,219] and reinforces the conclusion we are dealing with a highly viscous hydrodynamic lubricant.[218,219]

In the plastic regime, at $F_N = 52$ μN the relatively smooth plateaus observed indicate smooth sliding of our confined films. We do not see a sawtooth-like profile that would be indicative of stick-slip friction, and this further confirms the conclusion that the film is behaving like a viscous liquid. In Figure 6.12(a), the close-up of our friction cycle shows the film behaving like a liquid, similar to the pure $[C_4C_1P_{yrr}][TFSI]$ film,

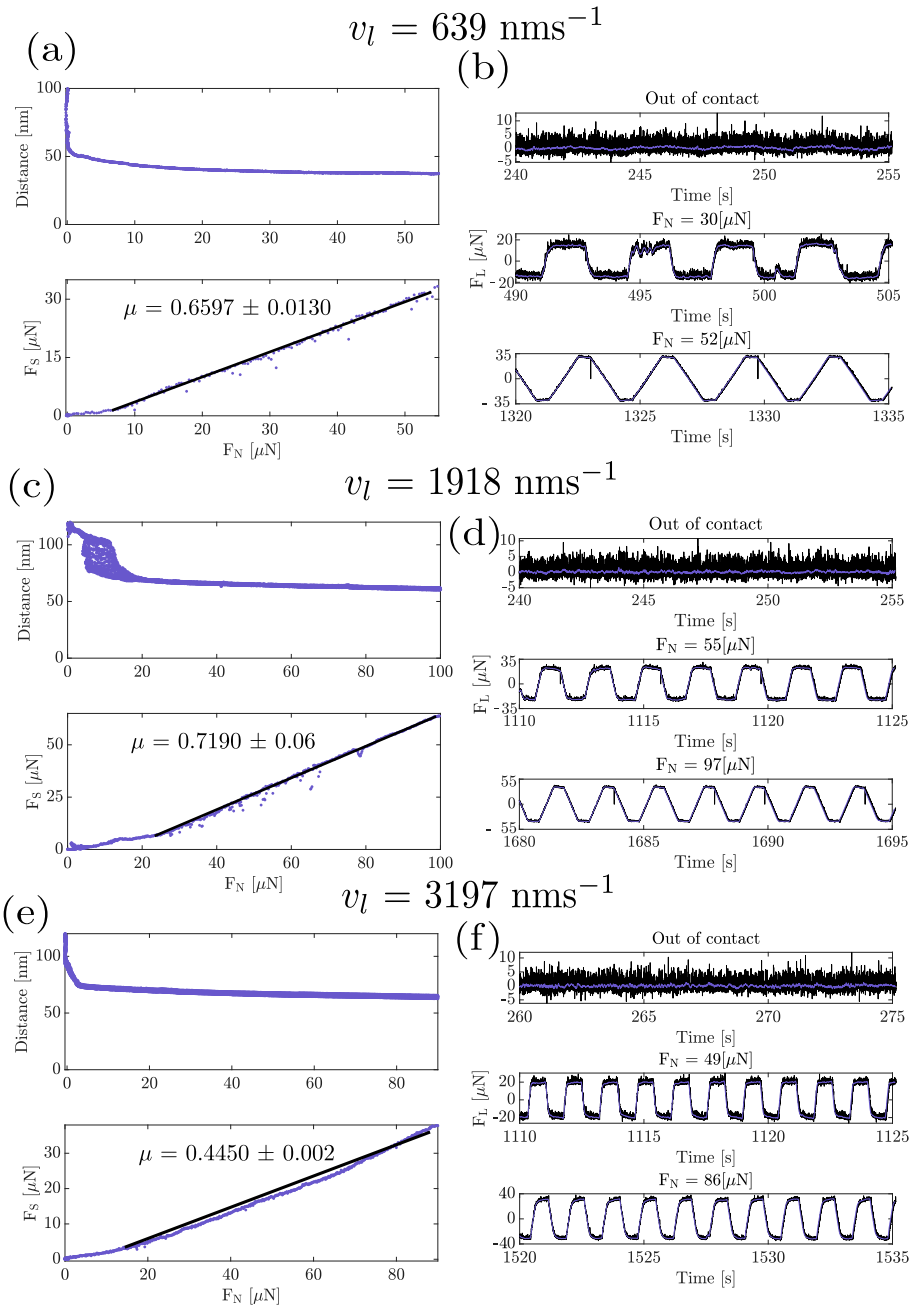


Figure 6.11: (a),(c), and (e) Representative surface separation, D, (top plot) and shear force, F_S,(bottom plot) as a function of the normal force, F_N, across a 50 vol % of $[P_{6,6,6,14}][(^iC_8)_2PO_2]$ in dodecane at a shearing frequency of (a) 0.3Hz, (c) 0.5Hz, and (e) 0.7Hz. Bottom plot: F_S with increasing F_N is shown in purple. (b), (d), and (f): Lateral friction signal,F_L, as a function of time with and without a smoothing filter in purple and black, respectively.

with a relaxation time of $\tau = 0.1$ s and smooth sliding. This behaviour remains in the 0.5Hz and 0.7Hz experiments.

However, as we change the shearing frequency, and therefore lateral velocity, the

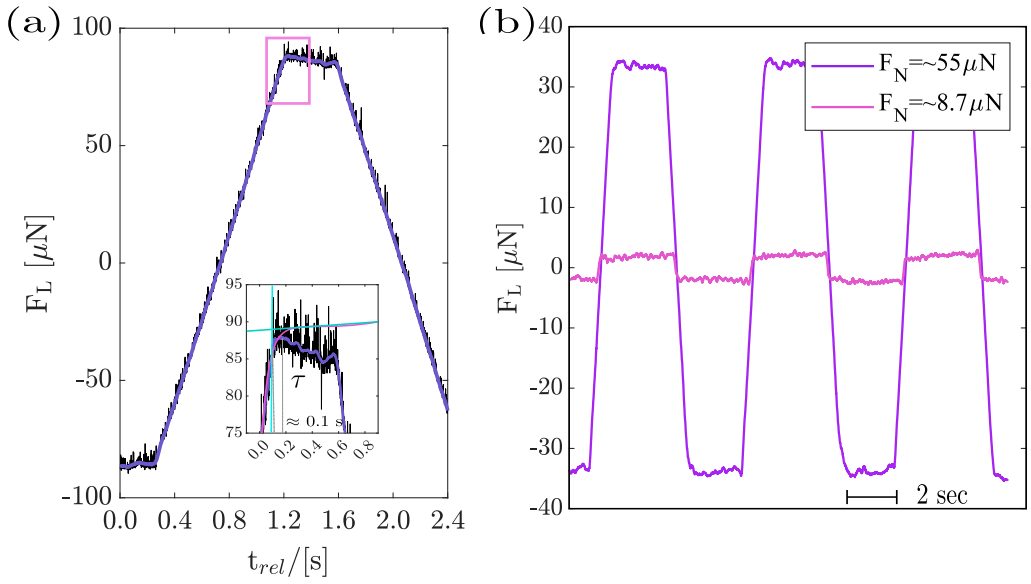


Figure 6.12: (a) Close-up of one friction cycle in 50 vol % $[P_{6,6,6,14}][(^iC_8)_2PO_2]$ in dodecane at 0.3Hz (v_l = 639 nm/s) with the relaxation profile shown in the inset with a $\tau \approx$ 0.1 s and (b) Shear response traces corresponding to specified normal loads.

coefficient of friction changed in an unexpected manner. Increasing the shear velocity from 639 nm/s to 1918 nm/s caused μ to increase to 0.719, but increasing the velocity further decreased μ to 0.445, as shown in Figures 6.11(c) and 6.11(e). This phenomenon has been previously observed by Yoshizawa *et al* in a system of dihexadecyldimethylammonium acetate, which is a surfactant with long amorphous alkyl chains, like our $[P_{6,6,6,14}][(^iC_8)_2PO_2]$.[157,170] This is called "shear-thickening", and it is where the "effective" viscosity of the liquid is generally higher than the bulk due to film -confinement,[1,157,184,220,221] suggests non-Newtonian behaviour of the film. It is related to the extent to which the long alkyl chains of the ions and dodecane are able to interdigitate, see Figure 6.13.

This is characterised by the *Deborah Number*:

$$D_{Deborah} = \frac{\text{characteristic relaxation time}}{\text{measurement of interaction time}} = \frac{\tau}{\tau_m} \tag{6.2}$$

Maximum friction will occur when $D_{Deborah} \approx 1$: the chains have enough time to interdigitate, but not enough time to disengage.[134,157]

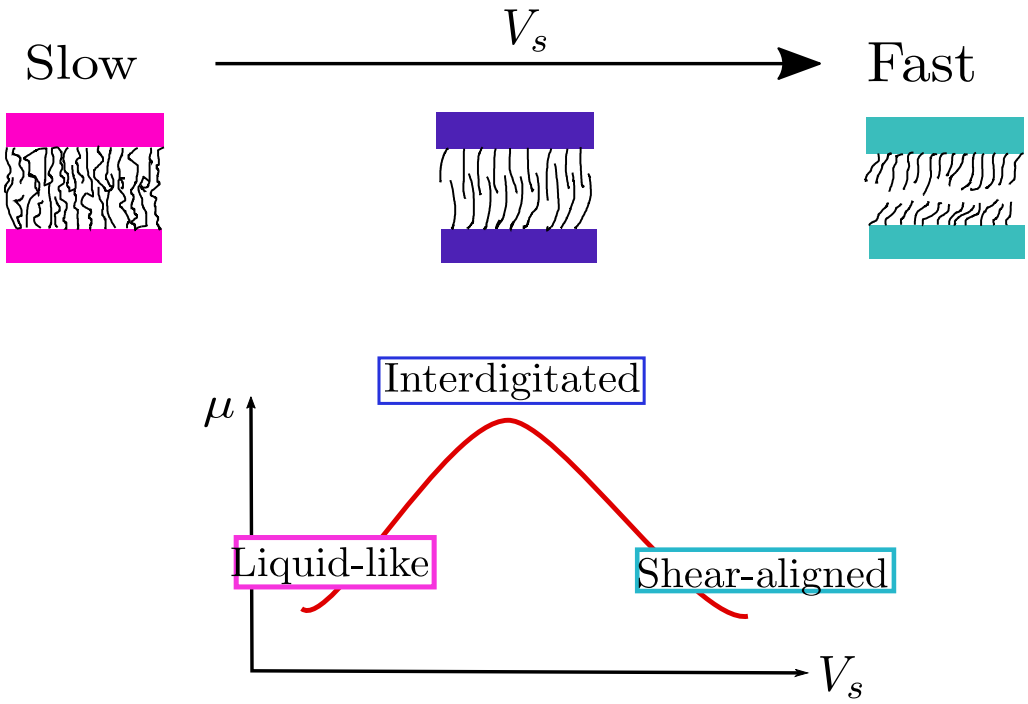


Figure 6.13: A schematic showing how the interdigitation of the alkyl chains is affected by shearing velocity and how this relates to the coefficient of friction. Adapted from [157]

The static film is amorphous, as implied by the normal force profiles of the 50 vol % mixture. Nevertheless, at low shear velocity (v_l) the film is still able to flow due to the presence of vacancies which allows movement of molecules and thus the film "creeps" giving a low friction force. At intermediate v_l , $D_{Deborah} \approx 1$, see Figure 6.13(a) and the alkyl chains and dodecane have time to interdigitate but not enough time to uncouple during the motion producing a higher friction force. For high v_l, the chains cannot interlink in the $\approx$ 1 s cycle, see Figure 6.14(b) and become shear-aligned, hence lower friction occurs. We have only investigated three sliding velocities so are unable to pinpoint exactly where the values of μ lie for the 50 vol % system. However, the small increase in μ from v_l=639 nm/s to v_l = 1918 nm/s suggests that we are initially probing the left-hand side of the peak, closer to the interdigitated region shown in Figure 6.13, rather than the lower friction on the far left of the relationship. This is also indicated by the presence of an elastic regime upon the change of shearing direction, in which the lenses are coupled, before deviating from linearity by viscous relaxation. This is due to a high

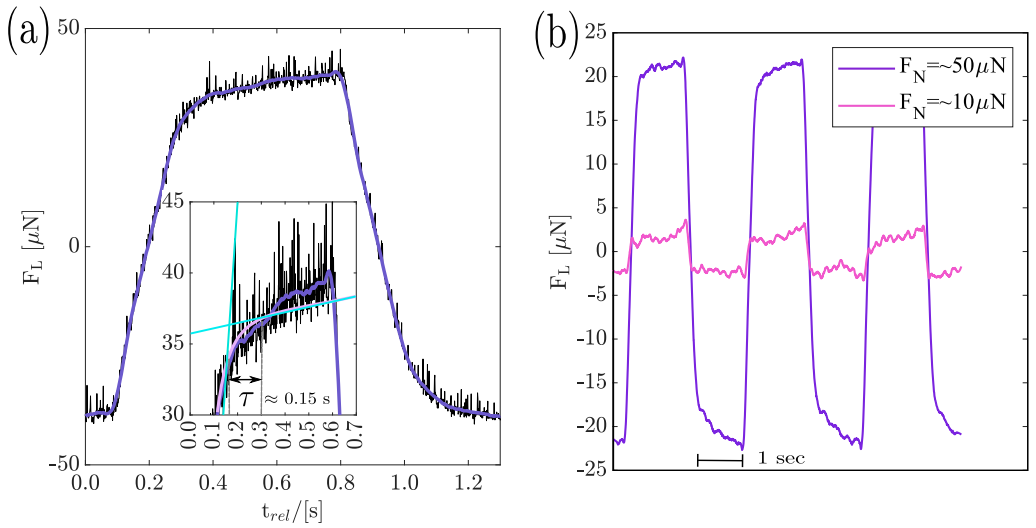


Figure 6.14: (a) Close-up of one friction cycle in 50 vol % $[P_{6,6,6,14}][(^iC_8)_2PO_2]$ in dodecane at 0.7Hz ($v_l = 3197$ nm/s) with the relaxation profile shown in the inset with a $\tau \approx 0.1$ s and (b) Shear response traces corresponding to specified normal loads.

degree of interdigitation between alkyl chains which must disengage to allow sliding to occur.[170]

6.3.3 | 1 vol % $[P_{6,6,6,14}][(^iC_8)_2PO_2]$, 99 vol % dodecane

A plot of distance and shear force against the normal force is shown alongside the trace of the shear response for a 1 vol % mixture at different normal loads in Figure 6.15(a-f). The friction coefficients of all the measurements, including as shear velocity is increased, are significantly lower than that of the 50 vol % mixture, ranging from 0.245 to 0.267. The values are also more constant: it is feasible that this is because this mixture is much less viscous and far closer to that of dodecane, as shown below. Therefore, we do not see the same changes in μ caused by the high viscosity and amorphous nature of the 50 vol % mixture. As expected from the retraction force profile in Figure 6.3, there is also a very small adhesion contribution to the friction, around 0.9 μN.

This means the behaviour of the system is tending towards pure dodecane as an adhesive contribution is also observed in its friction response.[178] There is less obvious curvature in the elastic-plastic transition and, in some cases, peaks are present which

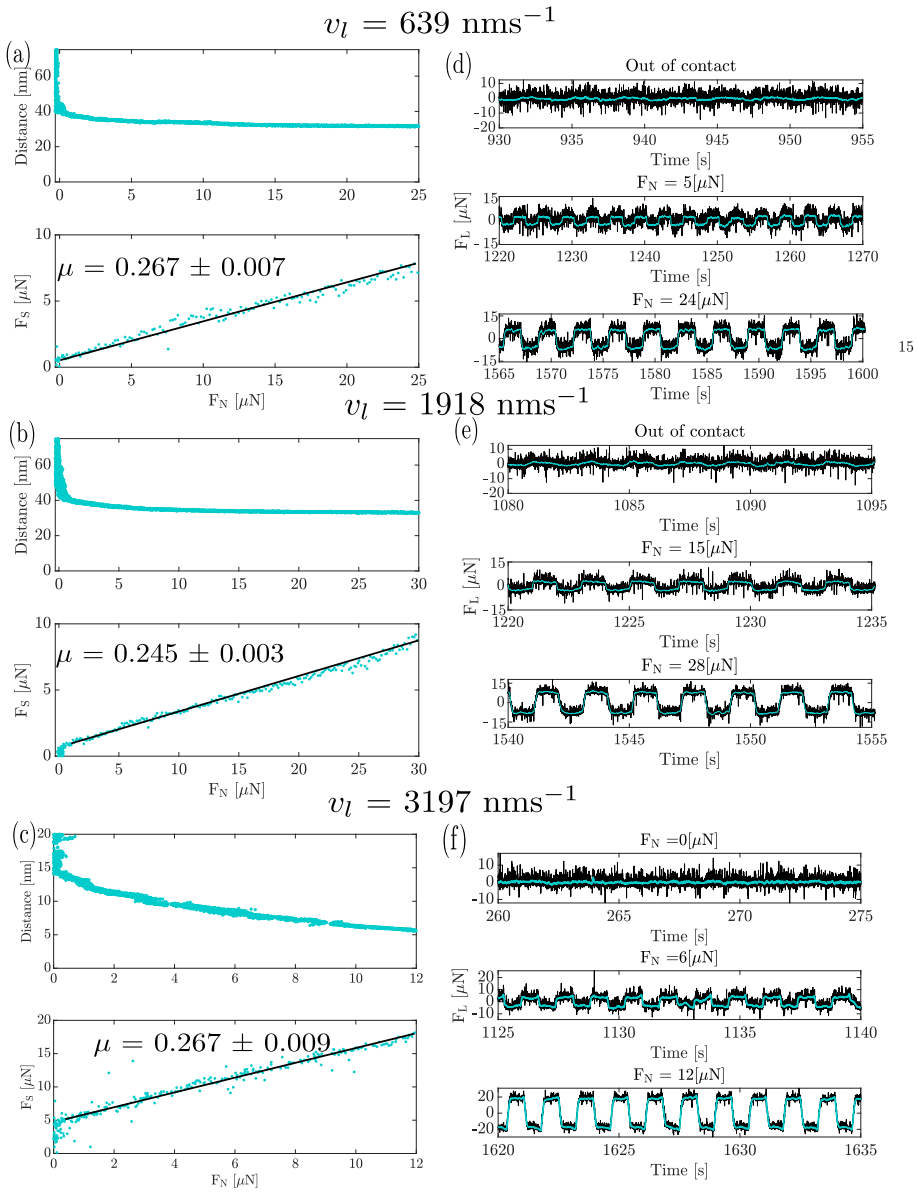


Figure 6.15: (a),(c), and (e) Representative surface separation, D, (top plot) and shear force, F_S,(bottom plot) as a function of the normal force, F_N, across a 1 vol % of $[P_{6,6,6,14}][(^iC_8)_2PO_2]$ in dodecane at a shearing frequency of (a) 0.3Hz, (c) 0.5Hz, and (e) 0.7Hz. Bottom plot: F_S with increasing F_N is shown in light blue, (b), (d), and (f): Lateral friction signal,F_L, as a function of time with and without a smoothing filter in light blue and black, respectively.

indicate a yield point with a finite yield force. However, liquid-like and solid-like behaviour are usually never clear cut: it is more of a spectrum, as can be seen in the differences between the 50 vol % and 1 vol % mixtures. The shear response shown in the lowest plot in Figure 6.15(d),(e), and (f) in suggests a shift towards a more solid-like friction response. A chaotic regime and then a smooth sliding

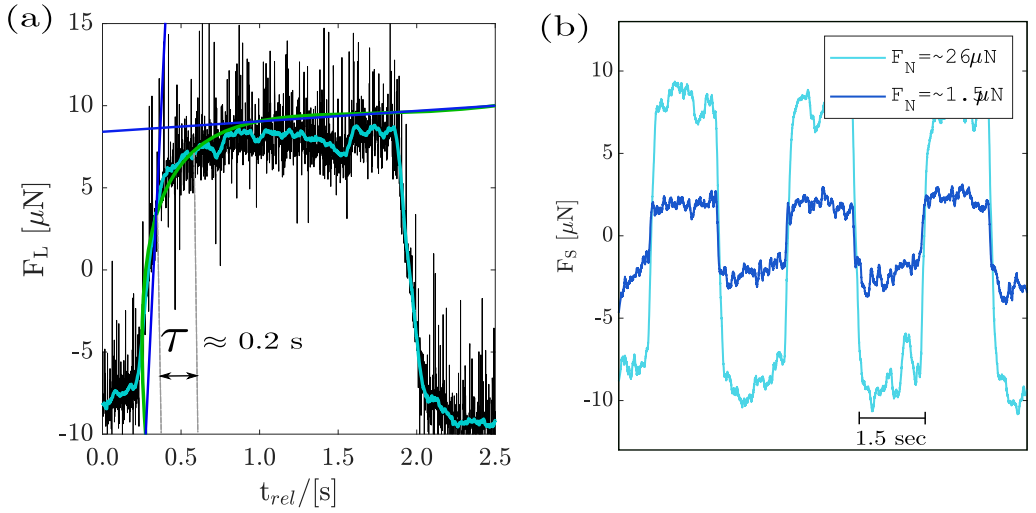


Figure 6.16: (a) Close-up of one friction cycle in 1 vol % $[P_{6,6,6,14}][(^iC_8)_2PO_2]$ in dodecane at 0.5Hz (v_l = 1918 nm/s) with the relaxation profile shown and the $\tau \approx 0.2$ s annotated and (b) Shear response traces corresponding to specified normal loads.

regime are recorded as v_l is increased, rather than stick-slip. In pure dodecane, as well as other organic liquids, the film undergoes a liquid-like to solid-like transition at nano-confinement (typically less than 10 nm).[76,178] Perhaps, if we were able to further confine this mixture, then a greater progression towards a definite solid-like response could be seen. This transition in response is something that also is present for both of the measurements at higher v_l.

In the measurement at v_l= 1918 nm/s, shown in Figure 6.15(c) and 6.16, the same linearity exists between F_S and F_N up to $F_N \approx 35$ μN as in the measurements at lower speeds. Yet beyond this value, the relationship deviates from linearity and μ increases anomalously by an order of magnitude.

6.3.4 | Pure Dodecane

Finally, we studied the lateral forces in nanometre condensed pure dodecane films. The results are shown in Figure 6.17. The first thing of note from these studies was that in all the layering regimes, from $n = 6$ to $n = 3$, we obtained a friction coefficient μ of 0.0009, see Figure 6.17(a). This observation of superlubric friction indicates that the mica in these studies was not perfectly aligned, as we obtained

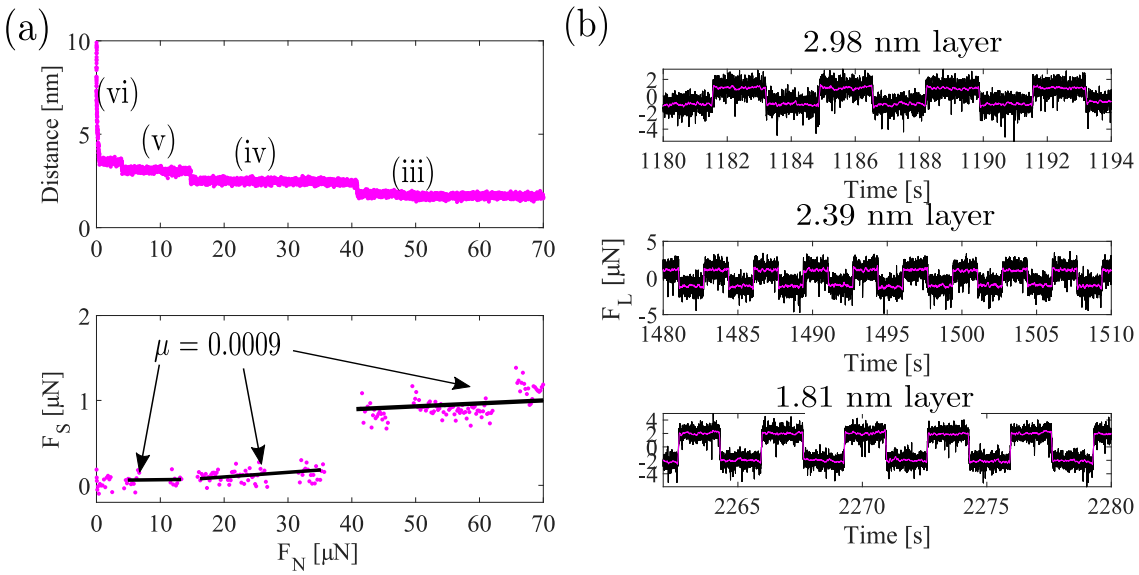


Figure 6.17: Representative (a) surface separation, D, (top plot) and shear force, F_S,(bottom plot) as a function of the normal force, F_N, across a pure dodecane film. Bottom plot: F_S with increasing F_N is shown in pink, the black line indicates F_S with decreasing F_N. The friction coefficient across layers (vi);(v);(iv); and (iii) is $\mu = 0.0009$, The vertical dashed lines in (a) highlight the simultaneous discrete steps in surface separation and shear force with normal force. (b) Lateral friction signal, F_L, as a function of time in layer (i), with and without a smoothing filter in pink and black, respectively.

values similar to those reported in 2019 with crystallographically misaligned mica.[178]

The second thing of note is that we do observe quantised friction in dodecane, but that it behaves more like a simple molecular liquid,[74–76,170,178,183] similar to our observations for PC in Chapter 5. The behaviour is more similar to a simple liquid because we do not see a great difference in the obtained friction coefficients, indicating that the friction is independent of layering.[74–76,170,178,183]This is expected for a system of this type, as there is no strict layering of cations/ anions that is found in ILs that can alter the shearing plane chemistry to lead to different friction coefficients for each confined film.

6.4 | Summary

In this chapter, condensed films of $[P_{6,6,6,14}][(^iC_8)_2PO_2]$ mixed with dodecane from 0 to 100 vol % were studied in the SFB. Using the SFB,we were able to study both the normal and lateral forces of these liquid films.

No layering was observed in our $[P_{6,6,6,14}][(^iC_8)_2PO_2]$ force profiles. This is likely to be a result of the film adopting a more amorphous and diffuse structure when compared to smaller and more spherical ILs.[218] The long alkyl chains of the cations and anions effectively prevent the film from packing as tightly as that predicted by the cubic approximation. As we bring our confining surfaces into closer contact, instead of discrete layers being squeezed out (which would result in the oscillatory force profile), we observe a non-oscillatory force with a repulsive element. In the 1 vol %, 50 vol %, and pure $[P_{6,6,6,14}][(^iC_8)_2PO_2]$, a deflection in the spring between 30 nm and 40 nm confirms that there is a long-range repulsion and this is likely to be a consequence of the diffuse packing.

In the 1 vol % mixture, the retraction profile revealed an attractive minima at 6nm. This had previously been reported in studies of pure dodecane,[178] making them attributable to dodecane. Indeed, this same attractive minima is found in our studies of pure dodecane, which showed an oscillatory force law that was consistent with the literature.

The frictional response of the $[P_{6,6,6,14}][(^iC_8)_2PO_2]$ nanofilms as a function of load were also presented. There was a linear relationship between F_N and F_S in the pure dodecane and 1 vol % systems. In the 50 vol % and pure $[P_{6,6,6,14}][(^iC_8)_2PO_2]$ system, there was instead significant curvature in the F_N vs F_S profiles. This curvature is likely a result of the viscosity of our confined films, and can be attributed to Couette Flow.[218,219] The lateral forces of these $[P_{6,6,6,14}][(^iC_8)_2PO_2]$ mixtures are overall liquid-like, and have a relaxation time that is expected from a viscous film. While in dodecane superlubric friction regimes ($\mu < 0.01$) are observed,[178] this result is not repeated in any of our $[P_{6,6,6,14}][(^iC_8)_2PO_2]$ mixtures. Instead in these systems, we report μ of 0.2 to 0.7.

These results overall indicate that while $[P_{6,6,6,14}][(^iC_8)_2PO_2]$ is an effective hydrodynamic lubricant, that when compared to a traditional model base oil, it does not act a boundary lubricant under the pressure conditions in the SFB experiments. This

does not discount the possibility of effective boundary lubricant effects at higher pressures or in macroscale contacts.

7 | Normal and Lateral Forces of $[P_{6,6,6,14}][TFSI]$

7.1 | Introduction

Looking at the results for our two IL systems so far, the $[C_4C_1P_{yrr}][TFSI]$ and $[P_{6,6,6,14}][(^iC_8)_2PO_2]$ have little in common. The strict layering and clear step-like profile seen in $[C_4C_1P_{yrr}][TFSI]$ is not present in $[P_{6,6,6,14}][(^iC_8)_2PO_2]$, and is instead replaced with an overall shapeless force profile. This result, was, however, expected: $[C_4C_1P_{yrr}][TFSI]$ is composed of smaller and more compact ions, while $[P_{6,6,6,14}][(^iC_8)_2PO_2]$ is made up of a highly branched cation and highly-branched anion,[218] making it difficult for the film to pack in that regular cation-anion-cation pattern seen in $[C_4C_1P_{yrr}][TFSI]$. To provide a link between the results from $[C_4C_1P_{yrr}][TFSI]$ and $[P_{6,6,6,14}][(^iC_8)_2PO_2]$, and to explore how the changing anion may affect both the normal and lateral forces, in this chapter we study trihexyltetradecylphosphonium bis(trifluoromethysulfony)imide ,$[P_{6,6,6,14}][TFSI]$, see Figure 7.1. Here the cation is in common with $[P_{6,6,6,14}][(^iC_8)_2PO_2]$, while the anion is in common with $[C_4C_1P_{yrr}][TFSI]$. This systematic study of three ILs $[C_4C_1P_{yrr}][TFSI]$, $[P_{6,6,6,14}][(^iC_8)_2PO_2]$ and $[P_{6,6,6,14}][TFSI]$, is useful as previous AFM and SFB studies have found that the changing of cations or anions can have profound effects on the structural[35,176,204,222,223] and friction forces.[174,223,224] Characterisation of the structural and frictional forces associated with the constituent ions therefore provides a practical route to 'tune' friction. $[P_{6,6,6,14}][TFSI]$ is therefore chosen as it an ideal bridge between the two previously studied systems, $[C_4C_1P_{yrr}][TFSI]$ and $[P_{6,6,6,14}][(^iC_8)_2PO_2]$.

More usefully, $[P_{6,6,6,14}][TFSI]$ is also a relatively well-studied IL on the nanoscale (AFM) and macroscale(TRB).[105,118,127,128,218] However, there are currently no SFB

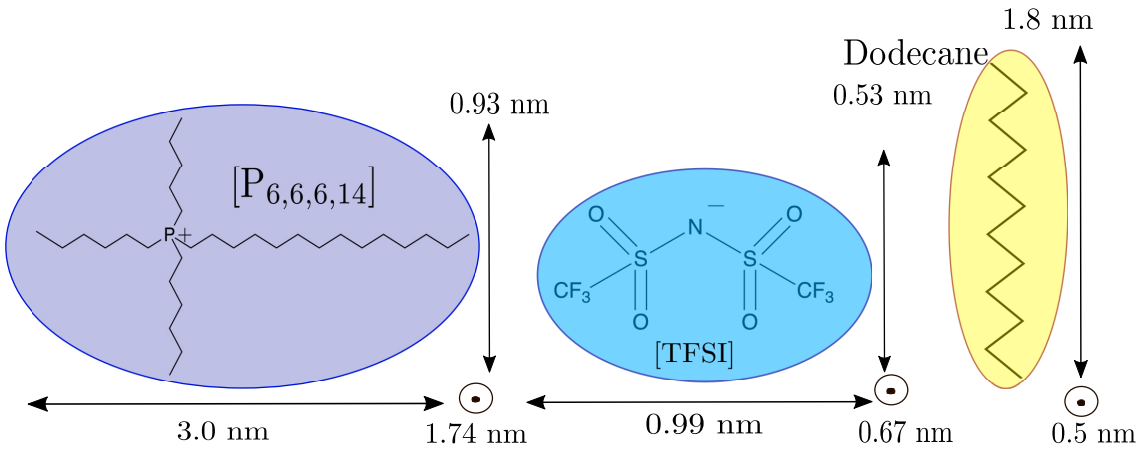


Figure 7.1: Chemical structure and sizes of $[P_{6,6,6,14}][TFSI]$ and dodecane. Ion sizes are estimated from geometry, bond lengths and covalent radii, associated with the most stable configuration found by energy minimization (Molecular Weight, $M_w = 763$ g/mol, density $\rho = 1.065$ gmL^{-1}, viscosity $\eta = 312$ mPa.s, and ion pair dimension, $D_m = 1.06$). Values are taken from[128,218]

experiments of $[P_{6,6,6,14}][TFSI]$ as a neat liquid and furthermore, there are no SFB experiments studying $[P_{6,6,6,14}][TFSI]$ in mixture with a common base oil.

In this chapter, experiments were performed on three different dilutions of $[P_{6,6,6,14}][TFSI]$ in dodecane: 100 vol % (20.7 mol %), 20 vol % (6.4 mol %) and 1 vol% (0.3 mol %), but only the studies of 100 vol % $[P_{6,6,6,14}][TFSI]$ these were successful, as the mixtures suffered from confinement-induced phase separation.

7.2 | Normal Forces of pure $[P_{6,6,6,14}][TFSI]$

Overall, the F_N/R profiles for the $[P_{6,6,6,14}][TFSI]$ systems did not show evidence of IL layering.

7.2.1 | Hydrodynamic Forces of pure $[P_{6,6,6,14}][TFSI]$

As $[P_{6,6,6,14}][TFSI]$ is expected to be highly viscous,[118] we need to investigate if there is a viscous contribution that is dominating our normal force profile. To do this, force profiles were measured at different approach velocities. In Section 5.3 of Chapter 5, a full explanation of this procedure was done, and requires us to fit our observed distance-time profile to a purely hydrodynamic force,[78] using Equation 5.1

and 5.2.

The computed C_{reg} values for [$P_{6,6,6,14}$][TFSI] is shown below.

Table 7.1: Comparison factors for high, low and intermediate velocity regimes for [$P_{6,6,6,14}$][TFSI] (η = 312 mPa s at 25°C) and R = 0.1 cm[78]

Regime	Velocity/ nm s^{-1}	C_{reg} x 10^6 /mPa s m^2
High	88	275
Intermediate	0.11	3.27
Low	0.02	0.696

7.2.2 | Fast Velocities

Figure 7.2 shows the data obtained when the top lens is moving at a fast velocity in [$P_{6,6,6,14}$][TFSI]. At these fast velocities, the viscous force is expected to dominate and the data is fitted by assuming a purely viscous force, with v_s= 22.2 nm/s and b= 7.4 ± 0.3 nm.[78,212] In this regime, the top lens is moving at v_s= 22.2 nm/s, as illustrated by the dashed-line. The beginning of the trajectory is fitted with v_s. As shown, this fit captures the initial curvature of the approach, and does not depend on the value of b. However, as we reach closer confinement (10 nm < D < 20 nm), the no-slip boundary condition is no longer appropriate and does not allow a good fit with the original data. The best fit is obtained with b = 17.3 ± 0.3 nm, which corresponds to a thick layer of $i \approx 16$. The log-linear representation of the orange plot in (a) is shown in Figure 7.2(c). We do not observe a linear decay that would be indicative of a long-range exponentially decaying electrostatic force.

7.2.3 | Intermediate Velocities

Measurements at an upper-intermediate velocity in pure [$P_{6,6,6,14}$][TFSI] are shown in Figure 7.3. In this regime, the top lens is moving at v_s= 4.55 nm/s, as illustrated by the dashed-line. The beginning of the trajectory is fitted using v_s, and while this does captures the initial curvature of the approach, the best fit is obtained with b = 13.9± 0.3 nm, which corresponds to a thick layer of $i \approx 13$. The log-linear

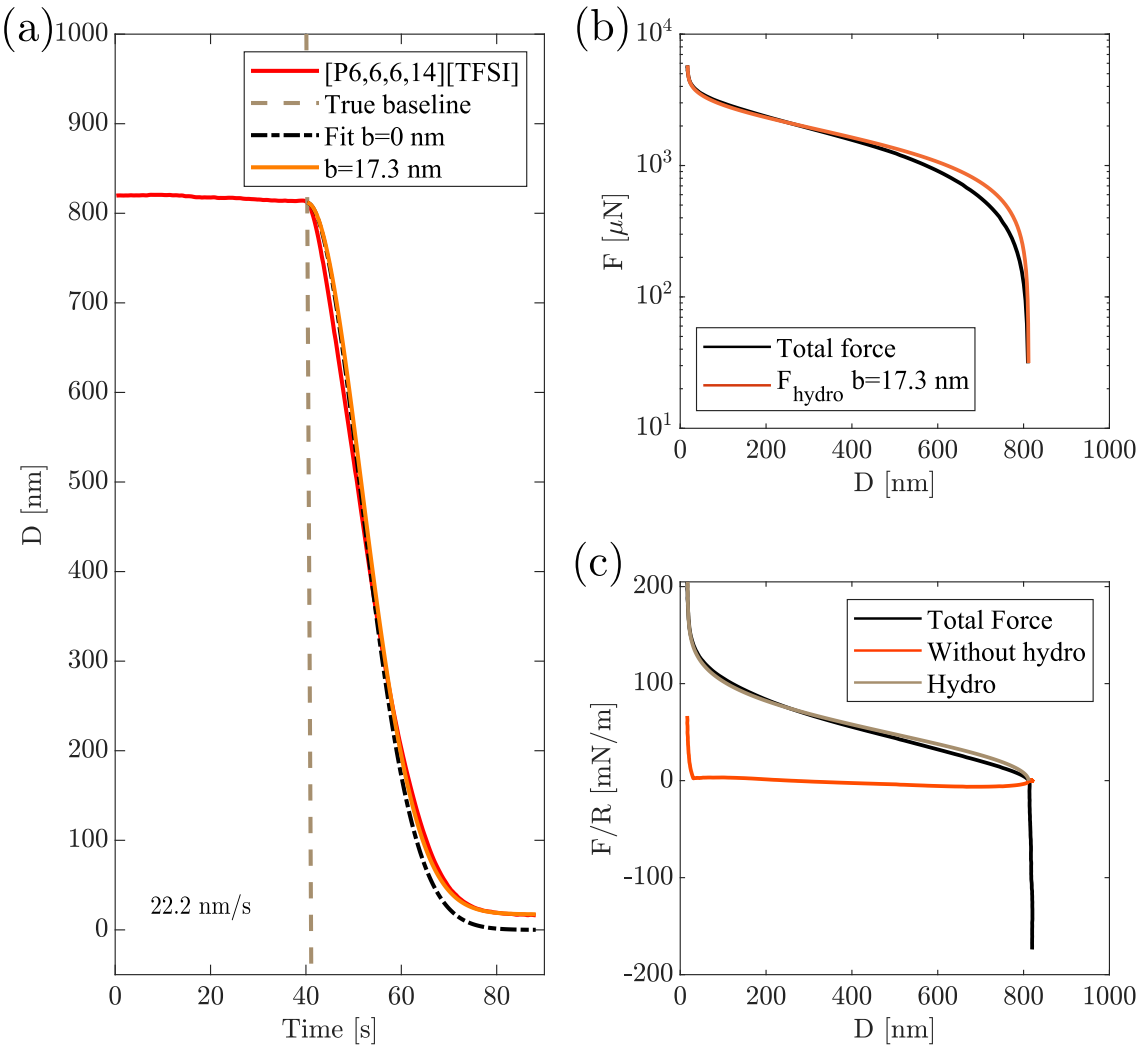


Figure 7.2: (a) Trajectory recorded when the top lens is moving at $v_s = 22.2$ nm/s (piezo motion indicated by the dashed line in grey). The red curve is the experimental signal: the black-dashed curve is the fit by the model with $b = 0$, the orange curve is the fit when b= 17.3 nm. (b) Same measurements, but with data presented in terms of force, in semi-log scales. The black curve is the total force, the orange curve is the viscous contribution (when fitting with b= 17.3 nm (c) F_N/R profile showing the total measured (black), the viscous contribution (grey), and the force without the viscous contribution (red).

representation of the blue plot in (c) is shown in Figure 7.3(c), and similar to the results obtained for the fast velocity system, we do not observe a linear decay that would be indicative of a long-range exponentially decaying electrostatic force.

7.2.4 | Slow Velocities

Measurements at a slow velocity in pure $[P_{6,6,6,14}][TFSI]$ are shown in Figure 7.4. In this regime, the top lens is moving at v_s= 0.083 nm/s, as illustrated by the dashed-

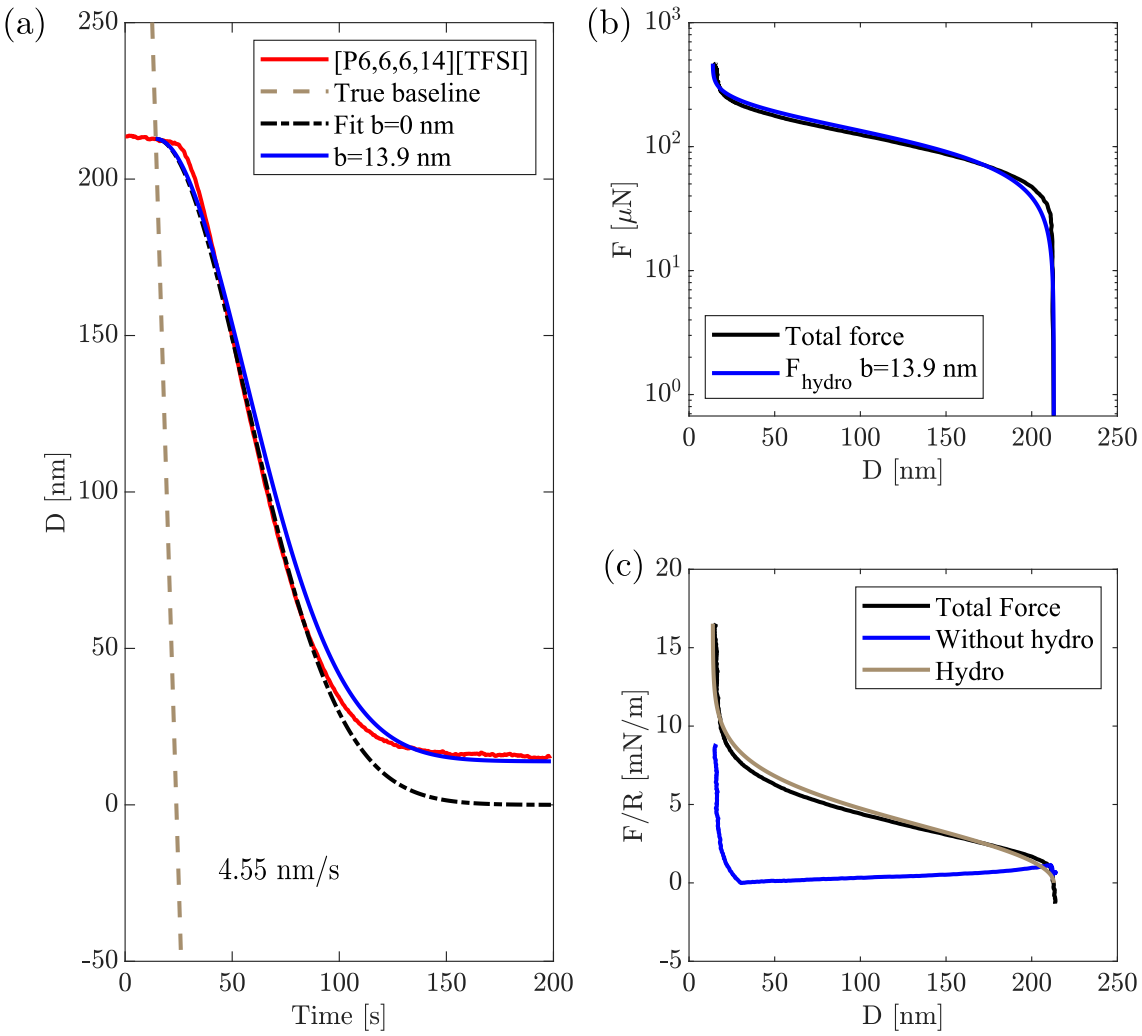


Figure 7.3: (a) Trajectory recorded when the top lens is moving at $v_s = 4.55$ nm/s (Piezo motion indicated by the dashed line in grey). The red curve is the experimental signal: the black-dashed curve is the fit by the model with $b = 0$, the blue curve is the fit when b= 7.4. (b) Same measurements, but with data presented in terms of force, in semi-log scales.The black curve is the total force, the blue curve is the viscous contribution (when fitting with b= 13.9 nm (c) F_N/R profile showing the total measured (black), the viscous contribution (blue), and the force without the viscous contribution (red).

line, and the best fit is obtained with $b = 16.4 \pm 0.3$ nm, which corresponds to a thick layer of $i = 15$.

7.2.5 | Structural Forces of Pure [$P_{6,6,6,14}$][TFSI]

From our F/R v D plot, see Figure 7.5, we are unable to resolve the steps that were previously seen in AFM study of this IL.[118,218] That paper reported average step lengths, or ΔD of $\approx$ 1.1 nm, which is in agreement with the calculated ion

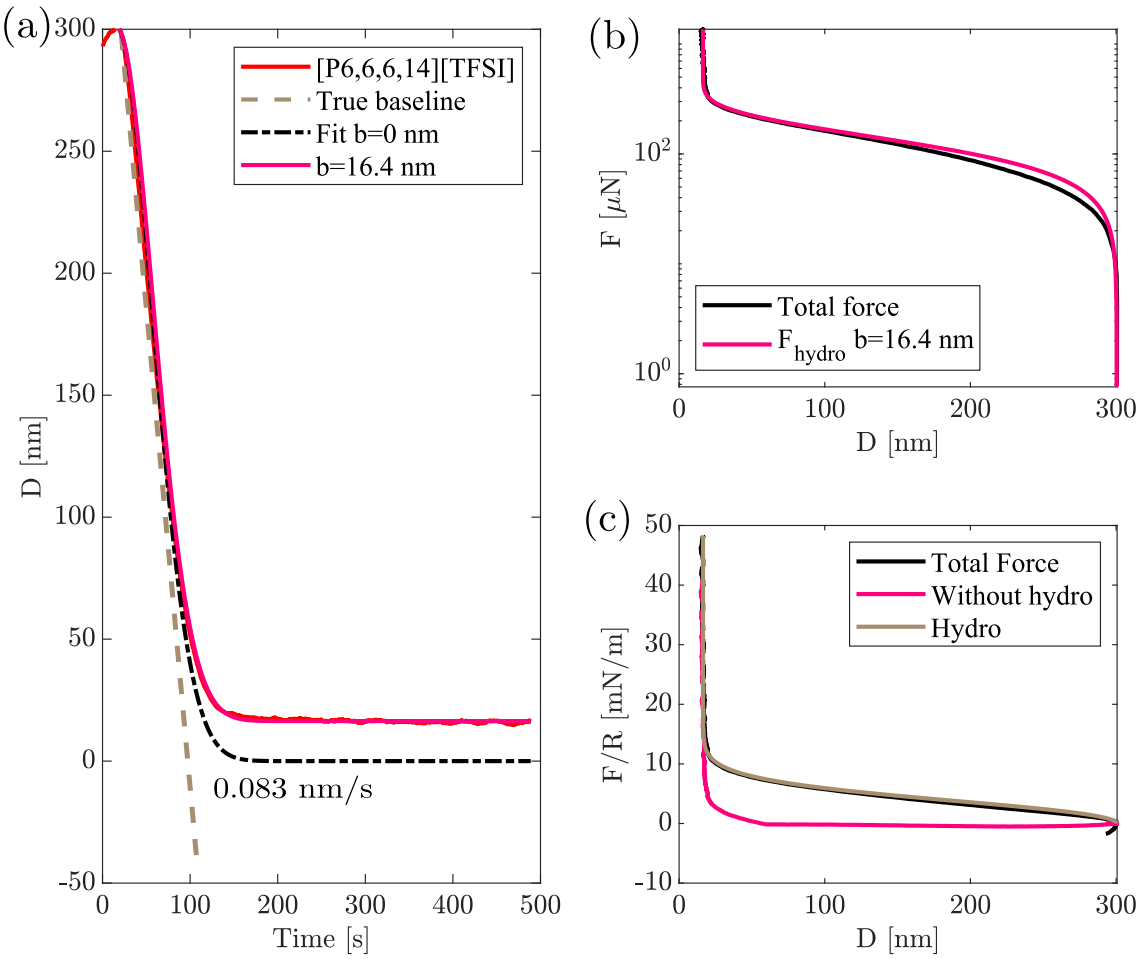


Figure 7.4: (a) Trajectory recorded when the top lens is moving at v_s = 0.083 nm/s (Piezo motion indicated by the dashed line in grey). The red curve is the experimental signal: the black-dashed curve is the fit by the model with b = 0, the pink curve is the fit when b= 16.4 nm (b) Same measurements, but with data presented in terms of force, in semi-log scales.The black curve is the total force, the pink curve is the viscous contribution (when fitting with b= 16.4) (c) F_N/R profile showing the total measured (black), the viscous contribution (grey), and the force without the viscous contribution (pink).

pair diameter, see Figure 7.1. They reasoned that the steric effects of the branched alkyl chains meant that use of a cubic packing approximation would no longer be valid.[118,218] The lack of a structural profile may be a result of the hydrodynamic forces present in the system. As stated, [P$_{6,6,6,14}$][TFSI] has a viscosity, η of 312 mPa s, and from the inset of Figure 7.5, we can see that the hydrodynamic contribution to the confined film obscures any long-range forces. Interestingly, when fitting our data with hydrodynamic forces in mind, similar to the process followed in Section 5.2, we get a slip length, b, of $\approx$ 15-18 nm, but even taking with taking those hydrodynamic

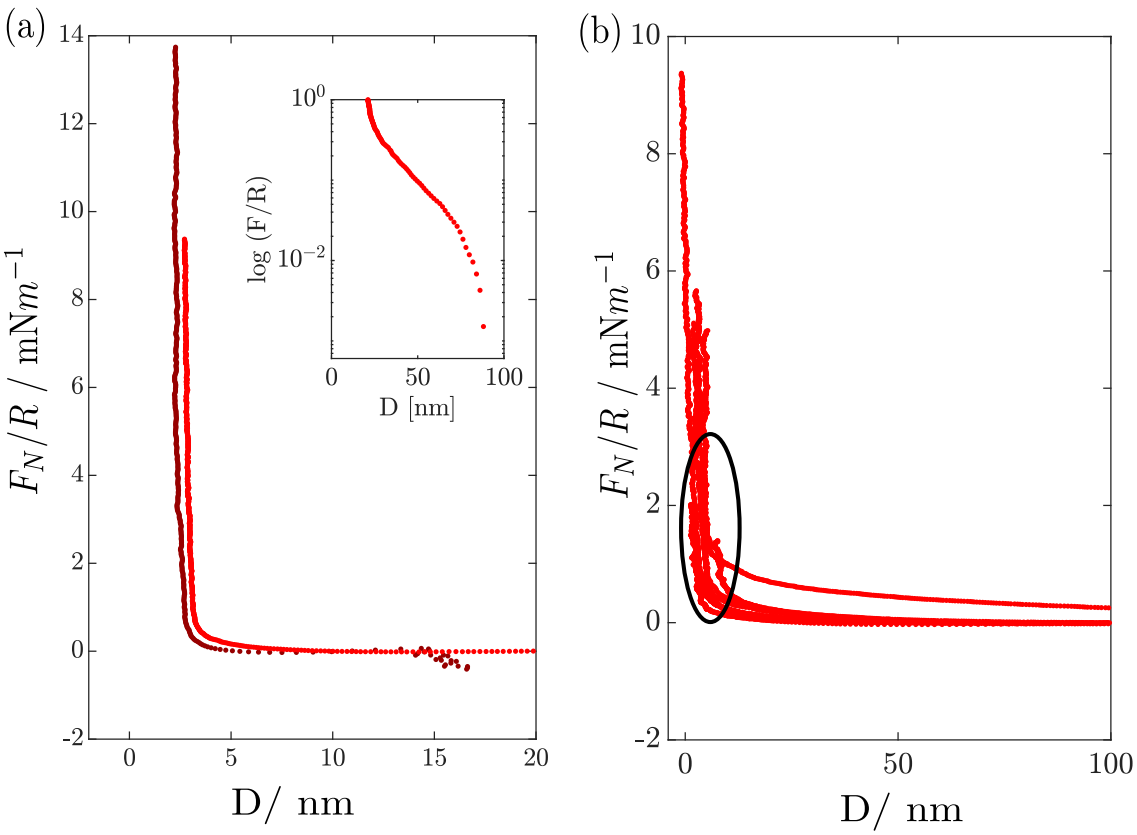


Figure 7.5: (a) Representative normal force, F_N, normalised by the radius of curvature, R, as a function of surface separation,D, measured in nm, profiles in pure [P6,6,6,14][TFSI], showing the profile on approach (red) and retraction (dark red).(b) All the approach profiles for [P6,6,6,14][TFSI] from one experiment plotted showing the normalised force F_N/R as a function of surface separation, D.

forces into account, we are unable to resolve structural forces below 10 nm. A

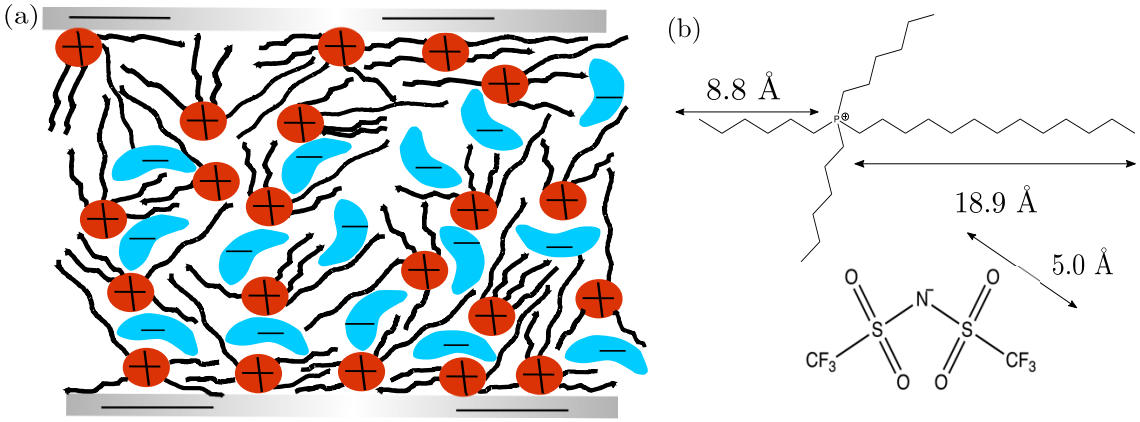


Figure 7.6: (a)Schematic illustrating the proposed nano-structure of the pure [P6,6,6,14][TFSI].(b) Image showing the molecular structure of [P6,6,6,14][TFSI], taken from.[217]

deflection in the spring, beginning at around 10 nm on the approach, see Figure

7.5(b), where it is circled, implies the existence of a long-range repulsion in our pure film.[26,59,62] This is because there is a favourable interaction between $[P_{6,6,6,14}][TFSI]$ and the surfaces, as a result of the ions' interaction with the mica's negative charge, and this must be overcome to squeeze out the intervening liquid.[59,62]

Given the structure of $[P_{6,6,6,14}][TFSI]$ and the 10 nm repulsive force, we can try to picture what the local structure may be. Importantly, aside from the geometric constraint of 10 nm, as this is an IL the local structure will need to be electroneutral,[40,41,62] and the $[P_{6,6,6,14}]$ cations will sit nearer to the mica than the [TFSI] anions. For this reason, there is likely to be a cation-rich boundary layer.[40]

Due to the electrostatic attraction between the cations and anions, the anions will then populate the area close to that cation-rich boundary layer.[40,42,62] From that initial 'structure', the cations and anions then adopt a more diffuse version of this.[40,42,62] Our long alkyl chains also impose a geometric constraint, as while they are flexible, the longest chain, see Figure 7.6(b), is 18.9 Å.[218]

These non-polar chains therefore help to make the liquid system more diffuse, and stop it from adopting that strict anion-cation-anion layering found in $[C_4C_1P_{yrr}][TFSI]$ that was the result of discrete energy minima. In $[P_{6,6,6,14}][TFSI]$, while the film will pack with regards to the geometric and electroneutral constraints, no discrete regimes are found.

Miscibility

Experiments on the 1 vol %, 20 vol %, and 80 mol % $[P_{6,6,6,14}][TFSI]$ in dodecane were attempted, but it was found that at these concentrations, that there was phase separation in the SFB. This was a surprising finding, as there had previously been AFM studies on $[P_{6,6,6,14}][TFSI]$ with hexadecane, and using the TRB, we were able to collect macroscale measurements of these mixtures.[114,122,124,127,128] To investigate this further, bench-top experiments on the miscibility of $[P_{6,6,6,14}][TFSI]$ with dodecane were performed.

The measurements were performed at atmospheric pressure, and the temperature and composition of the system was varied. Therefore, it is an isobaric phase study. The temperature was varied with the use of a water bath, and two temperatures were used (25°C, and 30°C), with measurements also taken on the benchtop where the temperatures was ≈ 22- 23 °C, and the composition was varied according to the molar fraction of [$P_{6,6,6,14}$][TFSI] in dodecane (X_{Il}) with the use of a volumetric pipette and scale. As mass wt is more accurate than volumetric, the mole fraction of [$P_{6,6,6,14}$][TFSI] was controlled using the mass wt.

A binary system has two components (C= 2) and typically tend to form one-phase systems and two-phase systems, although sometimes a three-phase system can also be formed.[115]

In an isobaric phase diagram, the lines of equilibrium or phase boundaries indicate the conditions at which multiple phases can coexist in equilibrium. The phase transitions from multi-phase to single phases occur at these boundaries, and the system moves up the isopleth $a-d$. When these liquid phases are not in equilibrium, a miscibility gap is present, and this is where the mixtures exists as two or more phases, and within this gap, the [$P_{6,6,6,14}$][TFSI] and dodecane are not completely miscible. At this point, this will stop any SFB measurements from being successful, as the optics will be negatively impacted by those phases, see Figure 7.7(b-c). The results are shown in Figure 7.7.

As shown, at all volume fractions of [$P_{6,6,6,14}$][TFSI] and dodecane, a two-phase mixture is observed at 298 K. When the mixtures are placed in a water bath for ≈ 10 minutes at 320 K, some volume fractions do form a single-phase mixture. The critical point (i.e the point at the maximum of the curve of the two-phase area, when the two liquid phases become identical and form a single phase) is annotated by an open circle.

Unfortunately, in the SFB we are currently unable to control using our set-up,

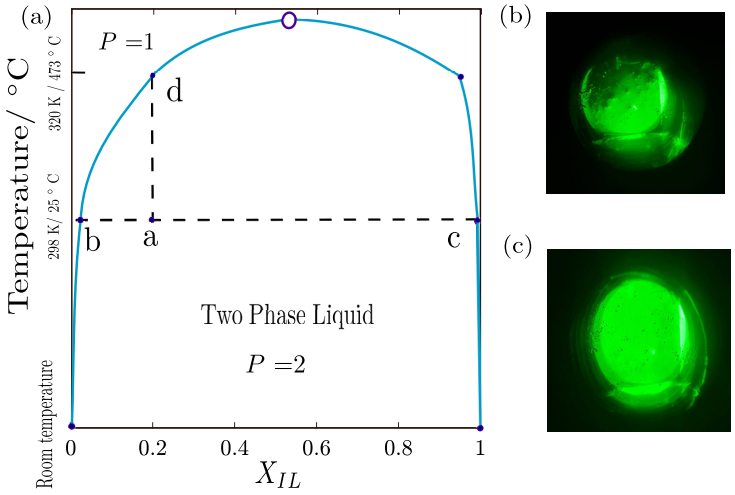


Figure 7.7: The isobaric phase diagram for the binary mixture of [P6,6,6,14][TFSI] and dodecane at room temperature 298K and 320 K plotted against the mol fraction (X_b) of [P6,6,6,14][TFSI] in dodecane. All phases are liquid and the open circle indicates the critical point. (b) and (c) Images showing the phase formation on the lenses during an SFB experiment.

and temperatures in the SFB room reach ≈ 22 - 24 °C. In the TRB, while the temperature is again not controlled, the sensors located on our TRB indicate that due to the fast motors, the temperatures reach ≈ 30 °C just within the area inside of the thick plastic covering. With this in mind, it is expected that at the shearing surfaces, the temperatures will exceed 30°C

7.3 | Lateral Forces of Pure [P6,6,6,14][TFSI]

Representative lateral force measurements are shown below in figures 7.8,7.9, and 7.10 when a condensed film of pure [P6,6,6,14][TFSI] was studied at three different shearing frequencies: 0.3Hz, 0.5Hz, and 0.7Hz.

7.3.1 | 0.3Hz/ 639 nm/s

The lateral forces at 0.3Hz shearing frequency or 639 nm/s shearing velocity, v_l, across a pure [P6,6,6,14][TFSI] film is shown below in Figure 7.8. As shown, the F_S vs F_N relationship does have the curvature that was seen in [P6,6,6,14][(^{i}C8)2PO2], and this is once more indicative of a hydrodynamic lubricant system.[1,188] that we have a maximum surface confinement of 5 nm, no boundary layer was reached even with

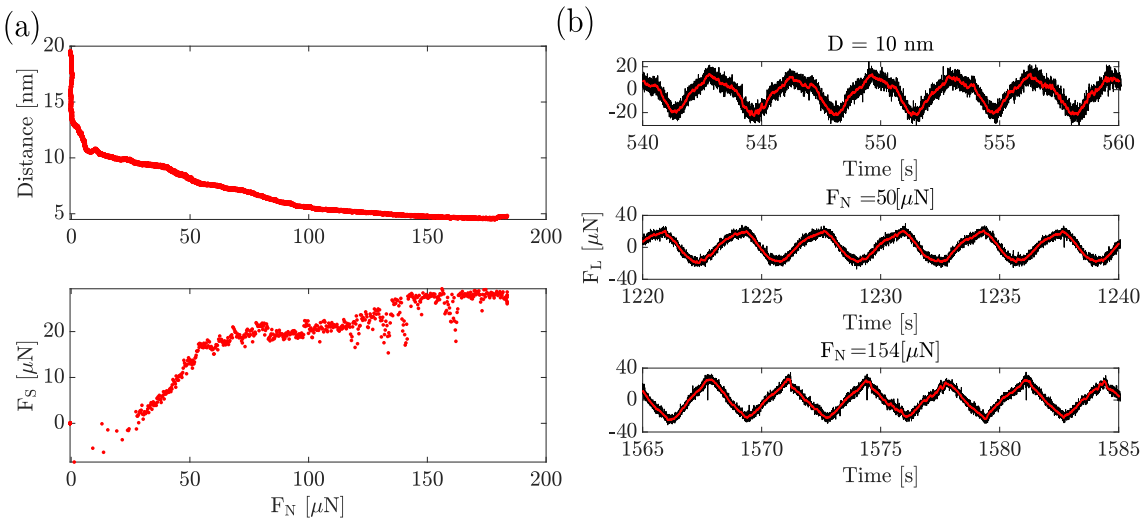


Figure 7.8: Representative (a) surface separation, D, (top plot) and shear force, F_S,(bottom plot) as a function of the normal force, F_N, across a pure [P$_{6,6,6,14}$][TFSI] film. Bottom plot: F_S with increasing F_N is shown in red, the black line indicates F_S with decreasing F_N.(b) Lateral friction signal, F_L, as a function of time with and without a smoothing filter in red and black, respectively.

200 μN of applied load. This shows that the pure [P$_{6,6,6,14}$][TFSI] film can resist squeeze out at these 'high' loads, which is a favourable result.[19]

Moreover, the lateral forces closely follow those of the applied triangular-wave motion, Figure 7.9(b) and indicates this film was either contaminated or the lateral forces were below the resolution of our system.

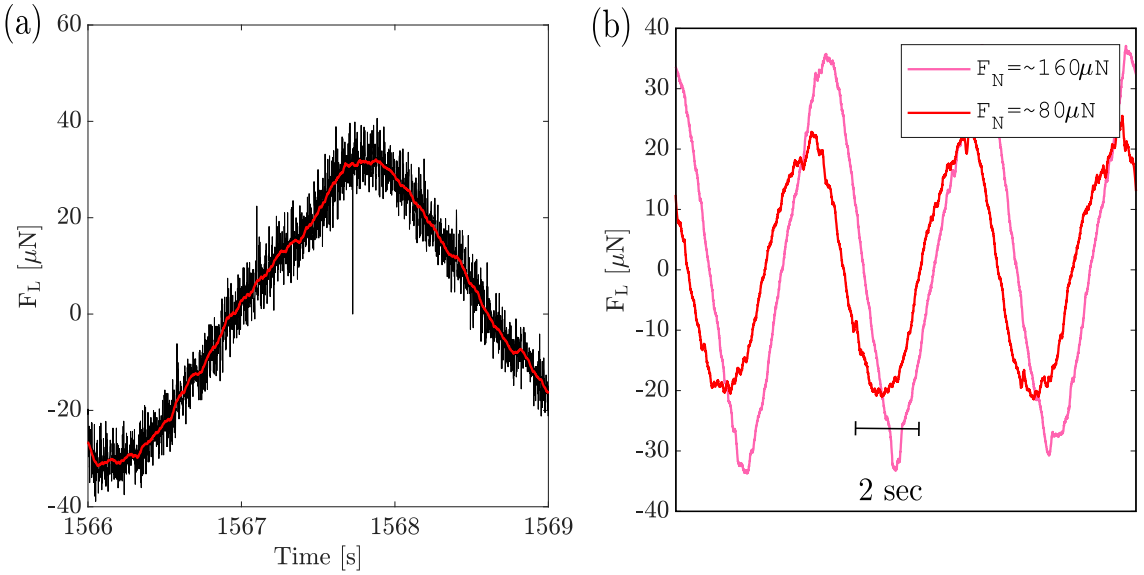


Figure 7.9: (a) Close-up of one friction cycle in pure [P$_{6,6,6,14}$][TFSI] at 0.3Hz (v_l = 639 nm/s) and (b) Shear response traces corresponding to specified normal loads.

7.3.2 | 0.5Hz/ 1918 nm/s

The lateral forces measured when a 0.5Hz shearing frequency (v_l= 1918 nm/s) is applied to a pure [P6,6,6,14][TFSI] film is shown below in Figure 7.10. At this shearing

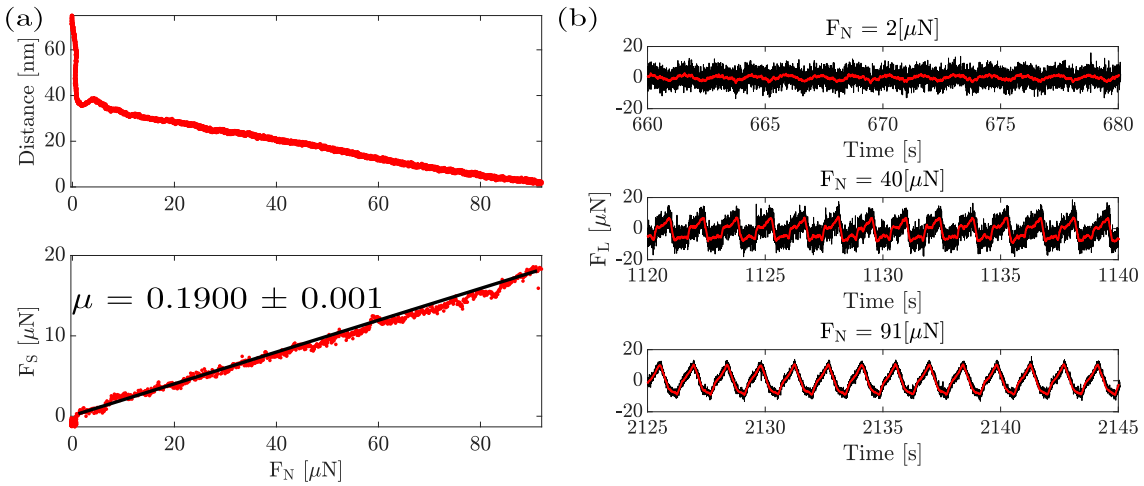


Figure 7.10: Representative (a) surface separation, D, (top plot) and shear force, F_S,(bottom plot) as a function of the normal force, F_N, across a pure [P6,6,6,14][TFSI] film. Bottom plot: F_S with increasing FN is shown in red. The friction coefficient is μ = 0.19 ± 0.001. (b) Lateral friction signal, F_L, as a function of time in at different applied loads, with and without a smoothing filter in red and black, respectively.

velocity we are able to obtain a friction coefficient, as the F_S v F_N does not have the curvature that prevented us from extracting μ in the 0.3Hz system. Looking at

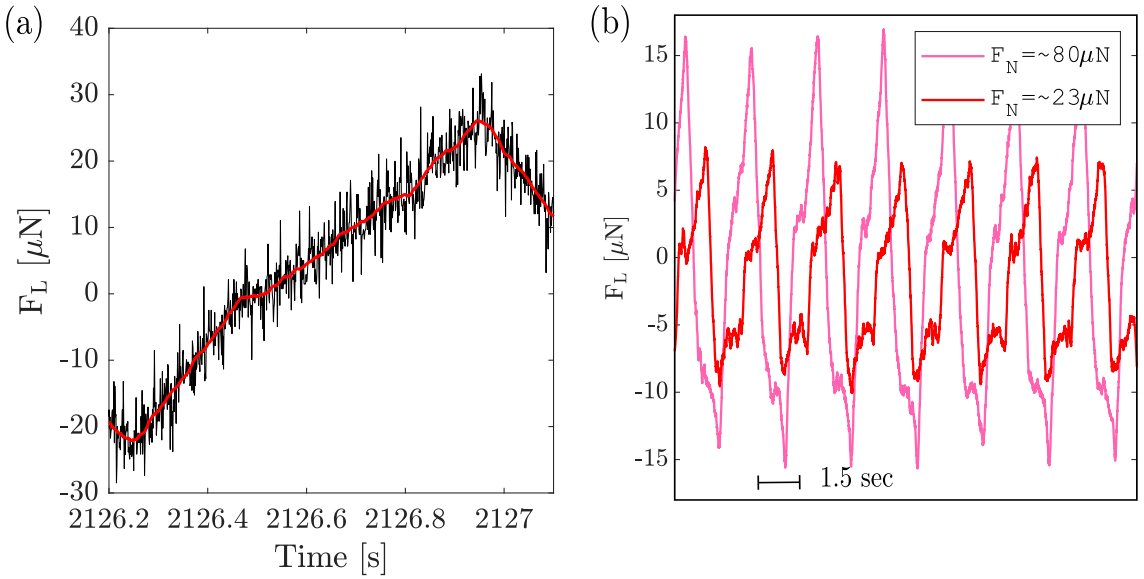


Figure 7.11: (a)Closeup of one friction cycle in pure [P6,6,6,14][TFSI] at 0.5Hz (v_l = 1918 nm/s) and (b) Shear response traces corresponding to specified normal loads.

a close-up, we can see that the friction forces are not what we would expect and we do not see a clear yield point. Instead, we see a sharp profile that is increasing in magnitude (where the shear springs are being bent), where we have small stiction peaks (that have the same gradient). At this point, while one surface is moving laterally, there is not the same smooth motion which would be indicative of 'smooth sliding', instead the film 'ratchets' and 'sticks'.

Looking at $[P_{6,6,6,14}][TFSI]$'s structure, this 'shear ratcheting' may be due to interdigitation of the long alkyl chains which causes 'shear thickening' .[1,157,170]In our system, the friction traces found at 0.5Hz may be due to the interdigitation or more simply 'locking' of the long alkyl chains that may be situated at the shear plane.[1,157]

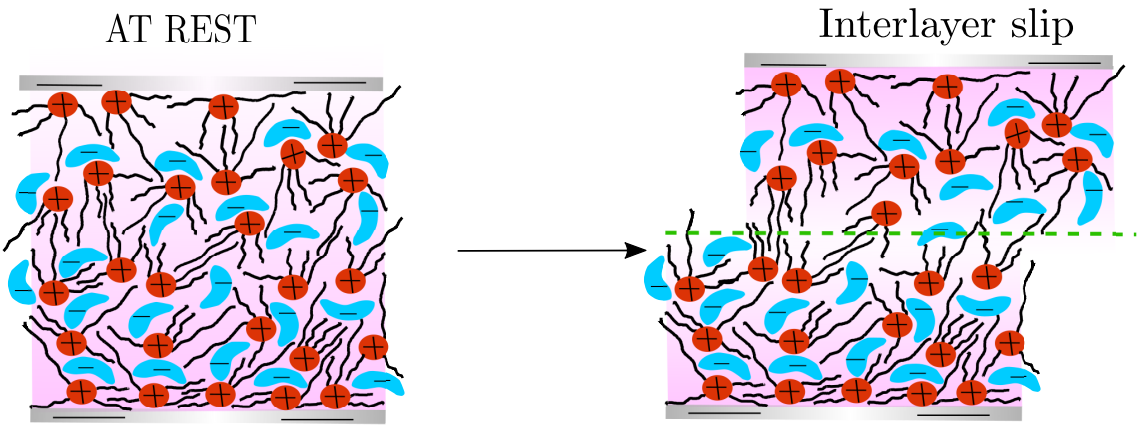


Figure 7.12: Schematic illustrating what may be causing the 'shear thickening' when a lateral velocity of 1918 nm/s is applied to the pure $[P_{6,6,6,14}][TFSI]$ nanofilm. In this schematic, the long alkyl chains of the cation undergo interdigitation that 'locks' the film, and may result in the shear ratcheting seen.

7.3.3 | 0.7Hz/ 3197 nm/s

The lateral forces measured when a 0.7Hz shearing frequency (v_l= 3197 nm/s) is applied to a pure $[P_{6,6,6,14}][TFSI]$ film is shown below in Figure 7.13. We obtain a friction coefficient of $\mu = 0.380$, and instead of the rough lateral profile found at 0.5Hz, we instead see a smooth sliding profile. Once more picturing the long alkyl chains, at a lateral velocity of 3197 nm/s, there is not enough time for these chains

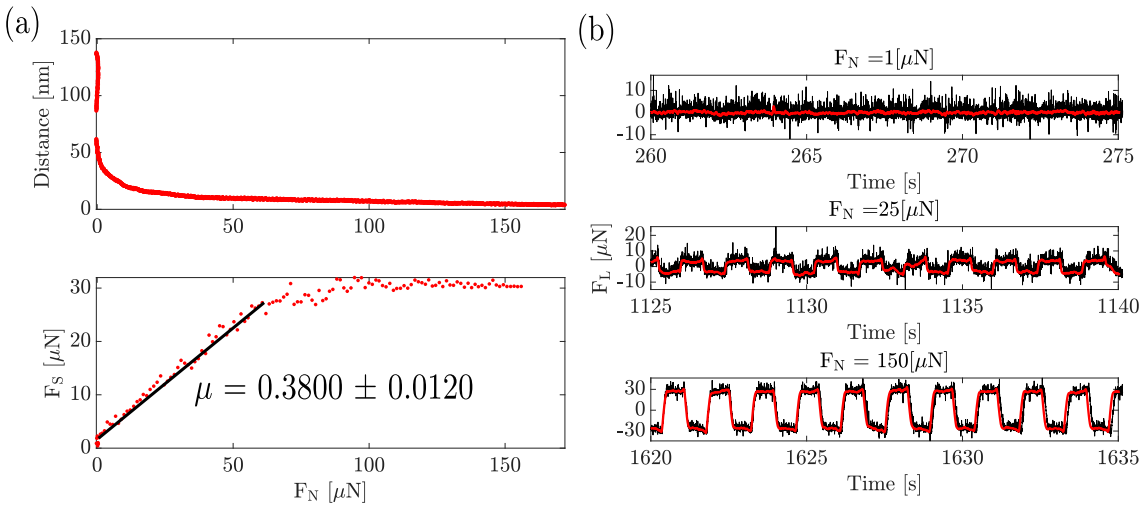


Figure 7.13: Representative (a) surface separation, D, (top plot) and shear force, F_S,(bottom plot) as a function of the normal force, F_N, across a pure [P6,6,6,14][TFSI] film. Bottom plot: F_S with increasing FN is shown in red, the black line indicates F_S with decreasing F_N. The friction coefficient is $\mu = 0.380$ (b) Lateral friction signal, F_L, as a function of time at different applied loads, with and without a smoothing filter in red and black, respectively.

to 'lock' and so our film undergoes smooth shearing.[1,157] Looking at the relaxation

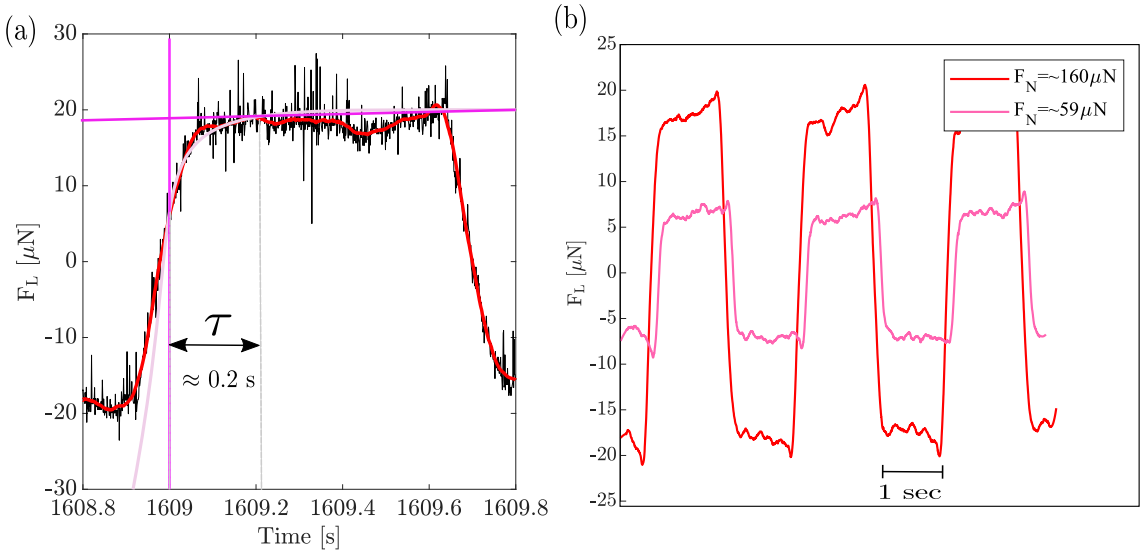


Figure 7.14: (a) Closeup of one friction cycle in pure [P6,6,6,14][TFSI] at 0.7Hz ($v_l = 3197$ nm/s), with the relaxation time $\tau \approx 0.2$ s plotted (b) Shear response traces corresponding to specified normal loads.

profile, see Figure 7.14(a) we obtain a relaxation time $\tau = 0.2$ s, which is between the value expected for a plastic and the value expected for an elastic regime This indicates that we do have a viscous film.[11,68]

7.4 | Summary

In this chapter, normal and shear forces across a pure $[P_{6,6,6,14}][TFSI]$ nanofilm was studied. Viscous forces dominated the normal force profiles at all approach velocities studied and fitting the data to an expression for b $\approx$ 13 - 17 nm. Normal force profiles are influenced by viscous forces in multiple ways:

1. The velocity of approach directly influences the magnitude of F_N/R through inadequate linear baseline fitting.

2. We cannot deconvolute any potential exponentially decaying electrostatic force from the viscous contribution.

3. 3. Adhesive minima cannot be described quantitatively.

Nonetheless,the structure and dynamics of the film can be analysed. Normal force profiles did not show any structural forces, making these observations a departure from previous AFM studies that reported 'squeeze-out' layers.[118,218] However, due to the larger contact area of the SFB when compared to the AFM and the long alkyl chains of the cations the lack of observable structural forces is reasonable, as we do not expect a discrete local structure to be formed. Instead, we reason that when confined in the SFB, the liquid film adopts a diffuse structure where the $[P_{6,6,6,14}]$ cations do lie next to the negatively charged mica surfaces and surround a disordered film system.

SFB studies of $[P_{6,6,6,14}][TFSI]$ mixtures with dodecane were not presented due to the formation of oil-liquid phases when confined in the SFB. These phases were on the microscale and interfered with the optics of our set-up. These observations of phase formation were also seen in bench-top experiments, and at room temperature, no mixture of $[P_{6,6,6,14}][TFSI]$ and dodecane were found to be miscible.This was surprising given AFM studies on $[P_{6,6,6,14}][TFSI]$- octane mixtures and our own studies on the tribometer using this liquid (see Chapter 8).[118,218]

The frictional response of the nanofilms as a function of load were also reported. While there was no evidence of quantised friction, the condensed films still showed overall good lubrication ability and had behaviour that was indicative of a viscous liquid-like film.[11,68] Interestingly, while the lateral friction signals showed a relaxation time between the elastic and plastic regimes, there was evidence of shear-thickening when a lateral velocity, v_l of 1918 nm/s was applied.[1,157,170] At this velocity, we believe that the long alkyl chains of the $[P_{6,6,6,14}]$ cation interdigitate and 'lock' and lead to the shear ratcheting seen in the lateral forces.

8 | Macroscale Tribological studies using a Tribometer

Having studied the IL solvent systems on the nanoscale setup in the SFB, it was found that when mixing ILs with solvents, there was a shift in the nanoscale behaviour. Importantly, in the case of $[C_4C_1P_{yrr}][TFSI]$-PC, by adding more and more solvent, the unique $[C_4C_1P_{yrr}][TFSI]$ friction characteristics were lost. In the $[P_{6,6,6,14}][(^iC_8)_2PO_2]$ system, while the 1 vol % did show good lubrication, it did not have the superlubricity that was present in both neat systems (pure $[P_{6,6,6,14}][(^iC_8)_2PO_2]$ and pure dodecane). These nanoscale experiments therefore do not show a positive result for those hoping ILs could be used as lubricant additives. However, as real

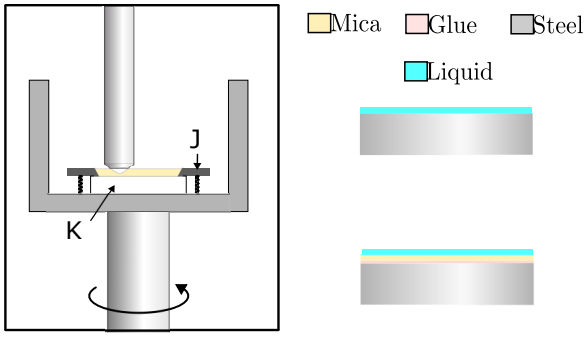


Figure 8.1: Image showing the side on of the tribometer apparatus as a cross-section of the liquid cup inset, where K is the solid substrate and J is the substrate clamp. The two different set-ups used in this thesis, steel-steel contact and mica-steel contact, are also shown

surfaces and real tribological systems are on the macroscale, it is important to see if these same nanoscale observations hold true on the macroscale. To investigate this, in this chapter we study a variety of IL- solvent systems in the TRB^3, shown in Figure 8.1.

Experiments were performed on four ILs, $[C_4C_1P_{yrr}][TFSI]$, $[P_{6,6,6,14}][(^iC_8)_2PO_2]$, $[P_{6,6,6,14}][TFSI]$ and $[P_{1,4,4,4}][TFSI]$, across their entire vol % range with a solvent.

$[C_4C_1P_{yrr}][TFSI]$ is studied across its whole vol % range with PC, while $[P_{6,6,6,14}][(^iC_8)_2PO_2]$, $[P_{6,6,6,14}][TFSI]$, and $[P_{1,4,4,4}][TFSI]$ are studied across their whole vol % range with dodecane. The chemical structure of $[P_{1,4,4,4}][TFSI]$ is shown below in Figure 8.2. All four IL-solvent systems were tested on both steel-steel and mica-steel contacts

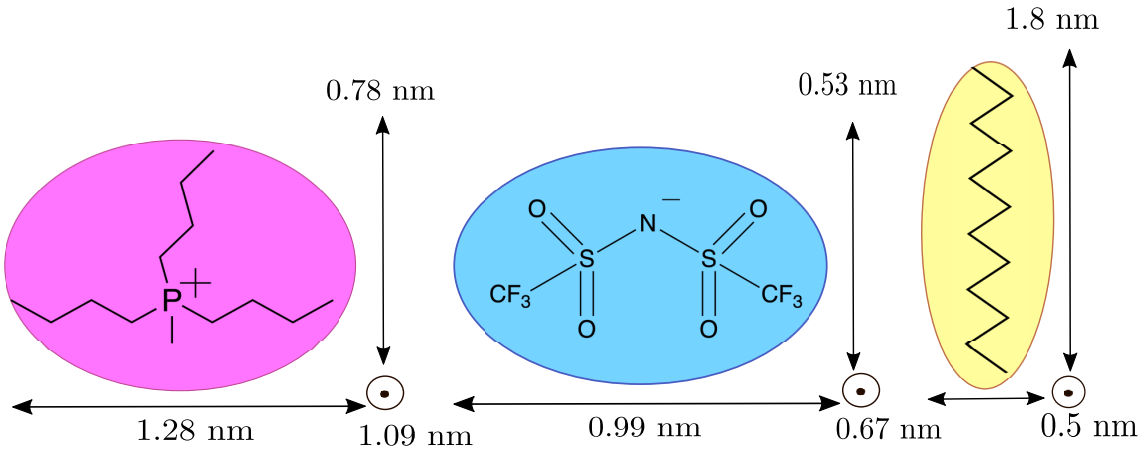


Figure 8.2: Chemical structure and sizes of $[P_{1,4,4,4}][TFSI]$ and Dodecane. Ion sizes are estimated from geometry, bond lengths and covalent radii, associated with the most stable configuration found by energy minimization. (Molecular weight, M_w,= 498 g/mol, density ρ = 1.260, viscosity η = 219 mPa s ion pair dimension D_m = 0.87 nm) and values are taken from[218]

at a rpm of 60, radius of 6.2 mm and speed of shearing of 0.05 ms^{-1}. Unfortunately, due to time restraints, it was not possible to quantitatively investigate surface wear by Atomic Force Microscopy (AFM) or tribochemistry by X-ray Photoelectron Spectroscopy (XPS). Instead, wear was measured qualitatively, by assessing the width and smoothness of the wear scar. The table below outlines where each IL-substrate system can be found in this chapter

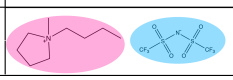
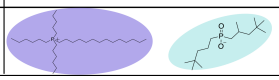
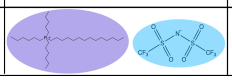
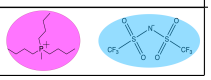
	Ionic Liquid			
Substrate	$[C_4C_1P_{yrr}][TFSI]$	$[P_{6,6,6,14}][^i(C_8)_2PO_2]$	$[P_{6,6,6,14}][TFSI]$	$[P_{1,4,4,4}][TFSI]$
Mica-Steel	8.1.1	8.2.1	8.3.1	8.4.1
Steel-Steel	8.1.2	8.2.2	8.3.2	8.4.2
Structure				

Figure 8.3: Table showing the organisation of sections within this Chapter.

8.1 | $[C_4C_1P_{yrr}][TFSI]$

8.1.1 | Mica-Steel contact

A plot of μ against volume fraction of $[C_4C_1P_{yrr}][TFSI]$ in PC for three different loads is shown in Figure 8.4(a). The trend observed in the mica-steel contact mea-

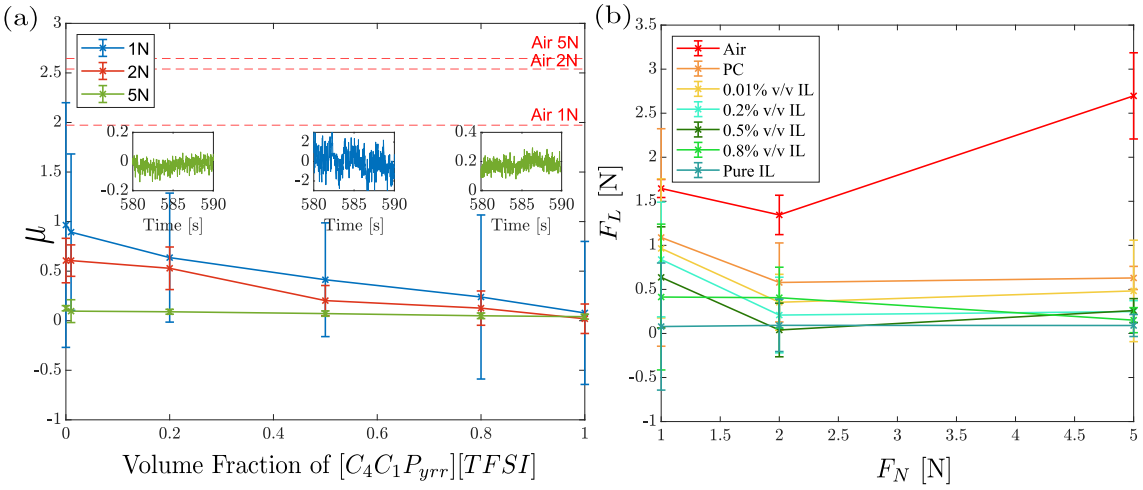


Figure 8.4: The friction response (a) in friction coefficient, and (b) in F_L, of $[C_4C_1P_{yrr}][TFSI]$ at varying volume fraction in PC for normal loads of 1 N, 2 N, and 5 N on a steel-mica contact.The insets show a raw friction trace for the indicated dilution and normal load.

surements is perhaps the expected outcome: as volume fraction of $[C_4C_1P_{yrr}][TFSI]$ is increased, the coefficient of friction and wear also decreased. This is a trend seen for all three normal loads used. Interestingly the value of μ seems dependent on the normal load, with higher μ being measured at 2 N and 5 N when compared to 1 N. This suggests that performance is not consistent at different loads. At the beginning of each measurement, the coefficient of friction generally shows a period of instability or wear-in period until a more steady-state value is reached: the phenomenon of wearing-in is something observed for all the ILs tested, regardless of normal load, dilution or surfaces in contact. The longevity of the steady-state period depends on the friction and wear performance of the lubricant. Deviation from steady state friction would result in either erratic friction or an increase in μ to a higher value, then becoming more stable again.

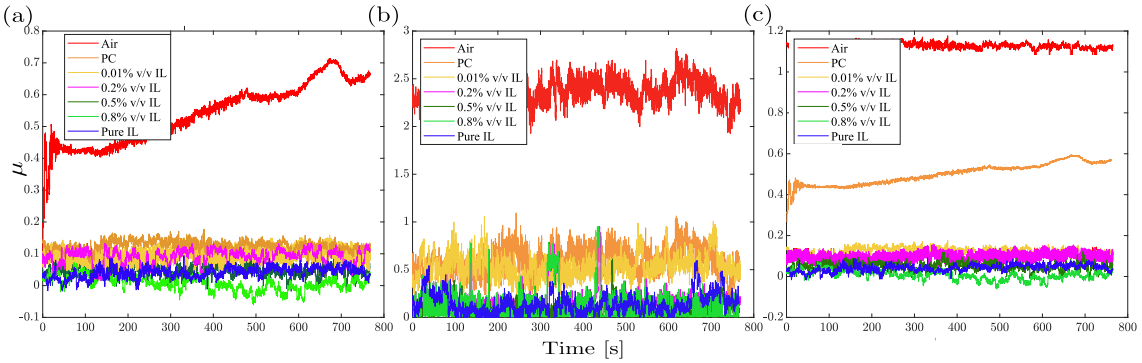


Figure 8.5: The friction response of $[C_4C_1P_{yrr}][TFSI]$ at varying volume fractions in PC for a normal load of in a mica-steel contact at (a) 1 N, (b) 2 N, and (c) 5 N.

Looking at the relationship between F_L and F_N, we see that the pure $[C_4C_1P_{yrr}][TFSI]$ overall has the most load-independent relationship, and measured lateral forces for this system are all ≈ 0.001, indicating a superlubric film. Importantly, when we do add 1 vol % to the PC film, the lateral force magnitude drops at all three measured loads, see Figure 8.5. This does mirror previous AFM results which again showed that a 1 in 100 dilution would produce favourable lubrication performance.[17,114]

When looking at the time-dependence of the friction coefficient μ at all loads, Figure 8.5(a-c), we can clearly see that all lubricant systems show a marked improvement from dry air sliding, and that adding 1 vol % did have a tangible impact.

Finally, at 5 N, see Figure 8.5(c), the influence of addition of 1 vol % $[C_4C_1P_{yrr}][TFSI]$ is very clearly shown, where the measured μ sharply drops from the pure PC (μ =0.4) to the 0.01 % v/v $[C_4C_1P_{yrr}][TFSI]$ (μ= 0.17).

8.1.2 | Steel-Steel contact

The steel-steel experiments closely mirrored those recorded on the mica-steel setup, see Figure 8.6(a). On the steel-steel, we do see higher friction forces at all loads and all mixtures, with the lowest recorded friction coefficient being 0.1, also see Appendix 10.1, 10.2, and 10.3. The increased friction forces on the steel-steel contact may be indicative of surface tribochemistry.[99,225,226] Indeed, previous XPS reports of imidazolium based cations found that when exposed to metal surface, $[C_4C_1P_{yrr}][TFSI]$

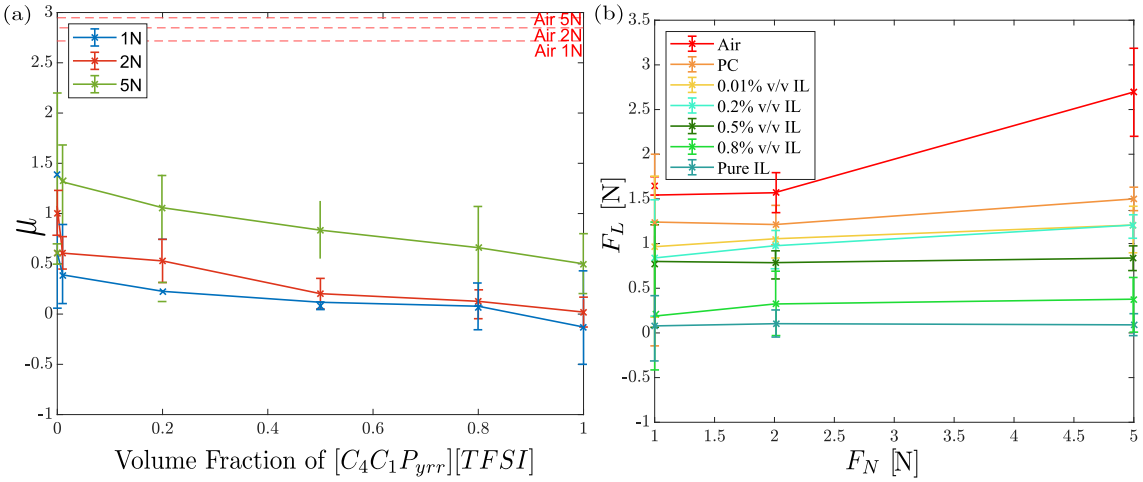


Figure 8.6: The friction response (a) in friction coefficient, and (b) in F_L, of $[C_4C_1P_{yrr}][TFSI]$ at varying volume fraction in PC for normal loads of 1 N, 2 N, and 5 N on a steel-steel contact.

had reacted,[99,225,226] and with this observation, and qualitative observations of the rough wear scars, we can infer that $[C_4C_1P_{yrr}][TFSI]$ broke down as a result of these high pressures, see Figure 8.8(d).[94,227]

8.2 | $[P_{6,6,6,14}][(^iC_8)_2PO_2]$

8.2.1 | Mica-Steel contact

A plot of μ against volume fraction of $[P_{6,6,6,14}][(^iC_8)_2PO_2]$ in dodecane for three different loads is shown in Figure 8.7(a). Interestingly the value of μ is similar at each load for a given dilution which suggests consistent performance by the $[P_{6,6,6,14}][(^iC_8)_2PO_2]$ lubricant system, which is a departure from $[C_4C_1P_{yrr}][TFSI]$.

Firstly, as shown, all lubricant mixtures, except pure dodecane, significantly reduced the wear and F_L compared to the measurements made in dry conditions. Secondly, there is an overall trend where the magnitude of F_L decreases with increases volume faction of $[P_{6,6,6,14}][(^iC_8)_2PO_2]$, see Figure 8.7(b) .

At 1 N applied load, we can see that our pure $[P_{6,6,6,14}][(^iC_8)_2PO_2]$ film outperforms all other films. However, at all loads, the pure PC film had similar performance to dry-air sliding, see Appendix 10.4, 10.5, and 10.6. This was because as the mica was

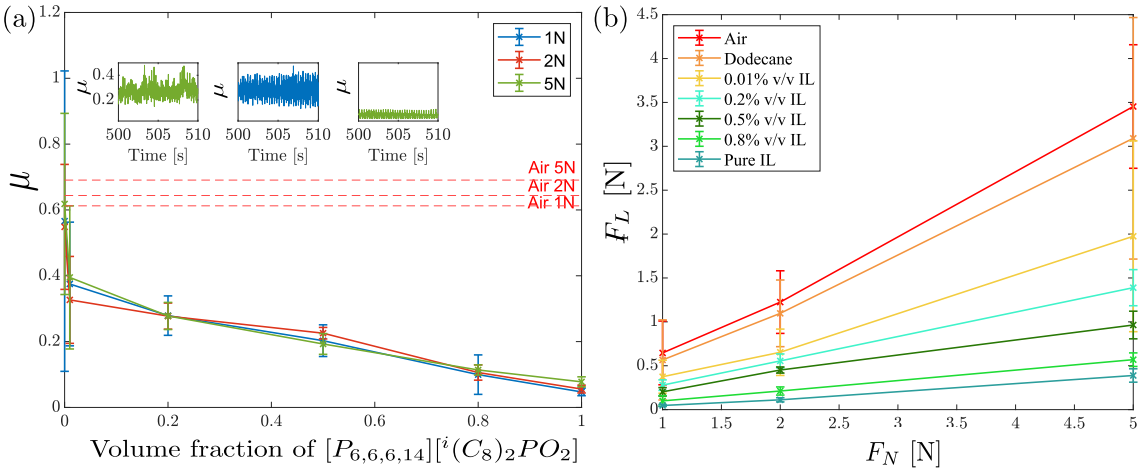


Figure 8.7: The frictional response, in (a) μ, and (b) F_L, of $[P_{6,6,6,14}][(^iC_8)_2PO_2]$ at varying volume fractions in dodecane for normal loads of 1 N, 2 N, and 5 N, on a mica-steel contact. The insets show a raw friction trace for the indicated dilution and normal load.

worn away, the mica formed a slurry with the dodecane and this was akin to liquid sandpaper, and rapidly increased the wear, see figure 8.8(b).[17] Appendix Figure

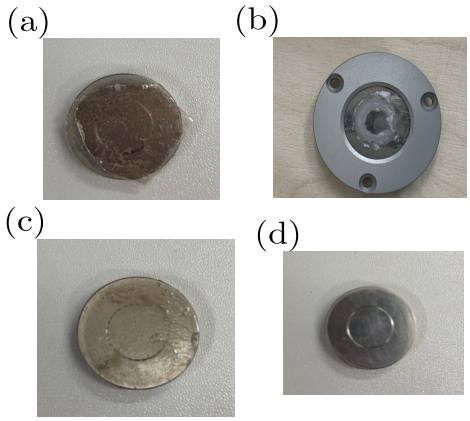


Figure 8.8: (a) Wear scar photo for a dilution of 1 vol % $[P_{6,6,6,14}][TFSI]$ in dodecane (b) photo of the slurry formed with $[P_{6,6,6,14}][(^iC_8)_2PO_2]$ in dodecane, (c) Photo of the slurry formed with $[P_{6,6,6,14}][(^iC_8)_2PO_2]$ in dodecane, and (d) Permanent wear scar photo after $[C_4C_1P_{yrr}][TFSI]$ in PC was subjected to a 5 N load.

10.4, 10.5, and 10.6 shows the measured friction coefficient μ as a function of time at all applied load across all $[P_{6,6,6,14}][(^iC_8)_2PO_2]$ films and a control measurement of air. Importantly, as we add 1 vol % $[P_{6,6,6,14}][(^iC_8)_2PO_2]$ to the dodecane, the average of the measured μ drops from ≈ 0.60 to ≈ 0.35, meaning that lubrication performance dramatically increases. This is another favourable result that indicates $[P_{6,6,6,14}][(^iC_8)_2PO_2]$'s use as an additive may be realistic.

However, at 5 N, Appendix 10.6, the PC film and the 1 vol % film begin to display unpredictable friction behaviour. Looking at the wear scars for these two systems it is clear that at 5 N, the mica is torn through and once more forms a slurry with the dodecane that increases friction, see Figure 8.8(c). This inconsistent behaviour is practically undesirable, and when inspected, the steel pucks which lay under the mica substrate also showed deep scarring, see Figure 8.8(c).

When more $[P_{6,6,6,14}][(^iC_8)_2PO_2]$ is added and the volume fraction increases to 2 vol %, the frictional response becomes more desirable and the average friction coefficient μ drops from 0.8 to 0.37, and continues to decrease with increasing volume fraction of $[P_{6,6,6,14}][(^iC_8)_2PO_2]$.

8.2.2 | Steel-Steel contact

Figure 8.9(a) shows a plot of μ against volume fraction of $[P_{6,6,6,14}][(^iC_8)_2PO_2]$ in dodecane for three different loads. The first point of note is that the same trend, as discussed for the mica-steel contact, exists for the steel-steel contact, albeit not as consistently between the normal loads at a given dilution. The values of μ are also

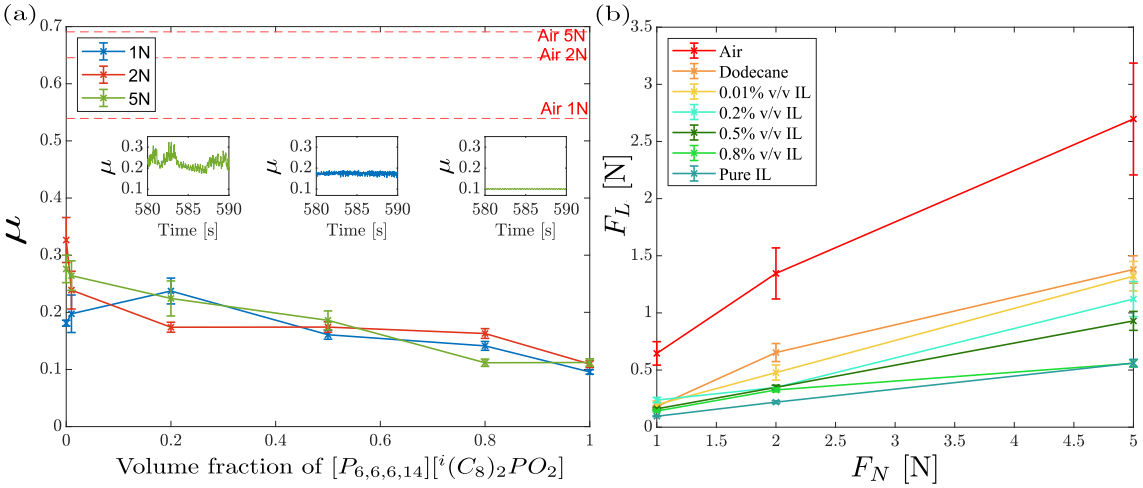


Figure 8.9: The frictional response, in (a) μ, and (b) F_L, of $[P_{6,6,6,14}][(^iC_8)_2PO_2]$ at varying volume fractions in dodecane for normal loads of 1 N, 2 N, and 5 N, on a steel-steel contact. The insets show a raw friction trace for the indicated dilution and normal load.

lower in this case as the steel substrate is harder and has a lower surface roughness

compared to worn mica, and is consistent with previous experiments, see Appendix 10.7, 10.8, and 10.9.

The friction and wear were significantly reduced compared to dry conditions for all lubricant mixtures, including pure dodecane. In spite of this, the friction and wear were higher in comparison to the the other ILs studied in this chapter.

From a practical note, of the four ILs tested on steel-steel contacts, this IL was the most miscible, providing complete mixing at all dilutions without the need for a water bath or sonication, meaning it interacts relatively strongly with dodecane.[17,115]

As a result of $[P_{6,6,6,14}][(^{i}C_8)_2PO_2]$'s stronger interaction with the dodecane, it is less able to form a protective boundary layer meaning lubrication performance was poorer. Whilst it is able to form a boundary layer, in a mixed lubrication regime the performance of its dilutions is perhaps hindered by its tremendous viscosity resulting in higher shear resistance. The higher dilutions of $[P_{6,6,6,14}][(^{i}C_8)_2PO_2]$ were closer in performance to the pure $[P_{6,6,6,14}][(^{i}C_8)_2PO_2]$ compared to the mica-steel contact, implying that boundary layer formation is improved for the steel contact. It is also possible that tribochemical reactions taking place also becomes a factor to consider,[98,116,179] and previous XPS studies have reported metal phosphates.[226,228]

For the 20 vol % dilution,see Figure 8.9(a) and (b), the lubricant performs better at 2 N than at 1 N, but at 5 N its performance is similar to 1 N. This indicates that the 2 N load is enough to initiate tribochemical reactions between $[P_{6,6,6,14}][(^{i}C_8)_2PO_2]$ and the steel; whereas at 1 N, the surface is merely protected by a boundary layer. At 5 N, however, it is imaginable that the tribofilm is unable to sustain the extra load resulting in similar performance to 1 N load.

Pure dodecane performed very well at 1 N, providing friction and wear performance comparable to 50 vol % of $[P_{6,6,6,14}][(^{i}C_8)_2PO_2]$. Although at higher loads, its performance was reduced, indicating an inability to sustain high normal loads and thus falls short compared to the pure $[P_{6,6,6,14}][(^{i}C_8)_2PO_2]$ and dilutions greater than 20

vol %.

8.3 | $[P_{6,6,6,14}][TFSI]$

8.3.1 | Mica-Steel contact

A plot of μ against volume fraction of $[P_{6,6,6,14}][TFSI]$ in dodecane for three different loads is shown in Figure 8.10(a). As shown, the dilutions of $[P_{6,6,6,14}][TFSI]$ all

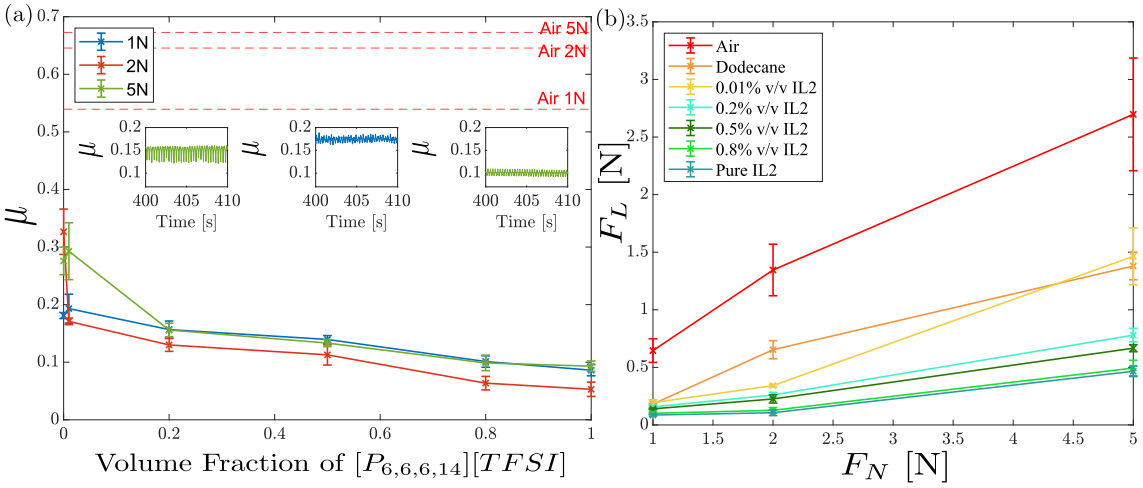


Figure 8.10: The frictional response of $[P_{6,6,6,14}][TFSI]$ at varying volume fractions in dodecane for normal loads of 1 N, 2 N, and 5 N at a mica-steel contact. The inset shows a raw friction trace for the indicated dilution and normal load.

represent an improvement from dry-air sliding. Additionally, the measured μ values at the volume fractions are similar for the different applied loads, showing that like $[P_{6,6,6,14}][(^{i}C_8)_2PO_2]$, $[P_{6,6,6,14}][TFSI]$ is a consistent lubricant When we add 1 vol % to dodecane, we do see a drop in the magnitude of F_L, and this trend continues with increasing volume fraction of $[P_{6,6,6,14}][TFSI]$.

At 1 N, when 1 vol % of $[P_{6,6,6,14}][TFSI]$ is added, there is a marked improvement and the 1 vol % has an average μ of 0.18, which is not too far off the average μ of the pure $[P_{6,6,6,14}][TFSI]$ system at 0.09, see Appendix Figure 10.7, 10.8, and 10.9.

Therefore the 1 in 100 dilution system does show good friction performance, and could be a cheap alternative to using the neat system. Moreover, these results show that while $[P_{6,6,6,14}][TFSI]$ may be an expensive system,[17] its superior lubrication

performance could be factored in, and depending on the use, could have a future as an industrial lubricant.

8.3.2 | Steel-Steel contact

Figure 8.11(a) represents the relationship between μ and volume fraction of $[P_{6,6,6,14}][TFSI]$ at three normal loads. Once again, the trend of μ increasing as the volume fraction of $[P_{6,6,6,14}][TFSI]$ is decreased is once more observed. The higher dilutions' performance was even closer to the pure IL. There is a slightly larger increase in μ from 20 vol % to 1 vol % than in the previous step which could imply that robust boundary layer formation is most affected between these dilutions. The performance of the

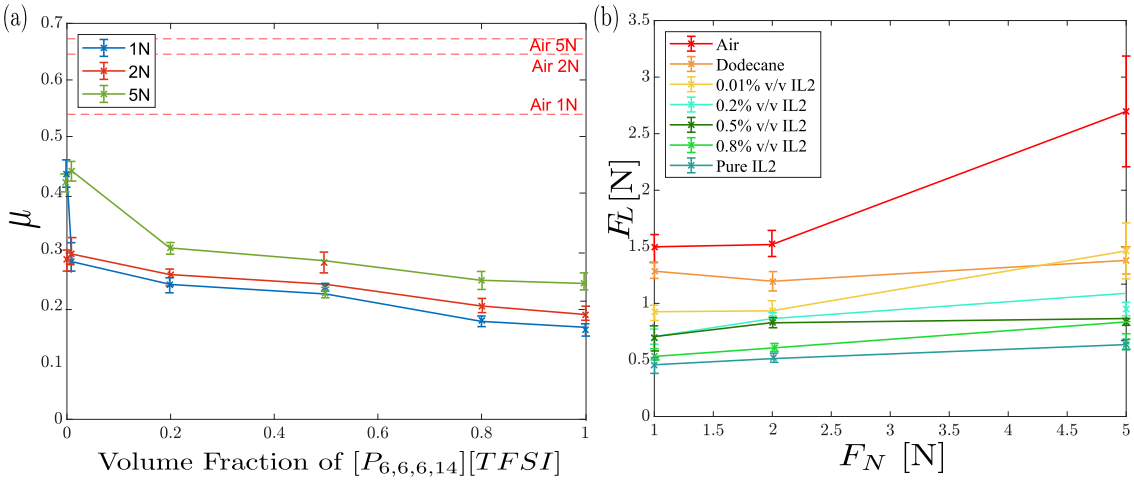


Figure 8.11: The frictional response, in (a) μ, and (b) F_L, of $[P_{6,6,6,14}][TFSI]$ at varying volume fractions in dodecane for normal loads of 1 N, 2 N, and 5 N, on a steel-steel contact.

$[P_{6,6,6,14}][TFSI]$ dilutions at different loads is very similar for 1 N and 5 N for all blends whereas the 2 N performance produced a value of μ around 0.03-0.05 lower, see Appendix 10.13 and 10.14. Similar to $[P_{6,6,6,14}][(^iC_8)_2PO_2]$, this suggests the involvement of tribochemistry and not just a boundary film. This is the case for every dilution which is perhaps due to the fluorine-containing TFSI anion which is known to be more reactive upon the shear-induced breakdown of the anion.[125] This could be confirmed by XPS.[125]

The dilutions' ability to maintain performance at 5 N load may also be attributed

to the long cation-alkyl chains which would help form a thick and smooth boundary layer via better self-assembly, aided by strong van der Waals interactions. The sharp increase in μ for 1 vol % at 5 N suggests that at 1 vol %, there is not a high enough concentration of $[P_{6,6,6,14}][(^iC_8)_2PO_2]$ to form a complete boundary layer. This poorly formed layer is unable to support the higher normal load and the ball penetrates the layer, resulting in greater steel-steel contact, leaving a wear scar resembling 8.8(d).

8.4 | $[P_{1,4,4,4}][TFSI]$

8.4.1 | Mica-Steel contact

A plot of μ against volume fraction of $[P_{1,4,4,4}][TFSI]$in dodecane for three different loads is shown in Figure 8.12(a). Once more, at all volume fractions of IL, the

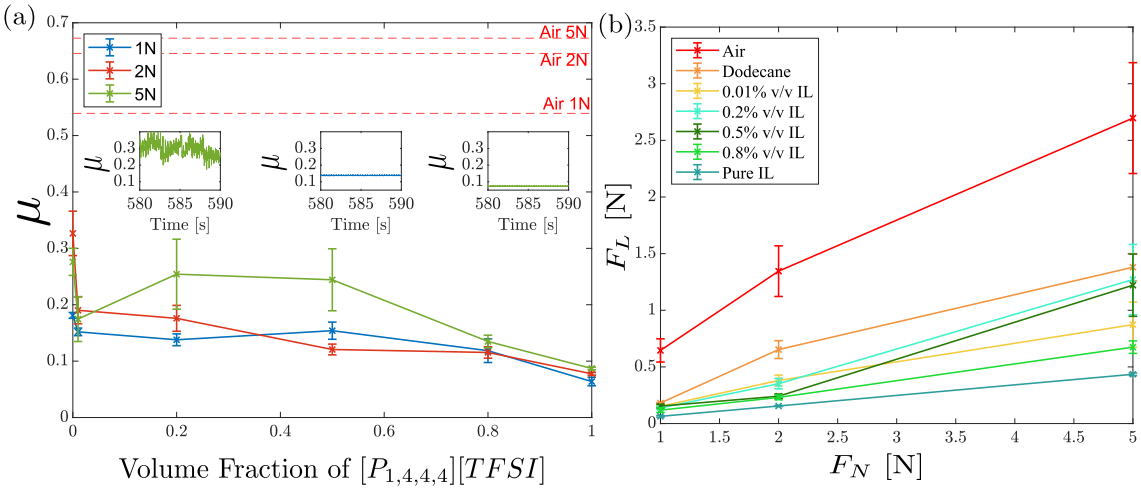


Figure 8.12: The frictional response of $[P_{1,4,4,4}][TFSI]$ at varying volume fractions in dodecane for normal loads of 1 N, 2 N, and 5 N at a mica steel-contact. The inset shows a raw friction trace for the indicated dilution and normal load.

lubrication performance of these $[P_{1,4,4,4}][TFSI]$ films is a massive improvement on dry air sliding.

However unlike the previous systems, there is no clear trend observed, as while overall μ is at a minimum in the neat $[P_{1,4,4,4}][TFSI]$ system, the friction coefficient actually increases with increasing volume fraction at some points, making this

film overall less reliable and consistent than the previous two phosphonium-based systems.

Looking at the μ v time trace,with increasing volume fraction of $[P_{1,4,4,4}][TFSI]$, the measured friction coefficients decrease, and the traces also become less chaotic making neat $[P_{1,4,4,4}][TFSI]$ a reliable lubricant. Interestingly, upon addition of 1 vol % to dodecane, there is not a sudden improvement in lubrication performance. However, when 20 vol % is added, the mixture does begin to show good lubrication performance with an average $\mu = 0.15$.

What sets the behaviour of $[P_{1,4,4,4}][TFSI]$ at 5 N apart is that the traces for 0.01, 0.2, and 0.5 v/v $[P_{4,4,4,1}][TFSI]$ are chaotic, see Appendix 10.16, 10.17, and 10.18, and this behaviour would not be suitable for any bespoke lubricant system.

8.4.2 | Steel-Steel contact

A plot of μ against volume fraction of $[P_{1,4,4,4}][TFSI]$ in dodecane for three different loads is shown in Figure 8.13(a). Similarly to the mica-steel system, the variation of μ with volume fraction was not consistent, once more showing the lack of reliable behavior in this particular liquid system. While at 1 N, its dilutions performed similarly in friction to $[P_{6,6,6,14}][TFSI]$ despite shorter cation-alkyl chains, at 2 N and 5 N the μ at some points increases with increasing $[P_{1,4,4,4}][TFSI]$ volume %. While at some volume %, the F_L did increase with the increasing load, for the 0.5 % system saw a decrease between 2 N and 5 N. However, at 1 vol %, the behaviour of the film returned to what was expected, and at 1 N and 2 N, the wear scar was also thin and smooth, see Figure 8.8(a).

8.5 | Summary

Overall, $[P_{6,6,6,14}][TFSI]$ and $[P_{1,4,4,4}][TFSI]$ were the most effective lubricants. They performed better than those of % of $[P_{6,6,6,14}][(^{i}C_8)_2PO_2]$ and $[C_4C_1P_{yrr}][TFSI]$in both friction and wear, reporting friction coefficients between 0.1 and 0.4, and no

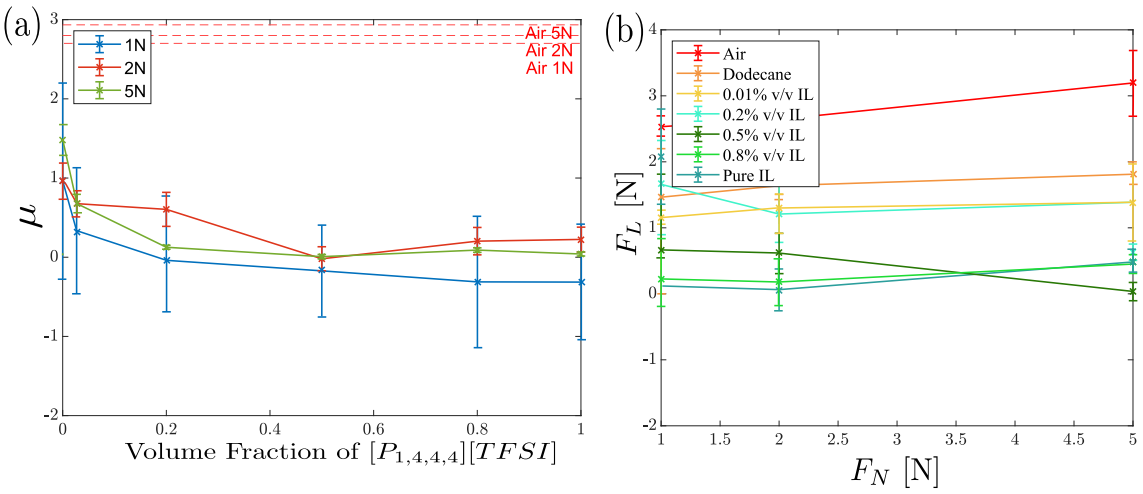


Figure 8.13: The frictional response, in (a) μ, and (b) F_L, of [$P_{1,4,4,4}$][TFSI] at varying volume fractions in dodecane for normal loads of 1 N, 2 N, and 5 N, on a steel-steel contact.

observable wear scars. This overall observation had already been reported by Cooper *et al* when they studied the neat liquids, and these results show it continues even with diluted in a base oil.[127]

These two ILs was slightly less miscible with dodecane, a result that proved a problem when trying to study I[$P_{6,6,6,14}$][TFSI] mixed with dodecane in the SFB. For [$P_{6,6,6,14}$][TFSI], the lower dilutions formed short-lived micro-emulsions whilst mixing,[208] and this may be due to the more densely charged TFSI anion when compared to the [$P_{6,6,6,14}$][($^{i}C_8$)$_2$$PO_2$] anion. Hence, the ions do not interact as strongly with the dodecane and are more able to form a complete boundary layer, and it did so in both the mica-steel and steel-steel contacts. The lower viscosity of this IL (η = 312 mPa s)[229] and of its dilutions compared to % of [$P_{6,6,6,14}$][($^{i}C_8$)$_2$$PO_2$] dilutions made it more successful for a mixed lubrication regime.

[$C_4C_1P_{yrr}$][TFSI] was the worst performing of the four ILs due to the TFSI anion and its shorter cation-alkyl chains; it was also the least viscous (74 mPa s).[78]This is deviation from the nanoscale studies, where [$C_4C_1P_{yrr}$][TFSI] had magnitudes lower friction coefficients than both [$P_{6,6,6,14}$][($^{i}C_8$)$_2$$PO_2$] and [$P_{6,6,6,14}$][TFSI]. This is likely to be due to the fact that while [$C_4C_1P_{yrr}$][TFSI] may be an excellent boundary lubricant in the SFB, the deep wear scars indicated that at these higher pressures,

it is easily squeezed out. Direct comparison between the neat $[P_{6,6,6,14}][TFSI]$ and $[C_4C_1P_{yrr}][TFSI]$ indicates that the change in cation was able to improve performance, and this is likely due to the longer-alkyl chains being able to adhere more effectively to both the steel and mica surfaces.[210] Considering the benefit of miscibility with oils, $[P_{6,6,6,14}][(^iC_8)_2PO_2]$, $[P_{6,6,6,14}][TFSI]$, and $[P_{1,4,4,4}][TFSI]$ and similar analogues can be identified as being future lubricant additives.[7]

Therefore, these tribometer results indicate that at the macroscale at least, there is a future for oil-soluble ILs as lubricant additives. Importantly, in all the liquids studied, even the addition of 1 vol % of all the ILs led to a drastic improvement in the lubrication.

9 | Conclusions and Outlook

The work in this thesis explored the structural and tribological properties of IL films. Of particular interest to this thesis was how these properties would be affected by dilution of our IL films with solvents. The study of the behaviour of diluted IL films is an important one, as while neat ILs may posses physiochemical characteristics which set them apart from trditional lubricants, the costs associated with using ILs holds them back from having any practical wide-scale industrial use. To investigate if ILs could one day become a lubricant additive, this thesis studied the lubrication of four IL-solvent mixtures on both the nanoscale, via the SFB, and the macroscale, via the TRB.

9.0.1 | Surface Forces Balance

Firstly, the normal forces of $[C_4C_1P_{yrr}][TFSI]$ mixed with PC were studied in Chapters 4 and 5. As previously concluded, the confined films of $[C_4C_1P_{yrr}][TFSI]$ did adopt odd-integer cation-anion-cation layers in the salt-dominant regime and transitioned to an all integer layering profile as the systems became solvent-dominant. This was reflected in the "switch" in the oscillatory wavelength from $\lambda_{osc} = 0.71$ nm to $\lambda_{osc} = 0.45$ nm, and notably this was a discontinuous switch.[90,91] When looking at the nanoscale friction behaviour, which are the first SFB or AFM reports of the $[C_4C_1P_{yrr}][TFSI]$-PC system, it was clear that the change in the structural forces also manifested in the frictional forces. This is a key conclusion of this work, and corroborates with simulation studies using ACN as the solvent.[230]

Importantly, these nanotribological results show that on addition of the polar solvent, the liquid films lose the unique frictional characteristics of IL films.[90,91,230] With increasing amounts of PC, our results found that while quantised friction was still present, i.e. a discrete linear relationship between F_S and F_N at discrete film

thicknesses, the friction coefficient, μ, itself did not vary with the changing number of IL layers.[178] This was different to what had previously been observed in pure IL systems, and in the experiments on the "salt dominant" $[C_4C_1P_{yrr}][TFSI]$.[11,19,103] In this thesis, we suggest that this is a result of the changing structure of our liquid films as the increasing content of PC begins to dominate and shifts the frictional forces from being similar to that of a highly-structured IL to a simple molecular liquid.[74–76,170,178,183] A finding such as this one suggests that more work needs to be done to examine the relationship between the structural and friction forces of ILs.

The need for this exploration was also clear from the results of $[P_{6,6,6,14}][(^iC_8)_2PO_2]$ and $[P_{6,6,6,14}][TFSI]$ when mixed with a model base oil, dodecane, shown in Chapters 6 and 7. While these experiments were initially inspired by AFM experiments carried out by Atkin,[114,117,118,127,128,217,218] the results from the SFB were drastically different.

In Chapters 6 and 7, the normal force profiles of dilutions of $[P_{6,6,6,14}][(^iC_8)_2PO_2]$ in dodecane and pure $[P_{6,6,6,14}][TFSI]$ were measured for the first time by the SFB, exhibiting a long-range monotonic repulsion distinct from the oscillatory profiles seen for other ILs in the literature.[62,71,91] Instead, it suggests an amorphous film structure exists. The detailed shear response of these dilutions were also measured, revealing relatively high coefficients of friction, which were much greater than those also reported in those initial AFM experiments.[114,117,118,127,128,217,218] The differences between the SFB results and those reported in the AFM can be reasoned by taking into account the much smaller contact area that the AFM tip can explore,[11] and highlights the importance of using nanoscale methodologies in tandem to get a complete picture of the structural and frictional forces.

The friction results for the $[P_{6,6,6,14}][(^iC_8)_2PO_2]$ in dodecane and pure $[P_{6,6,6,14}][TFSI]$, specifically the variation of μ with shearing velocity and the slow relaxation timescales did indicate that with its high viscosity $[P_{6,6,6,14}][(^iC_8)_2PO_2]$ is more a hydrodynamic lubricant than a boundary lubricant.[1,188] The behaviour at three different shear-

ing velocities indicated that the long-alkyl chains of the $[P_{6,6,6,14}][(^iC_8)_2PO_2]$ cation were prone to interdigitation or "shear-thickening" [1,157,184,221] at a critical v_s at 1310 nm/s, and it was reasoned that this seeming interplay of the alkyl-chain interdigitation indicated that the shearing was located within the film, and not along the mica surfaces. In recent years, the manipulation of "shear-thickening" has become an industry of its own, with "shear-thickening fluids", STF's, having a wide range of applications,,[184,221] and this could be another future use of ILs.

9.0.2 | Tribometer

Chapter 8 focussed on the macorscale friction measurements. These measurement, across a range of dilutions of $[C_4C_1P_{yrr}][TFSI]$ in PC, and $[P_{6,6,6,14}][(^iC_8)_2PO_2]$, $[P_{6,6,6,14}][TFSI]$, and $[P_{1,4,4,4}][TFSI]$ in dodecane demonstrated the importance of boundary layer formation for a many-asperity contact. The range in which the critical volume fraction of IL needed to maintain good friction and wear performance was also indicated by these experiments. The appreciable difference in friction and wear between a mica-steel contact and a steel-steel contact underlines how specific to an environment the friction response can be and hence why the study of friction is so challenging.

To compare friction at the nanoscale and at the macroscale, we must consider the lubrication regimes in which the measurements are recorded. In the SFB measurements, from the small surface separation and the atomic-smoothness of the mica, it is evident that we are probing a boundary lubrication regime for $[C_4C_1P_{yrr}][TFSI]$, and a hydrodynamic regime for $[P_{6,6,6,14}][(^iC_8)_2PO_2]$, and $[P_{6,6,6,14}][TFSI]$.

At the macroscale, while we are not controlling for surface separation, we are likely to be probing magnitudes greater length-scales. More importantly, the contact between surfaces is on many asperities rather than the single asperity contact of the SFB,[152] and the high normal loads distributed over these asperities produce contact pressures on the order of 10^9 Pa.[98] While the high friction coefficients and high con-

tact pressures seen in the tribometer may imply that we are probing the boundary regime, the implied additional influence of the viscosities of our IL dilutions may instead demonstrate we are probing a mixed lubrication regime, as a pure boundary layer lubrication regime would be independent of a dilution's bulk viscosity.[127] However, this change is tied to the cationic and anionic make-up of the various liquids, and it is difficult to divorce the effects of the viscosity from the effects of the chemical structure. For these reasons, it may be best to say that we are probing a 'hybrid' system thats sits between the boundary and mixed lubrication regimes.

Looking at our own results, the coefficients of friction measured on the nanoscale and the macroscale do seem to reflect the difference in the experimental set-ups. The coefficients of friction measured on the SFB for $[P_{6,6,6,14}][TFSI]$ and $[P_{6,6,6,14}][(^{i}C_8)_2PO_2]$ are significantly higher than the corresponding dilution measured on the tribometer for both mica-steel and steel-steel contacts, while much lower than those obtained for $[C_4C_1P_{yrr}][TFSI]$. We propose that these differences are a consequence of the different friction regimes being probed in the nanoscale and macroscale measurements.

At the nanoscale, the IL layering, and in the case of $[P_{6,6,6,14}][(^{i}C_8)_2PO_2]$ and $[P_{6,6,6,14}][TFSI]$, the interdigitation of alkyl chains are key. In the SFB, the more IL-dominant dilutions have higher viscosity and these produce higher shear resistance as a result of a highly amorphous, interdigitated bulk structure where energy dissipation arises from a viscous relaxation of the film. This leads to the $[P_{6,6,6,14}][TFSI]$ and $[P_{6,6,6,14}][(^{i}C_8)_2PO_2]$ films being ineffective boundary lubricants when compared to the more ordered $[C_4C_1P_{yrr}][TFSI]$.In the $[C_4C_1P_{yrr}][TFSI]$ film, the highly ordered alternating cation-anion layers provide accessible shear planes.

At the macroscale, adhesion to the surfaces and the viscosity contribution are the principle factors. Although, the viscosity contribution is more important when drawing comparisons between dilutions of different ILs, and we saw the high viscosity of $[P_{6,6,6,14}][(^{i}C_8)_2PO_2]$ negatively impacting its performance when compared to $[P_{6,6,6,14}][TFSI]$ and $[P_{1,4,4,4}][TFSI]$, the pivotal element for lubrication performance

at this length scale is the ability to resist the high pressures, and the more complete and robust the liquid film and its adhesion to the surfaces, the better friction and wear performance is observed.[7,15,228] Consequently, reducing the concentration of IL results in poorer performance, and we see more dramatic improvements on this length scale that what we saw at the nanoscale. Importantly, in these macroscale experiments, our IL dilutions consistently outperformed dodecane, opposite to what was seen in the SFB.

The study of dilutions of $[P_{6,6,6,14}][(^{i}C_8)_2PO_2]$, $[P_{6,6,6,14}][TFSI]$, and $[P_{1,4,4,4}][TFSI]$ in dodecane elucidated how the macroscopic friction response was affected by changing the anion present and reducing the cation-alkyl chain length. Considering the results of both the nanotribology and macrotribology experiments illuminates the role of ion structure and bulk properties in frictional behaviour, it is suggested that a more systematic study of this at both the nanoscale and macroscale is performed. Despite several studies of frictional behaviour in ILs or IL/oil mixtures at either the macroscale or nanoscale,[19,98,99,228]there are few studies that investigate both length-scales, and currently none using the SFB. Those that do focus solely on pure ILs rather than ILs as additives, and as already highlighted, this is where ILs are likely to find their most practical use.

9.0.3 | Outlook

ILs have become one of the most widely-studied and remarked upon electrolyte-systems in the last 20 years.One of the most important aspects of ILs is their conductivity and their relationship with a charged surface. While the SFB experiments presented in this work did make use of a negatively charged mica surface, this surface charge was not controlled.[192] A future direction of the work carried out in this thesis would involve the use of charge controlled surfaces, and indeed there have already been experiments on pure ILs that show that when confined by these charged surfaces, both the structural and frictional forces can be influenced.[67,118,192] Specif-

ically, work by Bresme *et al* showed that IL friction is electrotuneable.[224,230–233] Therefore, by using an alternative SFB setup, such as the mica-gold asymmetric system[67] or triple gold setup,[192] the electrotunability of IL mixtures could similarly be examined.

While the macroscale experiments did indicate that ILs can significantly influence the lubrication of majority oil systems, further work can be done. Firstly, the use of XPS[7,179] or time of flight ion mass spectroscopy[7,227] would be useful to confirm if there was indeed any tribochemistry at the surface, as the chemical stability of any lubricant system will need to be heavily characterised before any wide-scale industrial use is suggested.[7,18,234] Similarly, the use of TEM[7] and FIB SEM[7,229] would be useful to properly characterise those wear scars displayed in Chapter 8.

Finally, this thesis showed that it is important that a combination of both macroscale and nanoscale tribological studies are required to effectively measure the potential for ILs as lubricants or lubricant additives. As discussed above, however, these two systems are drastically different, and one of the future challenges will be developing a more exhaustive relationship between nanoscale friction and macroscale friction. One such experimental set-up that can be used to link the real-world tribological surfaces to the controlled SFB surfaces could be the use of metallic surfaces.[235]

Bibliography

[1] Israelachvili, J. N. *Intermolecular and Surface Forces, Third Edition: Revised Third Edition*; Academic Press: Oxford, 2011.

[2] Milnes-Smith, E.; Stone, C. A.; Willis, C. R.; Perkin, S. *Langmuir* **2022**, *38*, 4657–4668, PMID: 35395153.

[3] Fedorov, M. V.; Kornyshev, A. A. *Chemical Reviews* **2014**, *114*, 2978–3036, PMID: 24588221.

[4] Silvester, D. S.; Compton, R. G. *Zeitschrift für Physikalische Chemie* **2006**, *220*, 1247–1274.

[5] Bowden, F.; Tabor, D. *The Friction and Lubrication of Solids*; Clarendon Press: Oxford, 1950.

[6] Jost, P. *Lubrication (Tribology) - A report on the present position and industry's needs* **1966**,

[7] Somers, A. E.; Howlett, P. C.; MacFarlane, D. R.; Forsyth, M. *Lubricants* **2013**, *1*, 3–21.

[8] Nosonovsky, M. *Tribology Online* **2007**, *2*, 44–49.

[9] Holmberg, K.; Erdemir, A. *Friction* **2017**, *5*, 263–284.

[10] Hu, D. L.; Nirody, J.; Scott, T.; Shelley, M. J. *Proceedings of the National Academy of Sciences* **2009**, *106*, 10081–10085.

[11] Lhermerout, R.; Perkin, S. *Phys. Chem. Chem. Phys.* **2020**, *22*, 455–466.

[12] Davison, C. *Wear* **1958**, *2*, 59–63.

[13] Astruc, L.; Vargiolu, R.; Zahouani, H. *Wear* **2003**, *255*, 341–347, 14th International Conference on Wear of Materials.

[14] Zhou, F.; Liang, Y.; Liu, W. *Chemical Society Reviews* **2009**, *38*, 2590–2599.

[15] Canter, N. *Tribology & Lubrication Technology* **2005**, *61*, 15.

[16] Luo, J.; Liu, M.; Ma, L. *Nano Energy* **2021**, *86*, 106092.

[17] Qu, J.; Zhou, Y. *ACS Appl. Mater. Interfaces* **2017**, *9*, 3209–3222.

[18] Tang, Z.; Li, S. *Current Opinion in Solid State & Materials Science* **2014**, *18*, 119–139.

[19] Diederichs, C.; Lhermerout, R.; Perkin, S. *Lubricants* **2018**, *6*.

[20] Minami, I. *Molecules* **2009**, *14*, 2286–2305.

[21] Chen, Y.; Liu, W.; Ye, C.; Yu, L. *Chem. Commun.* **2001**, 2244–2245.

[22] Li, H.; Ibrahim, M.; Agberemi, I.; Kobrak, M. N. *The Journal of Chemical Physics* **2008**, *129*, 124507.

[23] Welton, T. *Biophys. Rev.* **2018**, *10*, 691–706.

[24] Lei, Z.; MacFarlane, D.; Chen, B.; Koo, Y.-M. *Chemical Reviews*

[25] Armand, M.; Endres, F.; MacFarlane, D. R.; Ohno, H.; Scrosati, B. *Nature Materials* **2009**, *8*, 621–629.

[26] Banquy, X.; Dobbs, H. A.; Gebbie, M. A.; Israelachvili, J. M.; Lee, A. A.; Perkin, S.; Rutland, M. W.; Smith, A. M.; Valtiner, M.; Warr, G. G. *Chem. Commun.* **2017**, *53*, 1214–1224.

[27] Shim, Y.; Kim, H. J. *ACS Nano* **2010**, *4*, 2345–2355, PMID: 20359243.

[28] Bermúdez, M.-D.; Jiménez, A.-E.; Sanes, J.; Carrión, F.-J. *Molecules* **2009**, *14*, 2888–2908.

[29] Ye, C.; Liu, W.; Chen, Y.; Yu, L. *Chem. Commun.* **2001**, 2244–2245.

[30] Bermúdez, M.-D.; Jiménez, A.-E.; Sanes, J.; Carrión, F.-J. *Molecules* **2009**, *14*, 2888–2908.

[31] Canongia Lopes, J. N. A.; Pádua, A. A. H. *The Journal of Physical Chemistry B* **2006**, *110*, 3330–3335.

[32] Gontrani, L.; Russina, O.; Lo Celso, F.; Caminiti, R.; Annat, G.; Triolo, A. *The Journal of Physical Chemistry B* **2009**, *113*, 9235–9240, PMID: 19527015.

[33] Bhargava, B. L.; Devane, R.; Klein, M. L.; Balasubramanian, S. *Soft Matter* **2007**, *3*, 1395–1400.

[34] Santos, C. S.; Murthy, N. S.; Baker, G. A.; Castner, E. W. *The Journal of*

Chemical Physics **2011**, *134*, 121101.

[35] Li, S.; Bañuelos, J. L.; Guo, J.; Anovitz, L.; Rother, G.; Shaw, R. W.; Hillesheim, P. C.; Dai, S.; Baker, G. A.; Cummings, P. T. *The Journal of Physical Chemistry Letters* **2012**, *3*, 125–130.

[36] Wang, Y.; Voth, G. A. *Journal of the American Chemical Society* **2005**, *127*, 12192–12193, PMID: 16131175.

[37] Mezger, M.; Pontoni, D.; Roth, R.; Richert, H.; Schroder, H. *J. Chem. Phys.* **2015**, *142*, 164707.

[38] Chen, Y. J.; Cheng, H. W.; Dienemann, J. N.; Mezger, M.; Stock, P.; Valtiner, M.; Weiss, H. *Langmuir* **2018**, *34*, 2637–2646.

[39] Triolo, A.; Russina, O.; Bleif, H.-J.; Di Cola, E. *The Journal of Physical Chemistry B* **2007**, *111*, 4641–4644, PMID: 17388414.

[40] Perkin, S. *Phys. Chem. Chem. Phys.* **2012**, *14*, 5052–5062.

[41] Hayes, R.; El Abedin, S. Z.; Atkin, R. *The Journal of Physical Chemistry B* **2009**, *113*, 7049–7052, PMID: 19438273.

[42] Atkin, R.; Hayes, R.; Warr, G. G. *Chem. Rev.* **2015**, *115*, 6357–6426.

[43] Qu, J.; Blau, P. J.; Dai, S.; Luo, H.; Meyer III, H. M.; Truhan, J. J. *Wear* **2009**, *267*, 1226–1231.

[44] Cao, Y.; Mu, T. *Industrial & Engineering Chemistry Research* **2014**, *53*, 8651–8664.

[45] Minami, I.; Kamimura, H.; Mori, S. *Journal of Synthetic Lubrication* **2007**, *24*, 135–147.

[46] Neves, C. M.; Carvalho, P. J.; Freire, M. G.; Coutinho, J. A. *The Journal of Chemical Thermodynamics* **2011**, *43*, 948–957.

[47] Tokuda, H.; Hayamizu, K.; Ishii, K.; Susan, H.; Watanabe, M. *The Journal of Physical Chemistry B* **2005**, *109*, 6103–6110.

[48] N.J, P. B. *Sliding Friction:Physical Principles and Applications*; Springer Berlin: Heidelberg, 2000.

[49] Atkin, R.; Jiang, H. J.; Warr, G. G. *Current Opinion in Green and Sustainable Chemistry* **2018**, *12*, 27–32.

[50] Arcifa, A.; Ewoldt, R. H.; Jurado, L. A.; Espinosa-Marzal, R. M.; Kim, H.; Rossi, A.; Schuh, J. K.; Spencer, N. D. *Phys. Chem. Chem. Phys.* **2016**, *18*, 22719–22730.

[51] Bhushan, B.; Palacio, M. *J. Vac. Sci. Technol. A* **2009**, *27*, 986–995.

[52] Pu, J.; Wang, L.; Mo, Y.; Xue, Q. *Journal of Colloid and interface science* **2011**, *354*, 858–865.

[53] Zhao, W.; Wang, Y.; Wang, L.; Bai, M.; Xue, Q. *Colloids and Surfaces A: Physicochemical and Engineering Aspects* **2010**, *361*, 118–125.

[54] Zhou, H.; Rouha, M.; Feng, G.; Lee, S. S.; Docherty, H.; Fenter, P.; Cummings, P. T.; Fulvio, P. F.; Dai, S.; McDonough, J.; Presser, V.; Gogotsi, Y. *ACS Nano* **2012**, *6*, 9818–9827.

[55] Albrecht, T.; Klein, J.; Perkin, S. *Phys. Chem. Chem. Phys.* **2010**, *12*, 1243–1247.

[56] Zhang, X.; Zhong, Y.-X.; Yan, J.-W.; Su, Y.-Z.; Zhang, M.; Mao, B.-W. *Chem. Commun.* **2012**, *48*, 582–584.

[57] Kirchner, K.; Kirchner, T.; Ivaništšev, V.; Fedorov, M. *Electrochimica Acta* **2013**, *110*, 762–771.

[58] I. Koltover; S.H.J. Idziak; P. Davidson; Y. Li; C.R. Safinya; M. Ruths; S. Steinberg; J.N. Israelachvili *J. Phys. II France* **1996**, *6*, 893–907.

[59] Horn, R. G.; Evans, D. F.; Ninham, B. W. *The Journal of Physical Chemistry* **1988**, *92*, 3531–3537.

[60] Christenson, H.; Horn, R. *Chemical Physics Letters* **1983**, *98*, 45–48.

[61] Browning, K. L.; Clarke, S. M.; Griffin, L. R.; Norman, S. E.; Perkin, S.; Smith, A. M.; Skoda, M. *Phys. Chem. Chem. Phys.* **2017**, *19*, 297–304.

[62] Atkin, R.; Warr, G. G. *J. Phys. Chem. C.* **2007**, *111*, 5162–5168.

[63] Mezger, M.; Schröder, H.; Reichert, H.; Schramm, S.; Okasinski, J. S.;

Schöder, S.; Honkimäki, V.; Deutsch, M.; Ocko, B. M.; Ralston, J.; Rohwerder, M.; Stratmann, M.; Dosch, H. *Science* **2008**, *322*, 424–428.

[64] Crowhurst, L.; Gosvami, N. N.; Niedermeyer, H.; Perkin, S.; Smith, A. M.; Welton, T. *Chemical Communications* **2011**, *47*, 6572–6574.

[65] Goriely, A.; Lee, A. A.; Perkin, S.; Vella, D. *J. Chem. Phys.* **2014**, *141*, 094904.

[66] Crowhurst, L.; Deyko, A.; Maier, F.; Perkin, S.; Rietzler, F.; Steinruck, H.-P.; Welton, T. *J. Phys. Chem. C.* **2013**, *117*, 5101–5111.

[67] Perez-Martinez, C. S.; Perkin, S. *Soft Matter* **2019**, *15*, 4255–4265.

[68] Perez-Martinez, C. S.; Perkin, S. *Langmuir* **2019**, *35*, 15444–15450.

[69] Bennewitz, R.; Hausen, F.; Hoth, J.; Muser, M. H. *J. Phys. Condens. Matter* **2014**, *26*, 284110.

[70] Dolan, A.; Gosvami, N. N.; Lovelock, K. R.; Perkin, S.; Smith, A. M.; Welton, T. *J. Phys. Chem. Lett.* **2013**, *4*, 378–382.

[71] Lovelock, K. R.; Perkin, S.; Smith, A. M. *Faraday Discussions* **2013**, *167*, 279.

[72] Parkes, M. A.; Perkin, S.; Smith, A. M. *J. Phys. Chem. Lett* **2014**, *5*, 4032–4037.

[73] Lynden-Bell, R.; Madden, P.; Perkin, S.; Salanne, M. *PNAS* **2013**, *110*, E4121.

[74] Klein, J.; Kumacheva, E. *J. Chem. Phys.* **1998**, *108*, 6996–7009.

[75] Klein, J.; Kumacheva, E. *J. Chem. Phys.* **1998**, *108*, 7010–7022.

[76] Klein, J.; Kumecheva, E. *Science* **1995**, *269*, 816–819.

[77] Blahušiak, M.; Štefan Schlosser *The Journal of Chemical Thermodynamics* **2014**, *72*, 54–64.

[78] Lhermerout, R.; Perkin, S. *Phys. Rev. Fluids* **2018**, *3*.

[79] Yu, G.; Zhao, D.; Wen, L.; Yang, S.; Chen, X. *AIChE Journal* **2012**, *58*, 2885–2899.

[80] Chan, D. Y. C.; Horn, R. G. *The Journal of Chemical Physics* **1985**, *83*, 5311–5324.

[81] Wang, Y.; Pilkington, G. A.; Dhong, C.; Frechette, J. *Current Opinion in Colloid and Interface Science* **2017**, *27*, 43–49.

[82] Banquy, X.; Gebbie, M. A.; Henderson, W. A.; Israelachvili, J. N.; Valtiner, M. *PNAS* **2013**, *110*, 9674–9679.

[83] Alcalde, R.; Aparcio, S.; Atilhan, M.; Gutierrez, A.; Trenzado, J. *Journal of Molecular Liquids* **2019**, *294*, 111632.

[84] McEwen, A. B.; Ngo, H. L.; LeCompte, K.; Goldman, J. L. *Journal of The Electrochemical Society* **1999**, *146*, 1687.

[85] Zhu, Y.; Murali, S.; Stoller, M. D.; Ganesh, K. J.; Cai, W.; Ferreira, P. J.; Pirkle, A.; Wallace, R. M.; Cychosz, K. A.; Thommes, M.; Su, D.; Stach, E. A.; Ruoff, R. S. *Science* **2011**, *332*, 1537–1541.

[86] Pivnic, K.; Bresme, F.; Kornyshev, A. A.; Urbakh, M. *Langmuir* **2019**, *35*, 15410–15420.

[87] Fendt, S.; Padmanabhan, S.; Blanch, H. W.; Prausnitz, J. M. *Journal of Chemical & Engineering Data* **2011**, *56*, 31–34.

[88] Seddon, K. R.; Stark, A.; Torres, M.-J. *Pure and Applied Chemistry* **2000**, *72*, 2275–2287.

[89] Philippi, F.; Rauber, D.; Eliasen, K. L.; Bouscharain, N.; Niss, K.; Kay, C. W. M.; Welton, T. *Chem. Sci.* **2022**, *13*, 2735–2743.

[90] Perkin, S.; Smith, A. M. *Phys. Rev. Lett.* **2017**, *118*.

[91] Coles, S. W.; Smith, A. M.; Fedorov, M. V.; Hausen, F.; Perkin, S. *Faraday Discussions* **2017**, *206*, 427–442.

[92] Pádua, A. A. H.; Costa Gomes, M. F.; Canongia Lopes, J. N. A. *Accounts of Chemical Research* **2007**, *40*, 1087–1096, PMID: 17661440.

[93] Christenson, H. K. *J. Chem. Soc., Faraday Trans. 1* **1984**, *80*, 1933–1946.

[94] Lu, Q.; Wang, H.; Ye, C.; Liu, W.; Xue, Q. *Tribology International* **2004**, *37*, 547–552.

[95] Atkin, R.; Cranston, E. D.; Rutland, M. W.; Warr, G. G.; Werzer, O. *Phys.*

Chem. Chem. Phys. **2012**, *14*, 5147–5152.

[96] Atkin, R.; El Abedin, S. Z.; Hayes, R.; Gasparotto, L. H.; Borisenko, N.; Endres, F. *The Journal of Physical Chemistry C* **2009**, *113*, 13266–13272.

[97] Hironaka, S. Boundary Lubrication and Lubricants. 2004.

[98] Otero, I.; López, E. R.; Reichelt, M.; Villanueva, M.; Salgado, J.; Fernández, J. *ACS Applied Materials & Interfaces* **2014**, *6*, 13115–13128.

[99] Jiménez, A.; Bermúdez, M.; Iglesias, P.; Carrión, F.; Martínez-Nicolás, G. *Wear* **2006**, *260*, 766–782.

[100] Bai, Y.; Cai, M.; Dong, R.; Ma, Z.; Liu, W.; Wu, Y.; Yu, B.; Yu, Q.; Zhang, C.; Zhou, F. *Chemical Engineering Journal* **2020**, *383*.

[101] Granick, S.; Greenfield, M.; Ohtani, H.; Ruths, M.; Zhu, Y. *Tribology Letters* **2003**, *15*, 127–134.

[102] de Freitas, A. A.; Perkin, S.; Lopes, J. N.; Shimzu, A. M., Karina Smith *J. Phys. Chem.* **2018**, *148*, 193808.

[103] Gosvami, N. N.; Lovelock, K. R.; Perkin, S.; Smith, A. M.; Welton, T. *Phys. Chem. Chem. Phys.* **2013**, *15*, 15317–15320.

[104] Xiao, H.; Guo, D.; Liu, S.; Pan, G.; Lu, X. *Tribology letters* **2011**, *41*, 471–477.

[105] Atkin, R.; Rutland, M. W.; Sweeney, J.; Webber, G. B. *Phys. Chem. Chem. Phys.* **2014**, *16*, 16651–16658.

[106] Arcifa, A.; Jurado, L.; Kim, H.; Leal, C.; Espinosa-Marzal, R. M.; Rossi, A.; Spencer, N. D. a. *Phys. Chem. Chem. Phys.* **2015**, *17*, 13613–13624.

[107] Israelachvili, J. N.; Pashley, R. M. *Journal of Colloid and Interface Science* **1984**, *101*, 511–523.

[108] Kawada, S.; Kodama, E.; Sato, K.; Ogawa, S.; Watanabe, M.; Okubo, H.; Sasaki, S. *Surface and Interface Analysis* **2019**, *51*, 17–20.

[109] Bresme, F.; Fajardo, O. Y.; Kornyshev, A. A.; Urbakh, M. *ACS Nano* **2017**, *11*, 6825–6831.

[110] Arcifa, A.; Espinosa-Marzal, R. M.; Rossi, A.; Spencer, N. D. *J. Phys. Chem.*

C. **2014**, *118*, 6491–6503.

[111] Espinosa-Marzal, R.; Han, M. *ACS Appl. Mater. Interfaces* **2019**, *11*, 33465–33477.

[112] Espinosa-Marzal, R. M.; Arcifa, A.; Rossi, A.; Spencer, N. D. *The Journal of Physical Chemistry Letters* **2014**, *5*, 179–184.

[113] Levins, J. M.; Vanderlick, T. K. *J. Colloid Interface Sci.* **2020**, *158*, 223.

[114] Atkin, R.; Cooper, P. K.; Forsyth, M.; Howlett, P. C.; Li, H.; Rutland, M. W.; Somers, A. E. *Phys. Chem. Lett.* **2014**, *5*, 4095–4099.

[115] Rodríguez-Escontrela, I.; Rodríguez-Palmeiro, I.; Rodríguez, O.; Arce, A.; Soto, A. *Colloids and Surfaces A: Physicochemical and Engineering Aspects* **2015**, *480*, 50–59.

[116] Forsyth, M.; Howlett, P. C.; Khemchandani, B.; MacFarlane, D. R.; Somers, A. E.; Sun, J. *ACS Appl. Mater. Interfaces* **2013**, *5*, 11544–11553.

[117] Atkin, R.; Cooper, P. K.; Cowie, S.; Li, H. *J. Phys. Chem. C.* **2017**, *121*, 28348–28353.

[118] Atkin, R.; Cooper, P.; Rutland, M.; Webber, G. *Phys. Chem. Chem.Phys.* **2016**, *18*, 23657–23662.

[119] Inada, T.; Minami, I.; Nanao, H.; Sasaki, R. *Tribol Lett* **2010**, *40*, 225–235.

[120] *Wear* **2006**, *261*, 1174–1179.

[121] Minami, I.; Kita, M.; Kubo, T.; Nanao, H.; Mori, S. *Tribology Letters* **2008**, *30*, 215–223.

[122] Yu, B.; Bansal, D. G.; Qu, J.; Sun, X.; Luo, H.; Dai, S.; Blau, P. J.; Bunting, B. G.; Mordukhovich, G.; Smolenski, D. *Wear* **2012**, *289*.

[123] Bermúdez, M.-D.; Jiménez, A.-E.; Sanes, J.; Carrión, F.-J. *Molecules* **2009**, *14*, 2888–2908.

[124] Qu, J.; Bansal, D. G.; Yu, B.; Howe, J. Y.; Luo, H.; Dai, S.; Li, H.; Blau, P. J.; Bunting, B. G.; Mordukhovich, G.; others *ACS Applied Materials & Interfaces* **2012**, *4*, 997–1002.

[125] Howlett, P. C.; Rutland, M. W.; Somers, A. E. *Tribol Lett* **2010**, *40*, 279–284.

[126] Liu, Z.; Song, Y.; Tse, J. *Tribology Lett* **2007**, *28*, 45–49.

[127] Atkin, R.; Aman, Z. M.; Cooper, P. K.; Li, H.; Staddon, J.; Zhang, S. *Frontiers in Chemistry* **2019**, *7*.

[128] Atkin, R.; Forsyth, M.; Howlett, P. C.; Li, H.; Rutland, M. W.; Somers, A. E. *Phys. Chem Chem. Phys.* **2016**, *18*, 6541–6547.

[129] Lee, A. A.; Perez-Martinez, C. S.; Perkin, S.; Smith, A. M. *Faraday Discuss,* **2017**, *199*, 239–259.

[130] Tabor, D.; Winterton, R. H. *Nature* **1968**, *219*, 1120.

[131] Horn, R. G.; Israelachvili, J. N. *J. Chem. Phys.* **1981**, *75*, 1400–1411.

[132] Derjaguin, B.; Landau, L. *Acta Physiochem* **1941**, *14*, 663–662.

[133] E.J, V. *J Phys Colloid Chem* **1947**, *51*, 631–636.

[134] Israelachvili, J. N. *Intermolecular and Surface Forces, Third Edition: Revised Third Edition*; Academic Press: Oxford, 2011.

[135] N., I. J.; E., A. G. *J. Chem. Soc., Faraday Trans* **1978**, *74*, 975–1001.

[136] Dzyaloshinskii, I.; Lifshitz, E.; Pitaevskii, L. *Advances in Physics* **1961**, *10*, 165–209.

[137] Chan, D. Y.; Pashley, R. M.; White, L. R. *Journal of Colloid and Interface Science* **1980**, *77*, 283–285.

[138] Horn, R.; Israelachvili, J. *Chemical Physics Letters* **1980**, *71*, 192–194.

[139] Klein, J.; Perkin, S. *Soft Matter* **2013**, *9*, 10438–10441.

[140] Akbulut, M.; Alig, A.; Carver, G.; Greene, W.; Israelachvili, J.; Kristiansen, K.; Meyer, E.; Min, Y.; Pesika, N.; Rosenberg, K.; Zeng, H. *Rep. Prog. Phys.* **2010**, *73*, 1–16.

[141] J., B.; A., C. N. E.; W., C. S.; van Engers C. D.; V., B.; T., M. A.; A., K.; S., P.; N., G. *Langmuir* **2014**, *30*, 11485.

[142] Mitchell, D. J.; Ninham, B. W.; Pailthorpe, B. A. *J. Chem. Soc., Faraday Trans. 2* **1978**, *74*, 1116–1125.

[143] Deyko, A.; Cremer, T.; Rietzler, F.; Perkin, S.; Crowhurst, L.; Welton, T.; Steinrück, H.-P.; Maier, F. *The Journal of Physical Chemistry C* **2013**, *117*, 5101–5111.

[144] Cremer, T.; Stark, M.; Deyko, A.; Steinrück, H.-P.; Maier, F. *Langmuir* **2011**, *27*, 3662–3671, PMID: 21361299.

[145] Mezger, M.; Schramm, S.; Schröder, H.; Reichert, H.; Deutsch, M.; De Souza, E. J.; Okasinski, J. S.; Ocko, B. M.; Honkimäki, V.; Dosch, H. *The Journal of Chemical Physics* **2009**, *131*, 094701.

[146] Lee, A. A.; Perkin, S.; Smith, A. M. *J. Phys. Chem. Lett.* **2016**, *7*, 2157–2163.

[147] Gebbie, M. A.; Dobbs, H. A.; Valtiner, M.; Israelachvili, J. N. *Proceedings of the National Academy of Sciences* **2015**, *112*, 7432–7437.

[148] de Carvalho, R. L.; Evans, R. *Molecular Physics* **1994**, *83*, 619–654.

[149] Groves, T. S.; Perez-Martinez, C. S.; Lhermerout, R.; Perkin, S. *The Journal of Physical Chemistry Letters* **2021**, *12*, 1702–1707, PMID: 33560858.

[150] Gao, J.; Luedtke, W.; Gourdon, D.; Ruths, M.; Israelachvili, J.; Landman, U. Frictional forces and Amontons' law: from the molecular to the macroscopic scale. 2004.

[151] Gaisinskaya-Kipnis, A.; Kampf, N.; Klein, J.; Ma, L. *Nature Communications* **2015**, *6*.

[152] Szlufarska, I.; Chandross, M.; Carpick, R. W. *Journal of Physics D: Applied Physics* **2008**, *41*, 123001.

[153] Manini, N.; Tosatti, E.; Urbakh, M.; Vanossi, A.; Zappieri, S. *85* **2013**, *Rev. Mod. Phys.*

[154] Mo, Y.; Szlurfarska, I.; Turner, K. T. *Nature* **2009**, *457*, 1116–1119.

[155] Wenning, L.; Müser, M. *EPL (Europhysics Letters)* **2001**, *54*, 693.

[156] Schwarz, U. D. *Journal of Colloid and Interface Science* **2003**, *261*, 99–106.

[157] Chen, Y.-L.; Israelachvili, J. N.; Yoshizawa, H. *J. Phys. Chem.* **1993**, *97*, 4128–4140.

[158] Borodich, F. *International Journal of Solids and Structures* **1993**, *30*, 1513–1526.

[159] Gourdon, J. N., Delphine Israelachvili; Klafter, J.; Urbakh, M. *Nature* **2004**, *430*, 525–528.

[160] Johnson, K. L.; Kendall, K.; Roberts, A. D. *Proceedings of the Royal Society of London Series A* **1971**, *324*, 301–313.

[161] Derjaguin, B.; Muller, V.; Toporov, Y. *Journal of Colloid and Interface Science* **1975**, *53*, 314–326.

[162] Luan, B.; Robbins, M. O. *Physical Review E* **2006**, *74*, 026111.

[163] Kampf, N.; Klein, J.; Yeredor, A.; Rosenhek-Goldian, I. *PNAS* **2015**, *112*, 7117–7122.

[164] Xu, R.-G.; Leng, Y. *Proceedings of the National Academy of Sciences* **2018**, *115*, 6560–6565.

[165] Berman, A. D.; Ducker, W. A.; Israelachvili, J. N. *Langmuir* **1996**, *12*, 4559–4563.

[166] Klein, J. *Phys. Rev. Lett.* **2007**, *98*, 056101.

[167] Thompson, P. A.; Robbins, M. O. *Science* **1990**, *250*, 792–794.

[168] Gourdon, D.; Israelachvili, J. N. *Physical Review E* **2003**, *68*.

[169] Lei, Y.; Leng, Y. *Phys. Rev. Lett.* **2011**, *107*, 147801.

[170] Yoshizawa, H.; Israelachvili, J. *The Journal of Physical Chemistry* **1993**, *97*, 11300–11313.

[171] Yoshizawa, H.; Israelachvili, J. *The Journal of Physical Chemistry* **1993**, *97*, 11300–11313.

[172] Diao, Y.; Espinosa-Marzal, R. M. *Nature Communications* **2018**, *9*.

[173] Gee, M. L.; Israelachvili, J. N.; McGuiggan, P. M. *J. Chem. Phys.* **1990**, *93*, 1895–1906.

[174] Li, H.; Rutland, M. W.; Atkin, R. *Phys. Chem. Chem. Phys.* **2013**, *15*, 14616–14623.

[175] Asencio, R. A.; Cranston, E. D.; Atkin, R.; Rutland, M. W. *Langmuir* **2012**, *28*, 9967–9976.

[176] Atkin, R.; Elbourne, A.; Rutland, M. W.; Sweeney, J.; Wanless, E. J.; Webber, G. B. *Chem. Commun.* **2013**, *49*, 6797–6799.

[177] Ruths, M.; Ohtani, H.; Grannick, S.; Greenfield, M. *Tribology Letters* **1999**, *6*.

[178] Hallett, J. E.; Perkin, S.; Smith, A. M. *PNAS* **2019**, *116*, 25418–25423.

[179] Liu, X.; Zhou, F.; Liang, Y.; Liu, W. *Wear* **2006**, *261*, 1174–1179.

[180] Doig, M.; Warrens, C. P.; Camp, P. J. *Langmuir* **2013**, *30*, 186–195.

[181] Bhushan, B.; Landman, U.; Israelachvili, J. N. *Nature* **1995**, *374*, 607–616.

[182] Berman, A. D.; Ducker, W. A.; Israelachvili, J. N. In *Physics of Sliding Friction*; Persson, B. N. J., Tosatti, E., Eds.; Springer Netherlands: Dordrecht, 1996; pp 51–67.

[183] Klein, J.; Kumacheva, E.; Perahia, D.; Mahalu, D.; Warburg, S. *Faraday Discuss.* **1994**, *98*, 173.

[184] Zarei, M.; Aalaie, J. *Journal of Materials Research and Technology* **2020**, *9*, 10411–10433.

[185] Barnes, A.; Bartle, K.; Thibon, V. *Tribology International* **2001**, *34*.

[186] .Shogrin, B.; Jones, R.; Herrera-Fierro, P. *Trib. Trans.* **1995**, *52*.

[187] Qu, J.; Luo, H.; Chi, M.; Ma, C.; Blau, P. J.; Dai, S.; Viola, M. B. *Tribology International* **2014**, *71*, 88–97.

[188] Dowson, D. *Wear* **1995**, *190*, 125–138.

[189] Campen, S.; Green, J.; Lamb, G. *Tribol Lett* **2012**, *48*, 237–248.

[190] Bovington, C.; Korcek, S.; Sorab, J. In *Lubrication at the Frontier*; Dowson, D., Priest, M., Taylor, C., Ehret, P., Childs, T., Dalmaz, G., Berthier, Y., Flamand, L., Georges, J.-M., Lubrecht, A., Eds.; Tribology Series; Elsevier, 1999; Vol. 36; pp 205–214.

[191] Lu, X.; Khonsari, M.; Gelinck, E. *J. Tribology* **2006**, *128*, 789–794.

[192] van Engers, C. D.; Balabajew, M.; Southam, A.; Perkin, S. *Review of Scientific Instruments* **2018**, *89*, 123901.

[193] Zheng, W.; Perez-Martinez, C. S.; Petriashvili, G.; Perkin, S.; Zappone, B. *Soft Matter* **2019**, *15*, 4905–4914.

[194] Hallett, J. E.; Hayler, H. J.; Perkin, S. *Phys. Chem. Chem. Phys.* **2020**, *22*, 20253–20264.

[195] Klein, J. *J. Chem. Soc., Faraday Trans. 1* **1983**, *79*, 99.

[196] Klein, J.; Kumacheva, E. *J. Chem. Phys.* **1998**, *108*, 6996–7009.

[197] Israelachvili, J. N. *Journal of Colloid and Interface Sciences* **1973**, *44*, 259–270.

[198] Levins, J. M.; Vanderlick, T. K. *J. Colloid Interface Sci.* **1993**, *158*, 223.

[199] Christenson, H. K.; Thomson, N. H. *Surface Science Reports* **2016**, *71*, 367–390.

[200] Briscoe, W.; Chai, L.; Dunlop, I.; Kampf, N.; Klein, J.; Kumacheva, E.; Perkin, S.; Raviv, U.; Seo, M.; Titmuss, S. *Langmuir* **2006**, *22*, 6142–6152.

[201] Chai, L.; Klein, J. *Langmuir* **2007**, *23*, 7777–7783.

[202] Perkin, S.; Zappone, B.; Zheng, W. *Rev. Sci. Instrum.* **2018**, *89*, 085112.

[203] Hallett, J. E.; Agg, K. J.; Perkin, S. *Proceedings of the National Academy of Sciences* **2023**, *120*, e2215585120.

[204] Adibnia, V.; Mirbagheri, M.; Latreille, P.-L.; De Crescenzo, G.; Rochefort, D.; Banquy, X. *Langmuir* **2019**, *35*, 15585–15591.

[205] Chen, Y. J.; Cheng, H. W.; Dienemann, J. N.; Merola, C.; Stock, P.; Valtiner, M. *Sci. Rep.* **2016**, *6*.

[206] Ogawa, S.; Okubo, H.; Kawada, S.; Kodama, E.; Sato, K.; Watanabe, M. *Surf. Interface Anal.* **2019**, *51*, 17–20.

[207] Heuberger, M.; Israelachvili, J. N.; Luengo, G.; Tsuchiya, M. *Journal of Food Science* **1997**, *62*, 767–773.

[208] Bandara, S. R.; Espinosa-Marzal, R. M.; Han, M.; Leal, C.; Kim, H. *Soft*

Matter **2019**, *15*, 9609–9613.

[209] Demirel, A. L.; Granick, S. *Phys. Rev. Lett.* **1996**, *77*, 2261–2264.

[210] Lundgren, S.; Ruths, M.; Danerlöv, K.; Persson, K. *Journal of Colloid and Interface Science* **2008**, *326*, 530–536.

[211] Abbott, A. et al. *Faraday Discuss.* **2018**, *206*, 549–586.

[212] Garcia, L.; Jacquot, L.; Charlaix, E.; Cross, B. *Faraday Discuss.* **2018**, *206*, 443–457.

[213] Espinosa-Marzal, R. M.; Han, M. *Lubricants* **2018**, *6*.

[214] Harrowell, P.; Jabbarzadeh, A.; Tanner, R. *Tribology International* **2007**, *40*, 1574–1586.

[215] Israelachvili, J. N.; Chen, Y.-L.; Yoshizawa, H. *Journal of Adhesion Science and Technology* **1994**, *8*, 1231–1249.

[216] Somers, A. E.; Howlett, P. C.; Sun, J.; MacFarlane, D. R.; Forsyth, M. *Tribology Letters* **2010**, *40*, 279–284.

[217] Atkin, R.; Cooper, P. K.; Darwish, T. A.; Le Brun, A. P.; Li, H.; Nelson, A.; Yepuri, N. R.; Warr, G. G.; Webber, G. B. *J. Phys. Chem. C.* **2018**, *122*, 24077–24084.

[218] Zhang, Y.; Rutland, M. W.; Luo, J.; Atkin, R.; Li, H. *The Journal of Physical Chemistry C* **2021**, *125*, 3940–3947.

[219] Deng, Z.; Klimov, N. N.; Solares, S. D.; Li, T.; Xu, H.; Cannara, R. J. *Langmuir* **2013**, *29*, 235–243.

[220] Lomakin, E.; Mossakovsky, P.; Bragov, A.; Lomunov, A.; Konstantinov, A. Y.; Kolotnikov, M.; Antonov, F.; Vakshtein, M. *Archive of Applied Mechanics* **2011**, *81*, 2007–2020.

[221] Minghai, W.; Kun, L.; Li, S. *Materials and Design* **2022**, *216*, 110570.

[222] Atkin, R.; Hayes, R.; Wakeham, D.; Warr, G. G. *J. Phys. Chem. B* **2009**, *113*, 5961–5966.

[223] Atkin, R.; Elbourne, A.; Voitchovsky, K.; Warr, G. G. *Chem. Sci.* **2015**, *6*,

527–536.

[224] Bresme, F.; Fajardo, O. Y.; Kornyshev, A. A.; Urbakh, M. *J. Phys. Chem. Lett.* **2015**, *6*, 3998–4004.

[225] Cai, M.; Liang, Y.; Yao, M.; Xia, Y.; Zhou, F.; Liu, W. *ACS Applied Materials & Interfaces* **2010**, *2*, 870–876.

[226] Mu, Z.; Zhou, F.; Zhang, S.; Liang, Y.; Liu, W. *Tribology International* **2005**, *38*, 725–731.

[227] Minami, I.; Kita, M.; Kubo, T.; Nanao, H.; Mori, S. *Tribology Letters* **2008**, *30*, 215–223.

[228] Weng, L.; Liu, X.; Liang, Y.; Xue, Q. *Tribology Letters* **2007**, *26*, 11–17.

[229] Fraser, K. J.; Izgorodina, E. I.; Forsyth, M.; Scott, J. L.; MacFarlane, D. R. *Chem. Commun.* **2007**, 3817–3819.

[230] Pivnic, K.; Bresme, F.; Kornyshev, A. A.; Urbakh, M. *ACS Applied Nano Materials* **2020**, *3*, 10708–10719.

[231] Bresme, F.; Fajardo, O.; Kornyshev, A.; Urbakh, M. *Sci. Rep.* **2015**, *5*.

[232] Bresme, F.; Fajardo, O. Y.; Kornyshev, A. A.; Pivnic, K.; Urbakh, M. *J. Phys. Chem. C.* **2018**, *122*, 5004–5012.

[233] David, A.; Fajardo, O. Y.; Kornyshev, A. A.; Urbakh, M.; Bresme, F. *Faraday Discuss.* **2017**, *199*, 279–297.

[234] Mahrova, M.; Pagano, F.; Pejakovic, V.; Valea, A.; Kalin, M.; Igartua, A.; Tojo, E. *Tribology International* **2015**, *82*, 245–254.

[235] Garcia, L.; Jacquot, L.; Charlaix, E.; Cross, B. *Faraday Discuss.* **2018**, *206*, 443–457.

10 | Appendix

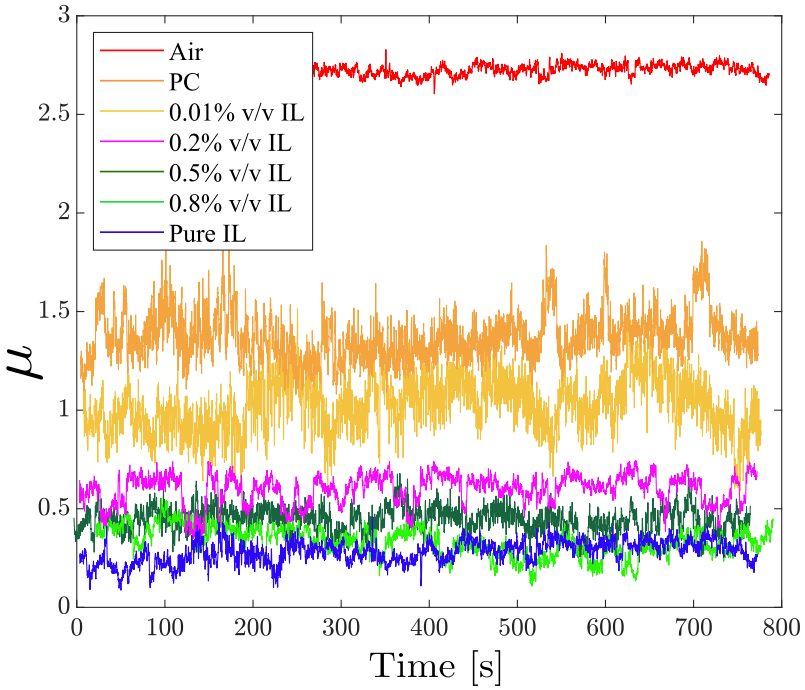


Figure 10.1: The friction response of $[C_4C_1P_{yrr}][TFSI]$ at varying volume fractions in PC for a normal load of in a steel-steel contact at 1N.

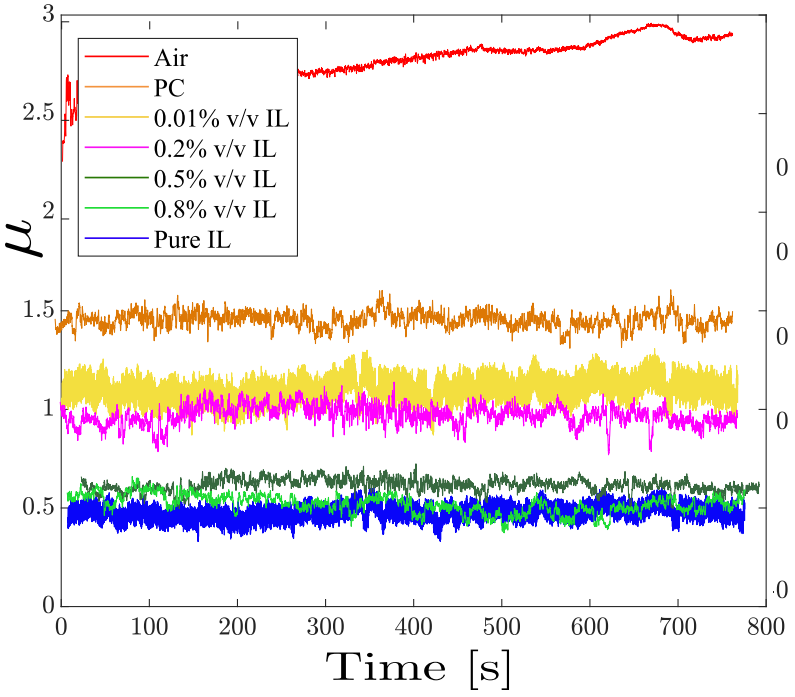


Figure 10.2: The friction response of $[C_4C_1P_{yrr}][TFSI]$ at varying volume fractions in PC for a normal load of in a steel-steel contact at 2N.

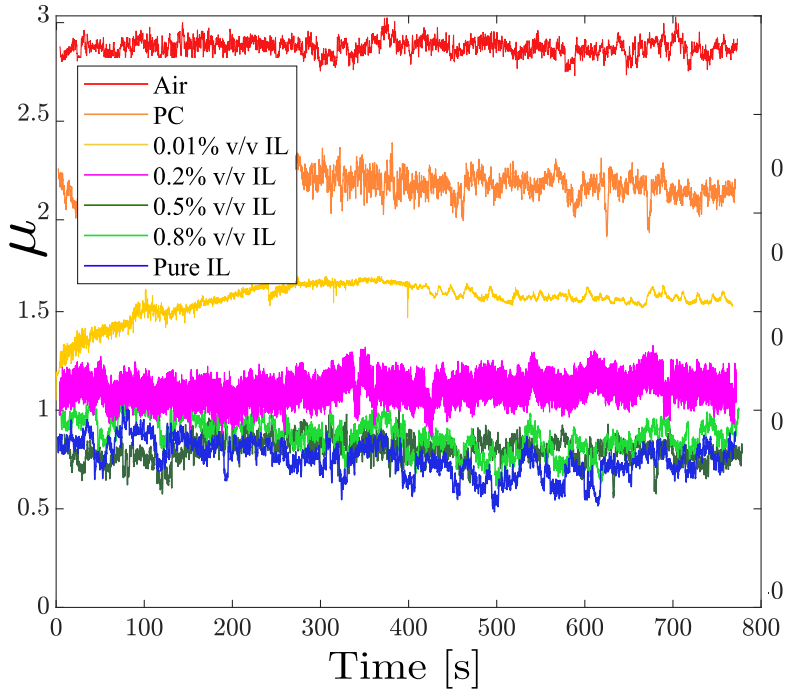


Figure 10.3: The friction response of $[C_4C_1P_{yrr}][TFSI]$ at varying volume fractions in PC for a normal load of in a steel-steel contact at 5N.

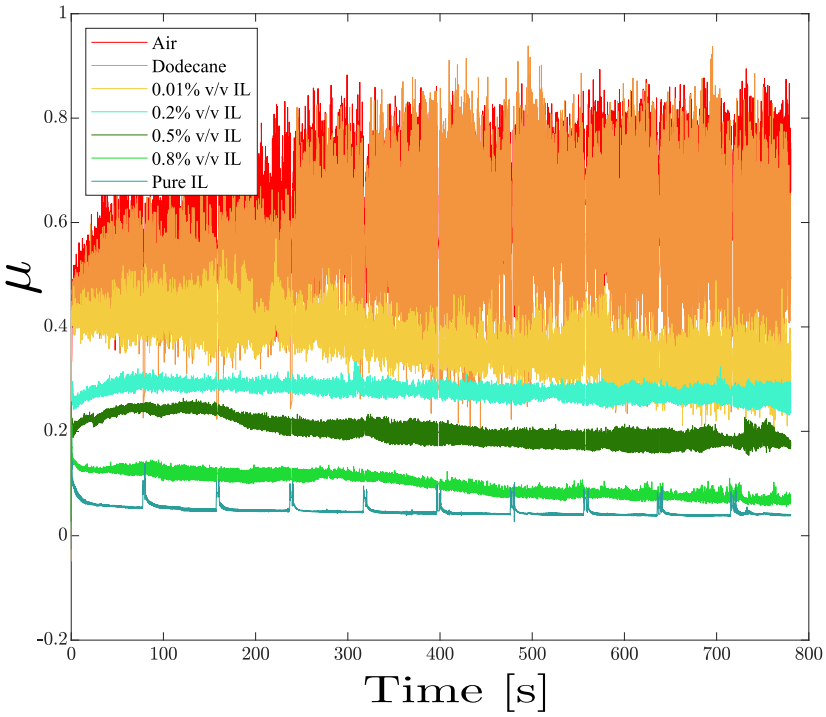


Figure 10.4: The frictional response of $[P_{6,6,6,14}][(^{i}C_8)_2PO_2]$ at varying volume fractions in dodecane for a normal load in a mica-steel contact at 1N.

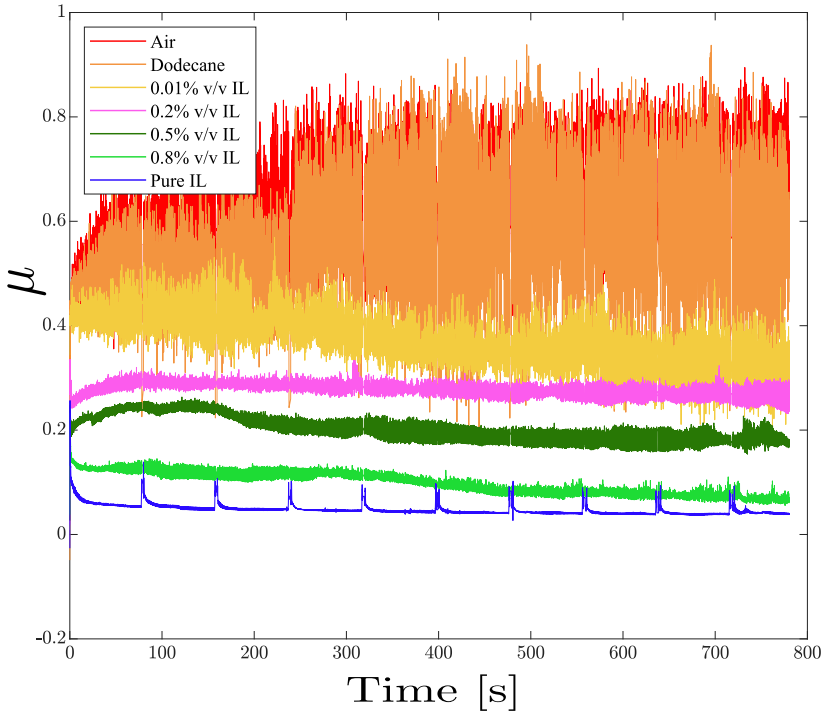


Figure 10.5: The frictional response of $[P_{6,6,6,14}][(^{i}C_8)_2PO_2]$ at varying volume fractions in dodecane for a normal load in a mica-steel contact at 2N.

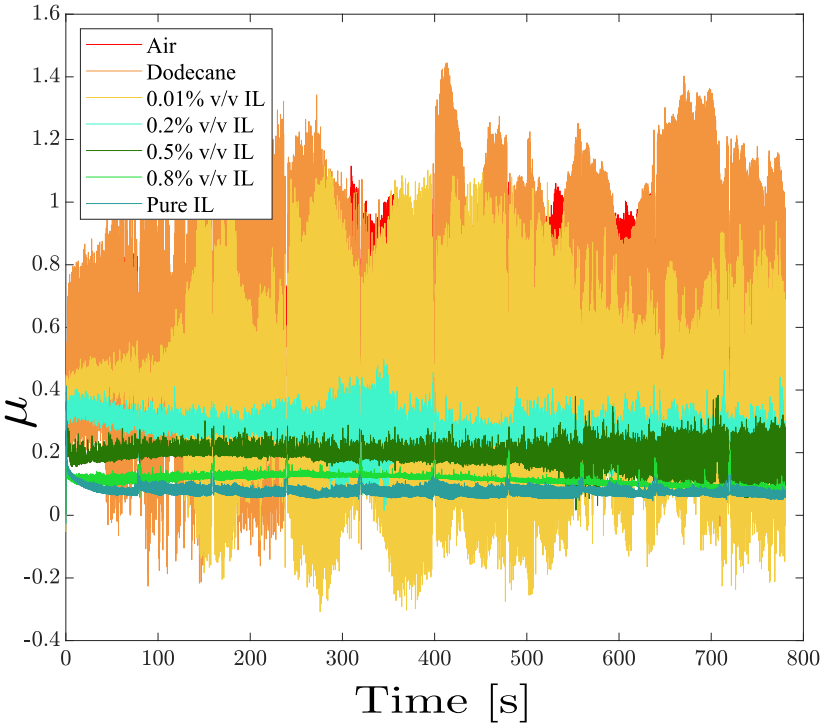


Figure 10.6: The frictional response of $[P_{6,6,6,14}][(^iC_8)_2PO_2]$ at varying volume fractions in dodecane for a normal load in a mica-steel contact at 5N.

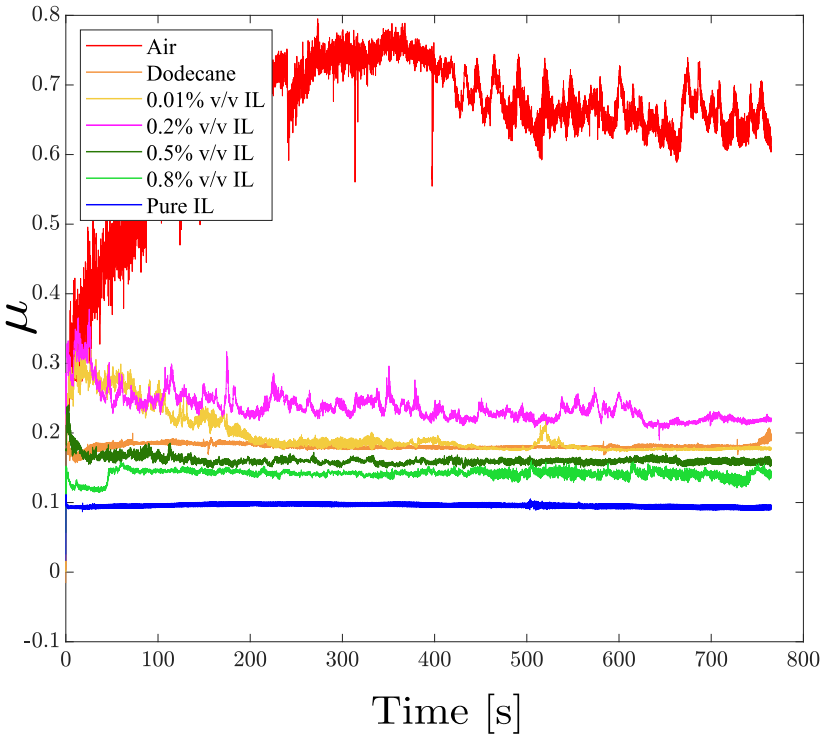


Figure 10.7: The frictional response of $[P_{6,6,6,14}][(^iC_8)_2PO_2]$ at varying volume fractions in dodecane for a normal load in a steel-steel contact at 1N.

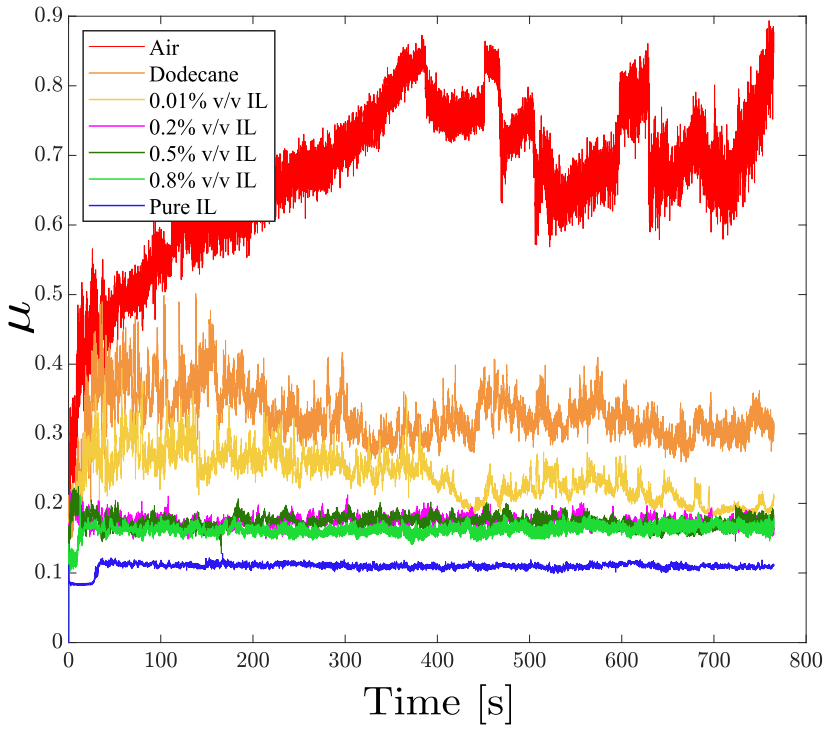


Figure 10.8: The frictional response of $[P_{6,6,6,14}][(^{i}C_8)_2PO_2]$ at varying volume fractions in dodecane for a normal load in a steel-steel contact at 2N.

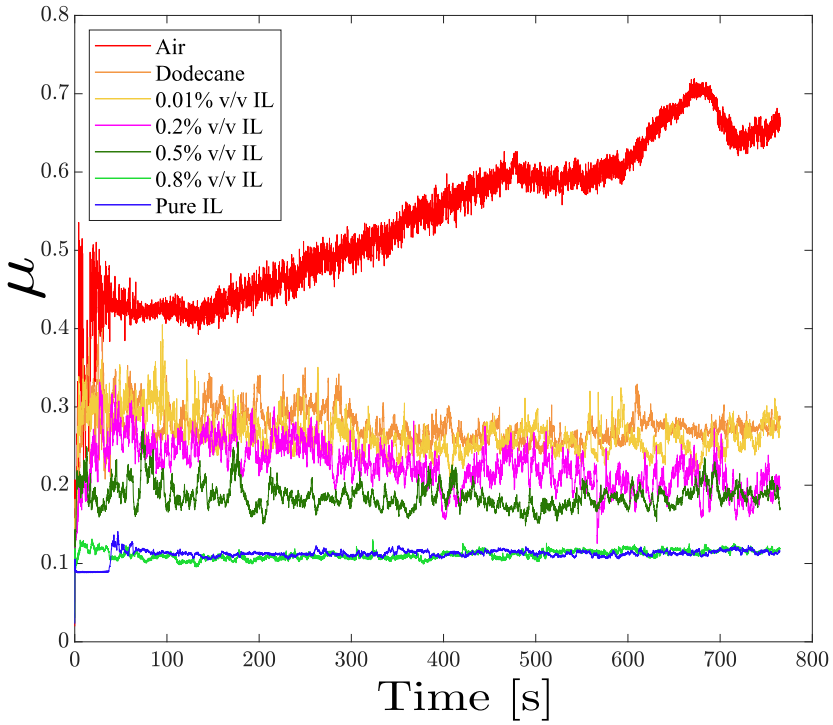


Figure 10.9: The frictional response of $[P_{6,6,6,14}][(^{i}C_8)_2PO_2]$ at varying volume fractions in dodecane for a normal load in a steel-steel contact at 5N.

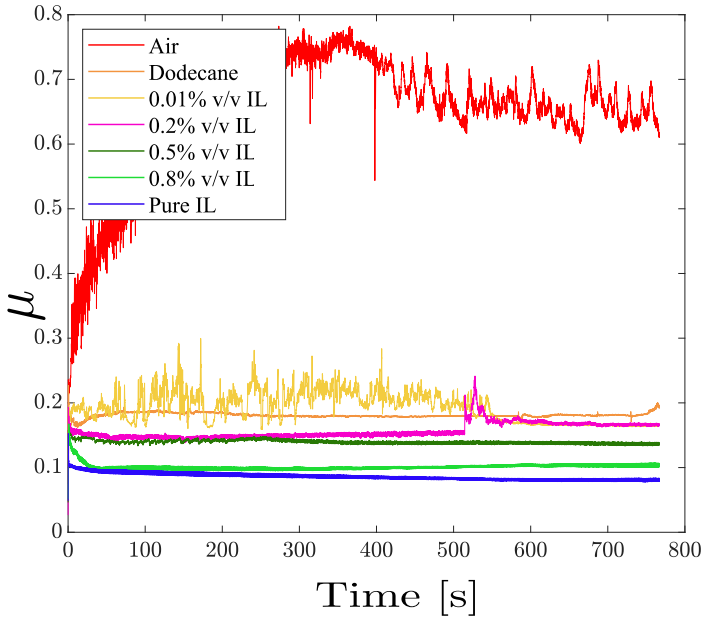


Figure 10.10: The frictional response of $[P_{6,6,6,14}][TFSI]$ at varying volumes fractions in dodecane for a normal load of 1N in a mica-steel contact.

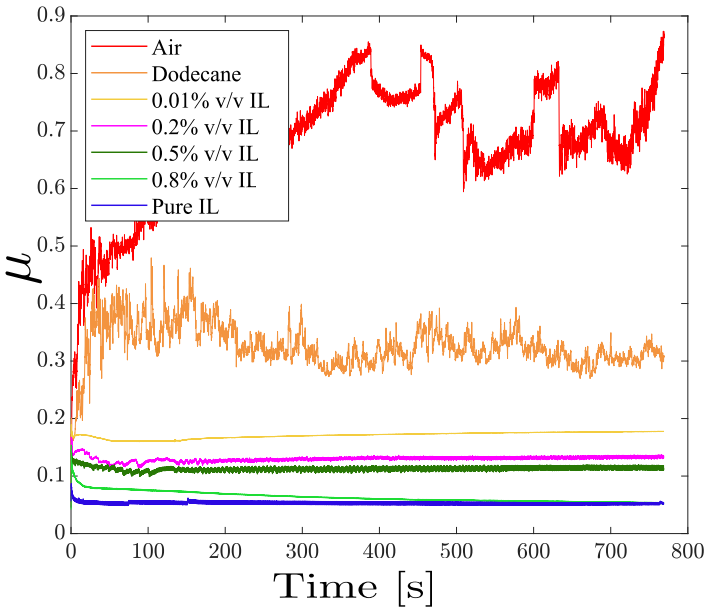


Figure 10.11: The frictional response of $[P_{6,6,6,14}][TFSI]$ at varying volumes fractions in dodecane for a normal load of 2N in a mica-steel contact.

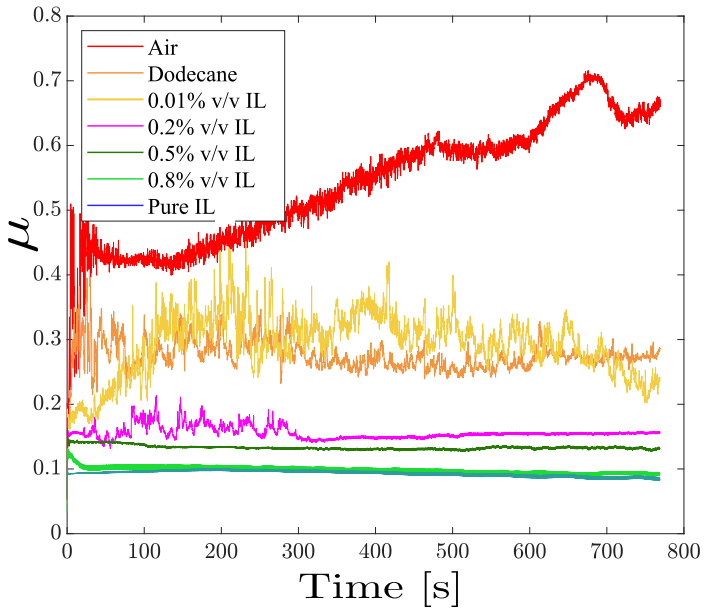


Figure 10.12: The frictional response of $[P_{6,6,6,14}][TFSI]$ at varying volumes fractions in dodecane for a normal load of 5N in a mica-steel contact.

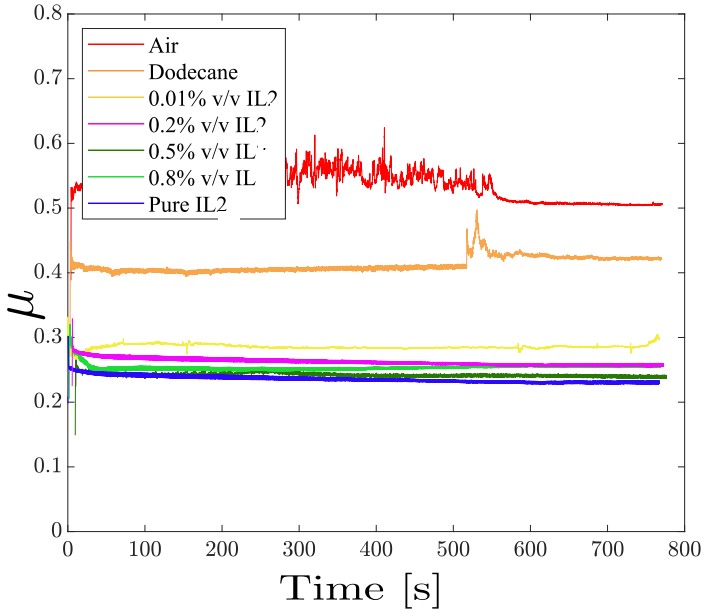


Figure 10.13: The frictional response of $[P_{6,6,6,14}][TFSI]$ at varying volume fractions in dodecane for normal loads of 1N at a steel-steel contact.

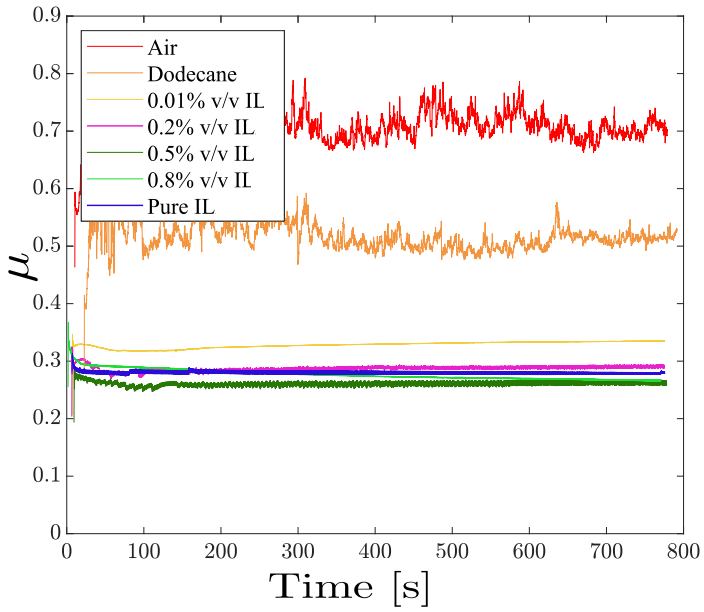


Figure 10.14: The frictional response of $[P_{6,6,6,14}][TFSI]$ at varying volume fractions in dodecane for normal loads 2N at a steel-steel contact.

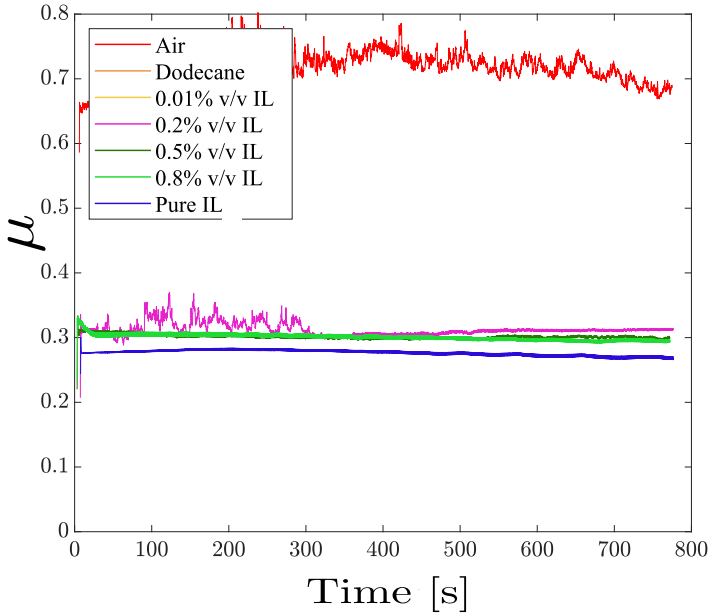


Figure 10.15: The frictional response of $[P_{6,6,6,14}][TFSI]$ at varying volume fractions in dodecane for normal loads of 5N at a steel-steel contact.

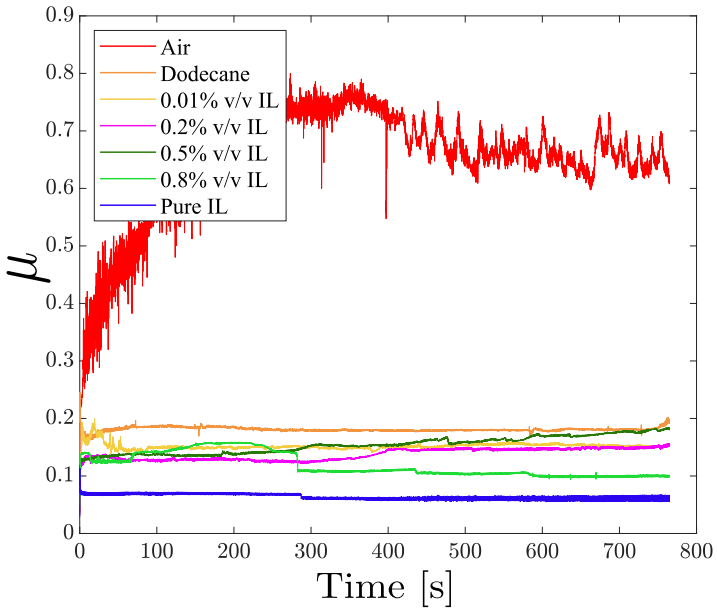


Figure 10.16: The frictional response of $[P_{1,4,4,4}][TFSI]$ at varying volume fractions in dodecane for a normal load of at a mica-steel contact at 1N.

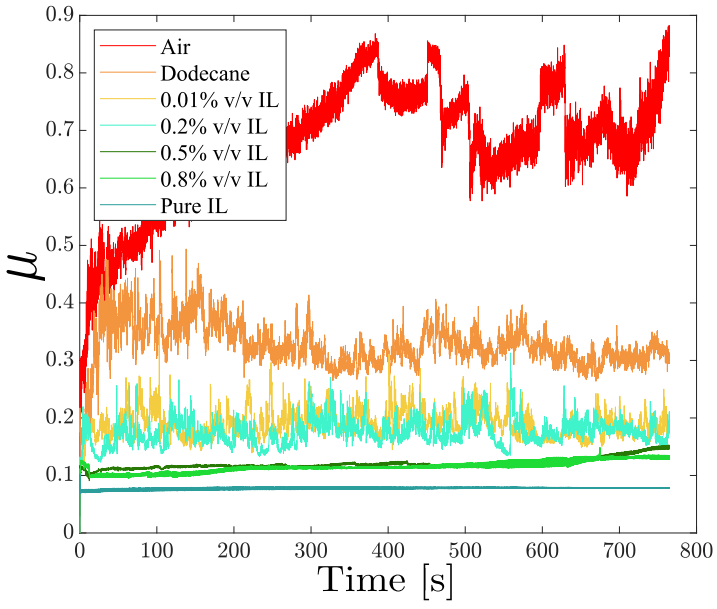


Figure 10.17: The frictional response of $[P_{1,4,4,4}][TFSI]$ at varying volume fractions in dodecane for a normal load of at a mica-steel contact at 2N.

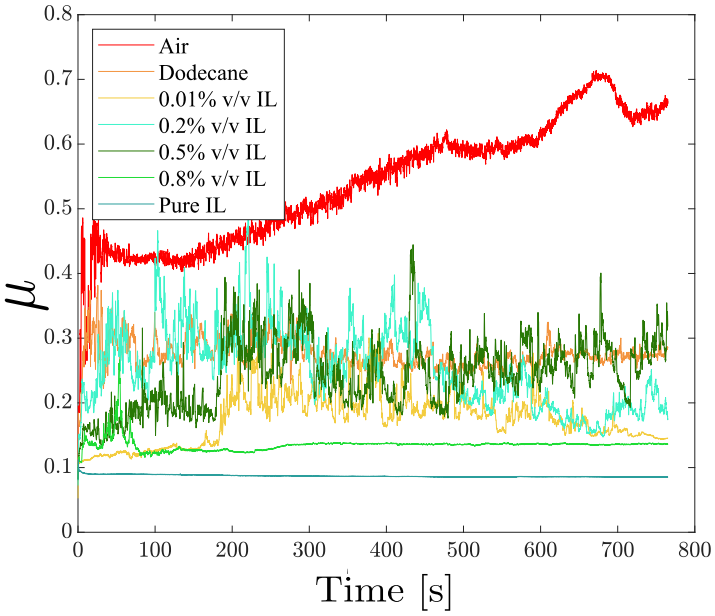


Figure 10.18: The frictional response of $[P_{1,4,4,4}][TFSI]$ at varying volume fractions in dodecane for a normal load of at a mica-steel contact at 5N.

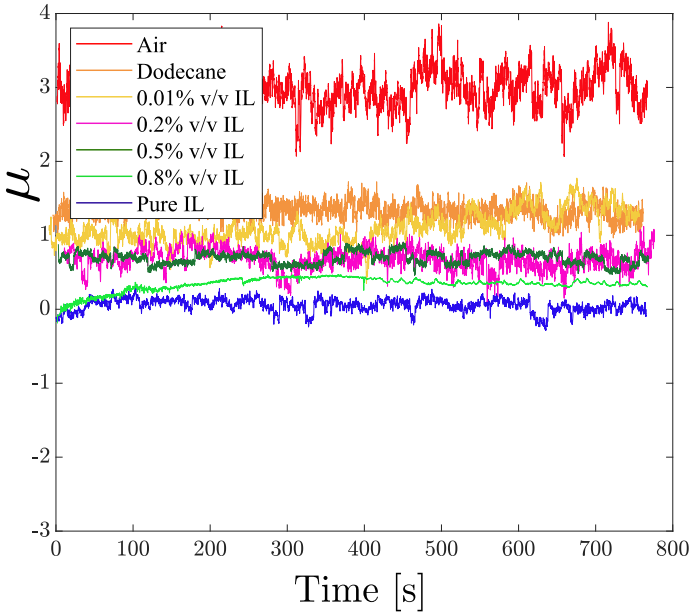


Figure 10.19: The frictional response of $[P_{1,4,4,4}][TFSI]$ at varying volume fractions in dodecane for a normal load of 1N at a steel-steel contact.

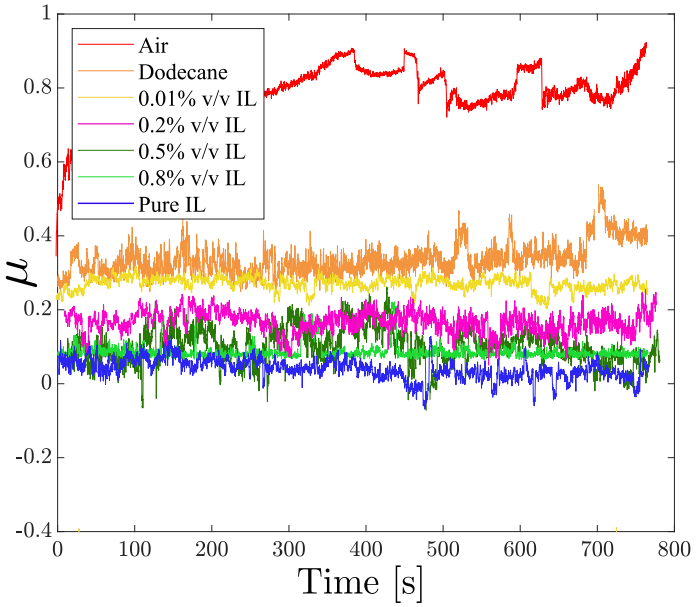


Figure 10.20: The frictional response of $[P_{1,4,4,4}][TFSI]$ at varying volume fractions in dodecane for a normal load of 2N at a steel-steel contact.

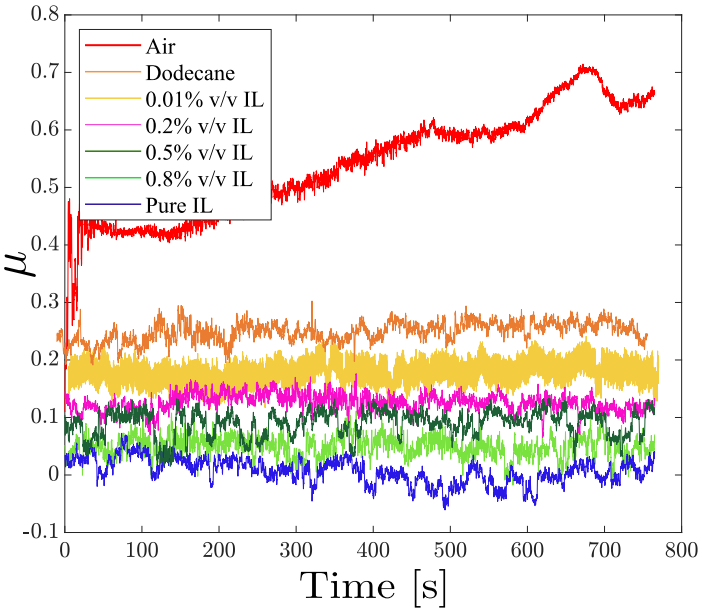


Figure 10.21: The frictional response of $[P_{1,4,4,4}][TFSI]$ at varying volume fractions in dodecane for a normal load of 5N at a steel-steel contact.